SAPIENZA
UNIVERSITÀ DI ROMA

Slow timescales in out of equilibrium systems: the case of vibrofluidized granular matter

Scuola di Dottorato "Vito Volterra"

Dottorato di Ricerca in Fisica – XXXIV Ciclo

Candidate

Andrea Plati
ID number 1540495

Thesis Advisor

Dr. Andrea Puglisi

A thesis submitted in partial fulfillment of the requirements
for the degree of Doctor of Philosophy in Fisica

October 2021

Thesis defended on 11th February 2022
in front of a Board of Examiners composed by:

Prof. Roberto Di Leonardo (chairman)

Dr. José Lorenzana

Prof. Roberto Benzi

Slow timescales in out of equilibrium systems: the case of vibrofluidized granular matter
Ph.D. thesis. Sapienza – University of Rome

This thesis has been typeset by LaTeX and the Sapthesis class.

Author's email: andrea.plati@uniroma1.it

Contents

Acknowledgements

Looking back on these three years, I'm grateful for how I grew up. Many people have been part of this personal and scientific growth. Here I want to acknowledge them.

I would like to thank my advisor Andrea Puglisi for his clear guidance during my research work. I really appreciated his ability to maintain a fair balance between, on one hand, valuing and giving direction to my efforts and on the other, leaving me enough space to reflect, act and make decisions independently. Most of the time, a quick chat with him was enough to refresh my mind and move on.

I would like to sincerely thank Alessandro Sarracino, Andrea Gnoli, Alberto Petri, Andrea Baldassarri and Sergio Ciuchi for working together and for contributing to my education in the field of granular systems and beyond. They shared with me interesting insights, useful advice and new points of view.

I would like to warmly thank Angelo Vulpiani, Giacomo Gradenigo, Fabio Cecconi and all the friends of the TNT group for having created so many opportunities for scientific and convivial exchange over the years. I have really nice memories of that.

A warm greeting and thanks also to Lucilla De Arcangelis, Eugenio Lippiello and Giuseppe Petrillo for working together on an important part of my PhD project.

Thanks to Giuseppe Foffi, Frank Smallenbourg and Etienne Fayenne for the new project started together and for the joint struggle against bureaucracy.

Special thanks to Marco Baldovin, Francesco Borra and Lorenzo Caprini. I keep precious memories of trips, scientific discussion, dialogues and conferences we shared together.

A warm hug to my friends of the physics department with whom I shared many lunches, coffees and beers during the last year.

Thanks to all the PiRoom inhabitants with whom I shared the place where both satisfying and frustrating moments of our research happened.

One thing I learned during my PhD is that there is everything outside the academy that saves you from the academy itself. The precarious condition of the younger generations, combined with the considerable mental energy required for research activities, means that a PhD project can become the perfect excuse for

isolating oneself and withdrawing from the world. Keeping commitments, responsibilities and affections in contexts other than the academic one has been, besides being beautiful in itself, also of fundamental importance for me to go through this path in a healthy way. There are many people that I acknowledge in this regard.

I want to heartily thank all my friends from the neighbourhood where I grew up. They represent the people with whom to spend peaceful moments, no matter what.

I'm very grateful to my roommates Ornella, Debora and Maya to have explored with me an alternative way to feel at home and with family.

I deeply thank my dear friend Naima for listening to me in those moments when I need to confide.

I want to thank my Buddhist comrades for all the experiences and dialogues shared together.

I want to thank also the comrades of officina, ciclofficina and de Lollis Underground. The experiences done in these contexts gave a special value to my life in Sapienza.

A special thank goes to my parents Maria Lucia and Riccardo and my sister Chiara for their continued support and deep affection.

And thanks to Miki for always being there.

Index of acronyms and abbreviations

In this thesis, many acronyms are used. They are defined at least one time in each chapter. However, for ease of reading, here is a summary of them.

BL/BR	Bottom Left/Bottom Right
CM	Center of Mass
DEM	Descrete Element Method
DOF	Degrees Of Freedom
DSMC	Direct Simulation Monte Carlo
FDR	Fluctuation-Dissipation Relation
FEM	Finite Element Method
FPE	Fokker-Planck Equation
GLE	Generalized Langevin Equation
HHP	Homogeneously Heated Phase
HM	Hertz-Mindlin
LE	Langevin Equation
MB	Maxwell-Boltzmann
MC	Molecular Chaos
MD	Molecular Dynamics
MSD	Mean Squared Displacement
ND	No Defects
NESS	Non-Equilibrium Steady State
NHHP	Non-Homogeneously Heated Phase
OU	Ornstein-Uhlenbeck
PBC	Periodic Boundary Conditions
PR	Persistent Rotation
PSD	Power Spectral Density
SD	Superdiffusion (Chap. 3), Symmetric Defects (Chap. 5)
SDE	Stochastic Differential Equation
TL/TR	Top Left/Top Right
VACF	Velocity Autocorrelation Function
VPSD	Velocity Power Spectral Density
w.r.t.	with respect to

Introduction

If during the observation of a natural phenomenon, a timescale much larger than the ones defined by external parameters is found, several questions may arise from the physical point of view. How does this timescale spontaneously emerge? Are there mathematical models for its description and prediction? Which are the variables where the memory is stored? In equilibrium and/or thermal systems there are many phenomena where an established theoretical framework to answer the above questions has been developed. The critical slowing down near a phase transition or the dynamical arrest in glass-forming liquids are two examples of that. Nevertheless, out of equilibrium and/or athermal systems often lack such clear benchmarks. In this thesis, we address the problem of emerging slow timescales in the context of non-equilibrium athermal systems through the study of vibrofluidized granular materials. Granular matter is ubiquitous in nature and very important for human activities. As a research field, it is relevant for both applications [168, 53, 104] and fundamental physics [97, 59, 135, 100]. In the physical description of a granular system, the internal degrees of freedom of the single units (i.e. the grains) are neglected implying energy dissipation. This, together with their athermal nature, makes granular materials inherently out of thermodynamic equilibrium. In the last three decades, they have become more and more relevant for the general understanding of nonequilibrium systems [82, 173], as well as for the development of fluctuating hydrodynamics [36, 87] and stochastic thermodynamics [73, 158].

This thesis focuses on the description and the modelization of a novel phenomenon discovered in a dense vibrated granular system thanks to the combined use of experiments and numerical simulations. It consists of the possibility for a disordered granular packing to convert the fast and unbiased mechanical vibrations to which it is subjected into a slow and directed collective motion. We point out that many applications in electronics and a lot of biological processes rely on analogous mechanisms that rectify unbiased fluctuations (ratchet effect) [89, 161]. During the thesis, we highlight the nonequilibrium aspects of the phenomenon under study and we discuss how it can be understood as a peculiar instance of the ratchet effect. The way the results are presented and the theoretical models we propose are designed to make our study useful also for research topics not strictly related to granular matter such as active matter, anomalous diffusion and classical transport.

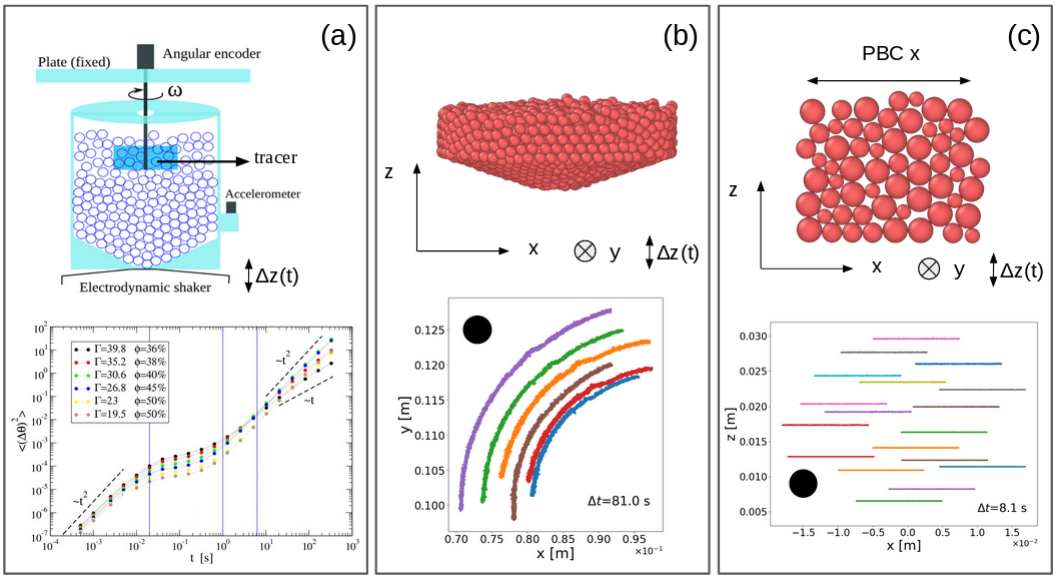

Figure 0.1. Different manifestations of the phenomenon on which this thesis is focused. For each panel, we show the data (bottom) and the system to which they refer (top). We started from the experimental evidence of superdiffusion at late times in the mean squared displacement of a rotational tracer immersed into a dense vibrated granular system for different shaking accelerations Γ (a). This anomalous diffusion is associated to long persistent drifts of the absolute angle $\theta(t)$ travelled by the blade. In order to relate this behavior to the grain dynamics (which cannot be directly measured in that experiments), we developed realistic simulations of the same setup unveiling slow collective rotations of the granular medium (b). This collective motion is strongly coupled with the tracer dynamics and originates its anomalous diffusion. Then, we simplified the geometry of the simulations considering quasi-2D setup with periodic boundary conditions (PBC) along the x-direction (c) that allowed a more detailed analysis of the persistent drifts and their relation with the spatial structure of the granular packings. This last study makes us realise that all the rectification phenomena mentioned so far can be explained by a ratchet effect governed by the interplay of frictional forces and the spatial symmetry breaking of the grain configuration. Each setup is vertically vibrated with a time-dependent signal $\Delta z(t)$, black circles are representative for the typical dimension of the grains. The aim of this figure is to have at a glance an idea of the phenomenology under study, details on the systems and the data analysis are provided in the main chapters of the thesis.

The background of our analysis is the experimental evidence of anomalous diffusion at late times in the dynamics of a tracer immersed in a dense vibrated granular fluid (Fig. 0.1a) [175]. A subsequent numerical study clarified that the origin of such an effect is a slow collective motion of the granular medium itself (Fig. 0.1b) [144]. Then, two different modelling approaches have been followed. The first one is a phenomenological theory aiming at reproducing the experimental and numerical results of the previous studies [146]; the second one consists of a lattice model to explain the emergence of long-range correlations and slow timescales in a driven granular system [148]. In order to understand the physical mechanisms underlying this phenomenon, further numerical analysis of a simplified numerical setup has been carried on. This unveiled the crucial relation between the transient symme-

try breaking induced by disorder in the granular medium and its slow drifts (Fig. 0.1c) [147]. Finally, considering that the external energy is supplied to the system on typical timescales much faster than the collective motion, we also performed a numerical investigation of the short-time granular dynamics [145]. Figure 0.1 summarises the main steps of our investigation. From both the tracer mean squared displacement and the grain trajectories, it is clear that we are dealing with a dynamics where many relevant timescales are involved: from fast vibrations to slow persistent drifts shared by many particles in the system. Examples of questions we are going to answer in the following chapters are: how to model this kind of motion? How do single grains participate in it? Which are the minimal ingredients for its occurrence?

Regarding the techniques adopted in the thesis, we use the Discrete Element Method (DEM) [55] for the numerical simulation of vibrofluidized granular systems in a wide range of geometries and density regimes. DEM simulations, that we implement through the LAMMPS package [1, 149], solve the grain-grain interactions and the grain-boundary ones starting from a visco-elastic contact model. This allows reproducing in silico the experimental setups with realistic proportions and material properties. From the theoretical side, the models we treat analytically take the form of multivariate stochastic differential equations with linearly coupled variables and Gaussian noises. In the phenomenological approach, we have three fundamental macroscopic variables: one is the tracer velocity while the remaining two are related to the dynamics of the granular fluid. For the lattice model, we consider a velocity field defined on a one-dimensional grid with viscous interactions. Each site of such a lattice ideally represents the average behaviour of a grain layer belonging to a higher dimensional system.

The structure of the thesis is the following. In chapter 1, we outline the motivations and the background of our research by providing a general introduction to granular matter and its relevance for non-equilibrium statistical mechanics. We also discuss the problem of the modelization of slow variables from a historical perspective. Chapter 2 reviews the experimental study on anomalous diffusion and reports a systematic comparison between experiments and simulations in order to validate our computational approach. Here we also explain how the DEM has been applied to our case study. In chapter 3, we discuss the numerical evidence of slow persistent drifts of the whole granular medium and the phenomenological model used to reproduce numerical and experimental results. Chapter 4 is devoted to the on-lattice model. Analytical results for the diverging characteristic times of the dynamics and the power-law decay of spatial correlation functions are provided. The role of disorder in the granular medium is discussed in chapter 5. There, we show that the mechanism underlying the formation of the granular collective drifts is a ratchet effect governed by the interplay of friction and asymmetries in the bulk structure. We then conclude, in chapter 6, with some insights into the fast timescales that characterize the energy transfer to vibrofluidized granular systems. A counter-intuitive nonmonotonic relation between the adsorbed energy and the input one is the main result of this study.

Chapter 1

Granular Matter: a toolbox for non-equilibrium statistical physics

1.1 Granular systems as emerging materials

In nature we find three main states of matter, they are the gaseous, the liquid and the solid one. The stability and the properties of these states are related to the specific way in which the molecules (i.e. their fundamental units) are organized.

Nevertheless, being "a whole" or "a building block" is not an intrinsic property of a physical system: it depends on the level of description that we, as humans that try to understand natural phenomena, decide to use. We can see a cell as the building block of a living organism or as a complex system made upon interacting macromolecules of various kind. And again macromolecules (as proteins) are themselves complex systems whose global properties cannot be trivially traced back to the behaviour of the single units.

This nesting doll of fundamental bricks can be interrupted at a given size provided that one is able to describe the more relevant effects of the smaller dolls as effective properties for the chosen scale. This procedure is called "coarse-graining" and it is usually very difficult to be performed in a rigorous way. Formally, it implies the marginalization of the non-relevant degrees of freedom. In many cases the right coarse-grained description is suggested by empirical observations or imposed by practical requirements. As we shall see, the physics at the coarse-grained level can be really different (and sometimes in apparent contradiction) with respect to the principles on which the lower levels are based.

Coming back to states of matter, one might ask: what about the behaviour of a material made of macroscopic objects? And what properties of the objects state of matter are relevant to understanding it? As usual in physics, the answer is: it depends. In this case, an important distinction is made on the interacting forces between these objects. If they are heavy enough to undergo gravitational interaction and there is sufficient free space between them, then the particular state of matter of which they are constituted is not relevant. One can map the problem into a N-body system where the single units are material points and their only relevant

property is the mass. This is what happens in many problems of astrophysics where the interacting units (for instance planets) are often formed by a mixture of gases, liquids and solids. In this context, a coarse-grain procedure is useful to derive the mean perturbative effects of heavenly bodies whose dynamics is characterized by timescales that are much faster than the ones of the planets [12, 114].

In this thesis, we treat another kind of system: granular materials. What we said so far allows us to define them as unambiguously as possible.

Definition of granular materials

Granular materials are macroscopic systems whose fundamental units (i.e. the grains) are macroscopic (mainly solid) objects confined in such a way to interact through reciprocal contact.

The concept of macroscopicity is then used in two ways. We have *macroscopic systems* because a large number of degrees of freedom is considered. This number is large enough to require a statistical description but not large enough to neglect fluctuations as in thermodynamics and hydrodynamics of thermal systems (see below). We have *macroscopic fundamental units* because we neglect the internal degrees of freedom of the grains. Then, all the energy stored in their thermal agitation is lost at the granular level of description. This fact is taken into account by the presence of inelastic interactions between the grains. Moreover, granular materials are athermal because the energy scale defined by their typical masses and dimensions is several orders of magnitude larger than the thermal one: $mgd \sim 10^{12} k_b T$. Here, g is the gravity acceleration, T is the room temperature, k_b the Boltzmann constant while $m \sim \mathcal{O}(\geq 10^{-6} kg)$ and $d \sim \mathcal{O}(\geq 10^{-4} m)$. Granular matter is ubiquitous and is strictly related to human life: Sand, raw materials, cereals, powders but also systems a bit farther from the anthropic scale as Saturn rings and debris in tectonic faults are all examples of granular materials (Fig. 1.1). The dimensions of the grains can then start from tens of micrometres without in principle an upper limit while their number can be $N_g \sim \mathcal{O}(\geq 10^2)$. The typical system sizes span several orders of magnitude but they are always much lower than the Avogadro number $N_A \sim \mathcal{O}(10^{23})$. From a statistical point of view, this makes fluctuations around mean values more relevant than for thermal systems: $\sigma(X)/\langle X \rangle \sim N_g^{-1/2} \gg N_A^{-1/2}$, where X is an additive observable (i.e. an observable obtained as a sum of single-grains observables), $\langle X \rangle$ its mean value and $\sigma(X)$ its standard deviation. Without departing from an empirical description, it is straightforward to note some peculiarities of granular materials, especially by comparing their behaviour with the molecular matter one. We all know that the sand in a bottle can be poured in a glass as water but, at the same time, no one would try to jump from a trampoline into a pool of sand as if it were water. Understanding how sand can manifest liquid-like properties rather than solid-like ones may sound like mere intellectual speculation. Nevertheless, by reformulating the same problem in an industrial context we realize that it is not: will the coal flow outside a hopper or will it remain stuck inside (Fig. 1.2)? Which are the parameters (hopper dimensions, grains shape, etc.) relevant to this problem? This represents just a particular instance of the rich phenomenology that granular matter exhibits in different conditions. Nevertheless, it makes clear why granular

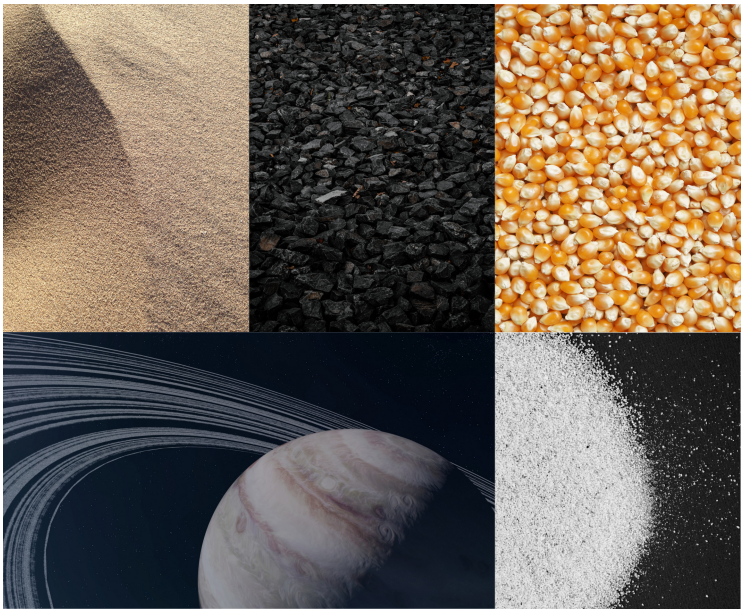

Figure 1.1. Examples of granular materials, from upper left to lower right: sand, coal, cereals, Saturn ring, salt. For credits see [2].

materials can be considered as a separate "emerging" state of matter that acquires meaning as the phenomena under study are far enough from the molecular scale.

1.2 The Science of Grains

This section aims to present granular materials as a scientific field with its historical stages, applications, methodologies and fundamental questions.

In the following paragraphs, after a brief historical overview, we will introduce non-equilibrium steady states (NESSs) in granular matter where a NESS can be reached thanks to a balance between external forcing and internal dissipation. We then present the phenomenology of vibrofluidized granular materials together with

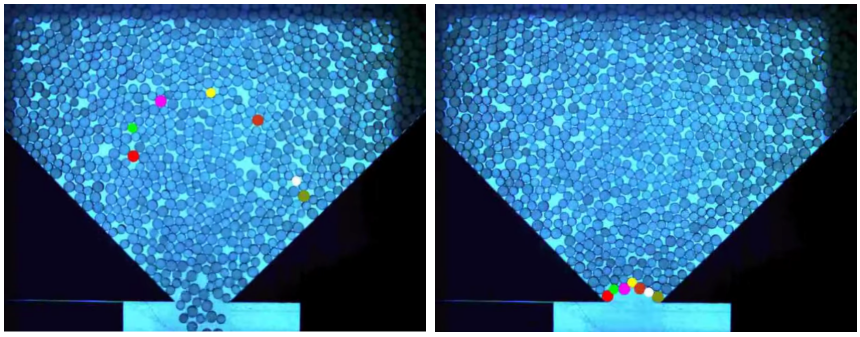

Figure 1.2. Right: grains flowing outside a hopper. Left: Grains jammed into a hopper. The obstruction is caused by the formation of a stable arc of grains close to the exit hole. Images reprinted from [190].

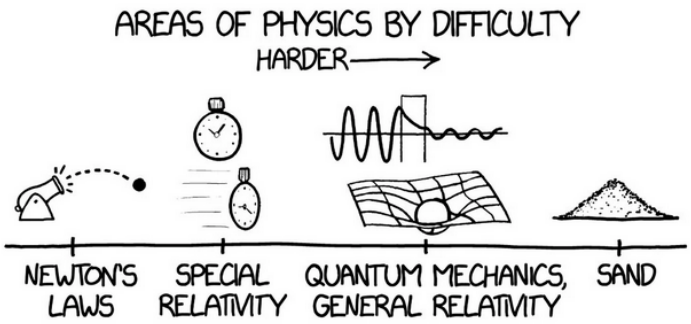

Figure 1.3. Hyperbolic representation of how the physics of granular materials is still nowadays a challegnig field of activity for researchers. The cartoon is taken from an article published in the New York Times in November 2020 [132].

a brief description of the main experimental, numerical and theoretical approaches used to study them.

1.2.1 A bit of granular history between applications and fundamental physics

Despite their apparent simplicity, granular materials are still nowadays a prolific field of research involving physicists, engineers and chemists all around the world [97, 59, 135] (see also Fig. 1.3 and [132] for a broad audience reference). As suggested by the previous paragraphs, granular phenomena are interesting both for applications and fundamental physics. On one hand, they are crucial for many kinds of industries (chemicals, food, pharmaceuticals, mining etc.) [168, 53] and for seismology [58]; on the other hand, they represent one of the most accessible systems to study non-equilibrium phenomena. Noteworthy behaviours for both perspectives reported in experiments and numerical simulations are for instance: the Brazil-nut effect [34], the ratchet effect [197, 81], spontaneous segregation of mixtures [178], acoustic fluidization in seismic fault [78], vibration-controlled viscosity [79]. They also exhibit a rich and complex rheological response [99, 80, 53]

From a historical point of view, it is worth saying that the interest in granular matter was stimulated by engineering [137, 32]. Nevertheless, during the last centuries, many famous physicists paid attention to the behaviour of these materials. They are for instance: C.A. Coulomb (1773), that highlighted the role of static friction for the stress propagation in granular media, M. Faraday (1831) who discovered convective phenomena in vibrated powders, O. Reynolds (1885) who studied the dilatation of sheared granular assemblies. An important contribution to the understanding of the static properties of these systems was given by H. A. Jannsen (1895) that measured the pressure exerted by a granular pile on its bottom as a function of the pile height $P(h)$ [98]. This profile follows the so-called Jannsen law $P(h) \propto 1 - \exp(-h/\Lambda)$ so it starts growing linearly (as the Stevino law) but then saturates to a constant value after a typical length scale Λ. The "microscopic" mechanism responsible for this behaviour is the formation of arches and vaults consisting of structures formed by grains that, thanks also to frictional contacts, discharge the

pressure on the side walls. Hourglasses work because of this: the flow of grains during the pouring is constant because the pressure is not determined by the (varying) total amount of sand in the upper septum. Just a slice of granular material high Λ contributes to it.

The great fascination of granular systems is also testified by the work of the scientist/soldier R. A. Bagnold: he made precise observations in the Lybian desert during World War II and once returned to London started to perform experiments on sand transport in air flows with a self-built wind tunnel. He determined the basic laws of this phenomenon and its book *Physics of Blown Sand and Sand Dunes* still represents an important instance of a systematic study on granular behaviours [14].

In the last three decades, the field of granular matter experienced a renewed season of scientific activity. The inefficiency of industrial processes involving granular materials [104], new technologies exploiting granular properties [91, 170] and a growing interest into applying statistical mechanics to athermal systems, stimulated scientists and institutions to invest (time and money) in this area of research. On the fundamental physics side, it is worth mentioning the seminal paper of Kadanoff [100] and the "tempting view" of de Gennes [59]: these two papers appeared in the same year reviewing recent studies on respectively dynamical and static granular phenomena. Through the suggestive perspectives that both authors depicted, a clear message about the importance of granular matter and its innovative aspects was sent to the whole scientific community. Also the technological progress in experimental techniques, as magnetic resonance [136], positron emission particle tracking (PEPT) [140], high-speed imaging; and numerical methods [55, 189] played an important role in this resurgence of interest. Coming closer to nowadays, granular materials have also become very important for other fields of modern physics such as jamming [25], active matter [60, 206] and stochastic thermodynamics [73, 158].

In this thesis, we are mainly interested in granular phenomena that exhibit intriguing deviations from standard equilibrium behaviours. We discuss some specific cases in Sec. 1.4.

1.2.2 Forcing and dissipation: a non-equilibrium balance

The properties of a granular system depend significantly on the external forces applied. Nature, applications and experimental setups present huge variety of mechanisms to confine and solicit granular assemblies. When just gravity and/or other constant forces is acting, the system can be at rest or flowing depending on how these forces are balanced by the confining geometry [164, 13]. By imposing a shear velocity at boundaries as in Couette cells [88, 174, 102] one can go from stick-slip dynamics [15] to homogeneous flows. Dense granular systems at rest can be subjected to tilting [125, 57, 105] or tapping [142] cycles with different protocols exhibiting a rich phenomenology over long timescales. In this thesis, we consider a particular forcing mechanism i.e. mechanical vibrations. Before concentrating on that (Par. 1.2.3) we want to discuss the external energy injection in granular media from the perspective of non-equilibrium statistical mechanics.

Many of the phenomena mentioned here and in the previous paragraphs are ascribed to the dissipative nature of granular systems, which is not easily treated via the introduction of effective parameters [156]. Moreover, energy dissipation pre-

vents the occurrence of stationarity for statistical observables. A granular system in absence of external forces is in the cooling state (CS) where the total momentum is conserved but the total energy is gradually lost via inelastic collisions [37]. Introducing an external driving that constantly pump energy into the system, a non-equilibrium steady state (NESS) can be reached. Nevertheless, the properties of such a stationary state are very different from the one that would be obtained in the same system with elastic collision. In the latter case, stationarity is a consequence of thermodynamic equilibrium. At the level of single collisions one can understand this difference as we sketch in Fig. 1.4. Here we see that the elastic collisions are symmetric under time reversal while the inelastic ones are not (see Caption for explanation). We note that this perspective on driven granular systems offers the possibility to really visualize the essence of the NESSs where a stationary probability distribution is present but the detailed balance is not satisfied. From Fig. 1.4 is also clear that the coexistence of forcing and dissipation imply an energy flux that constantly goes through the system and this is clearly a non-equilibrium feature. It is worth saying that also in the inelastic case, a rigorous time reversal involving all the internal degrees of freedom would restore the detailed balance. This makes even more clear the intrinsic non-equilibrium nature of granular materials: the choice of using macroscopic systems (the grains) as fundamental units and the inability to perform a full time reversal symmetry are entangled.

As anticipated in the previous paragraphs, the statistical properties of a granular NESS depend a lot on the specific driving condition. Also before introducing particular driving protocols, the occurrence of a rich phenomenology in driven granular materials can be understood by the following argument. In general, an energy injection mechanism can be parametrized by a set of parameters $\{p_i\}$ (for instance the gravity acceleration g or the imposed shear velocity ω_s) and every p_i can influence in a specific way the granular dynamics. For comparison, in equilibrium statistical mechanics, the set of external parameters related to thermal agitation reduces to only the temperature T or the total energy E. Then, at equilibrium, one can study how the macroscopic observables of a system depend on these external parameters (for instance $X^{\mathrm{EQ}}(T)$). We point out that the analogous problem for a NESS $X^{\mathrm{NESS}}(\{p_i\})$, represents the core of many studies on driven granular systems.

1.2.3 Vibrofluidized granular matter: Experimental setups and granular phases

If the walls of a container move with sufficiently strong vibrations, a granular medium confined in it fluidizes: Receiving energy from the impacts with the walls, the grains move and collide between each other as happens with atoms in a fluid. In this condition, the system is said vibrofluidized and a granular temperature can be defined as:

$$T_g = \frac{\left\langle m\left(\mathbf{v} - \langle \mathbf{v} \rangle\right)^2 \right\rangle}{\mathcal{D}} \tag{1.1}$$

where $\mathcal{D}$ is the dimension of the space, $\mathbf{v}$ is the velocity of the grains and m is their mass. The average $\langle . \rangle$ is a temporal average in the case of stationary states, otherwise, it has to be performed over independent realizations of the dynamics. Usually, vibrofluidization can be realized in experiments by connecting the container

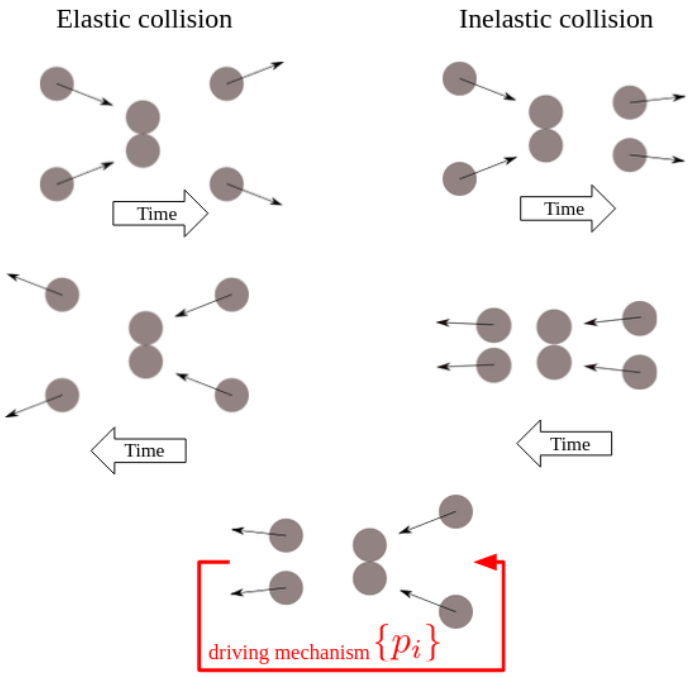

Figure 1.4. Elastic VS inelastic collision. In the elastic case, there is symmetry under time reversal so stationarity is a consequence of thermodynamic equilibration. In the inelastic case, friction breaks this time symmetry and one needs a driving mechanism that constantly supplies energy to the system in order to reach a NESS. This mechanism is described in general by a set of parameters $\{p_i\}$ that determines the specific properties of such a NESS. This sketch is an intuitive way to visualize how the violation of detailed balance and stationarity coexist in a driven granular system.

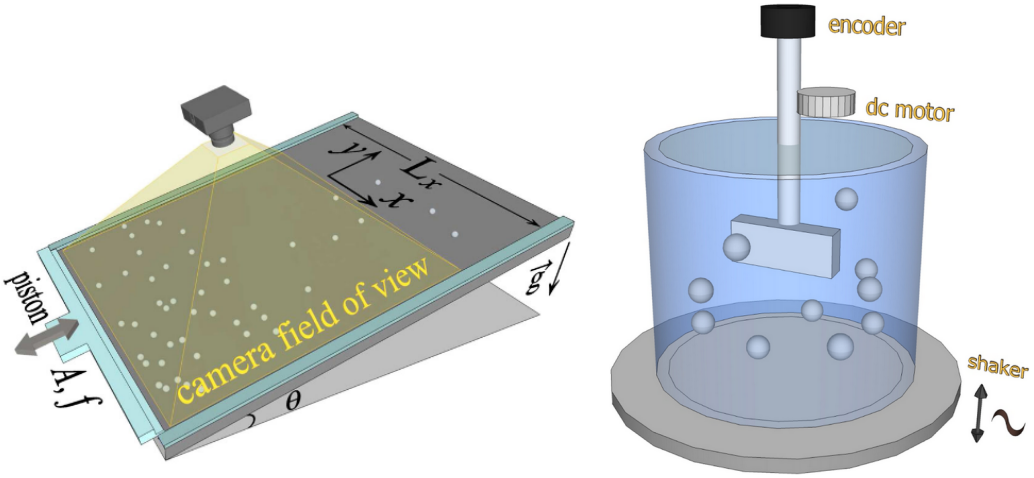

Figure 1.5. Experimental setups for the study of vibrofluidized granular materials. On the left, we have a quasi-2D geometry realized through an inclined plane with a vibrating bottom wall. Data acquisition is performed with a high-speed camera and the subsequent particle tracking. On the right, we have a 3D cylindrical-shaped setup with the base area connected to the shaker. In this case, the data acquisition can be done with a high-speed camera put on the top of the cylinder and/or by measuring the trajectory of an angular intruder suspended in the granular system. Although this last methodology gives only an indirect measure of the dynamics of the grains, it is very important in the case of dense granular fluids (See Par. 2.1.1). In this particular setup, the tracer can be also driven by a dc-motor to study the response of the vibrated system to an external solicitation. Images are reprinted from [150, 82].

with a shaker. This apparatus is generally controlled by a signal generator and an amplifier to have vibrations with the desired spectrum. In Fig. 1.5, we show two examples of experimental setups for vibrofluidization in quasi-2D and 3D geometries [150, 82]. Being generally realized in presence of gravity, an important control parameter in these experiments is:

$$\Gamma = a_{\max}/g \tag{1.2}$$

where $a_{\max}$ is the maximum acceleration of the walls during the vibrations.

In all these cases, the energy is supplied to the system non-homogeneously because the vibrating walls and the ones at rest (that just dissipate energy) are localized in space. Nevertheless, it is possible to obtain experimental conditions where the energy injection is approximately homogeneous by moving the particles with an air jet [101] or with a magnetic field in microgravity [9].

Depending on the particular kind of vibration, many phenomena have been observed in vibrofludized granular materials such as clustering [109], pattern formation [31], convection [150] and localized excitations [194, 48]. Here we want to concentrate on a particular feature of these systems, namely the formation of different "granular phases". As we shall see, in the granular context, different phases are distinguished by the properties of the velocity and density fields of the grains. In order to give also a better idea of the interplay between different shaking parameters, we consider a setup with sinusoidal forcing where the bottom wall is vertically vibrated as $\Delta z(t) = A\sin(2\pi ft)$. The two parameters are then the amplitude and the

frequency of the signal ($\{p_i\} = \{A, f\}$). In this condition, the maximum rescaled acceleration takes the form $\Gamma = (2\pi f)^2 A/g$ and another adimensional parameter called shaker strength is defined as $S = (2\pi f)^2 A^2/(gd)$ where d is the diameter of a grain. We note that the shaker strength is proportional to the shaker kinetic energy. One can immediately see that the same value of Γ or S can be obtained with different combinations of A and f. A non-trivial problem in vibrated granular systems is indeed to understand which is the main parameter that controls the onset of a particular granular phase. In [69] a systematic study of this kind has been carried on, we summarize it in Fig. 1.6. The diagrams shown correspond to three amplitudes A, so in each panel just f and F (the number of grain layers at rest) are varied (more details are provided in the caption of the figure). From the snapshots of the experiment, we can see the typical velocity and density fields that characterize the different phases. In the bouncing bed, the granular system acts as a single compact object that bounces on the vibrating bottom wall. In the gaseous regime, the forcing is strong enough with respect to the weight of the system to make the granular fully fluidized: this phase is characterized by a large mean free path of the grains and an almost homogeneous density field. In the convective phase, the velocity field is split into alternating upward and downward regions; it is observed at moderate F with a sufficiently high forcing. In the Leidenfrost state, we have a low-density region that "supports" a high-density one; this is similar to the homonymous phenomenon observed for a droplet poured on a hot surface (the lower side suddenly vaporizes while the upper remains liquid for a while). Finally, undulations can be observed for sufficiently heavy systems: here the bed develops standing waves oscillating at twice the period of shaking with a number of nodes that increases with the shaking intensity. By comparing the three panels, in which f is varied to span always the same interval of $\Gamma \in [0, 40]$, it is clear that almost all the phase transitions are governed by Γ (red transition points). Nevertheless, the bouncing bed $\leftrightarrow$ convection and the Leidenfrost $\leftrightarrow$ convection ones are governed by S (blue transition points).

The phase diagrams we have exposed give, in our opinion, a clear idea of how complex can be the behaviour of granular systems. This complexity is reflected also in the investigation methodology. Indeed, it often happens that different granular regimes (even when they are obtained in the same experimental setup) can require very different theoretical approaches to be understood and different numerical methods to be reproduced in silico. In the next two paragraphs, we give an overview of the main methodologies used to study granular matter.

1.2.4 Theoretical approaches

The presence of dissipative interactions and external forcing implies that the Hamiltonian H_g obtained as the sum of kinetic and potential energy of the granular degrees of freedom does not coincide with the true total energy of the system and it is not a conserved quantity. The complete Hamiltonian H of the system is the one that takes into account all the grain forming molecules. Associating a statistical weight to a given configuration C of the phase space as $p(C) \propto \exp(-\beta H_g(C))$ and calculating statistical observables as moments and cumulants of $p(C)$ results to be an unfounded approach. In addition to the failure of a general equilibrium-like ap-

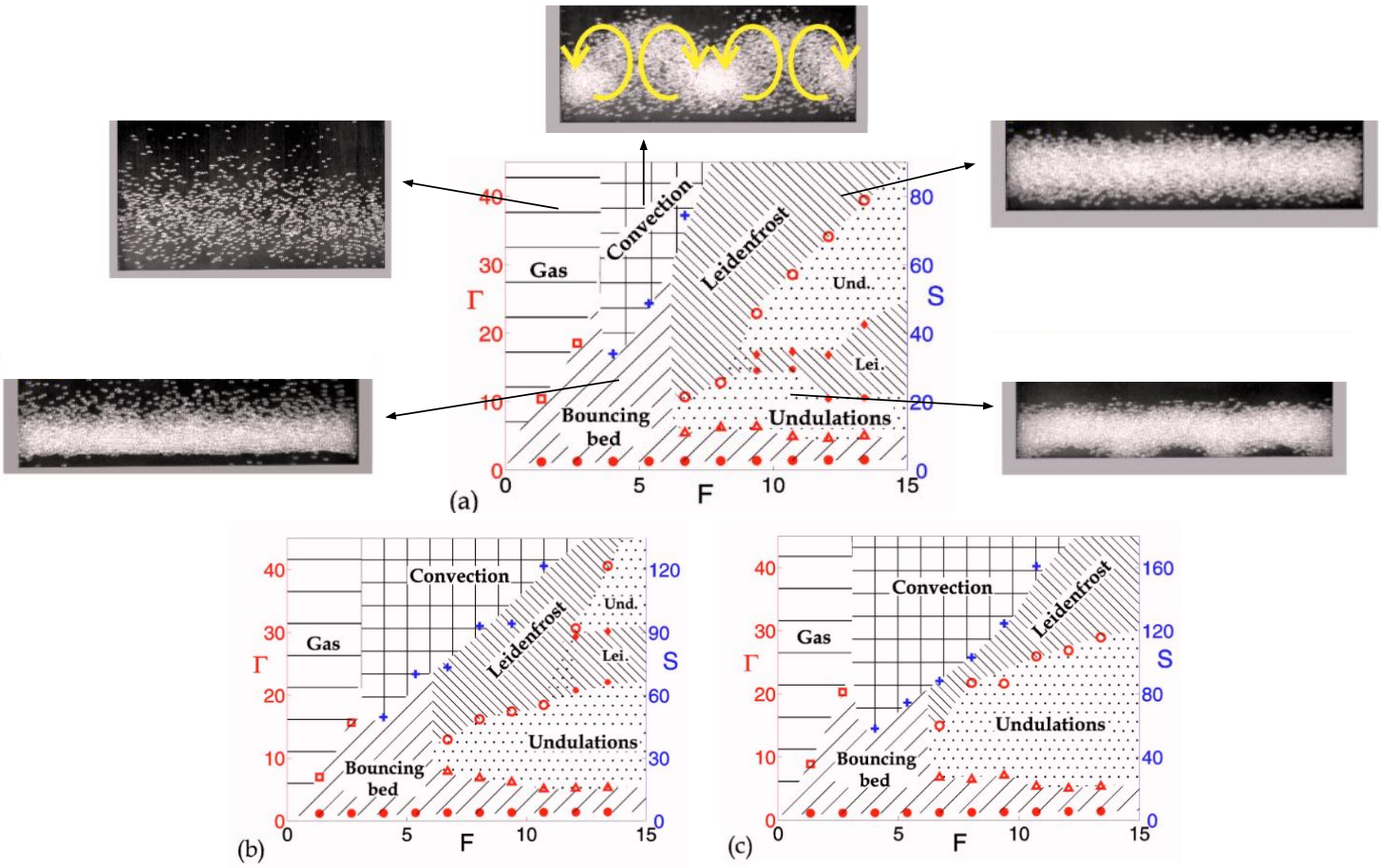

Figure 1.6. Phase diagrams of a vertical quasi-2D granular system shaken with a sinusoidal vibration for differetn driving amplitudes: $A = 0.002$ m (a), $A = 0.003$ m (b), $A = 0.004$ m (c). The control parameters varied in each graph are the number F of grain layers when the system is at rest and the driving frequency f. The relevant parameters for the transitions are Γ and S (see definitions in the text). To understand whether a particular transition is governed by the former (red points) or the latter (blue points), one has to plot the transition lines for each A in both a $\Gamma - F$ and a $S - F$ plane. The parameter for which the best collapse occurs is the one governing that particular transition. Images reprinted from [69]

.

proach, the rich phenomenology of granular matter still lacks of a unified theoretical framework. Many theories have been developed but very often they apply to specific conditions. A possible classification can be done by distinguishing theories that are valid in dilute conditions (where the dynamics of the grains is free except for brief collision) from the ones used in for dense systems (where the contact between particles is persistent). Here is a brief overview of the main theoretical approaches used to study granular matter.

Edwards thermodynamics

Almost thirty years ago, S. Edwards and coworkers proposed a theory for dense granular packings inspired by the ensembles of equilibrium statistical mechanics [66, 65]. The idea is to consider sets of mechanically stable configurations (i.e. where the total force acting on each grain is zero) and give the same probability to all the microstates with the same volume V. One can then define the number of microstates $\Omega(V)$, the Edwards entropy $S_{\mathrm{E}} \propto \ln \Omega(V)$, the compactivity $X^{-1} = \dfrac{\partial}{\partial V} S_{Ed}(V)$ and the effective volume defined as $Y = V - X S_{Ed}$. From this point of view, we have an equivalent microcanonical ensamble where V plays the role of the energy, X is the analogous of the temperature and Y is the free energy. By striking intermittently granular assemblies (tapping) the system can explore different configurations. This and other protocols have been used to test Edwards thermodynamics in models and experiments of compaction [41, 142, 163, 35, 177]. Generalizations of the Edwards approach has been proposed by including also frictional interactions in the force balance [28, 27] and applied to driven systems by considering also marginally stable configurations [85, 84]. Nevertheless, the real range of validity of this theory is still debated [50].

Kinetic Theory

In the fundamental theoretical study of granular fluids, an interest in the kinetics of gaseous states has grown from the end of the 20th century [100]. Granular gases consist of those states for which a description based on a modified Boltzmann equation is possible [47, 37]. For this type of granular fluids, it is possible to reproduce the classical approach of statistical mechanics and kinetic theory, with many analogies and some profound differences from molecular gases. Experiments on granular gases have confirmed the validity of this theory [108, 205].

The fundamental model underlying the granular kinetics is the gas of N hard inelastic spheres with a smooth surface. Grains have a diameter σ, a mass m_i and are described by their positions $\mathbf{r}_i$ and velocities $\mathbf{v}_i$. The system is usually confined in a cubic volume V with periodic boundary conditions. As the contact between two particles i and j is reached ($|\mathbf{r}_i - \mathbf{r}_j| = \sigma$) the grains collide while conserving momentum and dissipating a fraction of the kinetic energy:

$$\mathbf{v}_1' = \mathbf{v}_1 - \frac{m_2}{m_1 + m_2}(1+\alpha)(\mathbf{v}_{12} \cdot \hat{\boldsymbol{\sigma}})\hat{\boldsymbol{\sigma}} \tag{1.3}$$

where $\mathbf{v}_1'$ is the velocity of the sphere 1 after the collision with the sphere 2, $\mathbf{v}_{12} = \mathbf{v}_1 - \mathbf{v}_2$, $\hat{\boldsymbol{\sigma}}$ is the unitary vector in the direction defined by joining the centers

of the grains and $\alpha \in [0,1]$ is the inelastic coefficient. In the Grad-Boltzmann limit ($N \to \infty$, e $\sigma \to 0$, with $N\sigma^2$ constant), and assuming molecular chaos i.e. considering no space-temporal correlation between colliding particles, it is possible to write down a Boltzmann equation:

$$\frac{\partial}{\partial t}P(\mathbf{r},\mathbf{v}_1,t) + \mathbf{v}_1\frac{\partial}{\partial \mathbf{r}}P(\mathbf{r},\mathbf{v}_1,t) = \int_+ \mathrm{d}\hat{\boldsymbol{\sigma}} \int \mathrm{d}\mathbf{v}_2 (\mathbf{v}_{12}\cdot\hat{\boldsymbol{\sigma}}) \left\{ \frac{1}{\alpha^2} P[\mathbf{r},\mathbf{v}_1^*(\mathbf{v}_1,\mathbf{v}_2),t]P[\mathbf{r},\mathbf{v}_2^*(\mathbf{v}_1,\mathbf{v}_2),t] - P(\mathbf{r},\mathbf{v}_1,t)P(\mathbf{r},\mathbf{v}_2,t) \right\} \tag{1.4}$$

where $P(\mathbf{r},\mathbf{v}_1,t)$ is the probability density to have a sphere in $\mathbf{r}$ with a velocity $\mathbf{v}_1$ at time t; $\mathbf{v}_1^*, \mathbf{v}_2^*$ and $\mathbf{v}_1, \mathbf{v}_2$ are the velocities of two particles before and after a collision respectively (they are obtained by inverting the collision rule Eq. (1.3)). Finally, $\int_+ \mathrm{d}\hat{\boldsymbol{\sigma}}$ is an integration over the all collision angles that are consistent with the kinematic constraint $\mathbf{v}_{12}\cdot\hat{\boldsymbol{\sigma}} > 0$.

Eq. (1.4) is similar to the usual Boltzmann equation except for the factor $1/\alpha^2$ due to the dissipation in the collisions. As already mentioned, a free granular gas does not reach an equilibrium state but evolves indefinitely until losing all its kinetic energy. By preparing the initial state of the system in a homogeneous spatial configuration it is possible to observe the so-called homogeneous cooling where the positions remain homogeneously distributed while the velocity distribution evolves following a typical scaling: $P(\mathbf{v},t) = \frac{1}{v_0(t)} f(\mathbf{v}/v_0(t))$ with a characteristic speed $v_0(t) = \sqrt{T_g(t)}$. Here the granular temperature decreases with the Haff's law $T_g(t) = T_g(0)(1 + t/\tau)^{-2}$ where τ is a characteristic time that depends on the initial state and α. It is important to point out that that $f(\mathbf{c})$ is different from the usual Maxwell-Boltzmann distribution and presents tails with an exponential asymptotic behaviour. Under some conditions the free granular gas is unstable and a fluctuation can lead to an inhomogeneous regime with vortex structures and strong heterogeneities in the density field. The model described up to now is very far from reality because, in the experiments, external energy is supplied to obtain a stationary granular gas. In a theoretical description, this mechanism can be realized by inserting external stochastic forces in the grain dynamics. Also in these conditions, the presence of non-Maxwellian distributions with heavy tails and cluster formations has been observed [153, 154].

Granular Hydrodynamics

In order to obtain a hydrodynamic description for a granular fluid [36, 87], one can start from the Boltzmann equation (Eq. (1.4)). The density $n(\mathbf{r},t)$, the velocity $\mathbf{u}(\mathbf{r},t)$, and the granular temperature $T_g(\mathbf{r},t)$ hydrodynamic fields, are indeed

obtained as moments of the single-particle probability density $P(\mathbf{r}, \mathbf{v}, t)$ [189]:

$$n(\mathbf{r}, t) = N \int P(\mathbf{r}, \mathbf{v}, t) \mathbf{dv} \tag{1.5a}$$

$$n(\mathbf{r}, t)\mathbf{u}(\mathbf{r}, t) = N \int \mathbf{v} P(\mathbf{r}, \mathbf{v}, t) \mathbf{dv} \tag{1.5b}$$

$$\frac{3}{2} n(\mathbf{r}, t) k_b T_g(\mathbf{r}, t) = \frac{Nm}{2} \int [\mathbf{v} - \mathbf{u}(\mathbf{r}, t)]^2 P(\mathbf{r}, \mathbf{v}, t) \mathbf{dv}, \tag{1.5c}$$

where N is the total number of grains in the system. A procedure to derive the equation for the granular hydrodynamics is the Chapman-Enskog approximation. It consists of expanding $P(\mathbf{r}, \mathbf{v}, t)$ around an unperturbed Maxwell-Boltzmann reference assuming a small Knudsen number (i.e. the ratio between the mean free path and the typical length of gradients). Depending on the order at which such an expansion is truncated one finds different hydrodynamic description: the zeroth order describes the homogeneous cooling while at the second-order one obtains the granular Navier-Stokes equations [36]:

$$\frac{\partial}{\partial t} n(\mathbf{r}, t) + \frac{\partial}{\partial \mathbf{r}} [n(\mathbf{r}, t)\mathbf{u}(\mathbf{r}, t)] = 0 \tag{1.6a}$$

$$mn(\mathbf{r}, t) \frac{\partial}{\partial t} \mathbf{u}(\mathbf{r}, t) + mn(\mathbf{r}, t) \frac{\partial}{\partial \mathbf{r}} \mathbf{u}(\mathbf{r}, t) + \frac{\partial}{\partial \mathbf{r}} \mathcal{P}(\mathbf{r}, t) = 0 \tag{1.6b}$$

$$\frac{D}{Dt} T_g(\mathbf{r}, t) + \frac{2}{3n(\mathbf{r}, t)} \left(\mathcal{P} \frac{\partial}{\partial \mathbf{r}} \mathbf{u}(\mathbf{r}, t) + \frac{\partial}{\partial \mathbf{r}} \mathbf{q}(\mathbf{r}, t) \right) + T_g \zeta(\mathbf{r}, t) = 0 \tag{1.6c}$$

where $\frac{D}{Dt} = \frac{\partial}{\partial t} + \mathbf{u}(\mathbf{r}, t) \cdot \frac{\partial}{\partial \mathbf{r}}$, $\mathcal{P}_{ij}(\mathbf{r}, t) = n(\mathbf{r}, t) T_g \delta_{ij} - \eta \left(\frac{\partial}{\partial r_i} u_j + \frac{\partial}{\partial r_j} u_i - \frac{2}{d} \delta_{ij} \frac{\partial}{\partial r_l} u_k \right)$ is the pressure tensor (η is the shear viscosity), $q_i(\mathbf{r}, t) = \kappa \frac{\partial}{\partial r_i} T_g(\mathbf{r}, t) - \mu \frac{\partial}{\partial r_i} n(\mathbf{r}, t)$ is the heat flux (κ is the thermal conductivity, μ a new transport coefficient that has no an elastic counterpart) and $\zeta(\mathbf{r}, t) = \zeta_0 n(\mathbf{r}, t) \sqrt{T_g(\mathbf{r}, t)}$ is the so-called cooling rate. The coefficients η, κ, μ and ζ_0 are functions of the fixed parameter of the system. The novelty with respect to the usual Navier-Stokes equations is given by the presence of the term $T_g \zeta$ which represents the dissipation of internal energy due to collisions, and the term $\mu \frac{\partial}{\partial \mathbf{r}} n(\mathbf{r}, t)$, proportional to the density gradient, in the heat flux. These equations successfully describe granular flows at densities low enough, a condition that often require an inelastic coefficient $\alpha \simeq 1$.

Granular hydrodynamics has been very important for the study of many crucial behaviours of granular gases. For example, by imposing boundary conditions that mimic a vertically shaken setup one can show the existence of convection [150], transverse waves in the density field [162] and segregation phenomena in granular mixtures [192].

Vibrated grains in the dense state

In the above overview of theoretical approaches, we can identify two opposite regimes where analytical calculations are possible. Edwards thermodynamics regards stable configurations where all the particles are in contact with the neighbour ones in such a way to satisfy a force balance. Kinetic theory and hydrodynamics

are applied in dilute regimes where the single-particle dynamics is governed by interactions only in a small fraction of time (i.e. during the collisions). Moreover, these collisions must satisfy the hypothesis of Molecular Chaos (with eventually slight corrections); in other words, each collision "doesn't know (almost) anything" about the previous ones. The results reported in this thesis are mainly focused on vibrofluidized granular systems at *high* densities. In this state, the grains continuously vibrate around an almost fixed position with respect to the others performing very rare re-arrangements. We point out that this particular regime eludes both the aforementioned theoretical frameworks. On one hand, the spatial configuration of particles is almost fixed but vibrations (also when they are very small) never let the system in a mechanically stable configuration with well-defined force chains; on the other hand, the system is fluidized but the collisions are strongly correlated in space and time.

Nevertheless, it is worth mentioning that some recent extensions of the mode-coupling theory to granular fluids has been successfully applied to predict the glass transition [107, 187] and the rheological response [106] of dense randomly-driven regimes.

1.2.5 Numerical methods

Given the crucial dependence of granular behaviours on boundary conditions, it is very difficult to understand whether a particular experimentally observed phenomenon is a spurious effect due to some technical problems or not. Moreover, in analytical calculations, it is often necessary to verify the validity of some hypotheses done on observables that are not accessible in experiments. All this makes very useful the numerical study of granular materials because in the simulations one has total control of the parameters of the system and all the observables of interest are accessible. In this section we want to introduce the three main methods by which numerical simulations of granular systems are implemented, namely: molecular dynamics, direct simulation Monte Carlo and event-driven method.

Molecular dynamics

In molecular dynamics (MD) [131, 189], the equations of motion of all the N particles in the system are numerically integrated given their initial configuration. The particles are in general rigid bodies described by their centers of mass with position $\mathbf{r}_i$, the related velocities $\mathbf{v}_i$, the Euler angles $\boldsymbol{\phi}_i$ and the angular velocities $\boldsymbol{\omega}_i$ where $i \in \{1, \ldots, N\}$. The equations of motion in an inertial frame of reference read as:

$$\frac{d^2\mathbf{r}_i}{dt^2} = \frac{1}{m_i}\boldsymbol{F}_i(\mathbf{r}_j, \mathbf{v}_j, \boldsymbol{\phi}_j, \boldsymbol{\omega}_j, t) \tag{1.7a}$$

$$\hat{J}_i\frac{d^2\boldsymbol{\phi}_i}{dt^2} = \boldsymbol{M}_i(\mathbf{r}_j, \mathbf{v}_j, \boldsymbol{\phi}_j, \boldsymbol{\omega}_j, t) \tag{1.7b}$$

where the subscript j refers to all the particles in the system. $\boldsymbol{F}_i$ and $\boldsymbol{M}_i$ are respectively the total force and torque acting on the particle i, m_i is the mass and $\hat{J}_i$ the inertia tensor. Unlike molecular cases, in granular materials, long-range interactions are usually absent. The dynamics is governed by contact forces that

are different from zero only if the distance between the grains is smaller that the sum of their radii R_i:

$$\boldsymbol{F}_i = \sum_{j=1, j\neq i}^{N} \boldsymbol{F}_{ij}\Theta(|R_i + R_j| - |\mathbf{r}_i - \mathbf{r}_j|) + \boldsymbol{F}_i^e(t) \tag{1.8a}$$

$$\boldsymbol{M}_i = \sum_{j=1, j\neq i}^{N} \boldsymbol{M}_{ij}\Theta(|R_i + R_j| - |\mathbf{r}_i - \mathbf{r}_j|) + \boldsymbol{M}_i^e(t) \tag{1.8b}$$

where $\Theta(x)$ is the Heaviside step function and the superscript e refers to external forces/torques. The stability of these simulations depends crucially on the proper choice of the time-step dt used to discretise Eqs. (1.7), specifically it has to be small enough to correctly integrate the contact dynamics.

Once implemented with a realistic model of contact forces, an MD simulation for granular materials can reproduce a wide range of experimental conditions. However, a limitation of this approach is the fact that it is necessary to choose a very small dt to properly resolve the dynamics during the single collisions. Granular phenomena (as the ones studied in this thesis) can have typical timescales that are exceedingly longer than the duration of a collision. This leads to a large cost in terms of computational time.

Let us finally point out that the use of MD simulations for granular matter is commonly called discrete element method (DEM) [55]. This distinction from ordinary MD is related to the inclusion of rotational degrees of freedom and the use of contact forces. It is also distinguished from the finite element method (FEM) [94] where solids are described as a continuum on which differential equations for the effective fields are defined and numerically solved. The numerical studies presented in this thesis are mainly performed with DEM simulations, we discuss how to set up them for our case studies in Par. 2.2.1.

Event-Driven simulations

The fundamental assumption of event-driven simulations [118, 119, 128] is that, at each instant, at most one contact between two particles of infinitesimal duration occurs throughout the system. The idea is therefore not to go through the numerical solution of the Eqs. (1.7) but to consider the interactions between the grains as instantaneous collisions in which the particle velocities are updated according to certain rules defined by the contact model [39]. In principle, in these simulations, time is not discretized and the integration of motion jumps from a collision (i.e. an event) to the consecutive one (this explains also the name of the method). Once a collision has occurred and the state of the system updated accordingly, one has to identify the next event given the instantaneous configuration of positions and velocities. In order to use this approach, the microscopic dynamics during the collision must be such that we can express the collision rules in the following general form:

$$\mathbf{v}' = k_v(\mathbf{v}, \boldsymbol{\omega})\mathbf{v} \tag{1.9a}$$

$$\boldsymbol{\omega}' = k_\omega(\mathbf{v}, \boldsymbol{\omega})\boldsymbol{\omega} \tag{1.9b}$$

where $\mathbf{v}$ ($\mathbf{v}'$) and $\boldsymbol{\omega}$ ($\boldsymbol{\omega}'$) are respectively the linear and angular velocity of the single grain before (after) the impact while $k_v(\mathbf{v}, \boldsymbol{\omega})$ and $k_\omega(\mathbf{v}, \boldsymbol{\omega})$ are the two functions that link the old velocities to the new ones. These functions allow the application of the abstraction of instantaneous collisions without altering the physics of the problem. From this point of view, in event-driven simulations, it is crucial to know how k_v and k_ω depend explicitly on the velocities before the collision. The event-driven approach is very efficient since the computation of the forces (that consists of calculating k_v and k_v), is done only once for each collision.

The cases where this type of simulations are suggested are:

- Systems in which the collision time is expected to be much less than the time between two successive collisions. These certainly include granular gases but also denser situations as long as it is verified, through a preliminary comparison with MD, that the phenomena of interest are not affected by the idealization of instantaneous interactions.

- Systems in which the equations governing the interactions between the particles during the contact are unknown. Under these conditions, it is impossible to integrate the equations of motion according to the MD, however, it is sometimes possible to experimentally derive an estimate of Eqs. (1.9) and then implement an event-driven simulation.

Direct Simulation Monte Carlo (DSMC)

The Direct Simulation Monte Carlo (DSMC) [29, 30], also called BIRD method, is a numerical procedure to solve the Boltzmann equation (1.4), in both spatial homogeneous or non-homogeneous conditions. As in the methods presented above, the particles can evolve under the effect of (eventually null) external forces and undergo collisions with other particles.

To present the BIRD method, we consider N identical hard particles of diameter σ in d dimensions with positions $\mathbf{r}_i$ and velocities $\mathbf{v}_i$. The volume $V = L^d$ (with periodic boundary conditions PBC) is split in m_c cells of volume $V_c = V/m_c$. The size of these cells has to be smaller than the typical length of the inhomogeneities in the system so that they can be assumed as locally homogeneous. In addition to homogeneity, another important property that must hold inside the cells is Molecular Chaos (MC). For strong inhomogeneities, the resulting number of particles inside each cell N/m_c can be too small to avoid the probability of short-time recollisions that clearly break MC. In these cases a fictive number of particles $\tilde{N} = hN$ with $h > 1$ is simulated (the role of $\tilde{N}$ will be clear in the following).

Time is discretised in finite time-steps of length dt and at each time-step, the state of all particles is updated. External forces are integrated as in MD while collisions are treated with the following procedure performed in all the cells.

- denote by N_c the number of fictive particles in the cell, and by $n_c = N_c/(hV_c)$ the *real* density in the cell; finally, denote by $\boldsymbol{V}_c = \sum_i \mathbf{v}_i/N_c$ the average velocity in the cell and by $T_c = \sum_i |\mathbf{v}_i - \boldsymbol{V}_c|^2/(DN_c)$ the "temperature" in the cell

- compute the average number of collisions $\omega(n_c, T_c)dt$ for a particle in a homogeneous gas at density n_c and temperature T_c, assuming a distribution close to the Maxwellian (as the Sonine approximation truncated at the second polynomial [37])

- perform $C = N_c\omega(n_c, T_c)dt/2$ collisions. Note that the number of collisions is calculated with the *fictive* number N_c but the *real* density n_c.

Each collision is performed by repeatedly picking at random two particles i, j in the cell until they satisfy the kinetic constraint $v_r = (\mathbf{v}_i - \mathbf{v}_j) \cdot \hat{n} < 0$. The pair is then accepted with a probability proportional to $v_r\Theta(v_r)$, otherwise is rejected. Once the collision is accepted, the velocities are updated with the rules (1.3).

The DMSC has been widely used in the context of dilute vibrofluidized granular materials (see for examples [153, 139]). Alternative schemes of the BIRD method taking into account the Enskog correction [37] to the Boltzmann equation has been proposed to study systems with moderate densities [129].

1.3 Effective dynamics of slow variables

After the general introduction to granular materials, we dedicate this section to the other main subject of the thesis i.e. the modelization of slow timescales. Here we provide a brief historical overview of different approaches used to derive Langevin equations. The levels of description introduced in the first section regard both space and time. Generally, what is smaller is also faster. The derivation of an effective equation of motion for a large intruder in a bath of small particles is the classical framework in which one can experience this issue and its implications.

The discovery of Brownian motion for colloidal particles suspended in water [40] highlighted the need for a theoretical description of stochastic dynamics. Einstein in 1905 [67] and Langevin in 1908 [117], proposed two parallel approaches for this problem: the first one considers an equation for the temporal evolution of the probability distribution $p(\boldsymbol{X}, t)$ of finding the colloid in position $\boldsymbol{X}$ at time t (diffusion equation); the second one is based on the hypothesis that the Newton equation for the intruder consists of a deterministic part accounting for the Stokes law and a stochastic one that describes the random collisions with the fluid molecules. In modern terms, Einstein wrote the Fokker-Planck equation (FPE) of the problem in the overdamped case while Langevin used the corresponding stochastic differential equation (SDE) taking into account also the inertial effects. The Langevin equation (LE) reads:

$$M\dot{\boldsymbol{V}}(t) = -\gamma\boldsymbol{V}(t) + \sqrt{2\gamma k_b T}\boldsymbol{\eta}(t) \tag{1.10}$$

where M is the mass of the colloid, $\boldsymbol{V}(t)$ its instantaneous velocity and $\boldsymbol{\eta}(t)$ a Gaussian white noise with unitary variance $\langle \eta_i(t)\eta_j(t')\rangle = \delta_{ij}\delta(t - t')$. The viscous coefficient obeys the Stokes law $\gamma = 6\pi\mu R$ while the amplitude of noise is chosen by imposing the equipartition of energy between the intruder and the solvent: $\langle V_i^2\rangle = k_bT/M$. Here, μ is the viscosity of the fluid, T its temperature, R the radius of the colloid, and k_b the Boltzmann constant. By standard manipulation of Eq. (1.10), it is possible to relate the diffusion coefficient D, a quantity directly measurable from

the trajectory of the colloid, to the microscopic parameters of the fluid:

$$D = \lim_{t\to\infty} \frac{\langle (\boldsymbol{X}(t) - \boldsymbol{X}(0))^2 \rangle}{2t} = \frac{k_b T}{6\pi\mu R}. \tag{1.11}$$

These results, together with the pioneering experiments of J. Perrin [141], led to an experimental estimate of the Avogadro number ($N_A = R_g/k_b$ where R_g is the universal gas constant) providing a strong empirical confirmation of the atomistic hypothesis that was not yet widely accepted at that time [72].

LE and its generalizations are used to describe a wide class of phenomena in physics, biology, finance, economics and many other fields [76, 166, 33, 133, 75, 176] but its importance goes beyond these applications. The derivation of a LE for a small subset of (slow) observables in a system with a large number of degrees of freedom (DOF) is itself a crucial process where the problem of separation of timescales emerges in a clear way. The general question is the following: given a system whose state is described by the set of variables $\{X, V, x_1, \cdots, x_N, v_1, \cdots, v_N\}$ where $\{X, V\}$ are the DOF of a macroscopic intruder while $\{x_1, \cdots, x_N, v_1, \cdots, v_N\}$ are the ones of the microscopic particles of the fluid; how it is possible to derive an equation for $\{X, V\}$ where the effect of all the x_is and v_is are contained in (eventually stochastic) effective terms that depend just on $\{X, V\}$?

The first historical attempt to tackle this problem was carried on by Smoluchowsky in 1906 [184, 46]. He derived the linear form of the viscous friction felt by a heavy spherical intruder with mass M and radius R immersed in a dilute gas of light spheres with mass m and radius r. His approach was based on the statistical analysis of the collisions in the limit $M \gg m$ and $R \gg r$: according to the elastic collision rule (see Eq. (1.3) with $\alpha = 1$) the change of momentum of the intruder due to a single impact can be expressed as:

$$M\Delta\boldsymbol{V} = \frac{2mM}{m+M}(\boldsymbol{v} - \boldsymbol{V}). \tag{1.12}$$

One can then calculate the mean change of momentum per unit time by considering the analytical expression of the collision rate obtained for a sphere at rest with radius $r+R$ hit by a flux of pointlike particles moving at relative velocity $\boldsymbol{v}-\boldsymbol{V}$. Averaging this expression over all the impact angles and velocities $\boldsymbol{v}$ with a Gaussian weight $P(\boldsymbol{v}) \propto \exp(-m|\boldsymbol{v}|^2/(2T))$ (where T is the gas temperature), one obtains the linear viscous force $M\dot{\boldsymbol{V}} = -\gamma\boldsymbol{V}$ with the analytical expression of the drag coefficient γ as a function of the system parameters.

A non-phenomenological derivation of the full LE with also the stochastic term was performed by Van Kampen in 1961 [198]. This procedure considers the same system of the Smoluchovsky but the approach is different because Eq. (1.10) is recovered from the associated FPE obtained as a perturbative expansion of the Lorentz-Boltzmann equation for the intruder. The latter can be formally written as:

$$\frac{\partial P(\boldsymbol{V},t)}{\partial t} = \int d\boldsymbol{V}'[W_{tr}(\boldsymbol{V}|\boldsymbol{V}')P(\boldsymbol{V}',t) - W_{tr}(\boldsymbol{V}'|\boldsymbol{V})P(\boldsymbol{V},t)] \tag{1.13}$$

where $W_{tr}(\boldsymbol{V}|\boldsymbol{V}')$ is the transition probability to go from $\boldsymbol{V}'$ to $\boldsymbol{V}$ per unit time. It consists of an integral over all the possible collisions with the gas particles that

bring to an intruder velocity change $\boldsymbol{V}' \to \boldsymbol{V}$. The right hand side of Eq. (1.13) is a linear operator acting on $P(\boldsymbol{V}, t)$ that can be formally expressed through the Kramers-Moyal expansion [166]; at the second-order one obtains:

$$\frac{\partial P(\boldsymbol{V},t)}{\partial t} = -\frac{\partial}{\partial V_i}\left[D_i^{(1)}(\boldsymbol{V})P(\boldsymbol{V},t)\right] + \frac{\partial^2}{\partial V_i \partial V_j}\left[D_{ij}^{(2)}(\boldsymbol{V})P(\boldsymbol{V},t)\right] \tag{1.14}$$

where:

$$D^{(n)}_{j_1\dots j_n}(\boldsymbol{V}) = \frac{1}{n!}\int d\boldsymbol{V}'(V'_{j_1} - V_{j_1})\dots(V'_{j_n} - V_{j_n})W_{tr}(\boldsymbol{V}'|\boldsymbol{V}). \tag{1.15}$$

Van Kampen validated this expansion in the $m/M \ll 1$ limit with a rigorous procedure and showed that Eq. (1.14) is equivalent to the FPE corresponding to the SDE (1.10). We'll perform a more detailed discussion of this method applied to a heavy tracer in a dilute granular gas in Par. 1.4.1.

An even different approach has been followed by Rubin (1960), Turner (1960) and Zwanzig (1973) [169, 193, 215]. The first two authors considered a heavy impurity (mass M) in a harmonic chain with stiffness k formed by lighter particles (mass m) and calculated the velocity autocorrelation function $\rho(t) = \langle V(0)V(t)\rangle / \langle V^2\rangle$ of the impurity where the average is taken on the initial conditions. They found that $\rho(t) \sim \exp(t/\tau)$ for $m/M \ll 1$ where $1/\tau = 2\sqrt{km}/M$. In other words, the impurity has the same correlation function of a Brownian particle with a viscosity $\gamma = 2\sqrt{km}$. Almost ten years later a more general framework has been proposed by Zwanzig that considered the intruder as a particle (or a system of particles) immersed in a bath of harmonic oscillators and following an arbitrary non-linear Hamiltonian dynamics. He demonstrates that the intruder coordinates obey a non-linear generalized Langevin equation (GLE) that we report here in one dimension for simplicity:

$$\dot{X} = V \tag{1.16a}$$

$$\dot{V} = -U'(X) - \int_{\infty}^{t} \gamma(t-t')V(t')dt' + \eta(t) \tag{1.16b}$$

where U is a generic potential. This is a Langevin equation where the viscous force is an integral with a memory kernel and the noise is correlated in order to satisfy the fluctuation-dissipation relation: $\langle \eta(t)\eta(t')\rangle = 2T\gamma(t-t')$. The dynamics described by Eq. (1.16) is not Markovian but considering a large number of oscillators in the bath and imposing that their typical frequency ω_d is much faster than all the characteristic ones related to the intruder dynamics, one can approximate $\gamma(t)$ with $2\gamma\delta(t)$ recovering Markovianity.

After this overview, an additional remark must be done on the role of non-equilibrium. On the macroscopic side, the approach used by Einstein and Langevin is possible assuming the equipartition between the colloid and the bath that is a consequence of the equilibrium condition. Without the equilibrium assumption, there is no way to properly relate the viscous coefficient and the diffusive one as in Eq. (1.10). Then, a microscopic derivation becomes necessary. On this microscopic side, the difficulty related to non-equilibrium is the impossibility to assume *a priori* a Maxwell-Boltzmann (MB) distribution for the velocities of the bath particles. In

that cases, one has to justify the use of a MB by experimental and/or numerical evidence for the particular system under study [172] or perform calculations with taking into account the non-equilibrium statistical properties of the bath [181].

The common denominator of all the reviewed approaches is that the derivation of a LE requires a sufficient separation of timescales between the intruder and the bath dynamics. The possibility to use a viscous term and an uncorrelated noise to mimic the interaction with the bath is strictly related to the fast memory loss of the latter. In other words, anytime the macroscopic intruder collides with the surrounding particles it experiences a completely new state of the system where the effects of the past interactions have been forgotten.

In this thesis, we deal with granular systems at a high density where memory is often non-negligible. In Par. 1.4.2 and in the next chapters we will discuss how to treat these cases through the introduction of additional variables or, equivalently, the use of memory kernels as in Eq. (1.16) (see also Sec. 3.2).

1.4 Unveiling non-equilibrium in granular phenomena

As we said many times before, the presence of friction makes granular systems inherently out of equilibrium. Sometimes the phenomenological manifestation of non-equilibrium is evident as in granular convection and segregation of mixtures, sometimes it is hindered by specific mechanisms. For example, by just seeing a video of a vibrated granular gas [3], it is not always easy to distinguish the motion of the grains from the equivalent dynamics of the molecules in a thermal gas. More quantitatively, by measuring the probability distribution function of the velocities in a granular gas it is often difficult to observe a substantial deviation from the Maxwell-Boltzmann distribution without collecting large statistics. Here we discuss some examples of hidden non-equilibrium in granular phenomena and some methods to unveil it.

1.4.1 Granular Brownian Motion

Following the approach of Van Kampen mentioned in Sec. 1.3, it is possible to derive a LE for a granular intruder of mass M in a gas of grains with mass m in the limit $\epsilon = \sqrt{m/M} \ll 1$ [172]. In this case, the grain-grain interactions and the grain-intruder ones undergo the inelastic collision rule with restitution coefficient α reported in Eq. (1.3). The external driving mechanism is modelled by coupling each grain in the system (including the tracer) with a Brownian bath characterised by a drag coefficient γ_b and a temperature T_b. Assuming a Maxwell-Boltzmann distribution with variance T_g/m for the gas particles and exploiting the Enskog approximation for the factorization of the gas-tracer distribution function [37], an analytic expression of $W_{tr}(\boldsymbol{V}|\boldsymbol{V}')$ can be found allowing the explicit calculation of the Kramers-Moyal expansion coefficients from Eq. (1.15). Since they are $D^{(n)}_{j_1\dots j_n} \sim \mathcal{O}(\epsilon^{2n})$, the expansion can be truncated at the Langevin order. In two dimensions, one obtains a Fokker-Planck equation corresponding to the following SDE for the intruder:

$$M\dot{\boldsymbol{V}}(t) = -(\gamma_b + \gamma_g)\boldsymbol{V}(t) + \sqrt{2(\gamma_b T_b + D_g)}\boldsymbol{\eta}(t) \tag{1.17}$$

where $\gamma_g = \chi(1+\alpha)\sqrt{2\pi T_g m}$, $D_g = \gamma_g(\frac{1+\alpha}{2}T_g)$ and $\boldsymbol{\eta}(t)$ is a 2D Gaussian white noise such that $\langle \eta_i(t)\eta_j(t')\rangle \delta_{ij}\delta(t-t')$. Here, the prefactor $\chi = g_2(r+R)/l_0$ takes into account the mean free path of the intruder l_0 and the gas-tracer pair correlation function at the contact point $g_2(r+R)$ coming from the Enskog correction to the molecular chaos assumption. We point out that the granular temperature T_g is not a free parameter but it is related to the other ones trough a self-consistent equation obtained by imposing the granular gas to be stationary and decoupled from the intruder [172]. As expected, such an equation predicts $T_g = T_b$ in the elastic limit $\alpha = 1$ i.e. when the intruder equilibrates with the external bath.

Our remarks on the non-equilibrium properties of this system start by realizing that in Eq. (1.17) two thermostats are present: the first one, with temperature T_b, is related to the global bath, the second one, with temperature $T'_g = \frac{1+\alpha}{2}T_g$, arises from the granular gas. Nevertheless, this is just a consequence of how the LE is written. Indeed, Eq. (1.17) is equivalent to the SDE of a Brownian particle at equilibrium with a single thermostat with temperature:

$$T_{tr} = \frac{\gamma_b T_b + \gamma_g T'_g}{\gamma_b + \gamma_g} \tag{1.18}$$

However, it is useful to consider the energy injection rates associated to the two thermostats that are respectively [203]:

$$\begin{aligned} Q_b &= \langle \boldsymbol{V}(t) \cdot (\sqrt{2\gamma_b T_b}\boldsymbol{\eta}_b(t) - \boldsymbol{V}(t))\rangle = 2\tfrac{\gamma_b}{M}\,(T_b - T_{tr}) \\ Q_g &= \langle \boldsymbol{V}(t) \cdot (\sqrt{2\gamma_g T'_g}\boldsymbol{\eta}_g(t) - \boldsymbol{V}(t)\rangle = 2\tfrac{\gamma_g}{M}\left(T'_g - T_{tr}\right) \end{aligned} \tag{1.19}$$

where $\boldsymbol{\eta}_{b(g)}(t)$ are 2D Gaussian white noises. From the above expressions it is clear that the balance of the fluxes $Q_b = -Q_g$ is satisfied by Eq. 1.18.

This scenario clarifies the apparent contradiction of being far from equilibrium maintaining an equilibrium-like description for the tracer: by considering $\boldsymbol{V}(t)$ alone it is not possible to obtain separate measures of Q_b and Q_g. The only flux that can be measured is the total one $Q = M\langle \boldsymbol{V}\cdot\dot{\boldsymbol{V}}\rangle = 0$ in which the presence of non-zero energy currents is hidden. To summarize, if the separation of timescales is wide enough to assume molecular chaos, by tracking the trajectory of a single massive intruder into a driven granular gas, it is not possible to distinguish the far from equilibrium nature of the underlying dynamics. In the next paragraph, we shall see how this picture changes when memory effects arise in the macroscopic description of the system.

1.4.2 Using memory to detect non-equilibrium

In the previous paragraph, we saw that the macroscopic dynamics of a massive intruder immersed in a driven granular gas is reversible at the macroscopic level of description (i.e. Eq. (1.17) does not violate the detailed balance). This is a consequence of the fact that, by assuming the gas decoupled from the tracer and molecular chaos, the variable $\boldsymbol{V}(t)$ alone is enough to have a Markovian dynamics. In general, the effect of the fluid on the tracer depends also on the past and this can be modelled generalizing the LE with the introduction of memory kernels [215, 63]. In the following, we first discuss the case of a general non-Markovian stochastic

process where non-zero terms related to memory appear in the entropy production rate; then we provide some examples where non-equilibrium properties of a system can be measured thanks to memory effects.

The irreversible effect of memory

We consider a generalized Langevin equation (GLE) for a free particle in a fluid:

$$\dot{V} = -\int_{-\infty}^{t} \gamma(t-t')V(t') + \eta_c(t) \tag{1.20}$$

with the following memory kernel:

$$\gamma(t) = 2/\tau_0\delta(t) + \sum_{i=1}^{M} \frac{\gamma_i}{\tau_i} e^{-\frac{t}{\tau_i}} \tag{1.21}$$

and colored noise:

$$\langle \eta_c(t) \rangle = 0, \quad \langle \eta_c(t)\eta_c(t') \rangle = 2T_0/\tau_0\delta(t-t') + \sum_{i=1}^{M} T_i \frac{\gamma_i}{\tau_i} e^{-\frac{|t-t'|}{\tau_i}}. \tag{1.22}$$

For simplicity, here we consider just one component of the particle velocity. We recall that the thermal equilibrium condition is given by the fluctuation-dissipation relation (FDR) of the second kind:

$$\langle \eta_c(t)\eta_c(t') \rangle = T\gamma(|t-t'|). \tag{1.23}$$

When the above condition is satisfied, one has energy equipartition between the particle and the fluid, a canonical distribution and the FDR of the first kind is satisfied [124]:

$$R(t) = \overline{\delta V(t)}/\delta V(0) = T^{-1}\langle V(t)V(0) \rangle. \tag{1.24}$$

Here, δV represents an instantaneous perturbation of V while $\langle O \rangle$ and $\overline{O}$ refer to averages on the unperturbed and perturbed system respectively. From Eq. (1.21) and (1.22), it is straightforward to see that Eq. (1.23) holds only if $T_i = T \ \forall i$, otherwise the system is at non-equilibrium. By defining the M auxiliary variables:

$$V_i = \sqrt{\frac{\gamma_i}{\tau_i}} \int_{-\infty}^{t} dt' e^{-\frac{t-t'}{\tau_i}} \left(V(t') + \sqrt{\frac{T_i}{\gamma_i}} \eta_i(t') \right) \quad i \in [1, M] \tag{1.25}$$

it is possible to map the GLE (1.20) into a multivariate Ornstein-Uhlenbeck process $\dot{\mathbf{v}}(t) = -\hat{A}\mathbf{v}(t) + \hat{B}\boldsymbol{\eta}(t)$ where $\mathbf{v} = \{V, V_1, \ldots, V_M\}$, $\langle \eta_i(t) \rangle = 0$ and $\langle \eta_i(t)\eta_j(t') \rangle = \delta_{ij}\delta(t-t')$ with $0 \leq i, j \leq M$. Regarding the two matrices we have: $A_{ij} = \delta_{ij}\tau_j^{-1} + \sqrt{\gamma_i/\tau_i}(\delta_{i0} - \delta_{j0})$ and $B_{ij} = \delta_{ij}\sqrt{2T_i/\tau_i}$. In this way, we went from a non-Markovian description for the single variable $V(t)$ to a Markovian one for the $M+1$ dimensional vector $\mathbf{v}(t)$ where all the components are coupled. The reason of such a mapping will be clear in a few lines.

An important property of non-equilibrium systems is the irreversibility of the trajectories that can be quantified by the fluctuating entropy production:

$$\Sigma_t = \log \frac{P(\{\mathbf{v}(s)\}_0^t)}{(P(\{\mathcal{I}\mathbf{v}(s)\}_0^t))} \tag{1.26}$$

where $P(\{\mathbf{v}(s)\}_0^t)$ is the probability of observing a particular trajectory $\{V(s)\}_0^t$ and $\{\mathcal{I}\mathbf{v}(s)\}_0^t$ defines the reversed time evolution of the system. Now, exploiting the aforementioned mapping and following the calculation of [157], one obtains this explicit formula for the averaged entropy production rate:

$$\langle\dot{\Sigma}\rangle = \sum_{i=1}^{M} \sqrt{\frac{\gamma_i}{\tau_i}} \left(\frac{1}{T_0} - \frac{1}{T_i}\right) \langle V V_i\rangle. \tag{1.27}$$

From this very compact expression we note that: i) at equilibrium ($T_i = T\ \forall i$) $\langle\dot{\Sigma}\rangle = 0$ so the dynamics is reversible, ii) correlation between different variables manifests in the entropy production if the system is out of equilibrium.

In other words, the emergence of memory effects in the particle motion unveils the non-equilibrium nature of the system (i.e. the presence of more than one thermostat) at the macroscopic level of description.

Measurements of non-equilibrium properties

As the density of the granular gas increases, the assumptions done in Par. 1.4.1 are violated and memory effects become relevant in the tracer dynamics. An example of that is the backscattering effect that will be extensively discussed in the next chapter. For now, we just say that it manifests in the velocity autocorrelation function (VACF) of the tracer as a negative minimum at intermediate times [173]. Such a VACF cannot be described by the single exponential decay predicted by Eq. (1.17). As discussed in [173, 155], the backscattering effect is caused by the coupling between the tracer and the granular fluid. In the mode-coupling approximation scheme, it is possible to describe the dynamics of the intruder at moderate density by a GLE with a single exponential memory kernel then, following a procedure similar to the one discussed above, it can be mapped into a two-dimensional Ornstein-Uhlenbeck process:

$$\begin{aligned} \dot{V} &= -\tfrac{1}{\tau_0}(V - V_1) + \sqrt{2T_0/\tau_0}\eta_0 \\ \dot{V}_1 &= -\tfrac{1}{\tau_1}V_1 - \gamma_1\alpha V + \sqrt{2T_1\gamma_1\alpha^2}\eta_1 \end{aligned} \tag{1.28}$$

where V is the velocity of the tracer, V_1 represents the local velocity field of the surrounding gas particles, $\alpha = \tau_0/\tau_1$ and the η_is are Gaussian white noises with zero mean.

Contrary to Eq. (1.17), the above equations present two thermostats acting on two different variables so they can be used to estimate the deviation from equilibrium of the intruder dynamincs. Indeed, by numerical simulations at different gas densities on can track $V(t)$ (and eventually, with some arbitrariness, $V_1(t)$) to determine the parameters of the model by fitting the VACF defined as $C(t) = \langle V(t)V(0)\rangle/\langle V^2\rangle$ and the response function $R(t) = aC(t) + b\langle V(t)V_1(0)\rangle$ where a and $b \propto T_0 - T_1$ are known functions of the model parameters [202]. We see that, at equilibrium, $T_0 = T_1$ so $C(t) = R(t)$ and the FDR of the first kind is recovered. It has been shown that [173], at very low density, these two observables coincide confirming the equilibrium macroscopic description discussed in the previous paragraph (i.e. an additional variable is not necessary since $\langle V V_1\rangle = 0$). When the density of the

granular gas is increased, $C(t)$ differs from $R(t)$ signalling a clear deviation from equilibrium. Remarkably, the fitting procedure is good in both these two regimes so one can use the parameters of the model to measure the appearance of a non-zero entropy production by Eq. (1.27) in the special case of Eqs. (1.28) that gives: $\langle \dot{\Sigma} \rangle = \frac{1}{\tau_0} \left(T_0^{-1} - T_1^{-1} \right) \langle V V_1 \rangle$.

Measurements of the non-equilibrium properties of a granular tracer have also been obtained in experiments [82]. In this case, the trajectories of a driven intruder subjected to sharp changes of velocity δV together with the ones of the surrounding grains has been tracked. These measurements showed that $C(t)$ deviates from $R(t)$ as the density is increased enough to observe a non-zero cross-correlation between the tracer velocity and the local velocity field of the granular fluid. Moreover, the authors verified that for the emergence of such a non-equilibrium property, the effect of the correlation between variables is much more relevant with respect to the deviation from Gaussianity of the grain velocity distribution function.

1.4.3 Granular Brownian Ratchet

In Par. 1.4.1 we saw that the macroscopic dynamics of a Brownian tracer in a granular gas at low density does not reveal the non-equilibrium nature of the system. As we discussed in Par. 1.4.2, raising the density of the granular fluid makes possible the observation of many non-equilibrium properties. Here we want to talk about another mechanism to unveil non-equilibrium features in this kind of system: the ratchet effect [161, 89]. This phenomenon consists of the rectification of unbiased fluctuations and occurs when the time-reversal symmetry broken by non-equilibrium is accompanied by spatial symmetry breaking. The *Gedankenexperiment* proposed by Smoluchowsky and then extended and popularized by Feynman [185, 74], speculates about the possibility to realize an engine able to convert equilibrium thermal fluctuations into a directed motion violating the second law of thermodynamics. This is clearly not possible but there are cases in which only a subtle quantitative analysis clarifies that [74].

In our out of equilibrium case study, the ratchet effect can be realized thanks to an asymmetric shape of the tracer and works even in the dilute limit without the emergence of memory effects. In [51], the authors follow the same procedure sketched in Par. 1.4.1 but for an asymmetric tracer with a fixed orientation and forced to move in a single direction. The main difference is the presence of an integral over the tracer perimeter in the expression of the transition rate W_{tr}. The LE obtained in this way predicts a constant average velocity:

$$\langle V \rangle \propto (T_g - T_{tr}) \mathcal{A}_{\text{per}} \tag{1.29}$$

where we use the same notation of Par. 1.4.1. In view of the aforementioned differences in the calculations, the expressions of T_g and T_{tr} are not the same as above, but their physical meaning does not change. Regarding $\mathcal{A}_{\text{per}}$, it is a non-dimensional factor coming from the statistics of the grain-intruder collisions: its sign depends on the tracer symmetry with respect to the direction of motion. For symmetric shapes, we have $\mathcal{A}_{\text{per}} = 0$. From Eq. (1.29), we note that the average velocity is proportional to the difference between the two temperatures present in the

system, similar to what happens in thermal (i.e. not granular) Brownian ratchets [195]. Then, the sign of $\langle V \rangle$ depends on both the temperatures and the tracer shape. In the elastic case ($\alpha = 1$), we have $T_g = T_{tr}$ making $\langle V \rangle = 0$ as we expect at equilibrium. The granular ratchet effect has also been observed in experiments and realistic molecular dynamics simulations of 3D systems [68, 81, 83].

To conclude, we can say that an additional way to "discover" that a granular fluid is a non-equilibrium system consists of immerging into it an asymmetric intruder and observing its steady motion.

Chapter 2

Anomalous diffusion in a vibrated granular system

Generally, anomalous diffusion [186, 103] refers to the deviation from the asymptotic scaling $\langle (x(t) - x(0))^2 \rangle = \langle \Delta x(t)^2 \rangle \sim t^\alpha$ with $\alpha = 1$ of the mean squared displacement (MSD) with respect to a reference point $x(0)$ in a stochastic trajectory $x(t)$. The mechanism underlying this behaviour is well understood and very general because it is rooted in the limit theorems of probability theory. So the crucial problem in this context is to understand which are the conditions and the physical mechanisms that make possible the occurrence of an asymptotic exponent $\alpha \neq 1$. The $\alpha < 1$ case is called subdiffusion and the opposite one superdiffusion. Just to bring some examples, specific geometrical constraints and Levy walks, can bring respectively to subdiffusion and superdiffusion [90, 121, 182, 186]. In order to treat also analytically these asymptotic behaviours, the concept of fractional derivatives has been introduced in the field of stochastic processes [186, 103].

Nevertheless, in this thesis, we refer to anomalous diffusion in the specific case of the dynamics of an intruder that feels the effect of a thermal or athermal bath. We are then interested in deviations from the scenario predicted for an ordinary Langevin dynamics with a characteristic time τ. In such a scenario there are two regimes: the ballistic ($\langle \Delta x(t)^2 \rangle \sim t^2, \quad t \ll \tau$) and the diffusive one ($\langle \Delta x(t)^2 \rangle \sim t, \quad t \gg \tau$). In the first regime, the inertia of the intruder overcomes the damping effect of the bath resulting in a free motion, in the second one the fast collisions with the bath particles act as a memoryless random force (see Sec. 1.3) and ordinary diffusion is recovered. A deviation from this behaviour at any timescale of the intruder dynamics brings very useful information about the physics of the whole system, especially on memory effects that prevent an ordinary LE description. This is true also when the asymptotic behaviour remains diffusive.

In this chapter, we report experimental and numerical results for the diffusion of a tracer in a vibrofluidized granular medium. Several values of the driving parameters and packing fraction of the system are explored. For low driving and high densities, a strong deviation from the ordinary Brownian motion is observed signalling the emergence of multiple characteristic timescales in the system. The most relevant anomalous behaviour observed consists of the presence of a very long memory effect manifested with superdiffusion at late times in the MSD and a low-

frequency decay in the velocity power spectral density (VPSD) of the intruder. A subdiffusive plateau in the MSD and a backscattering peak in the VPSD are observed too: these are characteristic features of the cage effect due to the high density of the system.

Such results are obtained in a 3D confining geometry connected to an electrodynamic shaker that provides external energy: this experimental apparatus makes very complicated the particles tracking in the bulk that is usually done with tomography. The philosophy of the experiment is then to understand the properties of the whole granular fluid by looking at the diffusion of a tracer in it. Its anomalous behaviour is very interesting from this perspective. Our simulations aim to reproduce in silico the experimental setup in order to measure all the observables that are not accessible in the experiments. This allows to directly identify the phenomena of the granular medium that are responsible for the anomalous diffusion in the tracer dynamics (this will be done in Chap. 3). Nevertheless, to do that one has first to validate the numerical model and this can be done by directly comparing the results for the tracer in experiments and simulations: if a good agreement is found then one expects that also the phenomena strictly related to the dynamics of the grains observed in simulations are realistic.

The chapter is then structured as follow: we first describe the experimental setup and report the related results [175], then we discuss the numerical method used to simulate the experiments and finally we compare the data analysis obtained with the two approaches [144]. Here the main result is that in both cases we have the evidence of an extremely slow timescale (more than four orders of magnitude larger than the typical collision time) that dominates the long-time dynamics of the intruder as the granular medium becomes dense and cold enough.

2.1 Dynamics of a tracer I: experimental study

2.1.1 Experimental setup

The experiment realized in [175] is sketched in Fig. 2.1. It consists of a cylinder-shaped recipient (diameter 90 mm, maximum height 47 mm and total volume 245 cm^3), with an inverse-conical-shaped base, containing a number N of steel spheres (diameter $d = 4$ mm, mass $m = 0.27$ g), representing the "granular medium". The recipient is vertically vibrated through an electrodynamic shaker (LDS V450) fed with a noisy signal (spectrum approximately flat in the range $200 - 400$ Hz and roughly empty outside that range). The effect of the shaking is the fluidization of the granular medium, which - depending on N and Γ - stays in a steady gas (low N, high Γ) or liquid regime (high N, low Γ). The probe for diffusion is a blade (dimensions $35 \times 6 \times 15$ mm, inertia momentum $I = 353$ g mm^2) mechanically isolated from the container, that can rotate around a centered vertical axis and takes energy only from collisions with the granular medium. It performs a motion qualitatively similar to an angular Brownian motion: the angular velocity $\omega(t)$ of the blade and the absolute angle of rotation $\theta(t) = \int_0^t \omega(t')dt'$ are measured by an angular encoder (AEDA-3300) at a time resolution of 2 kHz and angular resolution of 40000 divisions per revolution. Two families of experiments have been performed: a series at high density ($N = 2600$), varying the shaking intensity

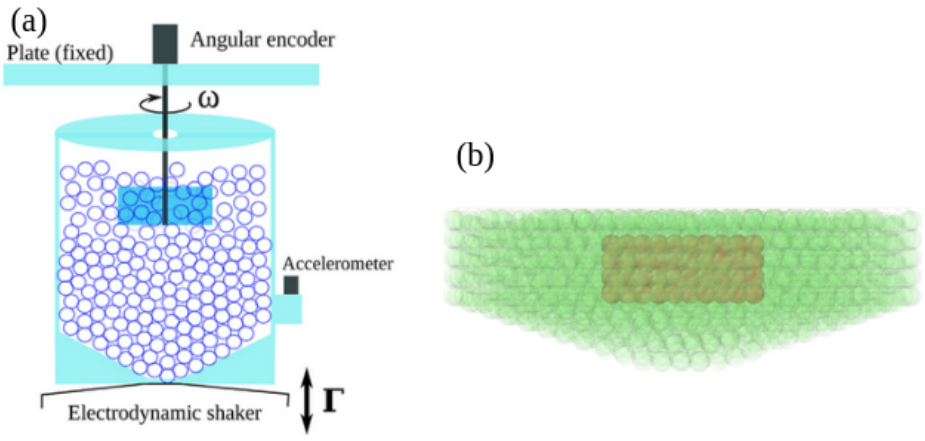

Figure 2.1. Experimental setup for the study of anomalous diffusion in vibrofluidized granular materials (a), see Par. 2.1.1 for a detailed explanation. In silico reproduction of the experimental setup (b), see Par. 2.2.1 for a detailed explanation. Both setups are shown in the case of a dense granular medium. Rendering of the simulations realized with OVITO [188]. Panel a is reprinted from [175].

amplitude such that $\Gamma = a_{\max}/g \in [19.5, 39.8]$, and a series at high shaking intensity ($\Gamma = 39.8$), varying $N \in [300, 2600]$. For more detailed information on the setup, see Supplemental Materials in [175].

2.1.2 Cage and superdiffusion

The experimental study was focused on two main observables: the mean squared displacement (MSD) of the travelled angle $\langle \Delta\theta(t)^2 \rangle$ and the velocity power spectral density (VPSD) of the blade defined as:

$$S(f) = \frac{1}{2\pi T} \left[\int_0^T dt \omega(t) e^{i(2\pi f)t} \right]^2 \tag{2.1}$$

where $T \sim \mathcal{O}(10^3 - 10^4)$ s is the total duration of the data acquisition. It is important to explicit the connection between these two observables that bring the same information in different ways. By the definition of the velocity autocorrelation function (VACF) as $C(t) = \langle \omega(t)\omega(0) \rangle$ and $\theta(t) = \int_0^t \omega(t')dt'$, one can easily show that:

$$\langle \Delta\theta(t)^2 \rangle = \int_0^t dt' \int_0^t dt'' \langle \omega(t')\omega(t'') \rangle = 2 \int_0^t dt'(t - t')C(t'). \tag{2.2}$$

Expanding the square in Eq. (2.1) one finds that $\lim_{t\to\infty} \langle \Delta\theta(t)^2 \rangle / t = 2\pi \lim_{f\to 0} S(f)$ so the limit in zero of the spectrum coincide with the diffusion coefficient provided that the above limits exist (that is not guaranteed in presence of anomalous diffusion). Moreover, $S(f)$ is also equivalent to the Fourier transform of the VACF in the steady state so the integral of the spectrum is proportional to the energy of the vane $\int df S(f) \propto \langle \omega^2 \rangle$

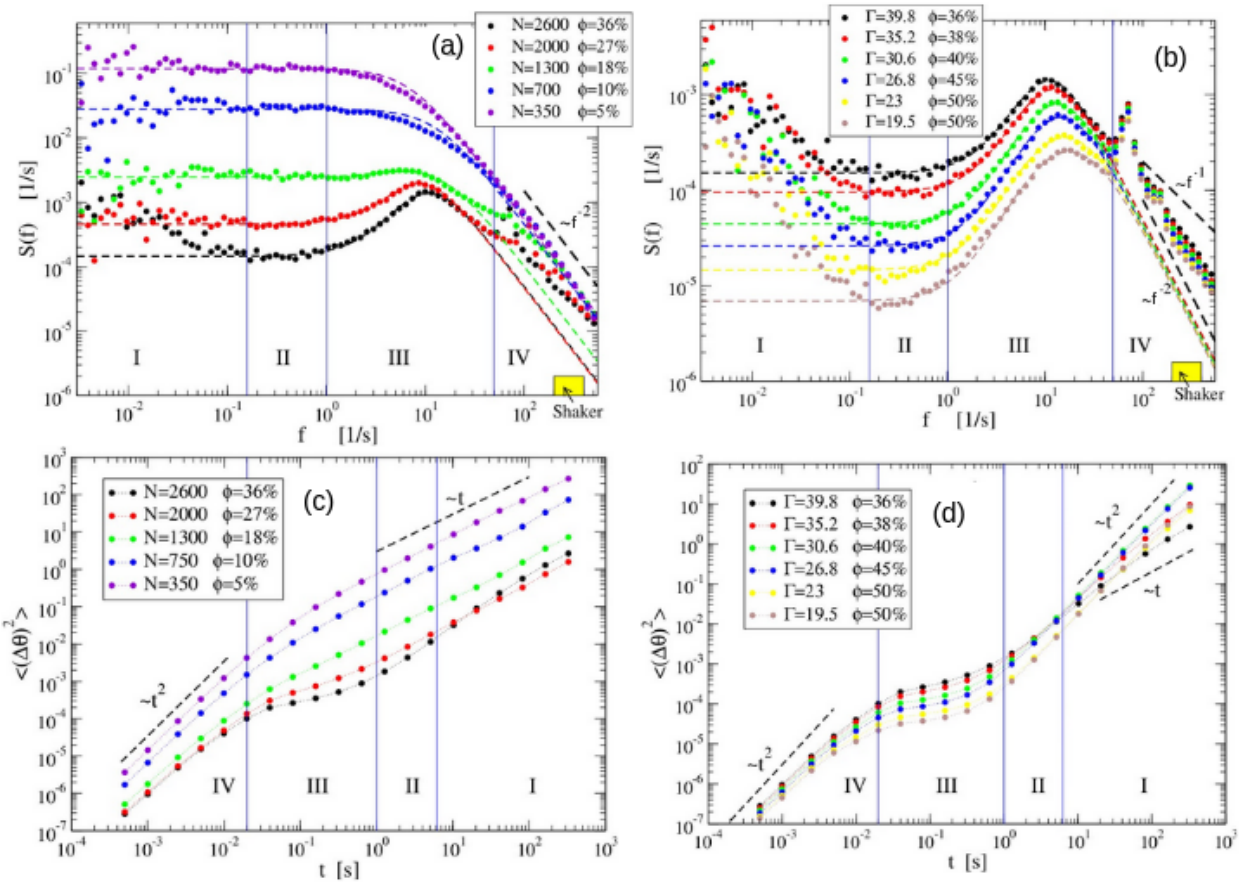

Figure 2.2. Experimental results for the vane dynamics. Velocity power spectral density at fixed $\Gamma = 39.8$ with a varying N (a) and fixed $N = 2600$ with a varying Γ (b). To avoid interference, the authors ensured that the shaker vibration is in a distant region ($200 - 400$ Hz) from the typical frequency where the backscattering peak and the low-frequency decay occur. A mechanical resonance is also observed at ~ 70 Hz in panel b, due to the non-perfect acoustic insulation of the plate on which the couple encoder/blade is mounted. The colored dashed lines refer to the predictions of a phenomenological model proposed in [175] and whose extensions are discussed in Sec. 3.2. Mean squared displacement at fixed $\Gamma = 39.8$ with a varying N (c) and fixed $N = 2600$ with a varying Γ (d). Subdiffusion at intermediate times and superdiffusion at late times in these two panels correspond to the backscattering peak and the low-frequency decay respectively. Images reprinted from [175].

In Fig. 2.2a-b, we present the main results in the form of the VPSD. In the series at fixed $\Gamma = 39.8$ shown in panel a, the spectrum changes shape dramatically as N varies. For $N = 300$ we have a flat plateau at low frequencies and a $f^{-\beta}$ with $\beta = 2$ decay at large ones. This is well approximated by a Lorentzian:

$$S(f) = \frac{D_{tr}}{\pi\gamma_{tr}^2[1 + (2\pi I f/\gamma_{tr})^2]} \tag{2.3}$$

which is exactly the result we expect for a process given by a LE for an angular velocity (i.e where the mass M is replaced by the moment of inertia I). We can

therefore state that for small packing fractions the vane motion is well approximated by the LE obtained analytically for the diffusion of a massive intruder in a dilute granular gas (Par. 1.4.1). Up to $N = 1300$ the shape of the spectrum remains the same but the global amplitude is reduced: this reflects the fact that increasing the number of particles promotes energy dissipation. To describe the remaining spectra, it is useful to split them in the four frequency regions highlighted in Fig. 2.2. At $N = 2000$, the VPSD curves in region III until a peak appears at a particular frequency $f^* \sim 10$ Hz and finally returns flat in regions II and I. This peak is interpreted as a transient trapping phenomenon, analogous to caging effects in low-temperature/high-density liquids. It is because, as the density increases, it is no longer possible to neglect the backscattering of the particles in the fluid. We can describe this situation by thinking that the particles hitting the blade at a certain instant bounce off the other grains and come back with a characteristic time $\tau^* = 1/f^*$ hitting the blade again. This is a first evidence of the memory effects that come into play in the vane dynamics as the packing fraction increases. Indeed, the collisions experienced at time distance $\sim \tau^*$ cannot be considered statistically independent. In the case of $N = 2600$ the scenario is even different: below the backscattering peak the spectrum curves again in region II developing a further decay in region I that seems to saturate just at very low frequencies. Since the asymptotic diffusion for large times is related to the behaviour of the spectrum at low frequencies, an increasing spectrum for frequencies tending to zero corresponds to a diffusion coefficient that does not tend to a constant value for long times. This indicates the presence of characteristic times of the system potentially longer than the duration of the whole experiment $T = 3600$ s which represent a second memory effect at large times in addition to the cage effect observed at intermediate times. The other set of experiments (Fig. 2.2b) shows that, by decreasing Γ at fixed N, the backscattering peak decreases spanning about a decade while its frequency position changes from 10 Hz to 20 Hz. If we consider f^* as a kind of characteristic frequency of the elastic response of the material in which the tracer is immersed then its value should be $\propto \sqrt{k}$ where k is an effective elastic constant of the granular system. From this point of view, we expect that a denser and/or "colder" granular medium is also stiffer. We can also observe that by decreasing Γ the decay of the spectrum for $f \to 0$ becomes steeper and the hinted plateau is completely absent. This means that the long memory effect is strengthened in cold systems. It is important to note that for dense/cold cases the high-frequency power-law decay in region IV presents an exponent $1 < \beta < 2$, close to 1 for the lowest values of Γ. This is the evidence of fast processes *inside a cage* (as $f \gg f^*$) occurring without a characteristic frequency [207].

What emerged in the analysis of the spectrum can be found in the MSD that we report in Fig. 2.2c-d. The four temporal regions corresponding to the frequency regions discussed above are marked on the graph. Referring again to the set of measurements with varying N, we note that the behaviour for small packing fractions also fits here with what is expected for an ordinary Brownian motion i.e. a ballistic $\propto t^2$ regime at small times (region IV) and a diffusive $\propto t$ one at large times (region I). As N increases, the cage effect is reproduced in the MSD with a subdiffusive regime in region III. Indeed, collisions with grains that are coming back after having bounced on other particles can clearly slow down the angular

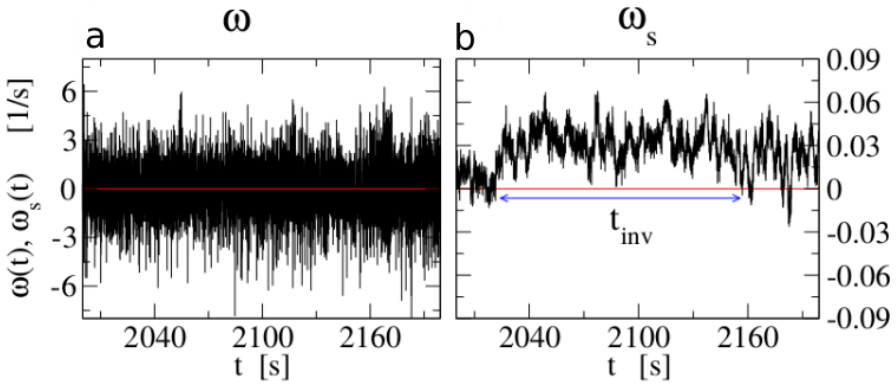

Figure 2.3. Comparison between the time evolution of the tracer velocity $\omega(t)$ (a) and its slow component $\omega_s(t)$ (b) defined in the text. Despite the total signal seeming to rapidly oscillate around a zero mean value, it contains a component strongly correlated in time with a lower amplitude.

motion of the vane. At the maximum packing fraction, we observe a trend $\propto t^\alpha$ with $\alpha > 1$ that hints at becoming diffusive again in the I region. Throughout the other series (panel d) both the cage slowing down in region III and the $\propto t^\alpha$ trend in regions II and I are present. Remarkably, in the coolest cases, $\alpha \sim 2$ and thus we observe a ballistic behaviour even after times comparable with the duration of the experiment. A direct inspection of the vane trajectories makes clear that this long memory effect is related to the presence of slow persistent angular drifts superimposed to the fast vibrations at short times. In Fig. 2.3 we compare the signal $\omega(t)$ and $\omega_s(t) = \frac{1}{\tau_f}\int_t^{t+\tau_f} \omega(t')dt'$, obtained with a running average over a time $\tau \geq 1$ s that filters out the fast component. Here it is clear that, although the fast dynamics seems to fluctuate around a zero mean value, long-time intervals t_s exist where the vane drifts very slowly in a given direction. A deeper insight into the t_s statistics is provided in [175].

2.2 Dynamics of a tracer II: numerical study

2.2.1 How to set up a DEM simulation for a granular system

In Par. 1.2.5 we introduced the general problem of studying granular systems with a numerical approach. We have reviewed different methods explaining which are the suggested conditions to use them. In the present case, we want to study a granular system in a wide range of densities: from dilute gas-like conditions where the grains interact through fast collisions to dense cases where the dynamics is mainly ruled by permanent contacts. Despite its high computational cost, the best approach in these conditions is the discrete element method (DEM). As anticipated, the DEM consists of molecular dynamics simulations with the following peculiarities needed for granular materials: the use of contact mechanics for the grains interaction, the presence of rotational degrees of freedom and the modelling of realistic confining geometries.

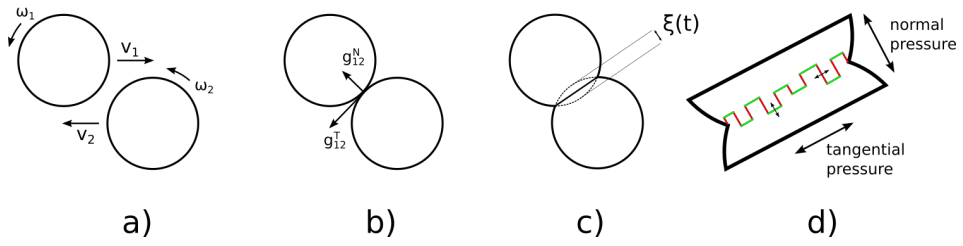

Figure 2.4. a: Two grains are going to collide with given linear and angular velocities. b: The contact between the grains starts with a normal and tangential relative velocity $\mathbf{g}_{12}^N$ and $\mathbf{g}_{12}^T$. c: Grain compenetration and definition of the instantaneous normal compression $\xi(t)$. d: Microscopic interpretation of the model: superficial asperities define a normal and a tangential surfaces of contact that enable respectively the transmission of impulse and angular momentum [39].

The Hertz-Mindlin model

We develop our simulations through the LAMMPS package (see [149, 1] and below for more information) using the Hertz-Mindlin (HM) model [212, 183, 39] to solve the dynamics during the particle-particle and particle-container contacts. This visco-elastic model takes into account both the elastic and the dissipative response to the mutual compression between the grains. In addition, it includes in the dynamics not only the relative translational motion but also the rotational one. The modelled forces are described by Eqs. (2.4) below and in Fig. 2.4 we can understand the physical meaning of the variables in play.

$$\boldsymbol{F}_{ij}^N = \sqrt{R_{ij}^{\text{eff}}}\sqrt{\xi_{ij}(t)}\left[(k_n\xi_{ij}(t) - m_{ij}^{\text{eff}}\gamma_n\dot{\xi}_{ij}(t))\cdot\mathbf{n}_{ij}(t)\right] \tag{2.4a}$$

$$\boldsymbol{F}_{ij}^T = \begin{cases} \boldsymbol{F}_{ij}^{\text{hist}} & \text{if} \quad |\boldsymbol{F}_{ij}^{\text{hist}}| \le |\mu\boldsymbol{F}_{ij}^N| \\ -\dfrac{|\mu\boldsymbol{F}_{ij}^N|}{|\mathbf{g}_{ij}^T(t)|}\cdot\mathbf{g}_{ij}^T(t) & \text{otherwise} \end{cases} \tag{2.4b}$$

$$\boldsymbol{F}_{ij}^{\text{hist}} = -\sqrt{R_{ij}^{\text{eff}}}\left[k_t\int\sqrt{\xi_{ij}(t')}\mathbf{ds}_{ij}(t') + m_{ij}^{\text{eff}}\gamma_t\sqrt{\xi_{ij}(t)}\mathbf{g}_{ij}^T(t)\right]. \tag{2.4c}$$

The equations and the figure are for two spherical particles with radius R_i, R_j, mass m_i,m_j position $\mathbf{r}_i$, $\mathbf{r}_j$, translational velocity $\mathbf{v}_i$, $\mathbf{v}_j$ and rotational velocity $\boldsymbol{\omega}_i$, $\boldsymbol{\omega}_j$. The relative velocity at the contact point is defined as $\mathbf{g}_{ij} = (\dot{\mathbf{r}}_i - \boldsymbol{\omega}_i \times R_i\mathbf{n}) - (\dot{\mathbf{r}}_j + \boldsymbol{\omega}_j \times R_j\mathbf{n})$ where $\mathbf{n} = (\mathbf{r}_i - \mathbf{r}_j)\,/\,|\mathbf{r}_i - \mathbf{r}_j|$ defines the normal direction; we call $\mathbf{g}_{ij}^N$ and $\mathbf{g}_{ij}^T$ the two projections, respectively normal and tangential, to the surface of contact. The instantaneous normal compression is represented by $\xi_{ij}(t) = R_i + R_j - |\mathbf{r}_i - \mathbf{r}_j|$ and its derivative is $\dot{\xi}_{ij}(t) = |\mathbf{g}_{ij}^N|$. Regarding the effective parameters we have $R_{ij}^{\text{eff}} = R_iR_j/(R_i + R_j)$ and $m_{ij}^{\text{eff}} = m_i, m_j/(m_i + m_j)$; here is important to mention that the wall surfaces are treated as spheres with infinite mass and radius. During the contact, the particles are subjected to a normal force $\boldsymbol{F}_{ij}^N$ and a tangential one $\boldsymbol{F}_{ij}^T$; both these components have an elastic and a dissipative

contribution multiplied by the couples of parameters k_n, k_t and γ_n, γ_t, respectively. In the normal force $\boldsymbol{F}_{ij}^N$ we can see an elastic term that descends from the Hertzian theory of contact mechanics [151] characterized by a non-linear dependence on the displacement. We recall that in the framework of the same theory it is also possible to derive the dissipative term [39]. The elastic part of the tangential force consists of a memory term that takes into account the history of the tangential displacement whose infinitesimal contribution is given by $\mathbf{ds}_{ij}(t) = \mathbf{g}_{ij}^T(t)dt$. Finally, we remark that the cases in Eq. (2.4)b implement the Coulomb friction condition with a coefficient μ. For more details and possible extensions of the Hertz-Mindlin contact force, we refer to [4].

It is now worth mentioning that during the numerical analysis of the system total angular momentum (see Par. 3.1.4), we discovered a bug in the source code of the Hertz-Mindlin model in LAMMPS [5]. The tangential forces in the grain-grain interaction were always applied on the surface of the particles (i.e. at one radius of distance from the centers) even during the mutual compenetration. This led to an unphysical source of external torque due to the couple of forces $\boldsymbol{F}_{ij}^T$ and $\boldsymbol{F}_{ji}^T$ applied at a distance $\xi(t)$ from each other (imagine two opposite forces on the compenetrated surface of the grains in Fig. 2.4c). This error is actually critical from a physical point of view because it breaks the conservation of the total angular momentum expected in internal (sphere-sphere) interactions. The correct application point, following the idea of deformable particles, would be in the middle of the segment that connects the two centers. From the stable release of June 2019 [6] a new granular package correctly working is available (our simulations are performed with a corrected source code).

Parameters calibration

Now we briefly discuss how to set the parameters of Eqs. (2.4) and the simulation time-step in relation to the properties of the real experiment. The elastic coefficients for two different materials in contact can be directly derived as

$$k_n^{ij} = \frac{4}{3}\left(\frac{1-\nu_i^2}{Y_i} + \frac{1-\nu_j^2}{Y_j}\right)^{-1} \qquad k_t^{ij} = 8\left(\frac{2-\nu_i}{G_i} + \frac{2-\nu_j}{G_j}\right)^{-1} \tag{2.5}$$

where Y is the Young modulus, $G = \frac{Y}{2(1+\nu)}$ the shear modulus and ν is the Poisson ratio [212, 151, 62]. When dealing with just one species we define $k_{n/t} = k_{n/t}^{ii}$. Direct formulas for γ_n and γ_t are lacking but it is a common strategy to choose them verifying *a posteriori* the good agreement with experimental data [189] . A widely accepted criterion to fix the simulation time-step is to choose it as a fraction of the Rayleigh time namely the time that a superficial acoustic wave takes to cross a single grain. It is related to the characteristics of the material in this way:

$$t_{\text{ray}} = \frac{\pi R_{\min}\sqrt{2\,(1+\nu)\,\rho/Y}}{0.163\nu + 0.8766}, \tag{2.6}$$

where ρ is the grain density and $R_{\min}$ the radius of the littlest grain in the system [159]. With this choice the contact dynamics is properly resolved because t_{ray} is usually much smaller than the typical collision times.

A realistic setup in silico

Here we explain how we used the DEM to rebuild in silico the experimental setup discussed in the previous paragraphs. The grains properties are the same of the real ones (Par. 2.1.1) corresponding to the density of steel $\rho = 8 \times 10^3$ kg/m^3. The conical-base-shaped cylinder is realized by defining the corresponding 3D region of space with its real proportion and making its inner boundaries interact as walls with Eqs. (2.4). The simulations start randomly pouring N grains in this region and, in order to supply energy to them, the container is forced to move in the vertical direction following a sinusoidal $z_p(t) = A\sin(2\pi ft)$. This is chosen to reproduce, by varying A at fixed $f = 200$ Hz, the same interval of maximum accelerations explored in the experiments with the noisy signal. For the sinusoidal signal, this shaking parameter takes the form $\Gamma = A(2\pi f)^2/g$. Different realizations of the dynamics can be obtained by changing the seed of the random pouring process. The vane is reproduced with a parallelepiped made of 10×4 grains overlapped by half a radius and glued together in such a way to behave as a single rigid body (Fig. 2.1b). Choosing their radius $R_v = 3.0$ mm and mass $m_v = 0.113$ g the same dimensions and inertia momentum of the realistic vane are obtained. It is worth noting that the surface of the numerical vane is not perfectly smooth but presents valleys of depth $R_v(1 - \sqrt{3}/2)$ due to the partial overlap of the grains.

Regarding the interaction parameters needed to implement Eqs. (2.4) we used Eqs. (2.5) for the elastic coefficients considering the grains as made of steel while the vane and the wall properties refer to the plexiglass ones. In appendix A we report a series of tables where we provide all the simulation parameters for every study treated in this thesis. We apply a general strategy widely exploited in granular DEM simulations that consists of lowering the Young modulus of the materials involved to reduce the integration time-step. We fix it as $dt = at_{\text{ray}}$ with $a \in [0.04, 0.2]$ depending on the specific simulations and, as we see from Eq. (2.6), $t_{\text{ray}} \propto Y^{-1/2}$. Working with a higher dt lowering the computational costs is very convenient provided that one has an experimental reference to verify that this artificial softening does not affect the phenomenology of the system in which one is interested. We reduce the Young modulus of steel and plexiglass of three and two orders of magnitude respectively. Through the comparison between experimental and numerical results for the dynamics of the tracer discussed in the next paragraph, we conclude that this strategy can be successfully applied in our case. Also the numerical values used for γ_n and γ_t, which cannot be fixed from the material properties, are justified *a posteriori* in the same way. It is worth saying that, before this direct comparison with experiments, we also performed some preliminary tests in simple conditions where one can easily predict the dynamics analytically such as a single grain bouncing on a flat surface or a collision between one grain and the vane. With this calibration, the simulation we perform to reproduce the typical one-hour-long experiments need the numerical integration of more than 10^8 time-steps. In the densest case ($N = 2600$) they take almost two days running in parallel on four processors.

The choice of LAMMPS

LAMMPS [149, 1] is a classical molecular dynamics code for simulations of gaseous, liquid or solid systems offering a rich choice of boundary conditions and interaction potentials. Particles of such systems can be atoms, molecules or polymers but also macroscopic bodies such as grains. The code is written in C++ and can be run on any machine that compiles it using a single processor or parallel programming. LAMMPS is a free open source software, so one can access the source files that implement its various functions, which may eventually be extended or modified by the user. The simulations are designed and run through specific input scripts in which the characteristics of the particles and their interactions are defined. Regarding our specific case LAMMPS is a good choice essentially for two reasons: On one hand, it is designed to optimize parallel programming on clusters; On the other hand, it presents many built-in commands that are very useful for granular simulations such as contact forces, visco-elastic walls (eventually moving) and the possibility to realize rigid bodies by glueing grains.

2.2.2 Numerical results

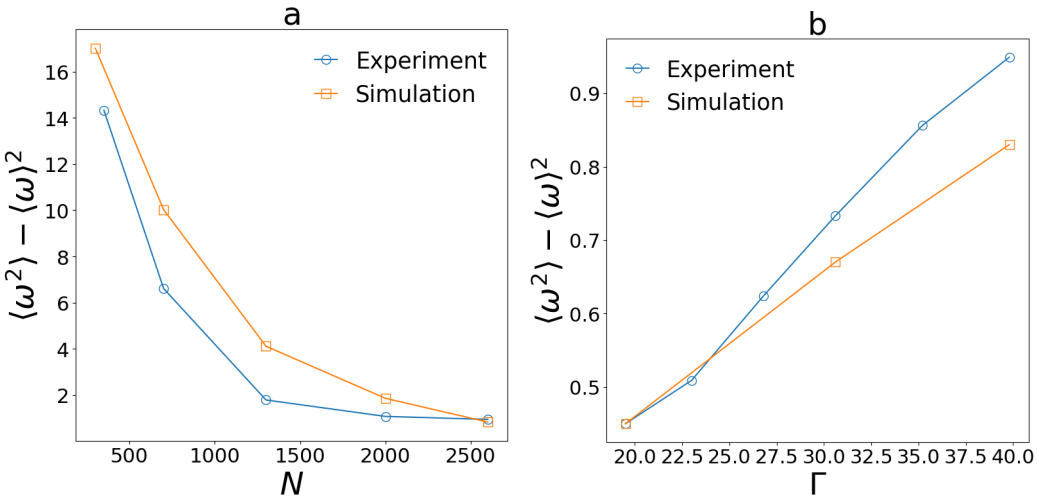

Figure 2.5. Variance of the angular velocity of the vane in comparison between experiments and simulations. a: $\Gamma = 39.8$ and varying N. b: $N = 2600$ and varying Γ.

Once developed realistic DEM simulations, we can use them to reproduce the experiments in silico. A preliminary analysis that we perform regards the variance of the vane velocity $\langle\omega^2\rangle - \langle\omega\rangle^2$ where the averages are taken on the stationary state. In Fig. 2.5 we compare this observable in experiments and simulations: The qualitative behaviour is the same with fluctuations that decrease with N (we recall that higher density means higher dissipation) and, quite intuitively, increase with Γ. More quantitatively, we see that the numerical trend when N varies is slightly "warmer" than the experimental one, except for the point at $N = 2600$; while varying Γ we start from a perfect agreement at $\Gamma = 19.5$ and then observe a deviation with lower variances in the simulation. As explained in the previous paragraph, the

Young modulus of the simulated grains is smaller than the real one. This can have a non-negligible effect especially in dense conditions where the contact dynamics results to be more dissipative for softer particles. This and also the non-perfectly smooth surface of the virtual vane can explain the quantitative deviation in Fig. 2.5b. For the left panel, we have an opposite quantitative disagreement for which we don't have a clear explanation. Maybe the use of sinusoidal shaking instead of a noisy one can play a role. Nevertheless, we don't look for a perfect agreement between experiments and simulations: as we shall see shortly the crucial point of our numerical analysis is to recover the presence of all the memory effects observed in the experiment. In general, it is evident that, although the shaker signal in the simulation is sinusoidal and the interaction coefficients of the viscoelastic model are not entirely realistic, the average fluctuations of the virtual vane does not deviate significantly from the real ones.

Now we can focus on the same analysis carried on in Par. 2.1.2. We show the numerical results for the VPSD and MSD in Fig. 2.6 which is the equivalent of Fig. 2.2 in the previous section. By a quick comparison between these two figures, it is clear that the qualitative behaviour at varying N at fixed Γ and vice-versa is well reproduced in both the observables: all the relevant correlation effects are present. In Fig. 2.6a, we have a Lorentzian shape of the spectrum in dilute cases, a low-frequency plateau followed by the backscattering peak at $N = 1750$ and the low-frequency decay plus backscattering at $N = 2600$. From panel b, we see that decreasing Γ at fixed N makes the peak shift to the right as in the experiment. Always according to experiments, these numerical results show the same correspondence between spectrum and MSD characteristics: high-frequency decay $\rightarrow$ ballistic regime at short time, backscattering peak $\rightarrow$ transient subdiffusion at intermediate times, low-frequency plateau $\rightarrow$ ordinary asymptotic diffusion, low-frequency decay $\rightarrow$ superdiffusion at late times (panel c and d). In other words, the MSD reflects the same phenomenology of the VPSD also in the numerics.

From the perspective of "different behaviours at different scales" discussed in the first chapter, an interesting consideration can be done by looking at Fig. 2.6d. Comparing the superdiffusive regimes at short and long times one can note an opposite behaviour as a function of Γ. The initial ballistic regime is faster (i.e. higher in the log-log plot) for larger Γ and the vertical order of the curves remains unchanged until the end of the cage. After that, an inversion of the order is observed and finally, at late times, one arrives to the opposite situation having faster superdiffusion in colder systems. This feature was also present in the experimental results (Fig. 2.2d) but with less clear evidence since just the four warmer MSDs ($\Gamma \in [26.8, 39.8]$) performed such an inversion. This is a clear example of a dynamical property of the system whose behaviour depends on the timescale of the observation. This will be a crucial point in the remainder of the thesis: in Sec. 3.1.3 we will show how it is related to the grain dynamics, in Sec. 3.2.5 we'll recover it in a phenomenological model and finally in Chap. 5 we'll suggest a physical explanation.

In conclusion, we want to show a direct comparison between numerical and experimental results for the tracer dynamics. In Fig. 2.7 we show the VPSD (a) and the MSD (b) in the hot/dilute case and the cold/dense one. Here we see again a good qualitative agreement in all the frequency and time regimes. The vertical shift between experimental and numerical curves reflects what we have seen for the blade

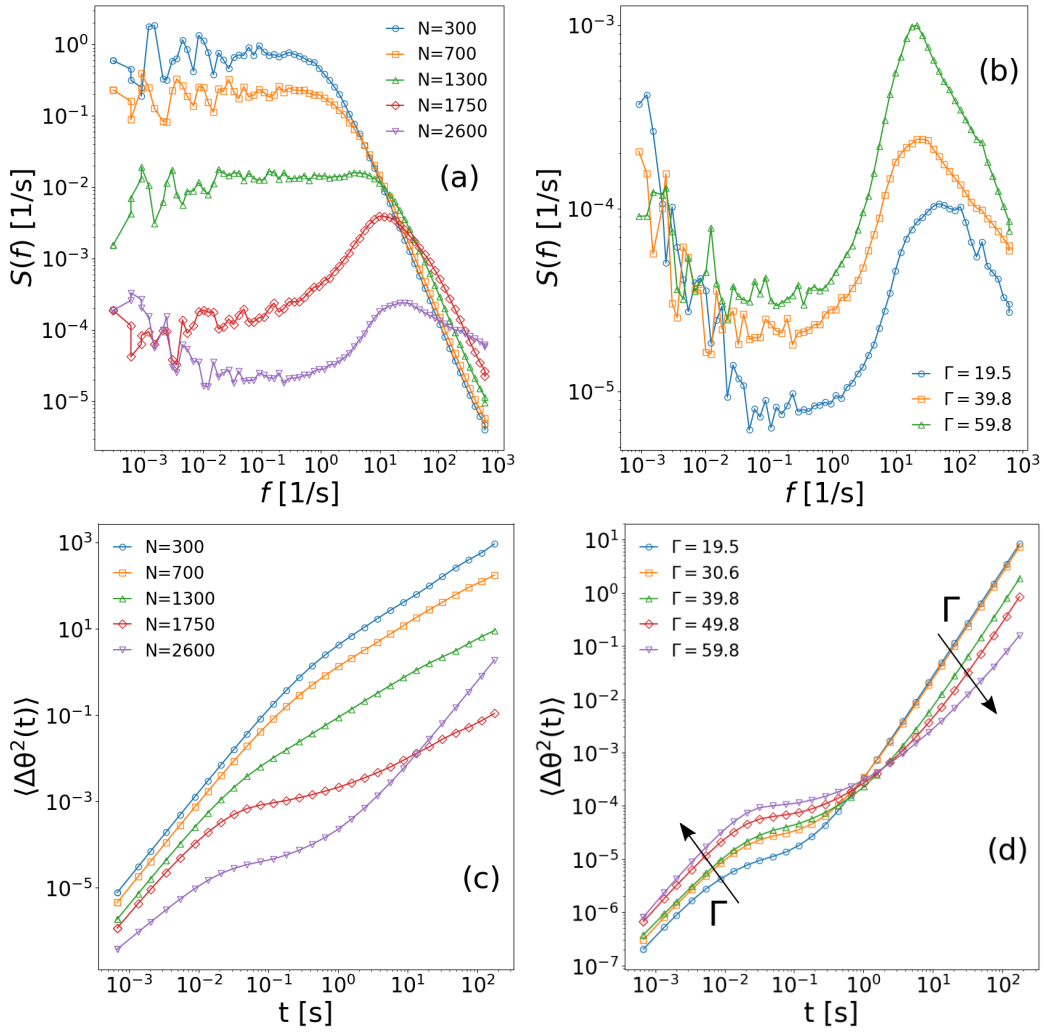

Figure 2.6. Numerical results for the vane dynamics. a: VPSD for $\Gamma = 39.8$ and varying N. b: VPSD for $N = 2600$ and varying Γ. c: MSD for $\Gamma = 39.8$ and varying N. d: MSD for $N = 2600$ and varying Γ. From this last panel, we see that, for a dense system, the short and the long-time part of the MSD behave oppositely as a function of Γ. Comparing this fgure with Fig. 2.2 we note a good qualitative agreement between experiments and simulations.

velocity variance in Fig. 2.5 namely that the numerical system is warmer for dilute conditions and colder for dense ones. The most striking quantitative difference is the high-frequency decay of the spectrum: going from dilute to dense systems in simulations, the power-law $f^{-\beta}$ change from $\beta = 2$ to $\beta < 1$ while in the experiments it remains always larger than 1. The motivation of this disagreement is not completely clear for us, probably its origin relies on some artefacts of the numerical model that emerge in the short-time dynamics. For example, the numerical tracer is not perfectly smooth and the numerical grains are softer than the realistic one. It is reasonable to think that a slowing down of the fast dynamics can be linked to these two factors. Nevertheless, examining in depth this behaviour is beyond the

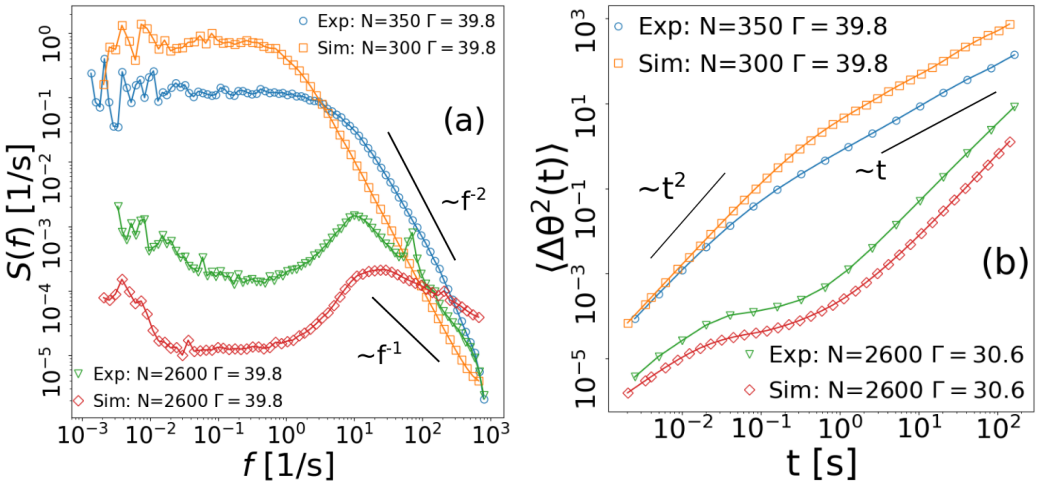

Figure 2.7. Direct comparison between experimental and numerical results for the vane VPSD (a) and MSD (b).

scope of this thesis where the main focus is on the long-time behaviours for which we always have a good agreement.

Chapter 3

Dynamical collective memory acting on slow timescales

Motivated by the experimental and numerical results on anomalous diffusion of Sec. 2.1 and 2.2, in this chapter we concentrate on the emergence of long memory effects in a dense granular system. We'll do that with different approaches. First of all, in Sec. 3.1, we start from the realistic DEM simulations of the experimental setup identifying and characterizing the granular properties in which the long memory is rooted. Then, Sec. 3.2 is devoted to discussing a family of phenomenological models able to reproduce the experimental and numerical data.

3.1 An emerging collective variable

In the previous chapter, we discussed cage subdiffusion and superdiffusion at late times of a tracer immersed in a granular medium at high density. DEM simulations of the realistic setup successfully reproduce the rich phenomenology observed in the experiments. Now we want to investigate the phenomena of the granular medium that are the origin of the superdiffusion in the dynamics of the tracer [144]. Contrary to the experiments, in the simulation, we can track the trajectories of all the grains so we can study all the desired granular observables. This allows us to identify a collective variable of the granular medium whose dynamics is strongly correlated to the tracer. It consists of a slow rigid body rotation of (almost) the whole granular medium able to drag the vane for a very long time. We'll give an overview of its dynamical properties concentrating on how the single grains participate in the collective motion.

3.1.1 A granular collective mode coupled with the tracer

Always referring to the numerical setup described in Par. 2.2.1, our first focus is on the most natural collective variable which could be coupled to the angular velocity of the blade, that is the average angular velocity of the granular medium (with

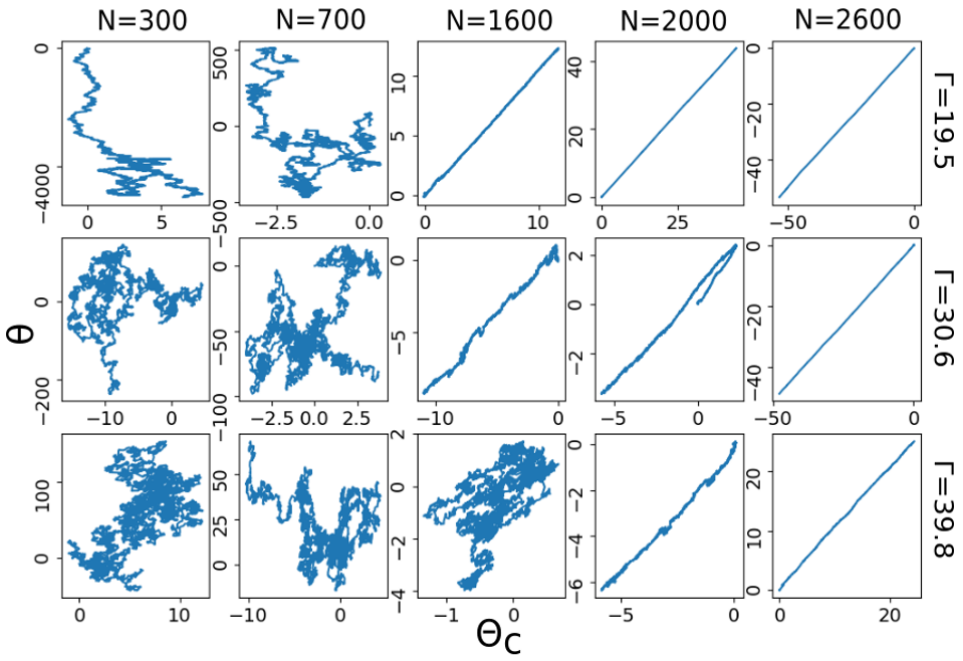

Figure 3.1. Scatter plot between the travelled angle of the blade $\theta(t)$ and the collective variable $\Theta_c(t)$ for several choices of N and Γ. We note that going from small-N/high-Γ to large-N/low-Γ, the two variables go from being uncorrelated to being strongly correlated. Image reprinted from [144].

respect to the central axis):

$$\Omega_c(t) = \frac{1}{N}\sum_{i=1}^{N}\dot{\theta}_i(t) \tag{3.1a}$$

$$\theta_i(t) = \arctan\left(\frac{y_i(t)}{x_i(t)}\right) \quad \dot{\theta}_i(t) = \frac{(\mathbf{r}_i(t)\times\mathbf{v}_i(t))_z}{r_i^2}, \tag{3.1b}$$

and its time-integral which represents a collective absolute travelled angle:

$$\Theta_c(t) = \int_0^t \Omega_c(t')dt' \tag{3.2}$$

We remind here that this collective angular velocity was previously studied in [82]. As explained in Par. 1.4.2, the coupling between this variable and the intruder was responsible for the violation of the FDR. Solid evidence that $\Theta_c(t)$ is meaningful with respect to the anomalous diffusive properties of the probe can be found in Fig. 3.1 that reports the parametric plot $\theta(t)$ (blade's angle) vs. $\Theta_c(t)$ (collective angle). It is immediately clear that a sort of crossover line exists in the plane of parameters N, Γ (with, in fact, a weak dependence on Γ coordinate): for small values of N and high values of Γ one has a regime where $\theta(t)$ and $\Theta_c(t)$ are mostly uncorrelated. On the contrary, for large N and small Γ a strong correlation emerges between the two signals. To express this quantitatively, we consider a covariance

$C(\Theta_c, \theta)$ defined as:

$$C(x,y) = 1 - \frac{\langle [x'(t) - y'(t)]^2 \rangle}{\langle (x'(t))^2 \rangle + \langle (y'(t))^2 \rangle}, \tag{3.3}$$

where $x'(t) = x(t) - \langle x \rangle$, $y'(t) = y(t) - \langle y \rangle$ and the average runs over data sampled for the whole simulation time (we recall that typical simulation times are 3600 s with a temporal step $\Delta t = 1.35 \cdot 10^{-5}$ s). Note that this estimator can also be rewritten as $C(x,y) = 2\langle x'(t)y'(t) \rangle / (\langle (x'(t))^2 \rangle + \langle (y'(t))^2 \rangle)$ that explicitly depends on the covariance. Fig. 3.2a confirms that this observable can be interpreted as an order parameter distinguishing between those two regimes, and that the crossover occurs, with a fair sharpness, at a value $N_c \sim 1300 \div 1600$ only weakly dependent upon Γ. In panels b-c-d of Fig. 3.2, we show a comparison between the trajectories of θ and Θ_c for three values of N in order to directly visualize the emergence of their coupling. The behaviour observed in panel b corresponds to $C < 0.2$, here the collective variable has not yet formed: the particles move independently of each other so Θ_c is not representative of a collective motion. Cases with $0.2 < C < 0.9$ correspond to panel c where the collective variable has clearly emerged but its influence on the vane dynamics is still not dominant. Finally, for $C > 0.9$ we have panel d where the vane results to be completely embedded in the granular medium and is dragged by the collective motion.

The results of the previous analysis make clear that in the dense/cold cases, when seen from the point of view of large timescales ($\gtrsim 1s$, roughly speaking), the dynamics of the blade is strongly correlated to the collective rotation of the granular medium, which is the real hallmark of the transition in the N, Γ plane.

3.1.2 Dynamical characterization of the collective rotation

The strong coupling between the collective rotation and the tracer dynamics suggests focusing on a new series of simulations *without* the rotating blade, with the aim of focusing upon the granular medium. Our analysis revealed that the behaviour of the granular medium is largely independent of the presence or absence of the blade, however, a blade-free simulation seemed to us *cleaner* to assess the minimal ingredients of the observed phenomenon. As done with the tracer in the previous chapter, here we focus on the dynamics of the collective variable by studying different observables that highlight its rich behaviour over many timescales. From the remainder of this chapter we refer to blade-free simulations.

Trajectories

We start by discussing the trajectories of $\Theta_c(t)$ in different conditions. In Fig. 3.3a we plot the series at fixed $\Gamma = 39.8$ and varying N. We observe typical Brownian trajectories for small and moderate densities whose fluctuation amplitudes decrease with N. At $N = 2000 - 2600$ we observe a persistent dynamics with a sudden change of direction around $t = 300 - 700$ s. By varying Γ at high density (Fig. 3.3b), we always see Θ_c travelling in a constant direction for long periods eventually interrupted by rare turns. We note that the typical behaviour of the persistent dynamics is not sensibly affected by the shaking parameter until reaching very high

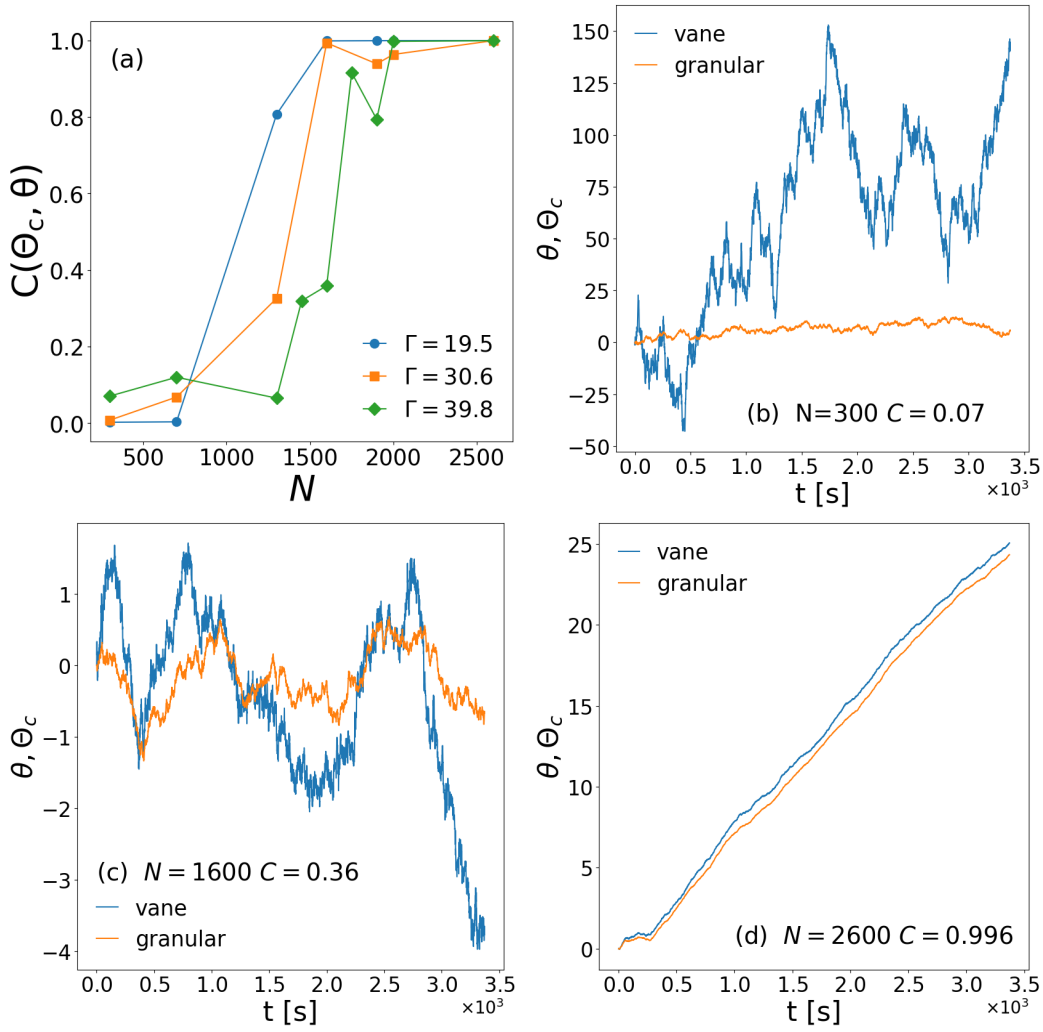

Figure 3.2. a: Correlation between the probe and the collective rotation as a function of N for different Γ. See Eq. (3.3) for the definition of C. a,b,c: Direct comparison between the trajectory of the angle travelled by the blade θ and the collective variable Θ_c for three values of N at a fixed $\Gamma = 39.8$. They help to explicitly visualize the correlation between the two variables for small, intermediate and high C.

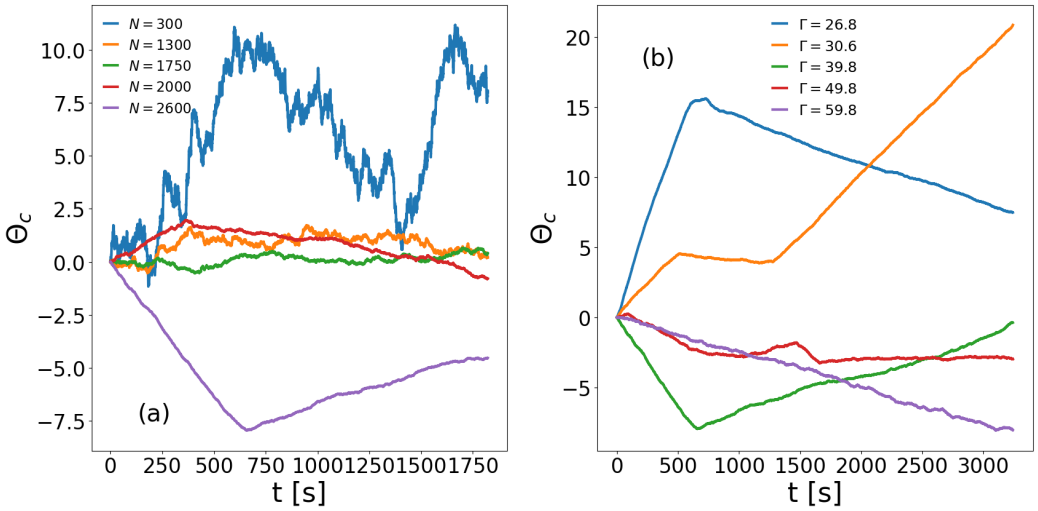

Figure 3.3. Trajectories of the collective travelled angle Θ_c at fixed $\Gamma = 39.8$ with a varying N (a) and at fixed $N = 2600$ with a varying Γ (b). In the left panel we see, up to $N = 1750$, a Brownian-like behaviour while for $N = 2000$ and 2600 we observe a persistent rotational drift interrupted by a sudden turn at $t = 300$ s and 700 s respectively. In the right panel, we always have persistent dynamics.

accelerations $\Gamma = 49.8 - 59.8$ where the drift is visibly reduced. A possible way to rationalize the crossover between Brownian-like trajectories and persistent ones is thinking that the average time between the rare turns is somehow related to the re-arrangements of the spatial configurations of the grains. So it is almost instantaneous in the gas phase but after a density threshold (in this case given by $N_c = 1750$), it becomes comparable with the duration of the whole simulation (cases with $N = 2000 - 2600$). This is just a conjecture for now; the interesting connection between spatial re-arrangements and changes of rotation speed or direction will be investigated more carefully in Chap. 5.

Mean squared displacement and velocity power spectral density

Here we discuss the velocity power spectral density (VPSD) of the collective variable $S_c(f) = (2\pi T)^{-1} \left| \int_0^T dt \Omega_c(t) \exp(i2\pi f t) \right|^2$ and the mean squared displcacement (MSD) $\langle \Delta\Theta_c^2(t) \rangle$ by varying N and Γ. In Fig. 3.4a we show the power spectra of Ω_c as N varies with $\Gamma = 39.8$ fixed. As for the tracer, we have a Lorentian shape at low densities while for $N = 2600$ we observe low-frequencies decay which signals the presence of long memory effects. Regarding the high-frequency decay, we have $\sim f^{-\beta}$ with $\beta = 2$ in the dilute cases and $1 < \beta < 2$ for the dense ones. So we do not observe the strong slowing down with $\beta < 1$ found in the VPSD of the numerical tracer and this support the interpretation given at the end of Par. 2.2.2. We also note that the mid-frequency peak, which was very pronounced for the vane, is only slightly hinted in the two densest cases. So, the two decays of the spectra at $N = 2600$ are separated by a plateau that spans almost 4 decades of frequencies. As a matter of fact, we do not expect any backscattering effect for the collective variable since there is nothing in the system that, at least intuitively,

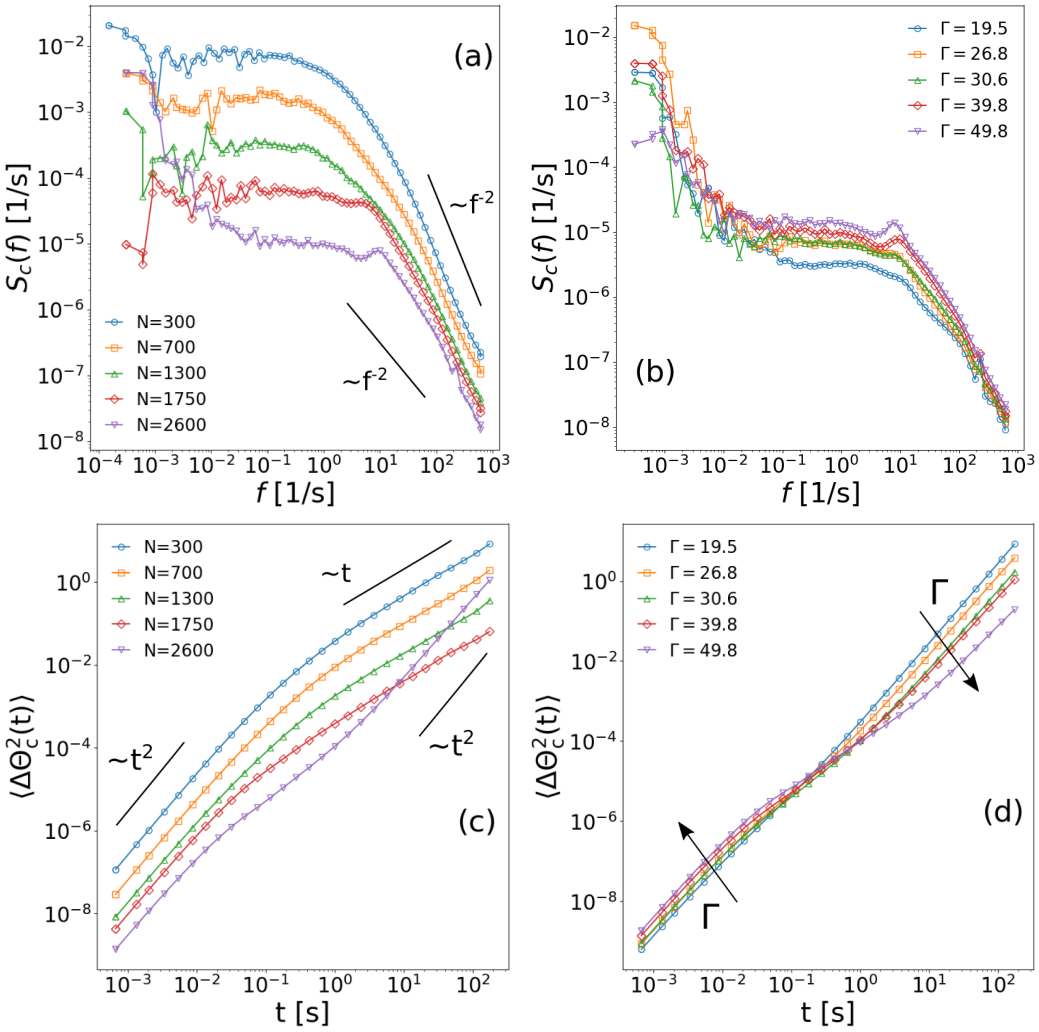

Figure 3.4. Numerical results for the collective dynamics. a: VPSD for $\Gamma = 39.8$ and varying N. b: VPSD for $N = 2600$ and varying Γ. c: MSD for $\Gamma = 39.8$ and varying N. d: MSD for $N = 2600$ and varying Γ. From panel d we see that the slowdown at intermediate times is responsible for the inversion of the MSD heights at different timescales. For example the MSD at $\Gamma = 49.8$ (purple triangles) starts above the one at $\Gamma = 19.5$ (blue circles) but ends up below it after the slowdown at $t \sim 0.5$ s.

could "cage" it. The hinted intermediate characteristic frequencies could be related to the motion of the single grains in their cage (see next paragraph) originating some weak global modes. Also for the collective variable, the MSD consistently reproduce what is observed in the spectra. In Fig. 3.4c we note that, as in the case of the vane, Lorentian spectra correspond to MSD in which there is a simple transition from ballistic motion to ordinary diffusion, while in the denser cases we have the emergence of superdiffusion at long times. As we expect from the absence of the backscattering peak in the spectra, we don't observe any cage subdiffusion in the MSD but just a weak diffusive slowdown at medium times for $N = 2600$. This is related to the intermediate plateau of the spectrum.

In Fig. 3.4b-d we report the analysis as Γ varies with $N = 2600$ for both spectra and MSDs. Regarding the former, we see that the increase of the external driving leads to greater evidence of the peak, which remains however very weakly marked, while the decrease of the external energy leads to a total disappearance of it. Regarding the width of the plateau, it increases with Γ. Consistently, the MSDs show that the mid-time slowdown becomes progressively less pronounced by decreasing Γ until the coldest case where the superdiffusion spans all the timescales. As for the tracer, the inversion of the vertical order of the MSDs from short to long times is observed (we recall Figs. 2.2d and 2.6d). We see that the intermediate slowdown allows the inversion of the height of different MSDs that start ballistically with a given vertical order. This behaviour tells us that raising the external driving directly injects more energy in the short-time dynamics of the grains. Then, the system results to be less coherent and this involves a delay in the emergence of the collective motion. This picture will be confirmed by the analysis of the single-particle dynamics in the next paragraph.

3.1.3 Single-particle dynamics

Once discussed the dynamical properties of Ω_c we now concentrate on how the single grains participate in this collective observable. In Fig. 3.5 we show the trajectories of 6 grains in the xy plane observed for different time intervals Δt in a dense case with collective motion. We see that on short timescales (panel a) each particle vibrates locally without any visible preferred direction. Increasing Δt (panel b), we start to see a deformation of the trajectory given by a persistent average motion whose angular displacement is still comparable with the fast fluctuations. After long times (panel c) we see the clear emergence of the collective rotation followed by the grains as material points of a rigid body. Finally, in panel d we show the trajectories (of all the grains) projected in the rz plane where r is the distance between the grain centers and the point of the central axis at the same height. Here we see the evidence of dynamical heterogeneity in the system: all the particles in the bulk coherently follow the collective drift while a minor fraction of them in the boundary regions (especially on the top) is freer to move and exhibit Brownian-like trajectories. This last plot shows that the collective motion is shared by the majority of the grains in the system and not just by a fraction of them localized around the tracer: the correlation between θ and Θ_c discussed in Par. 3.1.1 was not enough to confirm that. A nice way to synthesise the scenario offered by Fig. 3.5 is to compare the single-particle MSD $\langle \theta_i^2(t) \rangle$ (θ_i is defined in Eq. (3.1b)) with the collective one. We do that in Fig. 3.6 considering, for clarity reasons and to allow a sufficient high acquisition rate, a subset of 100 randomly chosen particles. As we expect, the major fraction of them exhibits a MSD with ballistic motion at short times followed by the cage subdiffusion and superdiffusion at late times. The remaining grains, whose dynamics explores the upper region of the container, perform an ordinary ballistic $\rightarrow$ diffusive behaviour. We recall that the vertical shift between the collective MSD and the one of the single grains gives a measure of the correlation between the particles. Indeed, the square of the average of M uncorrelated random variables x_i is $\mathcal{O}(x_i^2/M)$ while if they are perfectly correlated ($x_i = x \ \forall i$) then it is $\mathcal{O}(x^2)$. Keeping this in mind, and considering also $M\langle \Theta_c(t)^2 \rangle$ with $M = 100$ (red diamonds in Fig. 3.6),

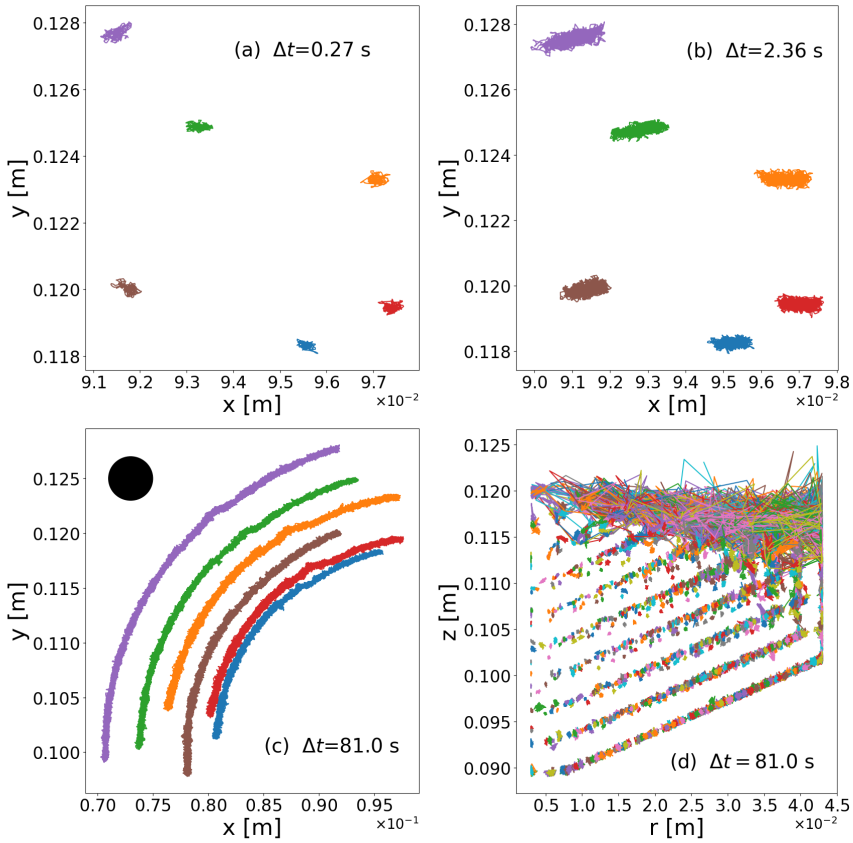

Figure 3.5. a,b,c: Trajectories of six grains during a simulation with $N = 2600$ and $\Gamma = 39.8$ tracked for three different time intervals. The overall dynamics can be described as the superimposition of a slow rigid-body rotation on individual fast vibratons. The black dot in panel c is the dimension of a grain in scale with the graph: we see that the amplitude of the fast fluctuations is a small with respect to the grain diameter. In panel d are the trajrctories of all the grains of the same simulation in the rz plane where $r = \sqrt{x^2 + y^2}$. Trajectories in the bulk follow the collective motion while some of the boundary ones exhibit a Brownian-like behaviour.

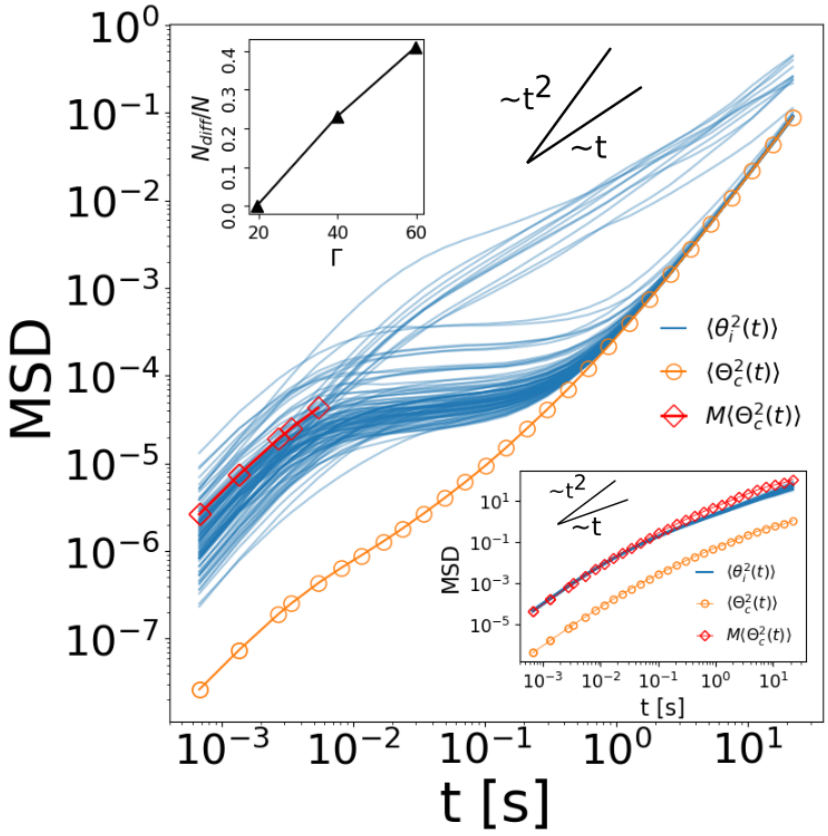

Figure 3.6. Mean squared displacement of $M = 100$ particles spread randomly in the system (lines) and the collective angle (symbols) for a simulation with $\Gamma = 39.8$ and $N = 2600$. Most of the grains participate in the drift exhibiting the ballistic $\rightarrow$ cage $\rightarrow$ superdiffusive bahavior. A small fraction of them, corresponding to the upper region of the system, performs ordinary diffusion. At short times there is more variability between the single-particle MSDs and they are, on average, M time larger than the collective one. At late times instead, they perfectly overlap. This signals that the correlation between different grains depends on the observation timescale (see the discussion in the text). Lower inset: comparison between collective and single-particle MSD for $N = 300$ at the same Γ. The vertical shift between them is the same for all the timescales. Upper inset: fraction of particles exhibiting ordinary diffusion as a function of Γ with $N = 2600$.

we observe that depending on the timescale the dynamics of the drifting particles can be completely uncorrelated as well as perfectly coherent. Specifically, the short-time motion (related to the dynamics *inside the cage*) is statistically independent for particles picked at random while the long-time one (related to the collective variable) is the same for all of them. For comparison, we show the same analysis for a dilute system in the lower inset. Here, as we expect in a gas, the dynamics of the tracked particles is always Brownian and uncorrelated over all the timescales. In the upper inset, we have also verified that the fraction of grains performing Brownian-like diffusion N_{diff}/N increases with Γ and this is probably an explanation of the opposite behaviour at different scales shown in Fig. 3.4d. Indeed raising Γ, have two main effects: on one hand, it provides more kinetic energy to the system (that is stored in the fast variables); on the other hand, it makes the collective motion less participated and consequently less energetic.

Thanks to this analysis, we have shown how dynamical heterogeneities in the dense system appear in two ways: depending on the spatial region the dynamics can be diffusive or persistent, depending on the temporal scale it can be uncorrelated or correlated.

3.1.4 Angular Momentum

Up to now, we concentrated on Ω_c because it is the collective variable that we found to be coupled with the tracer. It thus represents the link between the experiments and the DEM simulations. Nevertheless, aiming to understand the physical origin of this collective motion we can consider also other global observables. The study of angular momentum comes into play in this fashion. Almost all the results of this paragraph are still unpublished and contain many intriguing open questions. The total angular momentum with respect the central axis of the cylinder is defined as $M_c = M_c^{\text{ax}} + M_c^{\text{rot}}$ where $M_c^{\text{ax}} = \sum_i m_i \left(\mathbf{r}_i(t) \times \mathbf{v}_i(t)\right)_z$ that we call axial component being related to the revolution of the grains around the central axis of the container while $M_c^{\text{rot}} = \sum_i \frac{2}{5} m_i R_i^2 \omega_{zi}$ is the rotational component taking into account the single-particle angular velocity ω_{zi} around their own vertical axis. This observable is interesting because, contrary to Ω_c, we can perform simulations where M_c is a conserved quantity. Indeed, by switching off the tangential interactions between the wall of the cylinder and the grains the total external torque exerted on the system is zero. So, in addition to the regular non-conserving cases, we also performed simulations without tangential interactions with the walls. We have checked that in this conditions M_c^{ax} and M_c^{rot} fluctuate but their sum M_c remains constant to its inital zero value (within the numerical error). Since $M_c^{\text{ax}} = -M_c^{\text{rot}}$, their PSD perfectly coincide (see Fig. 3.7b).

Axial component

We start by discussing the axial angular momentum that, as we shall see shortly, is deeply related to the collective motion. In Fig. 3.7a we plot the spectrum of M_c^{ax} (i.e. the square modulus of its Fourier transform) for three Γs in a non-conserving system. We see that the long memory effect is present also in this observable. Moreover, we can see that the low-frequency component of its spectrum coincides

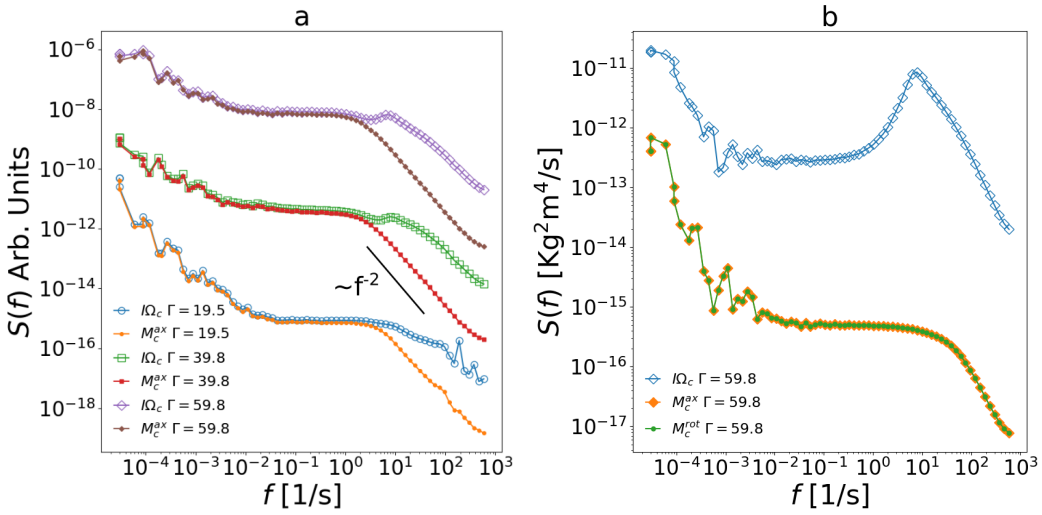

Figure 3.7. Comparison between the power spectral density of the axial momentum M_c^{ax} and the one of the collective angular velocity multiplied by the average inertia momentum of the system $I\Omega_c$. Panel a refers to a non-conserving system for three different Γs, here we note that the spectra of the two variables perfectly overlap up to the end of the mid-frequency plateau. Panel b shows the results for a simulation where the total angular momentum is conserved so the spectra of M_c^{ax} and M_c^{rot} coincide. Unlike the non-conserving case, the PSD of $I\Omega_c$ presents a marked backscattering peak and is vertically shifted with respect to the PSD of $M_c^{\mathrm{ax/rot}}$. All the data come from simulations with $N = 2600$.

with the one of the PSD of Ω_c rescaled with a constant I with the dimension of an inertia momentum. It is easy to rationalize this fact starting by the definition of the axial momentum and using Eq. (3.1b):

$$M_c^{\mathrm{ax}} = \sum_i m_i r_i^2 \frac{(\mathbf{r}_i(t) \times \mathbf{v}_i(t))_z}{r_i^2} = \sum_i m_i r_i^2 \dot{\theta}_i = I\Omega_c + M_{\mathrm{fast}} \tag{3.4}$$

where the last equality holds defining $I = \sum_i m_i r_i^2$ and expressing $\dot{\theta}_i = \Omega_c + \eta_i \ \forall i$ so that $M_{\mathrm{fast}} = \sum_i m_i r_i^2 \eta_i$. Following the phenomenology exposed in Par. 3.1.3, we are assuming that the angular velocity of all particles contains a slow contribution to the collective one and a fast decaying noise $\eta_i(t)$ (weakly correlated between grains) whose variance V_i depends on the position in space. In order to take into account the dynamical heterogeneity, we can assume V_i very small for particles in the bulk where all of them closely follow the collective motion, and higher on the top where they are freer to move diffusively (see Fig. 3.5d). In Eq. (3.4) we have M_c^{ax} expressed as $I\Omega_c$ plus a fast component and this explain why the spectra of this two observables coincide in the low-frequency region. In this sense Fig. 3.7a shows the same scenario depicted in Fig. 3.6 exploiting just global quantities. The value of I used to overlap the spectra is the time average of $m\sum_i r_i^2$ over all the entire simulation (we recall that grains have the same mass). We point out that this value is in fair agreement with the inertia momentum calculated considering a conical-shaped cylinder made of steel (the height of the cylindrical part is taken at rest, see Fig. 2.1b). This shows how our system behaves as a rotating rigid

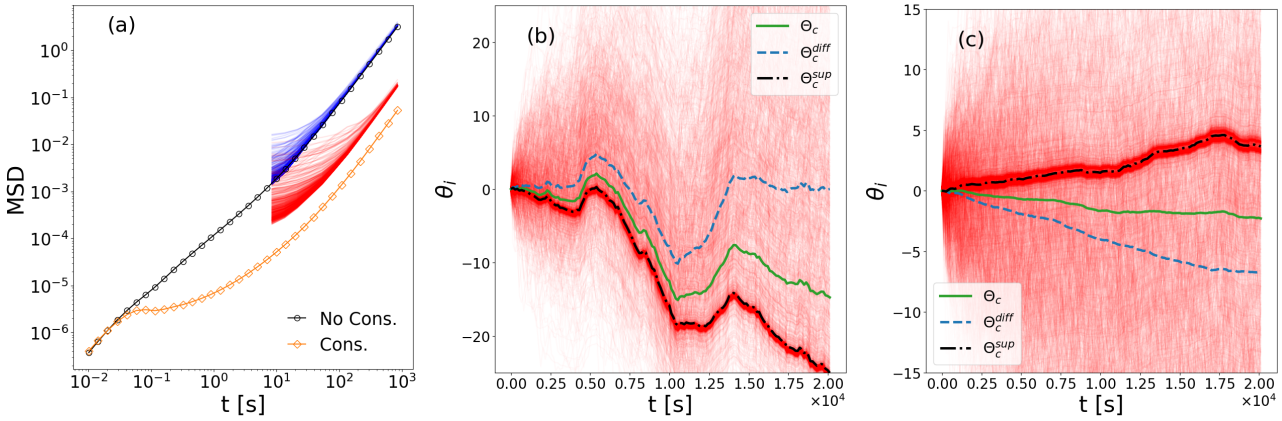

Figure 3.8. a: Collective (symbols) and single-particle (lines) MSD for a non-conserving system and a conserving one. In the latter, we note two main differences with respect to the former: a cage-like subdiffusion at intermediate times and a vertical shift between the collective and the single-particle superdiffusion at late times. b,c: Angular trajectories in a system with non-conserved (b) and conserved angular momentum (c). The red semi-transparent lines refer to the trajectories of the single grains θ_i: most of the particles follow the same motion highlighted by the intensity of the color. The non-transparent lines refer to the average motion calculated over all the particles (Θ_c), the diffusing ones ($\Theta_c^{\rm diff}$) and the superdiffusing ones ($\Theta_c^{\rm sup}$). These three quantities are more correlated in the non-conserving system (see the discussion in the text). All the data come from simulations with $N = 2600$ and $\Gamma = 59.8$.

body if observed over slow timescales while, over fast ones, its behaviour is more similar to a glass where particles move in their cage with just very rare escapes. It is also worth noting that the high-frequency decay in the PSD of $M_c^{\rm ax}$ follows an ordinary f^{-2} power-law. This signals a fast time decorrelation with a well-defined characteristic frequency that slightly shifts from 1 to 4 Hz by raising Γ. We still don't have a physical explanation of the different scaling at high frequencies for $M_c^{\rm ax}$ and $I\Omega_c$. In Fig. 3.7b we do the same comparison for a conserving case and we note a quite different scenario. First of all the spectrum of the collective variable shows a well-defined backscattering peak around 20 Hz and we never found it in a non-conserving case (see Fig. 3.4). Moreover, we see that the low-frequency regions of the two spectra do not overlap. To deepen this evidences it is useful to compare the single-particle MSD between a conserving and a non-conserving case (Fig. 3.8a). As shown in Fig. 3.6, we have also here the presence of many diffusing particles but we omit them for clarity reasons. We see that in the non-conserving system all the particles participate in the same collective motion (i.e. the late time superdiffusive regimes coincide) while in the conserving case the slope of the single-grain superdiffusion is higher (i.e. faster) than the global one. This explains why the two spectra of Fig. 3.7b are not overlapping: the assumption $\dot{\theta}_i = \Omega_c + \eta_i$ does not holds. A direct confirmation of that is given by Figs. 3.8b-c where we show the trajectories θ_i of all the grains highlighting the collective travelled angle calculated over all the particles Θ_c, over just the diffusive particles $\Theta_c^{\rm diff}$ and over the superdiffusive ones $\Theta_c^{\rm sup}$. In the non-conserving case (b) it is clear that Θ_c is a representative average because also the mean contribution of the diffusing particles

(that do not participate individually in the collective drift) is strongly correlated with the motion of the superdiffusive grains. This is quite intuitive if we think that, as suggested by Fig. 3.5d, the diffusive grains are all randomly jumping on the slow rotating bulk. On the contrary, in the conserving system (c), the total average results to be fairly different from $\Theta_c^{\rm sup}$ that represents the "real" collective travelled angle (i.e. the one travelled by the particles that actually participate in the persistent drift). This is because the average motion of the diffusive particles contains an unexpected slow component, just weakly correlated with $\Theta_c^{\rm sup}$, that affects the global average Θ_c. Note that in the conserving case $\Theta_c^{\rm diff}$ and $\Theta_c^{\rm sup}$ run in opposite directions. Formally, taking into account just the diffusing particles we can say that $\dot{\theta}_i^{\rm diff} = \Omega_c^{\rm diff} + \eta_i$ with $\Omega_c^{\rm diff} \simeq \Omega_c^{\rm sup}$ in the non-conserving case while $\Omega_c^{\rm diff} \neq \Omega_c^{\rm sup}$ in the conserving one.

We still don't have a clear explanation for this less coherent behaviour of the collective motion in the conserving systems as well as for the origin of the backscattering peak in the VPSD but we don't exclude that the two things can be connected. The backscattering in the tracer dynamics was easily explained by the cage effect of the surrounding granular fluid but which is the equivalent mechanism for the collective variable? And why it is present only in the conserving case? Probably the absence of external torque keeps alive some horizontal modes at intermediate frequencies that are destroyed in the realistic simulations. These modes could be linked to the phenomenon of the low-frequency oscillations (LFOs) [167, 209] but more extensive analyses are needed to verify it. Also the unexpected slow component of $\Theta_c^{\rm diff}$ has still to be fully understood. Even for this effect, we can think that the absence of an external source of angular momentum allows some slow conversions from the axial to the rotational component and vice-versa. These "fluxes" of momentum can be reflected in the dynamics of the mean rotational motion in such a way to make $\Theta_c^{\rm diff}$ and $\Theta_c^{\rm sup}$ less correlated.

Rotational component

Finding a long memory effect in the axial angular momentum of the conserving system directly suggests that also the rotational component have to exhibit it since $M_c^{\rm rot} = -M_c^{\rm ax}$ (Fig. 3.7b). The single-particle contribution to the axial component was clearly the slow collective rotation around the axis of the cylinder but what about the analogue for $M_c^{\rm rot}$? To start answering this we analyze the dynamics of single-particle rotational degrees of freedom. In Fig. 3.9 we show a subset of 130 trajectories of $\theta_{zi}(t) = \int_0^t dt' \omega_{zi}(t')$ for the conserving (panel a) and the non-conserving (panel b) system. In both cases we find a remarkable fact: for many grains, the single-particle rotations around their vertical axis show persistent dynamics. Both the verses of rotation are observed and seems to be equally distributed. Persistent rotations of grains have also been observed in a recent experiment [130] of a vibrated 2D vertical monolayer of disks. The authors relate this phenomenon to the local asymmetries of the granular packing: each grain vibrates into an anisotropic cage that favours a rotational direction with respect to the other. The results we showed, highlight the robustness of this phenomenon demonstrating that it is present also in a 3D system. The connection between single-grain rotations and collective motion is an intriguing perspective and in the next chapter we'll see how structural

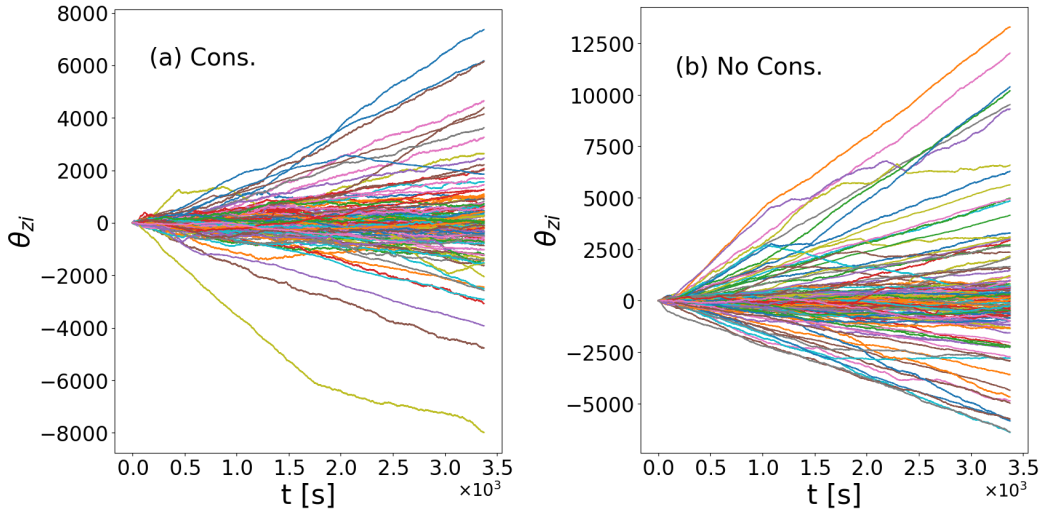

Figure 3.9. A subset of 130 trajectories of the single-particles rotations around their vertical axis for a non-conserving system (a) and a conserving one (b) with $N = 2600$ and $\Gamma = 59.8$. In both cases most of the grains exhibt a persistent dynamics.

asymmetries play a role also for collective drifts.

An important thing to note is that without a source of external momentum, the system self organizes in such a way to conserve the total momentum still exhibiting a persistent dynamics. This is clearly possible just because the angular momentum can be stored in both rotational and translational degrees of freedom and there is a transfer of momentum between these two forms during the dynamics. In different geometries, where the long memory is found in the total impulse, the presence of an external source of it becomes crucial (see Chap. 5).

3.2 Phenomenological models

Summarizing the experimental and numerical analysis, we can say that the long memory effects in which we are interested determine two observable phenomena: the superdiffusion (SD) for the dynamics of a tracer immersed in the granular medium [175], and persistent rotational motion (PR) of large parts of the granular medium [144]: both phenomena - strictly correlated - appear when the density is increased and/or the steady vibrofluidization is reduced, and take place over timescales in the range of $10 \div 10^3$ seconds, depending upon packing fraction and shaking parameters, while interactions occur on timescales of $10^{-3} \div 10^{-2}$ seconds. Interestingly these unprecedented SD and PR are superimposed to the usually observed fast phenomena occurring over small and medium timescales, such as subcollisional ballistic motion and transient dynamical arrest due to caging. Here we aim at elucidating some phenomenological stochastic models with few coarse-grained variables which are able to describe the SD and PR phenomena [146]. We stress that modelling collective motion in nonconservative systems, such as granular materials, is difficult since a general microscopic-to-macroscopic approach is not available: there is no Hamiltonian, no known stationary densities in phase space,

and not a known small set of relevant variables. Then, phenomenological coarse-grained models are a good alternative, provided that one has identified a few slow observables and collected a sufficient amount of data for their dynamics.

The models we are going to present are an extension and improvement of previous ones proposed in [113, 21] which was built to reproduce only the SD tracer behaviour: limitations of that models are that they are not entirely coherent with the observed tracer power spectra and does not describe the granular medium (i.e. it cannot account for PR). These models share minimality (in the spirit of Occam razor), in fact they include only linear couplings and additive independent noises, allowing for an exact analytical treatment: their goal is to characterize the existence of many timescales in the system and for this purpose non-linearity is not a crucial ingredient. A more general (not limited to linear coupling) Langevin approach has been also considered by applying a Langevin modelling recipe to experimental and numerical data [20, 21]. Linearly coupled models have been used before in granular modelling: for instance they can characterize the failure of fluctuation-dissipation relation for the dynamics of a tracer in certain models [157, 202, 173] as discussed in Par. 1.4.2, but have shown certain limitations when compared with experiments [82]. Linear modelling used for the purpose of quantifying non-equilibrium features have been also used, recently, in the single-flagellum dynamics of active particles [24].

We will proceed by first modelling PR of the granular medium and then using it to build a proper model for the intruder dynamics. We will show how the proposed models successfully fit the experimental/numerical data with a reasonable behaviour of the free parameters.

3.2.1 Existing Langevin models

A simple and old model of diffusion in dense liquids is the so-called Itinerant Oscillator model, where the tracer is caged in a (harmonic) potential well, whose minimum's position is not fixed but slowly diffuses [180, 204]: this model helped in rationalising spectra from neutron scattering experiments on liquids [160]. If diffusion of the potential minimum is slower than the particle's diffusion inside the well, then the behaviour of the tracer's mean squared displacement (MSD) shows a transient plateau (equivalent to the dynamical arrest or caging) followed by ordinary diffusion. If the dynamics inside the well is underdamped, the first part of the tracer's MSD time-dependence is ballistic $\sim t^2$. The after-cage part, however, is always of the ordinary diffusive type $\sim t$ as the tracer is slaved to the dynamics of the minimum's position which is purely diffusive. The extension of this model proposed in [113] was aimed at obtaining long superdiffusive regimes *after* the cage time discussed in Sections 2.1 and 2.2. In order to obtain this result, an underdamped dynamics was considered also for the position of the well's minimum. Such an extension takes the form of four coupled equations for the angular velocity and position of the rotating tracer, $\omega(t)$ and $\theta(t)$ respectively, and for the angular velocity and position of a collective slow variable which represents the effect of a large

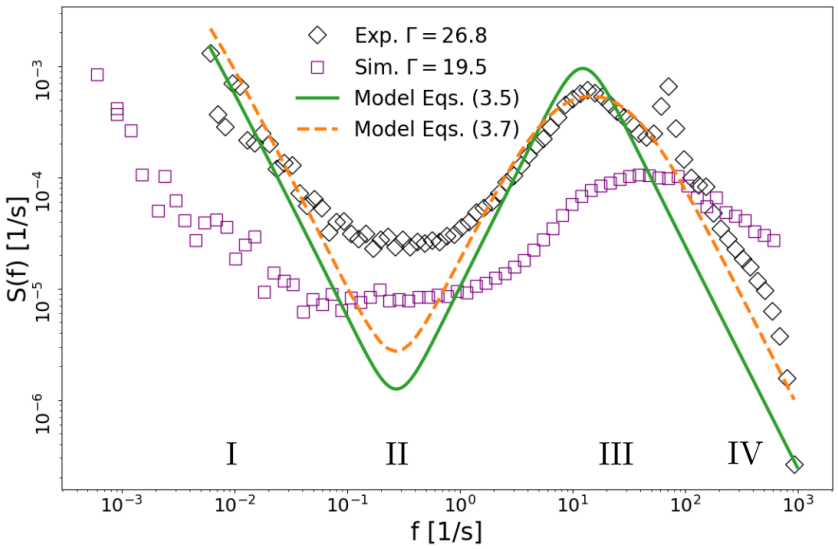

Figure 3.10. Comparison between the tracer VPSD in experiments/simulations and the ones predicted (just for the experiments) by Eqs. (3.5) and (3.7). The two models fail in reproducing the data in region (II) in the same way. Both experiments and simulations are performed with $N = 2600$. The experimental and numerical data have been already shown in Fig. 2.2 and 2.6 respectively.

group of particles surrounding the tracer (the cage), $\omega_0(t)$ and $\theta_0(t)$ respectively:

$$I\dot{\omega}(t) = -\gamma\omega(t) - k[\theta(t) - \theta_0(t)] + \sqrt{2\gamma T}\eta(t) \tag{3.5a}$$

$$I_0\dot{\omega}_0(t) = -\gamma_0\omega_0(t) + k[\theta(t) - \theta_0(t)] + \sqrt{2\gamma_0 T_0}\eta_0(t) \tag{3.5b}$$

$$\theta(t) = \int_0^t \omega(t')dt' \qquad \theta_0(t) = \int_0^t \omega_0(t')dt'. \tag{3.5c}$$

In the above equations $\eta(t)$ and $\eta_0(t)$ are independent Gaussian white noises with zero average and unitary variance, namely $\langle\eta(t)\eta(t')\rangle = \delta(t-t')$ and $\langle\eta_0(t)\eta(t')\rangle = \delta(t-t')$. The parameters I and I_0 are the inertia of the tracer and of the surrounding medium, γ and γ_0 are the dissipation felt by the two variables, and T and T_0 are "temperatures" (assuming unitary Boltzmann constant $k_B = 1$), see [173] and Par. 1.4.2 for a discussion of their physical interpretation. The coupling between the tracer and the collective variable, in this model, is represented by the term $-k[\theta(t) - \theta_0(t)]$ which is linear in the *positions*. With large enough values of I_0, the inertia of the cage, the model - which is analytically solvable - reproduces long-time ballistic superdiffusion.

A problem of this model however is its inability to entirely reproduce the VPSD which is put in evidence in Fig. 3.10. We recall the definition used here for velocity power spectrum

$$S(f) = \lim_{t_{TOT}\to\infty} \frac{1}{2\pi t_{TOT}} \left| \int_0^{t_{TOT}} \omega(t) e^{2\pi f i} dt \right|^2, \tag{3.6}$$

(where T is the total simulation time) which is also equivalent to the Fourier transform of the auto-correlation function in the steady state $\langle\omega(t)\omega(0)\rangle$. As extensively

discussed in Sec. 2.1 and shown in Fig. 3.10 the experimental/numerical power spectral density shows four main regions and the most evident discrepancy between theory and experiments/simulations is in the central plateau region (II): the inertial itinerant oscillator model is not able to reproduce it.

A second attempt to obtain a meaningful Langevin model for the angular velocity of the rotating tracer has been done in [21]. Its advantage is that it is the result of a general constructive method of Markovian model-building based upon the experimental data (the experimental time series of $\omega(t)$) and some guess about other possibly relevant variables (when data present non-Markovian character, other variables must be identified in order to obtain a proper Markovian embedding [19]). In such a method one is also able to verify that the chosen variables are consistent with the Markovian hypothesis. Such an advantage results in a more compact model, with a smaller number of parameters:

$$\dot{\omega}(t) = -A_1\omega(t) - A_2[\theta(t) - \theta_0(t)] + \sqrt{2B}\eta(t) \tag{3.7a}$$

$$\dot{\omega_0}(t) = -A_0\omega_0(t) + \sqrt{2B_0}\eta_0(t) \tag{3.7b}$$

$$\theta(t) = \int_0^t \omega(t')dt' \qquad \theta_0(t) = \int_0^t \omega_0(t')dt', \tag{3.7c}$$

where $\eta(t)$ and $\eta_0(t)$ are Gaussian noises with unitary variance. This model is a particular limit of the model guessed in [113], where the term $k[\theta(t) - \theta_0(t)]$ is negligible with respect to the other terms in Eq. (3.5b) indeed with the present definition, ω_0 evolves with a slow dynamics that does not admit fluctuations on the fast timescale of θ_1, so that such term is necessarily negligible. All other parameters are strictly related to the parameters of the model in Eq. (3.5): A_0, A_1, A_2, B and B_0 should be directly compared with γ_0/I_0, γ/I, k/I, $\gamma T/I^2$ and $\gamma_0 T_0/I_0^2$ respectively. This model well reproduces the mean squared displacement of the tracer with its final superdiffusive part (see [21]), while its comparison with the power spectrum is again unsatisfying in the central part, as in [113], see Fig. 3.10.

3.2.2 How many variables for it to be Markovian?

Models in Eqs. (3.5) and (3.7) both involve two independent white noises but they are anyway three-dimensional linear models in which the Markovian vector is $\boldsymbol{X}(t) = \{z(t), \omega(t), \omega_0(t)\}$ with $z(t) = \theta(t) - \theta_0(t)$. One may wonder if it is possible to obtain satisfying results with a two-variables linear model. We know from the data that a minimum request to entirely reproduce the phenomenon under study is a VPSD with two stationary points (a minimum and a maximum) for $f > 0$: is this property compatible with the most general form of a two-variables linear model? We write generic multivariate linear stochastic process as $\dot{\boldsymbol{X}}(t) = -\hat{A}\boldsymbol{X}(t) + \hat{B}\boldsymbol{\eta}(t)$, where $\boldsymbol{X}(t)$ is a vector of variables, $\boldsymbol{\eta}(t)$ a vector of white noises with zero mean and unitary variance while $\hat{A}$ and $\hat{B}$ are the matrices that define characteristic times, diffusion coefficients and eventually couplings of the variables. In two dimension, assuming independent noises between the variables, we have $\boldsymbol{X}(t) = \{x_0(t), x_1(t)\}$, $\boldsymbol{\eta}(t) = \{\eta_1(t), \eta_2(t)\}$ and:

$$\hat{A} = \begin{pmatrix} a & b \\ c & d \end{pmatrix}, \quad \hat{B} = \begin{pmatrix} D_1 & 0 \\ 0 & D_2 \end{pmatrix}. \tag{3.8}$$

We can now compute the spectral matrix through the following relation [76]:

$$\hat{S}(f) = \frac{1}{2\pi}(\hat{A} + i2\pi f)^{-1}\hat{B}\hat{B}^T(\hat{A}^T - i2\pi f)^{-1}, \tag{3.9}$$

obtaining for the spectrum of a single variable (for example $x_0(t)$):

$$S_{00}(f) = \frac{\frac{1}{2\pi}D_1^2d^2 + 2\pi D_1^2f^2 + \frac{1}{2\pi}D_2^2b^2}{(16\pi^4f^4 + 4\pi^2f^2\,(a^2 + 2bc + d^2) + a^2d^2 - 2abcd + b^2c^2)}. \tag{3.10}$$

Computing the first derivative we find $S'_{00}(f) = P(f)/Q(f)$ where $P(f) = c_1f^5 + c_2f^3 + c_3f$ with $c_1, c_2 < 0$. This polynomial cannot have a double stationary point in the region $f > 0$ so there is not any choice of parameters that reproduces the behaviour under interest here i.e. a low-frequency decay followed by a backscattering peak. These results do not change if we take $x_1(t)$ instead of $x_0(t)$. In view of this, using a three-variable model is an unavoidable choice if one wants to reproduce the experimental data through stochastic linear models.

Finally, regarding the famous Onsager's warning [138] *"how do you know you have taken enough variables, for it to be Markovian? "* up to now we can reply: *"we don't know... but at least three"*.

3.2.3 Linear model for the collective variable (two timescales)

The results presented in [144] and reported in the previous section demonstrate that the SD phenomenon displayed by the rotating tracer is a direct consequence of the PR phenomenon exhibited by the granular medium: while on small timescales the rotating tracer has its own dynamics with short free flights and rapid bounces against the boundaries of a local cage of surrounding grains, on long timescales the tracer is dragged by a persistent collective rotation of the medium. The velocity of such a medium rotation $\Omega_c(t)$ is defined in Eq. (3.1) and the absolute travelled angle in Eq. (3.2). As shown in Par. 3.1.2, when density is increased and vibrofluidization is weakened, $\Omega_c(t)$ exhibits long persistent drifts in both clockwise and anti-clockwise directions that imply the appearance of superdiffusion at late times in its MSD and a power-law decay at very low frequency in the VPSD.

The model we propose to reproduce these features is based on the principle that persistent memory can be reproduced by considering (at least) an auxiliary slow variable. An analysis of the data coming from numerical simulations showed, however, that in this particular case the modelling is even easier. We model the collective rotation as the sum of two independent variables: there is not a simple "natural" mechanism to couple fast and slow motion so, at the first level of approximation, we can consider them to be decoupled. We choose for simplicity two independent Ornstein-Uhlenbeck (OU) processes $\Omega_1(t)$ and $\Omega_2(t)$ with two different characteristic times $\tau_1 = I_1/\gamma_1$ and $\tau_2 = I_2/\gamma_2$ and, in general, two different temperatures T_1 and T_2. In summary the model is described by:

$$\Omega_c(t) = \Omega_1(t) + \Omega_2(t) \tag{3.11a}$$

$$I_1\dot{\Omega}_1(t) = -\gamma_1\Omega_1(t) + \sqrt{2T_1\gamma_1}\eta_1(t) \tag{3.11b}$$

$$I_2\dot{\Omega}_2(t) = -\gamma_2\Omega_2(t) + \sqrt{2T_2\gamma_2}\eta_2(t). \tag{3.11c}$$

In fact, the model can be rewritten with a smaller number of parameters: the only coefficients that count are τ_i and $q_i = T_i/I_i$ with $i = 1, 2$.

We are in the presence of a sum of two independent variables, therefore the PSD and the MSD are simply the sum of the two individual OU contributions:

$$\begin{aligned}\langle \Delta\Theta_c^2(t)\rangle &= 2q_1\tau_1 t + 2q_1\tau_1^2(e^{-\frac{t}{\tau_1}} - 1) \\ &\quad +2q_2\tau_2 t + 2q_2\tau_2^2(e^{-\frac{t}{\tau_2}} - 1) \qquad (3.12a)\end{aligned}$$

$$S(f) = \frac{q_1\tau_1}{\pi[1 + (2\pi f\tau_1)^2]} + \frac{q_2\tau_2}{\pi[1 + (2\pi f\tau_2)^2]}. \qquad (3.12b)$$

Our idea is then to consider one of the two characteristic times much larger than the other ($\tau_2 \gg \tau_1$). To make clear now the meaning of the two variables, we expect the slow component of the collective variable, Ω_2, to behave similarly to the filtered variable

$$\Omega_s(t) = \frac{1}{\tau_f}\int_t^{t+\tau_f} \Omega_c(t')dt', \qquad (3.13)$$

obtained with a moving average of $\Omega_c(t)$ over a time τ_f such that $\tau_2 \gg \tau_f \gg \tau_1$. In order to verify this conjecture we proceed in two ways: first we try to fit the numerical MSD and PSD via Eqs. (3.12), then we show that the superdiffusive part at late times of the collective MSD coincides with the MSD of the filtered variable $\langle \Delta\Theta_s^2(t)\rangle$ where $\Theta_s(t) = \int_0^t \Omega_s(t')dt'$.

In Fig. 3.11 we show how Eqs. (3.12) can fit the numerical data for two particular cases of control parameters ($N = 2600$, $\Gamma = 19.5 - 59.8$), postponing a more systematic analysis to Par. 3.2.5. To obtain the theoretical lines we have first performed a fit of the PDS via Eq. (3.12)b and then used the parameters inferred in this way also for the MSD (Eq. (3.12)a). We can see that the model properly predicts the behaviour of the two observables. In the PSD there is a good agreement at all the frequency regimes except for the high-frequency decay where a linear model can only predict a f^{-2} behaviour while the data show $f^{-\alpha}$ with $2 > \alpha > 1$. The MSD also exhibits an almost perfect agreement between data and model predictions at all timescales. We conclude that the idea of decomposing the total collective variable into two independent contributions that act at two well-separated timescales is reasonable. Looking at the numerical values of the fitted parameters in Tab. 3.1 one can can verify that $\tau_2 \sim t_{TOT} \gg \tau_1$.

In Fig. 3.11b we show the MSD of Ω_c and Ω_s for two values of Γ, one cold case and one hot case at similar density. For the cold case, i.e. at low Γ, we see that $\langle \Delta\Theta_c^2(t)\rangle$ is ballistic at all times except for the initial ones (the fast component is very weak so the slow one emerges immediately). In the warmer case, we can clearly distinguish the two contributions to the total MSD: the fast one that dominates the first times with its ballistic part and then diffuse, and the slow one that dominates the late times with superdiffusion. Regarding the filtered MSDs we can see that in both cases it emerges in the total one exactly at the beginning of the superdiffusive regime, at late times. In principle, it is not obvious that the filter used for Ω_s is able to isolate the slow component of a sum of two signals. We can clearly expect that $\langle \Delta\Theta_s^2(t)\rangle$ has to overlap the total MSD for $t > \tau_f$ but how can we be sure that it is really describing the MSD of Ω_2 i.e. the slow component of Ω_c? We try to answer this question with Fig. 3.12 where we study the effect of the filter

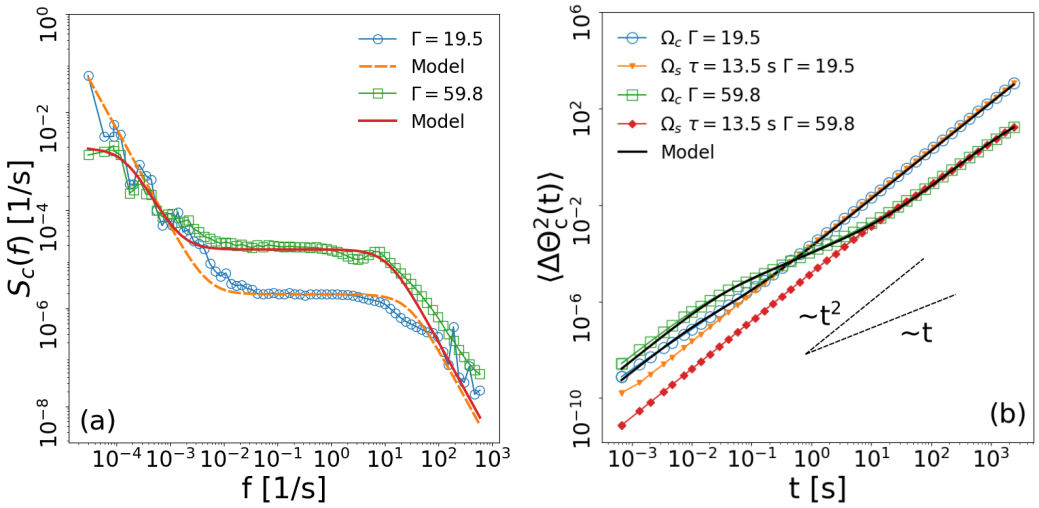

Figure 3.11. Comparison between the model predictions (3.12) and numerical data ($N = 2600$, $\Gamma = 19.5 - 59.8$) for the PSD of the collective variable (a) and its MSD (b). The simple model Eqs. (3.11) fits well the numerical data for both the observables. The fitted parameters are reported in Tab. 3.1. In the right panel, we can also see that the MSD of the filtered variable Ω_s "emerges" in the total one at the onset of superdiffusion.

on two qualitatively different signals for several choices of τ_f. We first discuss the MSD of the collective variable in a dilute case (N=300) where we have an ordinary ballistic-diffusive behaviour with just one relevant time scale [144]. We can see that in this case the filter lowers the energy of the ballistic part and stretches it up to times $t \sim \tau_f$ where the filtered MSD reunites with the original one. In the dense case (e.g. low Γ) the MSD has the ballistic-diffusive-superdiffusive behaviour with two relevant time scales (the fast τ_1 and the slow τ_2 of the aforementioned model) but we can consider a third one τ^* defined as the time for which the slow variable starts to dominate the total MSD (so the time when the late superdiffusion starts, close to τ_2). In this case, the filter acts as in the previous one but for $\tau_f > \tau^*$ it reaches a kind of saturation and leaves the shape of the MSD unchanged (see the yellow and the cyan-dashed lines that overlap). This implies that for $\tau_f > \tau^*$ the time in which $\langle \Delta\Theta_c^2(t) \rangle$ and $\langle \Delta\Theta_s^2(t) \rangle$ reunite coincide with τ^* and no more with τ_f. Given this last analysis, we can conclude that if in our data a contribution of a slow variable is present, this filter operation tends to isolate it.

To sum up, in this paragraph, we have provided evidence of two main facts:

- The collective variable behaves as the sum of two independent OU processes with different characteristic times $\Omega_c(t) = \Omega_1(t) + \Omega_2(t)$;

- A running average $\Omega_s(t) = \tau_f^{-1} \int_t^{t+\tau_f} \Omega_c(t')dt'$ with τ_f larger than the time τ_1 in which the fast component dominates, successfully isolates $\Omega_2(t)$ i.e. the slow component of Ω_c.

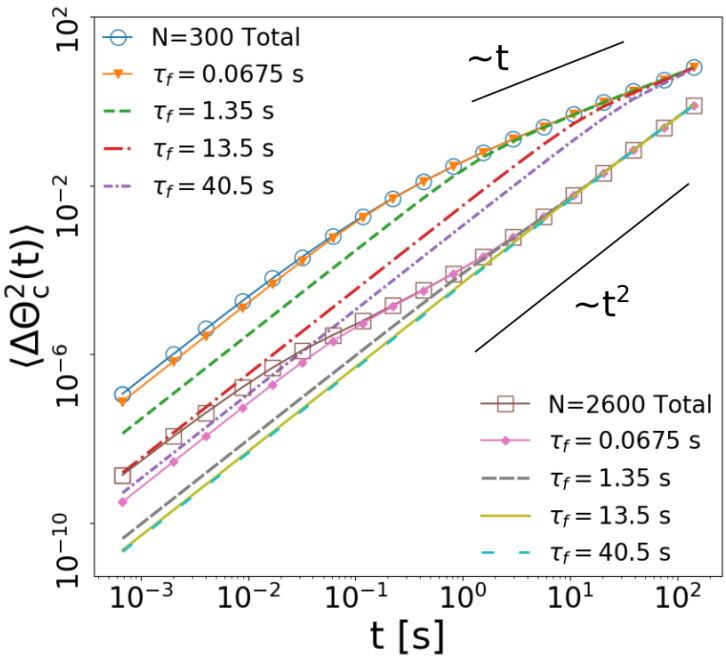

Figure 3.12. Collective MSD of the total signals and the filtered ones for several τ_fs and two values of N with fixed $\Gamma = 39.8$. The different behaviour of the filtered MSD when applied in the dilute or in the dense case clarifies that Ω_s is really representative of Ω_2 (see the discussion in the text).

3.2.4 Linear model for the tracer dynamics (three timescales)

Once we have a satisfying model for the collective granular motion, a model for the tracer's motion can be studied on a solid basis, with the aim of improving the model in [113]. The final model for the tracer appears as a system of three equations for three variables (where actually two of them are independent of each other).

Model derivation

To build this new model we have considered that the tracer is moving in a complex granular fluid: such a fluid has two characteristic timescales, as explained in the previous paragraph. The coupling between the tracer and the background granular fluid can be modelled in two different ways: as a conservative interaction that depends upon a relative *position* between the tracer and a representative fluid particle, or as a viscous interaction that depends upon the relative *velocity* between the tracer and the fluid. The first choice was adopted in [113], but our present study convinced us that the second choice gives a better comparison with data. For a viscous interaction, we were inspired by [173] were a linear model for a massive granular tracer in a granular fluid (in a planar, not cylindrical, geometry) was considered (see Par. 1.4.2). The tracer - characterized by velocity $V(t)$ - was coupled with the fluid - characterized by local velocity $V_1(t)$ - through a viscous drag term proportional to $V(t) - V_1(t)$. Depending on the specific region of the parameter space, this model can reproduce both ordinary Brownian motion and cage effects with the ballistic-

caged-diffusive behaviour in the MSD and the backscattering peak in the PSD. Therefore, it only lacks the superdiffusion at late times to properly describe the phenomenon under interest here. As we explained in Par. 3.2.2, we cannot expect such a complex behaviour from a linear model with two variables, therefore we have to insert a third one trying to be as less artificial as possible. To do so we leave the equation for the tracer unchanged and complicate the expression of the auxiliary variable making it coincide with the collective variable Ω_c relative to the subset of the granular particles in the bulk that actually influence the tracer dynamics. This quantity is always modelled by Eqs. (3.11) and defined by Eq. (3.1a) but with the mean operation extended just on the aforementioned subset of grains. We expect for it the same *qualitative* behaviour (but in general not quantitative) of the global collective variable studied in the previous paragraph: for this reason we decided not to introduce a new symbol for it. We end up with a three-variable linear model defined by the following equations:

$$I\dot{\omega}(t) = -\gamma(\omega(t) - \Omega_c(t)) + \sqrt{2T\gamma}\eta(t) \tag{3.14a}$$

$$\Omega_c(t) = \Omega_1(t) + \Omega_2(t) \tag{3.14b}$$

$$I_1\dot{\Omega}_1(t) = -\gamma_1\Omega_1(t) - \gamma_c\omega(t) + \sqrt{2T_1\gamma_1}\eta_1(t) \tag{3.14c}$$

$$I_2\dot{\Omega}_2(t) = -\gamma_2\Omega_2(t) + \sqrt{2T_2\gamma_2}\eta_2(t). \tag{3.14d}$$

Here we see that the bulk collective variable Ω_c acts as a local velocity field on the tracer whose velocity is $\omega(t)$. At the same time, the fast component of the collective variable Ω_1 is coupled with ω through a viscous constant γ_c. These last two ingredients originate the observed broad cage effect. The slow component Ω_2 is independent of the other variables and, as suggested by the numerical analysis, it will emerge at late times in the MSD and at small frequency in the PSD. Regarding the physical meaning of the coefficients we have for each variable an inertia I_i, a viscous coefficient γ_i and a temperature T_i. We note that the dilute limit (simple OU process for the tracer) is recovered by sending $\gamma_1/I_1 \to \infty$ and $\gamma_2/I_2 \to \infty$ while the model for the collective variable alone (Eqs. (3.11)) is obtained by setting $\gamma_c = 0$. With the procedure explained in Par. 1.4.2, it is possible to show that Eqs. (3.14) are equivalent to a generalized Langevin equation with an exponential decaying memory kernel and colored noise with exponential decaying correlation [157, 173]. This is consistent with a typical approximation done for Brownian Motion when, at high densities, the coupling of the tracer with fluid hydrodynamics modes, decaying exponentially in time (see [216], Cap 8.6 and 9.1), must be taken into account. Both for Eqs. (3.11) and (3.14) the number of independent parameters needed is actually smaller than the one used but we have kept some redundancy for the purpose of presenting more clear model equations. Now, rescaling all the equations by the inertia I_i we can rewrite the two models in a compact form that is more suitable

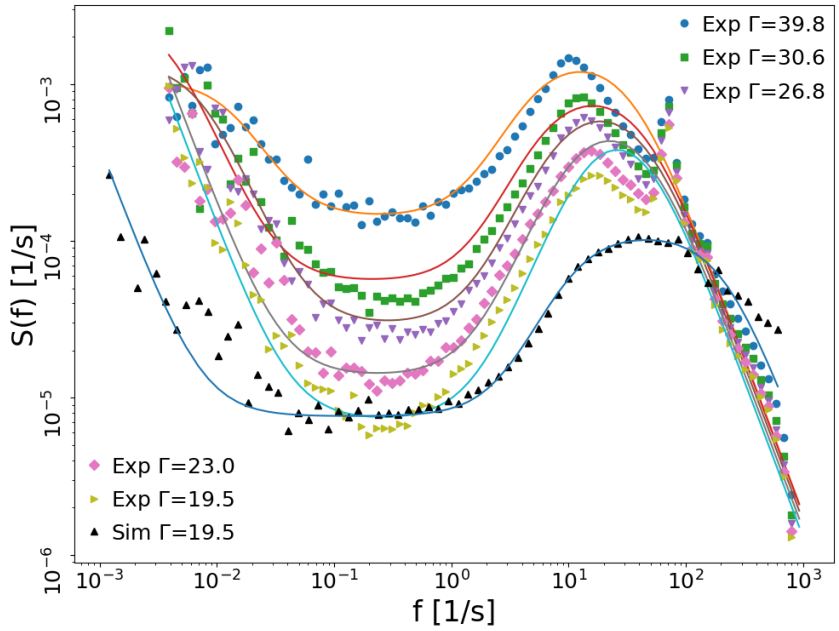

Figure 3.13. Comparison between experimental/numerical data and model (3.14) for the PSD of the tracer for many values of Γ and fixed $N = 2600$. The experimental and numerical data have been already shown in Fig. 2.2 and 2.6 respectively. Image reprinted from [146].

for reading the next paragraph. For the tracer we have:

$$\dot{\omega}(t) = -\frac{1}{\tau}(\omega(t) - \Omega_c(t)) + \sqrt{2\frac{q}{\tau}}\eta(t) \tag{3.15a}$$

$$\Omega_c(t) = \Omega_1(t) + \Omega_2(t) \tag{3.15b}$$

$$\dot{\Omega}_1(t) = -\frac{1}{\tau_1}\left(\Omega_1(t) + \alpha\omega(t)\right) + \sqrt{2\frac{q_1}{\tau_1}}\eta_1(t) \tag{3.15c}$$

$$\dot{\Omega}_2(t) = -\frac{1}{\tau_2}\Omega_2(t) + \sqrt{2\frac{q_2}{\tau_2}}\eta_2(t). \tag{3.15d}$$

where $\tau_i = I_i/\gamma_i$, $q_i = T_i/I_i$ and $\alpha = \gamma_c/\gamma_1$. Regarding the model for the collective variable alone we note that the rescaled form of Eqs. (3.11) (for the granular bulk dynamics when the tracer is absent) coincide with Eqs. ((3.15)b-d) once set $\alpha = 0$.

From Eqs. (3.15), we can derive an explicit formula for the VPSD of the tracer (see appendix B) and in Fig. 3.13 we show a comparison bentween its prediction and experimental/numerical data, finding good agreement in all the frequency regimes.

Physical interpretation of the model

The improvement with respect to the models defined by Eqs. (3.5) and (3.7) regards the form of the PSD. In the previous model, the peak and the valley of the PSD are specular i.e. their position and width depend upon the same combination of parameters so they cannot be changed independently (Fig. 3.10). The experimental and

numerical PSD show instead that the valley and the backscattering peak are never specular and in general this is coherent with the scenario suggested by the numerical simulations. Indeed, the valley is actually the crossover between the motion of the tracer inside the cage and the movement of the cage itself that enslaves the tracer. Once verified the presence of a persistent collective motion of the granular medium we can say that the cage moves as the collective variable on two timescales that are, with a good approximation, independent. In this picture, it is thus reasonable that the frequency (time) where the slow component emerges in the PSD (MSD) could change independently from what is happening at the characteristic frequency (time) of the backscattering (cage) effect and vice-versa. This is possible with Eqs. (3.15) by changing a combination of two parameters and leaving the others fixed (see Fig. 3.14).

The last aspect of the proposed model we want to discuss regards the physical meaning of couplings between variables in a system of Langevin equations. First, we note that also without the introduction of auxiliary variables the effect on the tracer of the surrounding fluid is intrinsically contained in the Langevin approach. Indeed, also for ordinary Brownian motion (Eq. (3.15a) without $\Omega_c(t)$) the characteristic time τ and the stationary variance q depend on the properties of both tracer and fluid [117]. The need of additional variables emerges just in presence of multiple timescales in the tracer dynamics. In view of this, referring to Eqs. (3.15), we can say that from an *energetic* point of view the effect of the granular medium on the tracer can be contained in q alone. Indeed, provided that $\tau \ll \tau_1$ and $q \gg q_1$, the fluctuations in the steady states of ω are not affected by the introduction of Ω_1. We can expect that this limit holds in our system because the inertia of the local collective variable I_1 is reasonably higher than the one of the blade I. We will confirm this expectation in the next paragraph in which our fitting procedure shows that q and the variance of ω are almost coincident as in a single-variable process.

These features are independent of α in Eq. (3.15c) so, in this limit, α represents the adimensional strength of a coupling that affects just the memory and not the energy of the tracer dynamics. In other words, the introduction of Ω_1 changes the shape of the PSD of ω leaving its integral unaltered (we remember here that if $\langle\omega\rangle = 0$ then $\int_0^\infty df\, S(f) = \langle\omega^2\rangle$). Remarkably, studying the derivative of $S(f)$, it is possible to see that $\alpha > 0$ is a necessary condition for the occurrence of the backscattering effect. So, in our model, this effect is possible only if the tracer is coupled with a variable that is influenced by the tracer itself. This fact is compatible with the intuitive physical mechanism with which backscattering is rationalized: the surrounding fluid is perturbed by the intruder and the latter feels with some delay in time the effect of this perturbation. Because of this mutual influence, we find even more appropriate the definition of Ω_c as a local field in Eqs. (3.14) and (3.15). Indeed, even if the whole granular medium can be reasonably unperturbed by the intruder, there will be always a local fraction of it that reciprocally interacts with the tracer giving rise to the backscattering effect.

This clarifies also how the tracer is coupled with Ω_2 that is not affected by ω. Indeed, the cage of surrounding grains has two main effects: confining the tracer with backscattering (coupling between ω and Ω_1 with reciprocal influence) and dragging it into the slow dynamics (coupling between ω and Ω_2 without reciprocal influence).

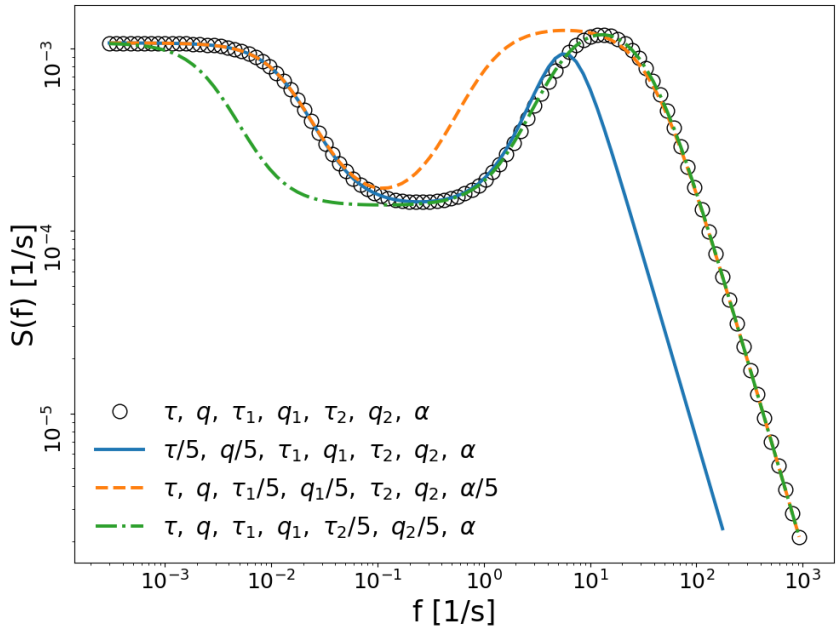

Figure 3.14. Four different shapes of $S(f)$, obtained by plotting the PSD of $\omega(t)$ computed from model (3.14) for different arbitrary choices of the parameters where $\tau_i = I_i/\gamma_i$, $q_i = T_i/I_i$ and $\alpha = \gamma_c/\gamma_1$. We show that it is possible to change the broadness of the valley independently from the one of the backscattering peak and vice-versa. Image reprinted from [146].

3.2.5 Physical meaning of the model parameters

In this paragraph, we attempt to systematically fit our model parameters with the results of the numerical simulations and experiments. This task has two main motivations. First, it may suggest a way to infer or guess the model's parameters (or their behaviour when physical parameters are varied) in general situations. Second, it makes more robust the identification of the model: a fuzzy or unintelligible behaviour of the model's parameter would be the symptom of a weakness of the model itself.

For this purpose we report in Tab. 3.1 the fitted parameters obtained for the collective variable (simulations) via Eqs. ((3.15)b-d) with $\alpha = 0$ and for the tracer (experiments and simulations) via Eqs. (3.15) for many values of Γ. We first concentrate on the numerical data for the collective variable Ω_c. From Eqs. (3.11) and (3.15) it is clear that the sum of two independent OU processes depends on four parameters: τ_1, q_1, τ_2, q_2 where τ_i is the characteristic time of the single process and q_i is its variance. In Par 3.2.3 we verified that Eqs. (3.11) properly reproduce the functional form of the numerical PDS and MSD, now we want to study how the fitted parameters behave as a function of Γ. In particular, we are interested to verify if their numerical values reflect the physical intuitions on which the model with two variables is based. In Fig. 3.15 we can clearly see that the parameters related to Ω_1 and Ω_2 show opposite behaviours: τ_1 and q_1 are increasing with Γ while τ_2 and q_2 are decreasing. The behaviour of q_1 is intuitive because we can reasonably think that this parameter grows with the "temperature" of the physical

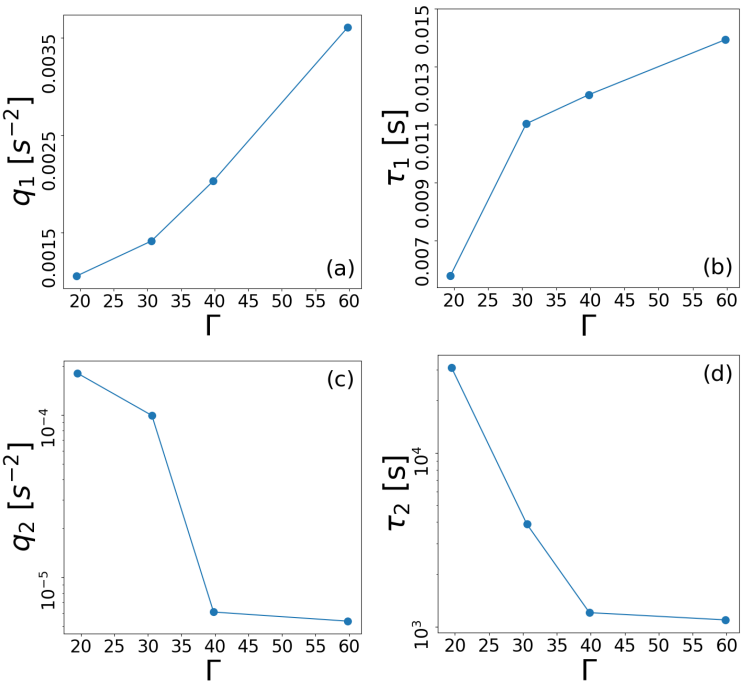

Figure 3.15. Fitted parameters for the collective variable (simulations) versus Γ with fixed $N = 2600$. Fit has been done via formula (3.12b) corresponding to model (3.15b-d) with $\alpha = 0$. Numerical values of the parameters are also reported in Tab. 3.1. Images reprinted from [146].

external driving (the shaker). The behaviour of τ_2 and q_2 corroborates our intuition that reducing Γ induces the emergence of a slow timescale whose persistency time (τ_2) and intensity (q_2) grow. The microscopic origin of this fact can be traced back to the single-particle dynamics discussed in Par. 3.1.3. There, we found that when a collective motion emerges a great fraction of particles participates, as a condensed state, to the collective motion and a smaller one still exhibits a gas-like behaviour. The slow contribution Ω_2 to the total variable Ω_c is mainly due to the particles in this condensed phase, whose number could be thought of as proportional to the effective inertia of Ω_2. Increasing Γ reduces the fraction of particles in the condensed phase and makes the single-grain dynamics less correlated. A direct consequence of that is the lowering of both τ_2 and q_2. The growth of τ_1 with Γ has not an easy explanation in our opinion. In dilute kinetic models the dissipative drag (here inverse of τ_1) is often related to the mean collision frequency (mediated through a ratio of masses and other factors): however this quantity may have opposite trends when Γ grows, i.e. it may increase because there is more energy (faster collisions) or it may decrease because there is a larger mean free path. Apparently, the second phenomenon dominates the first. The connection between dissipation and collision frequency, however, is reasonable for dilute gases but certainly not obvious in condensed phases.

Regarding the experimental data of the tracer, from Eqs. (3.15) we see that the number of free parameters for a fit is 7 and they are $\tau, q, \tau_1, q_1, \tau_2, q_2, \alpha$. We recall that q, q_1 and q_2 would be equal to the stationary variances of ω, Ω_1 and

	τ_1 [s]	q_1 [s^{-2}]	τ_2 [s]	q_2 [s^{-2}]	τ [s]	q [s^{-2}]	α
Γ=19.5 Tracer Sim.	9.6×10^{-2}	5.7×10^{-3}	1.1×10^{4}	2.0×10^{-2}	7.3×10^{-4}	4.4×10^{-1}	5.0
Γ= 19.5 Coll. Var. Sim.*	5.8×10^{-3}	1.1×10^{-3}	1.1×10^{4}	8.1×10^{-4}	\	\	\
Γ= 19.5 Coll. Var. Sim.	5.8×10^{-3}	1.1×10^{-3}	3.1×10^{4}	1.8×10^{-4}	\	\	\
Γ= 30.6 Coll. Var. Sim.	1.1×10^{-2}	1.4×10^{-3}	3.9×10^{3}	9.9×10^{-5}	\	\	\
Γ= 39.8 Coll. Var. Sim.	1.2×10^{-2}	2.0×10^{-3}	1.2×10^{3}	6.1×10^{-6}	\	\	\
Γ= 59.8 Coll. Var. Sim.	1.4×10^{-2}	3.6×10^{-3}	1.1×10^{3}	5.4×10^{-6}	\	\	\
Γ=19.5 Tracer Exp.	1.03×10^{-1}	1.0×10^{-3}	4.6×10^{3}	4.2×10^{-1}	2.8×10^{-3}	4.5×10^{-1}	6.8
Γ=23.0 Tracer Exp.	1.06×10^{-1}	1.1×10^{-3}	7.0×10^{3}	5.1×10^{-1}	2.8×10^{-3}	5.1×10^{-1}	5.0
Γ=26.8 Tracer Exp.	1.09×10^{-1}	1.2×10^{-3}	2.0×10^{1}	4.7×10^{-3}	3.0×10^{-3}	6.2×10^{-1}	3.7
Γ=30.6 Tracer Exp.	1.10×10^{-1}	1.4×10^{-3}	4.0×10^{1}	3.4×10^{-3}	3.3×10^{-3}	7.3×10^{-1}	2.8
Γ=39.8 Tracer Exp.	1.11×10^{-1}	2.0×10^{-3}	1.1×10^{1}	2.5×10^{-3}	4.2×10^{-3}	9.5×10^{-1}	2.1

Table 3.1. Numerical values of the fitted parameters for the collective variable in simulations via Eqs. (3.14)b-d with $\alpha = 0$ and the tracer in experiments and simulations via Eqs. (3.15). The first and the second* rows refer to the same simulation *with* the blade.

Ω_2, respectively, if these variables were not coupled. In our model with couplings one must consider the covariance matrix $\hat{\sigma}$ which is related to the noise amplitudes through $\hat{A}\hat{\sigma} + \hat{\sigma}\hat{A}^T = \hat{B}\hat{B}^T$ which also involves the coupling matrix [76]. However, considering the discussion about couplings at the end of Par. 3.2.4, and with the aim of reducing the freedom in the fitting procedure, we decided to set q to coincide with the variance of ω measured in experiments. We then verify *a posteriori* how good is this approximation. In Fig. 3.16a we compare experimental $\langle(\omega - \langle\omega\rangle)^2\rangle$ with the theoretical one calculated with fitted parameters and verify that our assumption is reasonable. The behaviour of q together with the ones of τ, τ_2 and q_2 shown in the same figure (panels b, c and d), is coherent with the phenomenology already explained for fast and slow parts of the collective variable of Fig. 3.15 (we remind that Ω_2 is totally independent of the other variables so q_2 always coincides with the variance of Ω_2). Indeed, the idea of our model is to consider the tracer (ω) enslaved by the collective variable: at short times it feels the effect of the fast component Ω_1 (high-frequency decay and backscattering peak) while at late times Ω_2 starts to dominate the entire dynamics with its persistent ballistic drifts. The motion of the tracer is then characterized by more than one characteristic timescale. Looking at Eq. (3.14a) it is quite natural to associate τ and q respectively to the characteristic time and the variance of the short-time dynamics of ω. It is therefore reassuring to find for these parameters similar behaviours to those observed for τ_1 and q_1 in numerical simulations (compare panels a and b of Fig. 3.15 and 3.16). Also the values of τ_1 and q_1 obtained from the experimental data via Eqs. (3.15) (not shown in figures but reported in Tab. 3.1) follow the same qualitative behaviour. Regarding couplings, our fitting procedure revealed the situation depicted at the

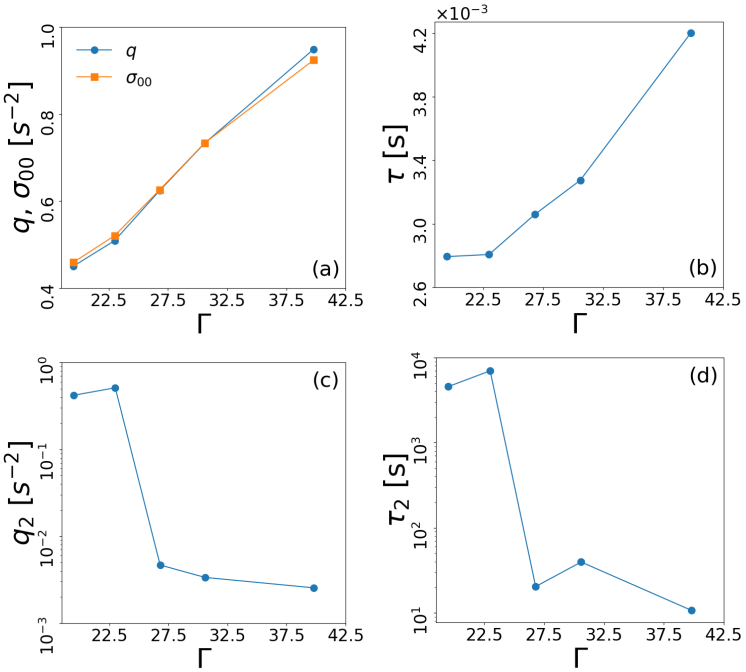

Figure 3.16. Fitted parameters for the experimental tracer versus Γ with fixed $N = 2600$. Fit has been done via formula B.2 in the appendix corresponding to Eqs. (3.15). Numerical values of the parameters are also reported in Tab. 3.1. Images reprinted from [146].

end of Par. 3.2.4. Looking at Tab. 3.1 and Fig. 3.16 we find that the effect on the tracer of the auxiliary variables is not relevant form an *energetic* point of view ($q \simeq (\omega - \langle\omega\rangle)^2\rangle$) but not negligible from a *memory* one ($\alpha > 1$ for all the fitted spectra).

The results reported in Fig. 3.16 regard the experimental tracer but, as is shown for one case ($\Gamma = 19.5$) in Fig. 3.13, we have also tested our model on the numerical data coming from the simulations *with* the blade. We note that the good agreement shown is obtained for values of τ_1, q_1, τ_2 and q_2 that are quite different from the ones coming from a direct fit of the two components of the collective variable in simulations *with* or *without* the blade (see first, second and seventh rows of Tab. 3.1). This is not surprising because, as already stated at the end of Par. 3.2.4, the variable Ω_c actually coupled to the tracer, in Eqs. (3.14) and (3.15), is a *local* collective variable. The latter reasonably differs - quantitatively - from the global one because of a considerable spatial heterogeneity of granular temperature and diffusivity (see Par. 3.1.3).

As a final remark it is worth saying that, since both the presented models contain several independent parameters, it is not surprising that they reproduce all the available data. Less trivial is the fact that the fitted parameters behave coherently and are consistent with the phenomenological arguments on which such models are based. In particular, they are able to capture the opposite behaviours at different timescales discussed in Par. 2.2.2 and 3.1.2.

Chapter 4

Long-range correlations and slow timescales in a granular lattice model

In the phenomenological models discussed in Sec. 3.2, the presence of a slow collective mode in the system is introduced by hand, based upon the empirical evidence. In that case, the goal was to find a reasonable linear model able to reproduce the experimental/numerical power spectral density and mean squared displacement. In this chapter, we concentrate on the more general problem of how long-range correlations and slow timescales can emerge in a granular model starting from some basic characteristics of dense vibrofluidized granular systems [148]. Since we want to proceed with analytical calculations and provide qualitative predictions, we will consider an extremely simplified lattice model that, nevertheless, incorporates the main features of the real system under study. The slow collective dynamics discussed in the following is characterized by power-law decaying spatial correlations and long relaxation times in a velocity field defined on a one-dimensional lattice with interactions mediated by viscous friction. We will show that this behaviour is observed in the non-equilibrium stationary state (NESS) obtained by coupling only the boundaries of the system with a thermal bath. We call this phase Non-Homogeneously Heated Phase (NHHP). If the particles in the bulk are also put in contact with a bath, a different regime is found and we call it the Homogeneously Heated Phase (HHP). Its spatial correlation function is an exponential with a characteristic length scale that goes to infinity when the contact between the bulk and the bath vanishes.

The chapter is organized as follows. In Sec. 4.1 we introduce the lattice model and discuss its relation with granular systems and other models in the literature. The formal solution of the model in the framework of multivariate linear stochastic processes is also provided. Sec. 4.2 contains the main results of our calculations i.e. the analytical expressions of spatial correlations and characteristic timescales in the NHHP and HHP. We finally dedicate Sec. 4.3 to some remarks about the relation between the model predictions and the collective dynamics observed in the realistic systems. Then, to verify whether localization phenomena can hinder the collective mode of the NHHP, we also investigate what happens if one introduces

random couplings between the variables.

4.1 The Model

4.1.1 Definition and phenomenology

We consider a velocity field on a one-dimensional lattice of size L. The ith particle interacts with their nearest neighbors j through a viscous force with coefficient γ: $F_i = -\sum_j \gamma(v_i - v_j)$. The boundary (bulk) sites are coupled with an external bath defined by a drag coefficient γ_b (γ_a) and corresponding temperatures which can be different if at the boundaries or in the bulk. Considering particles with unitary mass the equations for the model are:

$$\dot{v}_i = -(2\gamma + \gamma_a)v_i + \gamma(v_{i+1} + v_{i-1}) + \sqrt{2\gamma_a T_a}\eta_i(t) \tag{4.1a}$$

$$\dot{v}_1 = -(\gamma + \gamma_b)v_1 + \gamma v_2 + \sqrt{2\gamma_b T_1}\eta_1(t) \tag{4.1b}$$

$$\dot{v}_L = -(\gamma + \gamma_b)v_L + \gamma v_{L-1} + \sqrt{2\gamma_b T_L}\eta_L(t) \tag{4.1c}$$

Where the first equation holds for $1 < i < L$ and the $\eta_i(t)$s are Gaussian white noises with unitary variance: $\langle \eta_i(t)\eta_j(t')\rangle = \delta_{ij}\delta(t - t')$.

In this model, the way in which energy is supplied to the system is consistent with the fluctuation-dissipation theorem. Indeed, for each viscous force ($\gamma_{a(b)}$) there is a stochastic counterpart at finite temperature ($T_{a(b)}$). This is actually not true for the interaction force defined by γ because it is related to the viscosity of the material that forms the grains. Thus, the associated temperature (typical of the thermal agitation at the molecular scale) can be reasonably neglected in a granular context. We refer to NHHP when $\gamma_a = 0$ so that just the first and the Lth sites are heated, while in the HHP we consider a general $\gamma_a \neq 0$. We note that the HHP is not strictly spatially homogeneous because viscous coefficients and temperatures depend on the position: we refer to it as *homogeneously heated* meaning that in this phase *all* the particles are coupled with a bath.

As we discuss in the next paragraphs, this is a linear model and a full solution can be found in the context of multivariate stochastic processes. Nevertheless, numerical integration of Eqs. (4.1) can be useful to have a physical insight into the phenomenology in play. In Fig. 4.1 we show some instantaneous snapshots of the system in the stationary state for three different conditions: HHP with $T_a \neq 0$, HHP with $T_a = 0$ and NHHP. We note that in the NHHP (panel c) almost all the velocities are aligned with similar moduli while in the HHP we have smaller aligned domains with moduli that decay sharply moving away from the boundaries when $T_a = 0$ (panel b) and a random configuration when $T_a \neq 0$ (panel a). This comparison makes clear that - in terms of correlations - the key parameter is γ_a rather than T_a: indeed a situation where the sites experience a slow collective dynamics is only found in the NHHP. In Fig. 4.1d the typical correlation time for each site is shown and we can see that in the NHHP the dynamics is extremely slower with respect to the other two conditions. It is worth noting that this model does not present any directional asymmetry so the true mean value of the velocity field (i.e. obtained by an average over long times or equivalently over all the realizations of the noises) is zero also in the NHHP, even if the single-time configurations clearly show an explicit

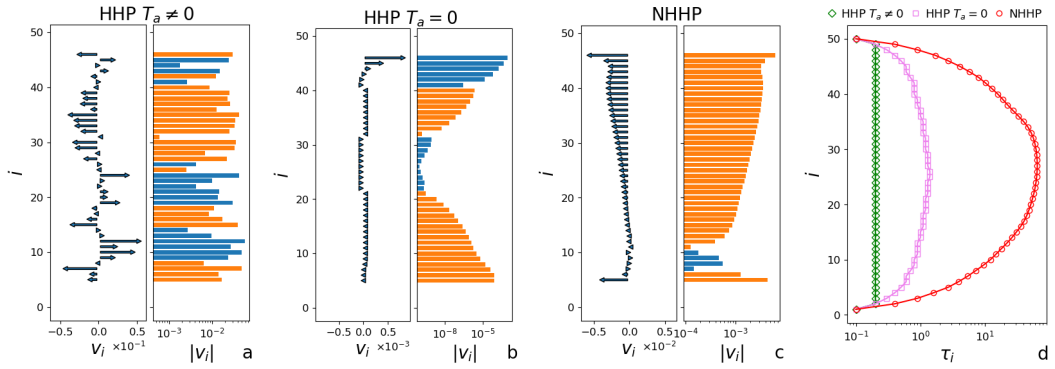

Figure 4.1. a,b,c: Snapshots of the velocity field in the stationary state of the HHP (with and without thermal noise in the bulk) and the NHHP. We exclude the first five (really hot) sites near the boundaries to have a more clear view of the field. Each panel shows the vectors in linear scale and the moduli in log scale in order to better appreciate the phenomenology of the system. Orange and blue bars discriminate the two directions. We note that a great cluster of particles with same direction and similar modulus is found in the NHHP only, signalling that in terms of correlations the key parameter is γ_a rather than T_a. d: Autocorrelation times for each site defined as the time τ_i for which $\Gamma_i(\tau_i) = 0.4$. The autocorrelation function is defined as $\Gamma(t') = \lim_{t\to\infty}\langle v_i(t)v_i(t+t')\rangle / \langle v_i^2(t)\rangle$ where the brackets refer to a time average on the stationary state. We note that in the NHHP the dynamics is far slower than in the HHP also when $T_a = 0$. The snapshots are obtained by numerical integration of Eqs. (4.1) with $L = 50$, $\gamma = 5$, $\gamma_b = 10$, $\gamma_a = \{3, 0\}$, $T_1 = T_L = 0.002$, $T_a = \{0.002, 0\}$ after a time $t_M = 10^8/\gamma$ and with a temporal step $dt = 0.05/\gamma$. Images reprinted from [148].

global alignment. The phenomenology of the NHHP can then be described as the occurrence of slow and collective fluctuations around the expected mean value.

4.1.2 Relation with real granular systems and other models

We note that the kind of interactions used in Eqs. (4.1) is the same that we have in the viscous contributions of the normal/tangential components of the Hetz-Mindlin model (see Eqs. (2.4)). In view of this, we can say that if we fix the centers of L grains on the lattice sites so that they are partially overlapped, then the dynamics of the particles' velocities would be given by Eqs. (4.1). Neglecting the dynamics of positions (they don't appear at all in Eqs. (4.1)) is surely the most relevant approximation of our approach: in the appendix C.5 we briefly discuss how to go beyond it toghether with some connections with dense active systems.

Nevertheless, our model can realistically represent the physical condition found in the realistic setup that we studied in experiments and simulations. Indeed, for low driving energies, we find that the particles are always arranged in a dense packing where they vibrate in permanent contact with each other experiencing very rare and slow re-arrangements. This implies if the geometry is narrow enough, that just the external layers of the system are in direct contact with the vibrating walls while the others never touch them. This last fact tells us that, in addition to the specific form of the viscous forces and the permanent interactions, also the way in which the external energy injection is modelled in the NHHP resembles the conditions

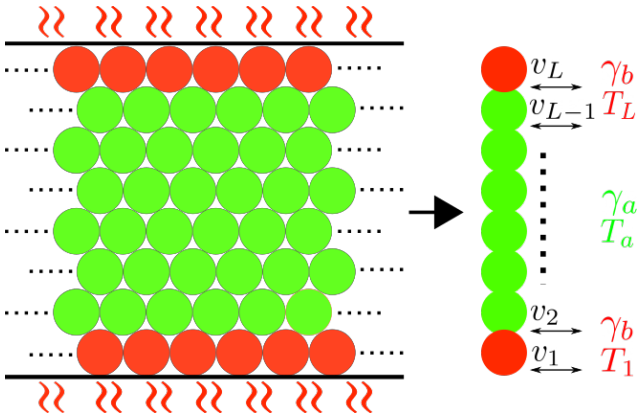

Figure 4.2. Sketch of the model and relation with higher dimensional systems. On the left, we suggest a hypothetical 2D dense granular system where particles are roughly located on the vertices of a regular lattice. In Chap. 5 we show numerical results of DEM simulations for this kind of system. A possible mapping from the 2D to the 1D system involves replacing the mean horizontal velocity on the ith layer of the 2D system with the v_i of the 1D system. The dynamics in the vertical direction is neglected, an approximation which is justified by the presence of the vertical confinement, while the periodic boundary conditions (indicated by the dotted lines) are representative of a 'free' direction in which the grains can flow without obstacles. Red grains are in direct contact with the external source of energy coming from the boundaries (γ_b,$T_{1(L)}$) while the green ones are in contact with the bulk bath, which is switched off in the NHHP. In order to apply this mapping to our experimental/numerical system in the cold/dense state (Par. 2.1.1), one has to consider it as a set of vertically stacked cylindrical slides with just the lower one interacting with the external source of energy. In this case, the free direction of motion is represented by the rotation around the central axis. Image reprinted from [148].

of a vibrated granular system in a dense state. Moreover, if layers of particles are mapped into lattice sites, a 1D chain can also be representative of a higher dimensional system (see Fig. 4.2). On the other hand, the HHP can represent a setup where all the particles interact with the vibrating walls, as it happens for instance in vibrated monolayers [152].

The idea of considering velocity fields defined on lattices, i.e. neglecting the evolution of the positions and density fluctuations in the dynamics, has been widely exploited in granular literature [16, 112, 17] especially for dilute systems. In these previous works, however, there is no continuous interaction, but only instantaneous collisions occurring between pairs of neighbouring grains picked up at random, at every time-step. Many results have been obtained by solving (analytically or numerically) the corresponding master equation or performing its hydrodynamic limit, revealing that these models are a powerful tool to investigate complex phenomena observed in experiments and simulations of realistic granular systems such as shock waves, anomalous transport and current fluctuations [143, 123].

To summarize motivations and background, our model reflects three main characteristics of dense granular materials in vertically-vibrated setups i.e. viscous forces, permanent contacts and energy injection localized at the boundaries. It can be then considered as the high-density variant of a well-established family of models previously investigated.

4.1.3 Compact SDE formulation of the model

Defining the vectors $\boldsymbol{V} = (v_1, \dots, v_L)$, $\boldsymbol{\eta}(t) = (\eta_1(t), \dots, \eta_L(t))$ and the adimensional parameters $\beta = \gamma_b/\gamma$, $\alpha = \gamma_a/\gamma$ then we can rewrite Eqs. (4.1) as a multivariate Ornstein-Uhlenbeck process obtaining the following stochastic differential equation (SDE):

$$\dot{\boldsymbol{V}} = -\hat{A}\boldsymbol{V} + \hat{B}\boldsymbol{\eta}(t) \tag{4.2}$$

where $\hat{B} = \mathrm{diag}(\sqrt{2\gamma_b T_1}, \sqrt{2\gamma_a T_a}, \dots, \sqrt{2\gamma_a T_a}, \sqrt{2\gamma_b T_L})$ and:

$$\hat{A} = \gamma \begin{pmatrix} 1+\beta & -1 & & & \mathbf{0} \\ -1 & 2+\alpha & -1 & & \\ & \ddots & \ddots & \ddots & \\ & & -1 & 2+\alpha & -1 \\ \mathbf{0} & & & -1 & 1+\beta \end{pmatrix} \tag{4.3}$$

is a $L \times L$ tridiagonal symmetric matrix.

The information about space-time correlations of the system are encoded in the two times correlation matrix $\hat{\sigma}(t,s)$ whose entries are defined as $\sigma_{jm}(t,s) = \langle v_j(t) v_m(s) \rangle \equiv \langle [v_j(t) - \langle v_j(t) \rangle] [v_m(s) - \langle v_m(s) \rangle] \rangle$. We now define the quantity of principal interest in the upcoming analysis i.e. the static spatial correlation function of the velocity field:

$$\zeta_{jm} = \frac{\sigma_{jm}}{\sqrt{\sigma_{jj}\sigma_{mm}}} \quad \text{where} \quad \sigma_{jm} = \langle v_j v_m \rangle \,. \tag{4.4}$$

With this definition we have $\zeta_{jm} = 1$ if $j = m$ or $v_j = v_m$ and $\zeta_{jm} = 0$ if $\langle v_j v_m \rangle = 0$. It is then clear that our goal is to solve Eq. (4.2) and find the stationary correlation

matrix $\hat{\sigma} = \lim_{t\to\infty} \hat{\sigma}(t,t)$ that exists if $\hat{A}$ is positive semi-definite. In this conditions, regardless the symmetry of $\hat{A}$, the correlation matrix can be found by inverting the relation [76]:

$$\hat{A}\hat{\sigma} + \hat{\sigma}\hat{A}^T = \hat{B}\hat{B}^T. \tag{4.5}$$

Nevertheless, a more direct way to obtain an analytic expression of $\hat{\sigma}$ can be followed exploiting the fact that $\hat{A}$ is symmetric. In this case there exist a unitary matrix $\hat{S}$ such that $\hat{S}\hat{S}^+ = \hat{I}$ and $\hat{S}^+\hat{A}\hat{S}{=}\hat{S}^+\hat{A}^T\hat{S} = \hat{\lambda} = \mathrm{diag}(\lambda_1, \lambda_2, \ldots, \lambda_L)$ where $\hat{I}$ is the identity matrix, the λ_js are the eigenvalues of $\hat{A}$ while S_{ji} is the jth component of the ith eigenvector of it. With these hypotheses and in the case of $\hat{B} = \mathrm{diag}(b_1, \ldots, b_L)$ we can write the two-times (with $t \geq s$) covariance matrix in the non-stationary case:

$$\hat{\sigma}(t,s) = \hat{S}\left(\hat{C}(t,s) + \hat{G}(t,s)\right)\hat{S}^+ \tag{4.6}$$

where:

$$\hat{C}(t,s) = \exp(-\hat{\lambda}t)\hat{S}^+\langle \boldsymbol{V}(0), \boldsymbol{V}^T(0)\rangle \hat{S}\exp(-\hat{\lambda}s) \tag{4.7a}$$

$$G_{jm}(t,s) = \frac{\left(e^{-\lambda_j(t-s)} - e^{-(\lambda_j+\lambda_m)s}\right)\sum_n S^+_{jn}S_{nm}b_n^2}{\lambda_j + \lambda_m}. \tag{4.7b}$$

The first matrix represents the transient and the brackets refer to the average over initial conditions while the NESS is described by $\lim_{s\to\infty} G(t,s)$. Without noises, Eq. (4.7a) would be the solution of Eq. (4.2) representing the correlations in the cooling state. We note that the two correlation matrices have different mathematical structures. The consequences of that together with some properties of the cooling state are discussed in the appendix C.4 while in the next paragraphs we will neglect $\hat{C}$ concentrating on the NESS. Defining $\hat{\sigma}(t') = \lim_{t\to\infty}\hat{\sigma}(t+t',t)$ and through Eqs. (4.6) and (4.7b) it is also possible to evaluate the single-particle autocorrelation function $\Gamma_j(t') \equiv \sigma_{jj}(t')/\sigma_{jj}(0)$:

$$\Gamma_j(t') = \frac{1}{\sigma_{jj}}\sum_k q_{jk}S^+_{kj}e^{-\lambda_k t'}, \quad q_{jk} = \sum_{ls}\frac{S_{jl}S^+_{ks}S_{sl}b_s^2}{\lambda_l + \lambda_k} \tag{4.8}$$

from which is clear that, as expected for a linear system, the autocorrelation function is a sum of exponential terms with different characteristic times that are given by the inverse of the eigenvalues $\tau_k = 1/\lambda_k$.

We will derive σ_{jm} in a specific case where the diagonalisation of $\hat{A}$ can be done analytically and then follow a numerical technique of diagonalisation [22] to show the robustness of our main results i.e. power-law decay of spatial correlations. Before doing that, we briefly review what techniques have been used to solve similar problems highlighting the differences with the present case.

These kinds of lattice models, and also more complex ones (with higher dimension and second-order dynamics), when translational invariance holds, can be mapped in a system of independent equations for the modes in the Bravais lattice allowing a full solution [44]. However, our model (both NHHP and HHP) has no periodic boundary conditions and the bath parameters depend on the particular site position. Assuming translational invariance would mean giving up some crucial

aspects of our investigation. To keep a reasonable connection with dense granular matter it is important to have a source of energy that acts differently at the boundary and in the bulk of the system. Nevertheless, in Par. 4.2.2 we'll discuss some common aspects between the HHP and translational invariant systems. In the general case with space-dependent parameters, correlations can be studied diagonalising the matrix $\hat{A}$ or by exploiting Eq. (4.5) combined with physical constraint on $\hat{\sigma}$. The former strategy, used by us and recently applied in [95, 71], when possible, is more convenient because it gives access also to time-dependent properties. The latter has been used to study temperature profiles in non-equilibrium harmonic chains [165]. It is important to stress that a crucial difference between our model and the aforementioned ones is that we deal with interactions acting on relative velocities and not (only) on displacements. Indeed, we have a direct competition between baths $\gamma_{a(b)}$ and interaction γ in $\hat{A}$, while in heated harmonic chains only the coupling constants appear in the interaction matrix.

Toeplitz condition

In order to obtain an explicit form of Eq. (4.6) we consider the case of $\gamma_b = \gamma + \gamma_a$ so that $\beta = 1 + \alpha$ making $\hat{A}$ a Toeplitz matrix whose eigenvalues and eigenvectors are respectively:

$$\lambda_j = \gamma(2 + \alpha - 2\cos(j\Pi)), \quad S_{jm} = \sqrt{\frac{2\Pi}{\pi}} \sin(jm\Pi) \tag{4.9}$$

where $\Pi = \pi/(L+1)$. Replacing these in Eq. (4.7b) and taking $t = s \to \infty$, Eq. (4.6) becomes:

$$\sigma_{jm}(\alpha) = \frac{2\Pi^2}{\gamma\pi^2} \sum_{lk} \frac{\sin(jl\Pi)\sin(mk\Pi)\left[\sum_n b_n^2 \sin(ln\Pi)\sin(kn\Pi)\right]}{\Delta(\alpha) - \cos(k\Pi) - \cos(l\Pi)}, \tag{4.10}$$

where $\Delta(\alpha) = 2 + \alpha$. The sums run from 1 to L and:

$$b_n^2 = \begin{cases} 2(\gamma + \gamma_a)T_1, & n = 1 \\ 2\gamma_a T_a, & 1 < n < L \\ 2(\gamma + \gamma_a)T_L, & n = L. \end{cases} \tag{4.11}$$

We point out that Eq. (4.10) is symmetric with respect the center of the lattice (i.e. $\sigma_{1m} = \sigma_{L(L+1-m)}$) if the coefficients b_n are too.

4.2 Results

4.2.1 Power-Law correlations and slow timescales in the NHHP

We first study the NHHP so we put $\gamma_a = 0$ and use the Toeplitz condition that now reads $\gamma_b = \gamma$ so $\beta = 1$. Exploiting the limit for large systems ($L \gg 1$), we can exchange sums with integrals as $\Pi \sum_{k=1}^{k=L} f(k\Pi) \to \int_0^\pi dz f(z)$. We note that in Eq. (4.10), when $\gamma_a = 0$, the sum over n is actually made of two terms. The one multiplied by $\gamma_b T_L$ has a sign that depends on the parity of l and k and this brings

to a subleading contribution if one considers $L \gg 1$ and $j, m \ll L$ (see appendix C.1). Neglecting it and defining

$$\Sigma_{jm}(\alpha) = \int_0^\pi dzds \frac{\sin(jz)\sin(ms)\sin(z)\sin(s)}{\Delta(\alpha) - \cos(z) - \cos(s)} \tag{4.12}$$

we obtain the covariance matrix for the NHHP:

$$\sigma_{jm}^{\mathrm{NHHP}} = \frac{4T_1}{\pi^2}\Sigma_{jm}(0). \tag{4.13}$$

The integral contained in $\Sigma_{jm}(0)$ is difficult to be explicitly evaluated but the following asymptotic behaviours can be derived in the limit $L \gg m \gg 1$:

$$\sigma_{mm}^{\mathrm{NHHP}} \sim \frac{1}{m^2} \tag{4.14a}$$

$$\sigma_{1m}^{\mathrm{NHHP}} \sim \frac{8T_1}{\pi m^3} \tag{4.14b}$$

$$\zeta_{1m}^{\mathrm{NHHP}} \sim \frac{1}{m^2} \tag{4.14c}$$

As explained in the appendix C.2, these results are obtained by expressing $\sigma_{jm}^{\mathrm{NHHP}}$ as a power series of $(jm)^{-1}$ by multiple integrations by parts and estimating opportune upper bounds. The limit $L \gg m \gg 1$ is important because we want to study the asymptotic behaviour of the correlations in the range for which they are not affected by the opposite boundary of the system. This is the reason why we predict just a decay for the variance σ_{mm} even if it must grow approaching the Lth site if $T_L \neq 0$. This growth for large m is given by the term proportional to $\gamma_b T_L$ that we have neglected going from Eq. (4.10) to Eq. (4.13).

Eq. (4.14c) clearly states that the bulk sites are correlated with the first (heated) one by a power-law decay with exponent 2. Regarding the correlations between particles in the bulk, they show a decay even slower than a power-law. We discuss them in appendix C.6. Regarding timescales, looking at Eq. (4.8) and at the specific form of the eigenvalues of $\hat{A}$ in Eq. (4.9) for $\alpha = 0$, we see that, when $j/L \ll 1$, the slowest timescales in the single-particle autocorrelation function behave as:

$$\tau_j^{\mathrm{NHHP}} = 1/\lambda_j \sim \tau L^2 \tag{4.15}$$

where $\tau = 1/\gamma$. We note that the emergence of characteristic times that scale with the system size together with scale-free correlations is fully consistent. Thus, the information that influences the dynamics of every particle comes from all across the system and so the time to receive it must increase with the system size.

4.2.2 Finite Correlation Length and Times in the HHP

The emergence of scale-free correlations is often considered a remarkable fact in physical systems. Nevertheless, we are now dealing with a model so it is important to understand if this result is found just by an algebraic coincidence or if it is consistent with the usual framework in which scale-free correlations are understood i.e. a particular limit for which a finite correlation length diverges. The study of the

HHP comes into play to provide evidence of this last scenario. We point out that by studying the HHP with periodic boundary conditions, and therefore assuming translational invariance (i.e. extending Eq. (4.1a) to all the particles in the system), it is quite easy to derive an exponential decay for the stationary spatial correlation function. This can be done by expressing Eq. (4.1a) in the Bravais lattice or by studying the continuous limit of $\dot{\sigma}_{jm} = \langle v_j \dot{v}_m + v_m \dot{v}_j \rangle = 0$. Nevertheless, we want to study the passage from the HHP to the NHHP when $\gamma_a \to 0$ so we proceed with space-dependent parameters from Eq. (4.10). This expression, in the HHP, contains all the contributions given by Eq. (4.11). Performing the large system limit and taking into account just the leading terms we arrive at the following expression for the covariance matrix in the HHP (see appendix C.3 for details):

$$\sigma_{jm}^{\mathrm{HHP}}(\alpha) = \frac{2\alpha T_a}{\pi} \int_0^\pi dz \frac{\sin(jz)\sin(mz)}{\Delta(\alpha) - 2\cos(z)} + \frac{4T_1}{\pi^2} \left[1 + \alpha \left(1 - \frac{T_a}{T_1}\right)\right] \Sigma_{jm}(\alpha) \quad (4.16)$$

where we see that for $\alpha = 0$ Eq. (4.13) is recovered. It is important to note that trying to express the above equation as a power series of $(m)^{-1}$ one finds that all the coefficients are zero signalling a decay faster than every power-law. In order to go straight to the result we consider homogeneous amplitude of noises i.e. $T_1 = T_L = T_a\gamma_a/(\gamma + \gamma_a)$ so that the second term of Eq. (4.16) vanishes. In this condition, the matrix $\hat{B}$ is proportional to the identity so the system can reach thermodynamic equilibrium. We then take the Fourier transform $\tilde{\sigma}_{j\omega}(\alpha) = \int dm \exp(i\omega m)\sigma_{jm}^{\mathrm{HHP}}(\alpha)$ and study the limit $\omega \ll 1$ ($m \gg 1$):

$$\tilde{\sigma}_{j\omega}(\alpha) \propto \int_0^\pi dz \frac{\delta(\omega - z)\sin(jz)}{\Delta(\alpha) - 2\cos(z)} \sim \frac{\sin(j\omega)}{\alpha + \omega^2} \quad (4.17)$$

whose inverse Fourier transform for $m > j$ is proportional to an exponential with characteristic length $\sqrt{\alpha}$, so we have that $\sigma_{jm}^{\mathrm{HHP}}(\alpha) \sim \exp(-\sqrt{\alpha}m)$. This last result is valid for a generic $j \ll L$ so it holds also for particles in the bulk. We note that $\alpha \to 0$ is a singular limit because the pole of the last term of the above equation tends to the real axis. Regarding variances that we need to calculate ζ_{jm} we can write :

$$\sigma_{mm}^{\mathrm{HHP}}(\alpha) = \frac{2\alpha T_a}{\pi} \int_0^\pi dz \frac{\sin^2(mz)}{\Delta(\alpha) - 2\cos(z)} = T_a \sqrt{\frac{\alpha}{4 + \alpha}} + o(m^{-1}), \quad m \gg 1 \quad (4.18)$$

as we expect, in the HHP the asymptotic temperature is a constant that we explicitly calculate in C.3. We point out that this variance has two reasonable limiting cases: for $\alpha = 0$ it is $o(m^{-1})$ consistently with the NHHP while $\lim_{\alpha\to\infty} \sigma_{mm}^{\mathrm{HHP}}(\alpha) = T_a$ representing the condition for which the external bath overcomes the interaction so that the variables are in equilibrium with the thermostats.

From this and by the definition of Eq. (4.4) we can conclude that spatial correlations in the HHP follow an exponential decay with a finite characteristic length scale ξ:

$$\zeta_{jm}^{\mathrm{HHP}} \sim e^{-m/\xi} \quad m \gg 1, \quad \xi = \alpha^{-1/2}. \quad (4.19)$$

In C.3 we show that this trend holds also without equal noise amplitudes so it is not strictly related to the equilibrium condition. We note that looking at this result

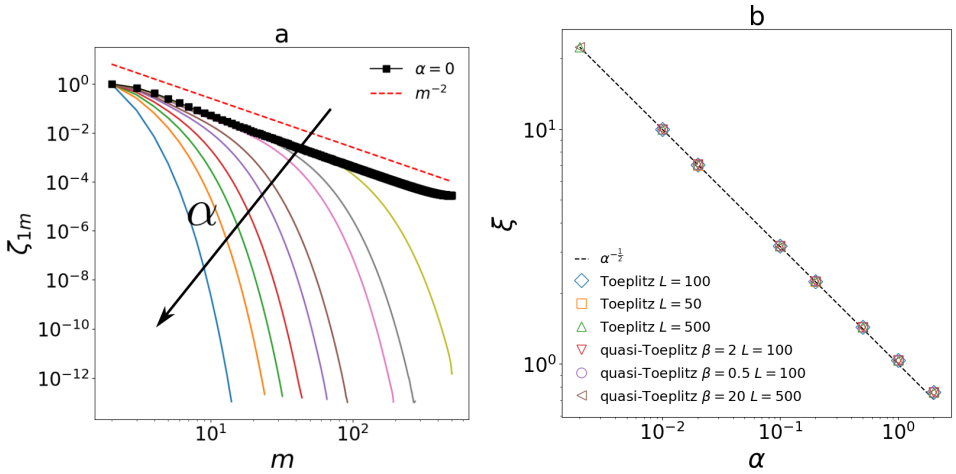

Figure 4.3. a: Spatial correlation function calculated via Eq. (4.4). The entries of $\hat{\sigma}$ are obtained from Eq. (4.6) with $t = s \gg 1$ and diagonalising $\hat{A}$. The parameters of the system are: $L = 500$, $\gamma = 5$, $\beta = 1 + \alpha$ (i.e. Toeplitz condition) and $\alpha \in [0.002, 5]$. We observe an exponential decay with a growing correlation length that turns into a power-law when $\alpha = 0$. b: Scaling of the correlation length obtained from an exponential fit of $\zeta_{1m}^{\mathrm{HHP}}$ for different combinations of parameters. We can see that the relation $\xi = \alpha^{-1/2}$ does not depend on the microscopic details of the system. Quasi-Toeplitz cases are discussed in Par. 4.2.3. In both panels we used $T_1 = T_a = 0.001$ and $T_L = 0$. Images reprinted from [148].

in the framework of critical phenomena we would have a critical point at $\alpha_c = 0$ and a correlation length that diverges as $\xi \sim (\alpha - \alpha_c)^{-\nu}$ with a critical exponent $\nu = 1/2$. This critical point would then coincide with the NHHP. Indeed, in this phase, the system behaves as in a critical regime where spatial correlations exhibit a power-law decay. Nevertheless, we make clear that this is just an analogy and we don't interpret our results as a phase transition. Moreover, it is important to remind that an equivalent equilibrium phase transition governed by temperature could not occur because we are considering a 1D system. In equilibrium cases, there is actually a transition at zero temperature but it coincides with a physical state with no dynamics. In other words, the model described by Eqs. (4.1) can't be mapped into an Ising or Heisenberg-like Hamiltonian system maintaining the same properties. We also note that the same scaling relation between correlation length and characteristic time of the bath has also been found in dilute granular systems with a hydrodynamic approach [87] and in dense active systems [43]. Nevertheless, in these two translational invariant systems, the equivalent limit for $\alpha = 0$ is meaningless because in the first case it removes the driving while in the second one it implies a deterministic constant self-propulsion. In Fig. 4.3 we show that the exponential to power-law crossover and the scaling for ξ derived in the large system limit are clearly visible also for finite-size lattices.

In order to discuss also the characteristic timescales in the HHP, we note from Eq. (4.9) that $\lambda_j > \gamma_a \ \forall \ j$ and so for finite α and $j/L \ll 1$ we have that:

$$\tau_j^{\mathrm{HHP}} \sim 1/\gamma_a = \tau_a. \tag{4.20}$$

This result is consistent with the fact that being correlated with a finite fraction of the system implies a finite time to receive the information that effectively determines the dynamics.

To conclude the comparison between HHP and NHHP, we stress that the difference between the two phases is originated in the structure of the eigenvalues of $\hat{A}$. In particular, for both space and time correlations, the crucial ingredient is that the spectrum of $\hat{A}$ accumulates in γ_a for $L \gg 1$ (Eq. (4.9)). Consequently, it accumulates to a finite value in the HHP and to zero in the NHHP. The crossover between the two phases is then governed by the limit $\alpha \to 0$ that brings to diverging correlation lengths and times.

4.2.3 Beyond the Toeplitz case

Up to now, we have considered the special case $\beta = 1 + \alpha$ for which $\hat{A}$ is a uniform Toeplitz matrix. Now we want to study the system with a general viscous constant $\gamma_b \neq \gamma + \gamma_a$ at the boundaries. Are the results obtained in the previous paragraphs still valid also in this more general case? To answer this question, we follow a procedure, systematically explained in [22], to diagonalise quasi-uniform Toeplitz matrices i.e. matrices that deviates from the Toeplitz form just for a few external borders. It does not give an analytical expression of the eigenvalues and eigenvectors but assures some constraints on their form and allows finding their values by numerically solving a set of transcendental equations. In order to uniform our notation with [22] we note that $\hat{A} = \gamma(2+\alpha)\hat{I} - \gamma\hat{A}'$ where:

$$\hat{A}' = \begin{pmatrix} x & 1 & & & \mathbf{0} \\ 1 & 0 & 1 & & \\ & \ddots & \ddots & \ddots & \\ & & 1 & 0 & 1 \\ \mathbf{0} & & & 1 & x \end{pmatrix} \tag{4.21}$$

and $x = 1 - \beta + \alpha$ so that for $\beta = 1 + \alpha$ we recover the Toeplitz case. Once defined λ'_j (S'_{ij}) as the eigenvalues (eigenvectors) of $\hat{A}'$, then $\lambda_j = \gamma(2+\alpha) - \gamma\lambda'_j$ and $S_{jm} = S'_{jm}$. If the eigenvalues are parametrized as $\lambda'_j = 2\cos(k_j)$ then we can find them by solving:

$$k_j = \frac{\pi j + 2\phi(k_j)}{L+1}, \quad \phi(k) = k - \tan^{-1}\left(\frac{\sin(k)}{\cos(k) - x}\right) \tag{4.22}$$

that determine the allowed values of k_j. The entries of the eigenvector matrix $\hat{S}$ can then be directly obtained starting from the numerical solution of Eq. (4.22) [22].

Once calculated all the λ_j and the S_{jm} we can use Eq. (4.7b) in the stationary case to obtain the covariance matrix and consequently the correlation functions. In Fig. 4.4 we show the correlation function for some quasi-Toeplitz cases for both the HHP and the NHHP finding the same asymptotic behaviour obtained for the Toeplitz one in Fig. 4.3a. Also the scaling for ξ in the HHP does not change (see Fig. 4.3b). We note that the difference in terms of parameters between Toeplitz and quasi-Toeplitz cases is that in the former we have just one adimensional ratio

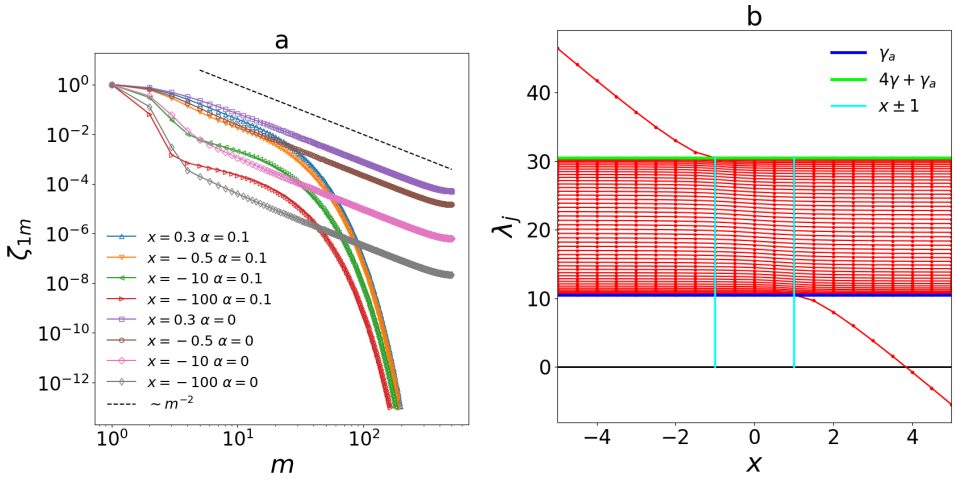

Figure 4.4. a: Spatial correlation function for different quasi-Toeplitz cases in both HHP and NHHP. We can see that the two phases are stable also for large values of negative x. The entries of $\hat{\sigma}$ are obtained from Eq. (4.6) for $t = s \gg 1$ and diagonalising $\hat{A}$. b: Spectra of $\hat{A}$ for different values of x and $\alpha = 2.1$. The spectra always accumulate at the boundary of the band $[\gamma_a, 4\gamma + \gamma_a]$ and out-of-band eigenvalues can occur only for $|x| > 1$. We also note that, in the range of interest for the NHHP ($x \in [-\infty, 1]$), the spectra are always positive assuring the stability of the system. In both panel we used $L = 500$, $\gamma = 5$, $T_1 = T_a = 0.001$ and $T_L = 0$. Images reprinted from [148].

between viscous constants i.e. $\alpha = \gamma_a/\gamma$ while in the latter we can independently fix $\beta = \gamma_b/\gamma$ and α.

Given the form with which eigenvalues are parametrized they can take values only in the band $\lambda'_j \in [-2, 2]$ and equivalently $\lambda_j \in [\gamma_a, 4\gamma + \gamma_a]$. Nevertheless, for absolute values of x large enough, out-of-band eigenvalues can occur [22]. This fact would compromise the existence of a stationary state in the NHHP because $\hat{A}$ would cease to be positive semi-definite. A more refined inspection of the spectral properties is then needed. Being $\beta > 0$ by definition we are sure that $x \in [-\infty, 1)$ in the NHHP. For $L \gg 1$ and $|x| > 1$ two out-of-band eigenvalues $\lambda^{\text{out}}_{1,2}$ emerge converging to a common value given by $\lambda^{\text{out}}_{1,2} = \gamma(2 + \alpha - x - x^{-1})$ that, in our case, is strictly positive preventing any problem of stability (see Fig. 4.4b). Moreover, as shown in the same panel, we can see that the spectrum of $\hat{A}$ always accumulates at the boundary of the band independently from the value of x. This is also clear by taking $j/L \ll 1$ or ~ 1 in Eqs. (4.22) and verifying that k_j tends respectively to 0 or π. Consequently the λ'_js always accumulate in 2 and the λ_js in γ_a. This generalizes our result about the power-law decay in the NHHP (i.e. with $\gamma_a = 0$) for any $\gamma_b > 0$ because, as explained in the previous paragraphs, its origin relies in the accumulation of the λ_j spectrum in zero (see also Fig. 4.4b).

4.3 Discussion

4.3.1 Can we understand a global persistent motion as a slow collective fluctuation?

We studied spatial and temporal correlations in the NESS reached by a velocity field with viscous interactions defined on a lattice and coupled with Brownian baths. The model reproduces three main characteristics of vibrated granular matter at high density i.e. dissipative forces, permanent contacts and non-homogeneous energy injection. The typical correlation lengths and times have a finite characteristic scale when the bulk particles are coupled to an external bath (HHP regime). However, such a scale diverges with the system size as in a scale-free scenario when the thermal bath is removed from the bulk particles and kept acting on the boundary sites only (NHHP regime). Solving this model as a diagonalisable multivariate Ornstein-Uhlenbeck process, we unveiled the role of non-homogeneous heating in the development of slow and collective dynamics. We conclude that keeping the bath only at the boundaries allows having a driven NESS in which the internal (deterministic) dynamics - and the corresponding propagation of information and fluctuations - is not hindered by external disturbances. From a mathematical point of view, this is reflected in the spectral properties of the interaction matrix that accumulates in zero also in the presence of noises at the boundaries of the lattice. These findings shed light on the emergence of collective behaviour in dense granular matter. Nevertheless, their relationship with the slow collective rotations discussed in the previous sections is not direct. Understanding persistent rotations as an instance of the NHHP in a realistic system is a tempting view that, however, cannot be confirmed by the study of this model alone. As already stated, in the NHHP there is no explicit spatial symmetry breaking and so a persistent collective drift of the whole system in a given direction is possible thanks to the slow and strongly correlated fluctuations of the velocity field around its unbiased (null) mean value. In the realistic experiments and simulations, we can't exclude *a priori* an (eventually transient) spatial symmetry breaking due to the amorphous structure of the dense granular packing. In Chapter 5, we will report a detailed analysis that confirms the crucial role of the asymmetry in the structure of the granular assembly for the formation of spontaneous persistent drifts. In particular, we'll show that in DEM simulations of ordered granular packings similar to the one shown in Fig. 4.2, no persistent dynamics is observed. Nevertheless, the connection between persistent dynamics in realistic systems and the NHHP of this model can be traced back less directly; we'll discuss this in the same chapter.

Setting aside for the moment its relevance with respect to our experimental setup, it is important to stress that this model demonstrates how the key properties of dense vibrofluidized granular systems namely dissipative forces, permanent contacts, and localized energy injection, can be minimal ingredients for the emergence of scale-free correlations and slow timescales in a granular lattice model. Further investigations of this model, considering both harmonic and viscous interactions, are promising steps towards the understanding of more general non-equilibrium systems such as active matter and biological assemblies.

4.3.2 Robustness against disorder: how correlations of random couplings prevent Anderson localization

The long-range correlations found in the NHHP are the signature of collective modes in the velocity field that travel without obstacles through the system. If the correlation function has a typical decay length ξ then one can divide the system in almost independent subsystems of size ξ but this is not the case of power-law decay that are scale-free. In other words, the excitations producing such correlations are global and not local.

In condensed matter physics, the equivalent situation is obtained when the wave function ψ is delocalized i.e. when the probability distribution $|\psi|^2$ of a quantum state initially confined in a finite region extends throughout the system during its time evolution. In 1958, P. W. Anderson demonstrates that in a quantum system represented by a lattice with a random tight-binding potential no delocalization at all can take place if the disorder is sufficiently strong [11, 116, 70]. In particular, in the one-dimensional case, the system is *always* localized no matter how strong is disorder. This phenomenon is called Anderson localization or strong localization. The Anderson tight-binding one-dimensional model reads:

$$i\hbar\frac{d\psi}{dt} = H\psi \tag{4.23}$$

with a random Hamiltonian H that acts on a state ϕ as:

$$(H\phi)_k = E_k\phi_k + \phi_{k+1} + \phi_{k-1} \tag{4.24}$$

where $k \in Z^d$ and the E_ks are random numbers uniformly distributed in the interval $[-E, E]$ with $E > 0$. Actually, the original case studied by Anderson was more general but this simple situation is enough for the purpose of our analysis. For the same reason, we will always refer to uniform distributions for the disorder. In this model, the probability distribution $|\psi(k,t)|^2$ evolved from an initially localized state ψ_0 behaves as:

$$\sum_{n\in Z^d} |\psi(n,t)|^2|n| \leq C \tag{4.25}$$

uniformly in time for any d if $E/\hbar$ is sufficiently large or for arbitrary E if $d < 2$. Eq. (4.25) gives a formal condition for Anderson localization i.e. an initially localized state remains localized within C at any time; on the contrary, for a delocalized wave function, the same quantity grows with time. The occurrence of strong localization is related to the spectral properties of H and we will return later on this point. The reason of such a digression is given by the fact that Anderson localization is a phenomenon that is not restricted to the quantum scales but refers to the general problem of wave transport in a disordered medium. Many subsequent studies has been dedicated to localization in classical models and macroscopic systems [126, 93, 134, 49, 8]. In the present case, by looking at Eq. (4.2) and noting that in the NHHP (i.e. for $\alpha = 0$) the interaction matrix acts on a state $\boldsymbol{V}$ as:

$$(-\hat{A}\boldsymbol{V})_k = \gamma(-2v_k + v_{k+1} + v_{k-1}) \quad k \neq 1, L \tag{4.26}$$

we realize that our purely dissipative granular lattice model has a mathematical structure very similar to the tight-binding model defined by Eq. (4.24) in one dimension.

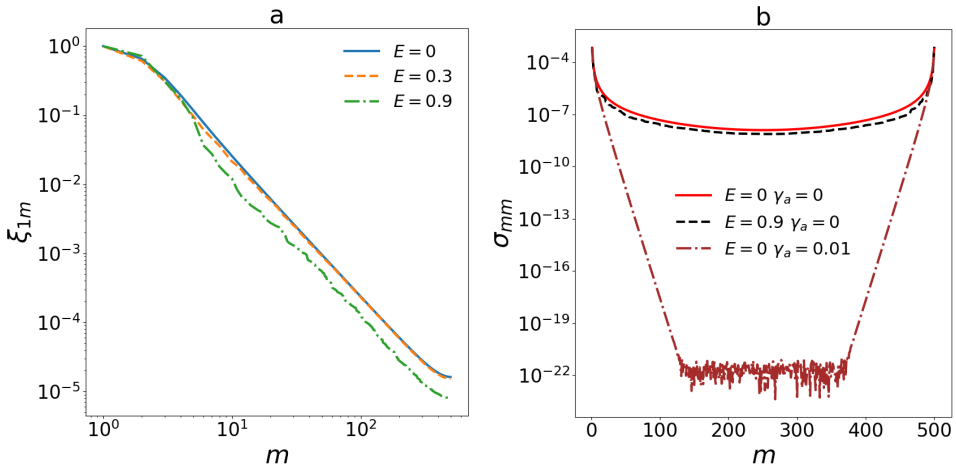

Figure 4.5. a: Spatial correlation function in the NHHP ($T_1 = 0.001$, $T_L = 0$) with and without random couplings. The introduction of quenched disorder does not alterate the power-law decay. b: Comparison between the temperature profiles in the NHHP ($T_1 = T_L = 0.001$, with and without disorer) and in the HHP with $T_a = 0$. We note that the NHHP with random couplings (dashed line) is more heat-conducting than the HHP (dash-dotted line). For both panels $L = 500$, $\gamma = 5$, $\gamma_b = 7$.

Once given these preliminary notions a natural question arises: can the introduction of spatial disorder induce strong localization in our lattice model preventing the occurrence of NHHP? In summary, we are interested in testing the robustness of the NHHP against the introduction of disorder in the granular lattice model. To do that we apply some standard analysis used to characterize the occurrence of Anderson localization to the disordered version of Eqs. (4.1) (see a quick overview of these methods in appendix D)

Granular lattice model with random couplings

Regarding the granular lattice, the first thing to discuss is how reasonably introduce disorder in the interaction matrix $\hat{A}$. In order to have the equivalent of the Anderson tight-binding one could add independent random entries on the principal diagonal by setting $\hat{A}'_{ii} = \gamma(2 + \alpha + \epsilon_i)$ with ϵ_i uniformly distributed in $[-E, E]$ and $E \leq \alpha$ (note that the diagonal entries has to be larger than 2 to reflect the positivity of local drag coefficients). Nevertheless, this would be the equivalent of introducing a random external viscosity on each site resulting in a perturbation of the HHP with $T_a = 0$ that, even unperturbed, has a different behaviour with respect the NHHP (see the Fig. 4.1 and Par. 4.2.2). Another option is to introduce off-diagonal disorder putting randomness on the upper and lower diagonal: $\hat{A}'_{ij} = \gamma\left[2\delta_{ij} - (1 + \epsilon_{i+1})\delta_{ij-1} - (1 + \epsilon_{i-1})\delta_{ij+1}\right]$. Also this solution is not consistent with our description because it is in contrast with the Newton's third law: $F_{ij} = \gamma(v_i - \epsilon_{ij}v_j)\delta_{ij\pm1} \neq -F_{ji}$. Introducing disorder in $\hat{A}$ consinstently with the physics of the model can be done by using random couplings in the viscous interaction: $F_{ij} = \gamma(1 + \epsilon_{ij})(v_i - v_j)\delta_{ij\pm1}$ with $\epsilon_{ij} = \epsilon_{ji}$ uniformly distributed in $[-E, E]$ where $E < 1$.

This brings to the following random matrix:

$$\hat{A}'_{ij} = \gamma\left[(2 + (\beta - 1)(\delta_{i1} + \delta_{iL}) + \epsilon_{i-1} + \epsilon_i)\delta_{ij} - (1 + \epsilon_{i+1})\delta_{ij-1} - (1 + \epsilon_i)\delta_{ij+1}\right] \tag{4.27}$$

that is symmetric semi-positive definite and takes into account the presence of the boundary bath β. We point out that with this notation the index of the random numbers ϵ_i runs up to $L-1$ and $\epsilon_0 = \epsilon_L = 0$. In order to study the effect of this perturbation on the NHHP we first look at the spatial correlation function ξ_{1m}. In Fig. 4.5a we compare few cases with different E obtained from Eq. (4.6) by a numerical diagonalization of $\hat{A}'$ with a fixed realization of the disorder (i.e quenched disorder). We can see that increasing the magnitude of the randomness through E does not change the functional form of the power-law decay. The only visible effect is the appearance of a jerky behaviour at large m due to the specific realization of the ϵ_is. Another observable useful to characterize the occurrence of strong localization is the temperature profile represented by σ_{mm}. In our model, if $T_a = 0$, the system receives external energy only at the boundary sites so the heating of the bulk ones is possible just through diffusion. In Fig. 4.5b we compare the temperature profile in the NHHP (with and without disorder) and in the HHP with $T_a = 0$. As we expect from the presence of self (γ_a) and/or mutual (γ) viscous friction, in all these cases we see that the temperature decreases moving away from the edges. Nevertheless, the bulk plateau of σ_{mm} is far higher in the NHHP cases than in the HHP with $T_a = 0$ where only a finite region (proportional to γ_a^{-1}) near the boundaries is effectively heated. What we would expect in a strongly localized NHHP was the presence of a similar absence of heat transport but not related to the introduction of a self drag coefficient.

All this confirms that the collective modes of the NHHP are not hindered by the introduction of random couplings in the interaction matrix. To rationalize that, a small discussion of how strong localization is related to the spectral properties of the time evolution operators (i.e. H in quantum system and $\hat{A}'$ in our model) is needed. Strong localization occurs when *all* the eigenvectors $\mathbf{S}_j = \{S_{1j} \cdots S_{Lj}\}$ are strong localized i.e. with a peak on a random site j^* that exponentially decays with a characteristic length l called localization length. At this point, it is worth saying that in some systems can exist a mobility edge [116] namely a threshold above which states are localized and below which they are delocalized (the notions of above and below can be exchanged). If the mobility edge does not exist then all the states are localized. In a localized system, l does not scales with L in the thermodynaimc limit and each eigenvector corresponds to a different j^* whose position is unocrrelated with respect the value of the associated λ_j. To have an intuitive idea of how strong localization would prevent the occurrence of long spatial correlation and heat transport in our system we can consider the extreme case with $l = 0$ where all the $\mathbf{S}_j$s are non-zero just on j^*. In this case we have $S_{ij} = \delta_{ij}$ and considering Eq. (4.10) written for generic eigenvectors and eigenvalues in the NHHP $\sigma_{jm} \propto \sum_{lk} S_{jl} S_{mk}[b1^2 S_{l1} S_{k1} + b_L^2 S_{lL} S_{kL}]/(\lambda_k + \lambda_l)$; it is straightforward to see that $\sigma_{1m} \propto b1^2 \delta_{1m}$ and $\sigma_{mm} \propto (b_1^2 \delta_{1m} + b_L^2 \delta_{Lm})$. Clearly the case with a finite l is not that easy but the final effect would be always the presence of short range spatial correlations and temperature profiles substantially different from zero only near the boundaries in contact with the thermal bath.

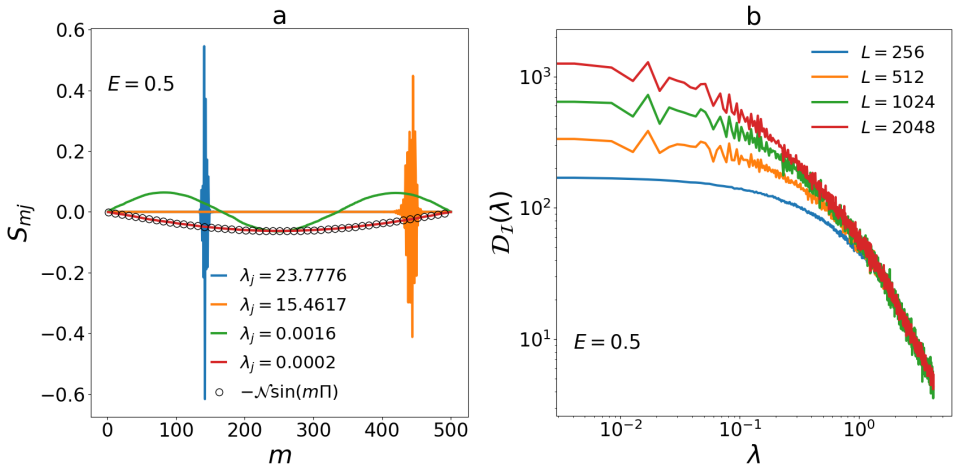

Figure 4.6. a: Delocalized and localized eigenvectors for the same system in the NHHP with random couplings and $L = 500$. They correspond respectively to low and high eigenvalues λ_j. We note that the eigenvector associated with the lowest eigenvalue is the same that one obtains without disorder (compare the red line and the black circles). $\mathcal{N} = \sqrt{2/(L+1)}$. b: IPR density for different values of L. For high λ the curves collapse signalling localized states. For low λ, $\mathcal{D}_{\mathcal{I}}(\lambda)$ grows linearly with L signalling delocalized states (see the discussion in the text and in appendix D). For both panels $\gamma = 5$, $\gamma_b = 7$.

As we have shown in Fig. 4.5, in the disordered NHHP the scenario is completely different also for large value of E. The reason is that the eigenvectors of $\hat{A}'$ are only partially localized. In Fig. 4.6a we plot a few $\mathbf{S}_j$s for $E = 0.5$; it is clear that some of them are strongly localized while others are spread all over the lattice maintaining the oscillatory behaviour typical of the ordered system. Remarkably, we note that the minimum eigenvalue ($\lambda = 0.0002$) corresponds to an eigenvector that has approximately the same shape of $\mathbf{S}_1$ in the non-disordered case (see Eq. (4.9)). A more systematic analysis of the mutual presence of localized and delocalized modes is reported in Fig. 4.6b where the density of the inverse participation ratio (IPR) is shown. Given an interval of values in the spectrum, this observable quantify the effect of the localized states within such an interval. As explained in appendix D, the regions of the spectrum where the IPR grows linearly with the size of the system correspond to delocalized states while an IPR independent from L is a clear signature of localization. From this perspective, Fig. 4.6b clarify what is going on in our system: we have localization in the high-frequency region of the spectrum and delocalization in the low-frequency one (remember that the λ_js are inverse of time). Because of this, we speculate the existence of a finite frequency mobility edge. Studying the IPR for different values of E (not shown) reveals that the delocalized region of the spectrum shifts to the left when the amount of disorder is increased. This is fully coherent with the presence of a mobility edge in our system but a detailed analysis of that goes beyond the scope of the thesis. As a final remark, we point out that in this paragraph we have provided some evidence of the robustness with respect to the introduction of spatial disorder of the NHHP *in the steady state*. Nevertheless, the presence of some localized modes can significantly

affect the transient. Thus, a promising perspective is to study the dynamics of the velocity field starting from different initial conditions through numerical integration of Eqs. (4.1) with random couplings.

A simple argument of delocalization

Once understood that the robustness against Anderson localization in our model is due to the presence of low-frequency delocalized modes, we want to provide a simple analytical argument to rationalize why in presence of disordered couplings we have delocalization for any value of E. For simplicity, we consider the case of periodic boundary condition (PBC) where it is easy to show that the fundamental state (unperturbed by disorder) is $\mathbf{S}_1$ =cost with $\gamma_1 = 0$. We discussed three ways of introducing disorder in our system and now we show how the random matrix $\hat{A}'$ with PBC acts on $\mathbf{S}_1$ =cost for each one of them:

$$\hat{A}' S_{i1} = \begin{cases} (2+\varepsilon_i)\, S_{i1} - S_{(i+1)1} - S_{(i-1)1} \text{ Anderson} \\ 2S_{i1} - (1+\varepsilon_i)\, S_{(i+1)1} - (1+\varepsilon_{i-1})\, S_{(i-1)1} \text{ off-diagonal} \\ (2+\varepsilon_i+\varepsilon_{i-1})\, S_{i1} - (1+\varepsilon_i)\, S_{(i+1)1} - (1+\varepsilon_{i-1})\, S_{(i-1)1} \text{ rand. coup.} \end{cases} \tag{4.28}$$

We clearly see that only with random couplings $\mathbf{S}_1$ =cost is still an eigenvector with a null eigenvalue. This argument is not a demonstration that the fundamental state remains approximately the same also with fixed boundary conditions as suggested by Fig. 4.6a but it gives an idea of how the correlation in the disorder can assure the presence of delocalized modes. A rigorous proof also for fixed boundaries can be probably found but it goes beyond the scope of this thesis.

Chapter 5

The granular ratchet

Up to now, we have discussed many aspects of the occurrence of slow characteristic timescales in a dense vibrofluidized granular system. Once reported their experimental evidence in a tracer dynamics [175] in Chap. 2, we explained their origin by a numerical analysis that unveiled a granular collective mode which is properly described by a phenomenological and a lattice model [146, 148] (Chap. 3). However, the physical mechanism underlying the formation of such collective rotations in the real system is still not clear (see also the discussion of Par. 4.3.1). We dedicate the present chapter to tackle this problem by focusing on simplified numerical setups where the conversion of vertical vibration into steady motion is understood in its essential ingredients [147]. Such systems are quasi-2D and 3D dense vibrated granular packings exhibiting a global collective translation along the free directions of motion allowed by the presence of periodic boundary conditions (PBC). This choice is also motivated by the recent discovery of persistent dynamics in the rotational degrees of freedom of vibrated disks in a similar setup [130].

The analysis we propose makes clear that the collective motion of dense vibrated granular systems can be understood as a ratchet effect [89, 161] governed by the interplay of frictional forces and asymmetries in bulk structure.

The chapter is organized as follow: in Sec. 5.1 we describe the numerical setup and characterize the collective motion of the packings, Sec. 5.2 is devoted to the study of correlations between structure and dynamics while in Sec. 5.3 and 5.4 we motivate and discuss the interpretation of the phenomenon as a ratchet effect. A minimal ratchet model that captures the main qualitative features of the numerical results is proposed. Finally, in appendix E we consider the role of the single-particle rotations.

5.1 Vibrated simple granular packings

5.1.1 Numerical setup

We simulate a system of N spherical grains confined by hard walls and/or periodic boundary conditions (PBC) with different geometries.

Each grain has radius R_i, mass m_i and is described by the coordinates of its position $r_{\alpha i}$, velocity $v_{\alpha i}$ and angular velocity $\omega_{\alpha i}$; where $\alpha = \{x, y, z\}$ and $i = \{1, \cdots, N\}$. Also in this study, the grain-grain and grain-boundary contact forces

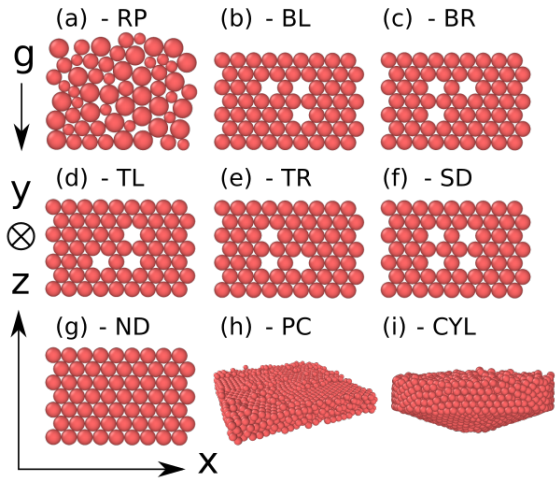

Figure 5.1. Snapshots of the geometry used in the simulations. Quasi-2D vertical layers can be random polydispersed with $N = 60$ (a) or ordered monodispersed (b-g) with eventually defects ($N = 63, 60, 59$). The defect nomenclature is related to the position of the grain the breaks the symmetry, from panel b to g we have: bottom left (BL), bottom right (BR), top left (TL), top right (TR), symmetric defects (SD), no defects (ND). Polydispersity is implemented by mixing in equal proportions three species of radii $R_i = \{1.5, 2.0, 2.5\}$ mm. In the monodisperse cases, including the 3D cubic setup (h) and the conical based shaped cylinder (i), we have $N = 2600$ and $R_i = R = 2$ mm. Rendering of the simulations realized with OVITO [188]. Images reprinted from [147].

follow the Hertz-Mindlin (HM) model (see Par. 2.2.1). In addition to the cylindrical container treated in the previous chapters (Fig. 5.1i), two other kinds of geometries are considered and shown in Fig. 5.1: i) quasi-2D geometries (cases a-g) with two parallel vertical walls of width $L = 32$ mm separated by a distance $d = 2 \arg\max_i R_i$. The boundaries in the x direction can be hard or periodic (we mostly concentrate on the latter case) while the z direction is confined by an upper and lower hard wall; ii) a full 3D geometry with base area $A = 98 \times 98$ mm^2 and PBC along both x and y directions (Fig. 5.1h). In all these geometries, the bottom wall is hard and moves as $z(t) = A\cos(2\pi t)$ injecting energy into the system, also here characterized by the maximum rescaled acceleration $\Gamma = A(2\pi f)^2/g$,where g accounts for gravity. In all the presented analyses we always vary Γ by A at fixed f. Regarding the quasi-2D setups, we prepare the initial state of the packings in two main ways; The first one consists in randomly pouring a polydisperse assembly of grains in the container, initial velocities are zero but during the pouring dynamics they acquire energy and rapidly reach a stationary statistics; the second one is obtained by placing a monodisperse assembly on a hexagonal lattice with the possibility to have vacancies in certain sites, while the particles initial velocities are drawn from a Gaussian distribution with zero mean and a variance small enough to keep the crystal stable. For the 3D cases, we simply pour monodisperse grains into the containers. Since the latter do not satisfy the right proportions for crystallization the resulting packings are fairly disordered. The monodisperse packings with quasi-2D geometry (b-g in Fig. 5.1) can be without defects (g), or with four symmetric

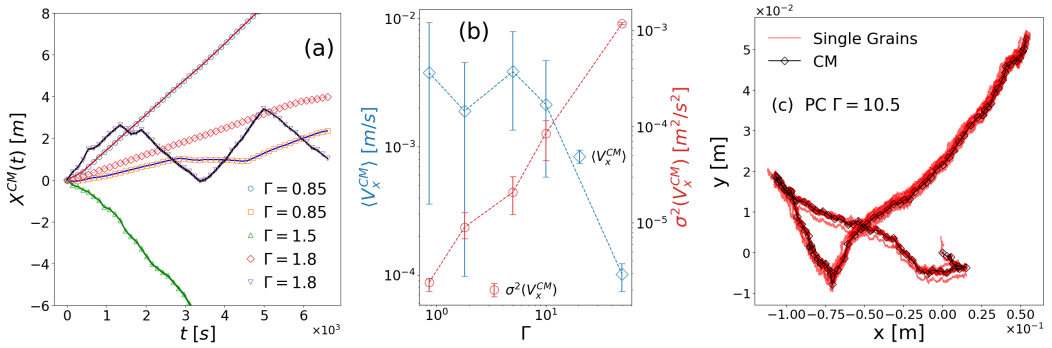

Figure 5.2. a: $X^{CM}(t)$ (symbols) and $x_i(t)$ for all the grains i in the system (lines) for quasi-2D random packings: the grains move coherently with the CM. Simulations with the same Γ refer to different random realizations. b: Comparison between $\sigma^2(V_x^{CM})$ and $\langle V_x^{CM} \rangle$, obtained averaging over three independent random realizations. c: Trajectories in the xy plane for a substet of 37 grains (lines) and the center of mass (symbols) in the PC geometry (Fig.5.1h). For panels a,b $f = 100$ Hz while for panel c $f = 200$ Hz. Images reprinted from [147].

defects (f), or with three defects placed to break in different ways the symmetry of the crystal with respect the horizontal and the vertical direction. The polydisperse quasi-2D packing (5.1a) is inspired by a recent experimental and numerical study [130] with shaken disks (without PBC): for Γ low enough the authors unveiled a persistent net angular velocity of each disk. As a preliminary analysis (reported in appendix E.1) we verified that such persistent rotational modes are observed also in our simulations of spheres with both hard walls and PBC. Remarkably, we found it in all the geometries explored here. However, in this chapter, we focus on a different phenomenon, namely a collective horizontal persistent drift of the grains, superimposed on the previously observed rotational modes. For this reason, from now on, we always refer to results with horizontal PBC.

5.1.2 Drifting disordered packings

We start from polydisperse (disordered) packings in the quasi-2D geometry. By tracking the trajectories of the particles for almost 7200 seconds (physical units can be compared with real experiments, see Par. 2.2.1) we can observe that - at low values of Γ - all the system is moving coherently with the center of mass (CM) along the x-axis i.e. the free direction allowed by PBC. This can be seen in Fig. 5.2a where we show some examples of time evolution of the x coordinate of the CM $X^{CM}(t) = M_{\text{tot}}^{-1} \sum_i m_i x_i(t)$ at different Γ and with different initial configurations of particles. We note that, even with the same Γ, each random packing exhibits a peculiar behaviour: we can have approximately constant drifts with very different magnitude (circles and squares) or an intermittent drift with very sharp verse changes (upside-down triangles). In 5.2b, considering the x component of the CM's velocity $V_x^{CM}(t)$, we also verify that short-time properties as the time variance $\sigma^2\left(V_x^{CM}\right)$ are fully determined by the driving parameters (small errorbars), while the slow cooperative dynamics (characterized by its time average $\langle V_x^{CM} \rangle$), sensibly depends on the packing configuration (large errorbars). Nevertheless, raising Γ up to

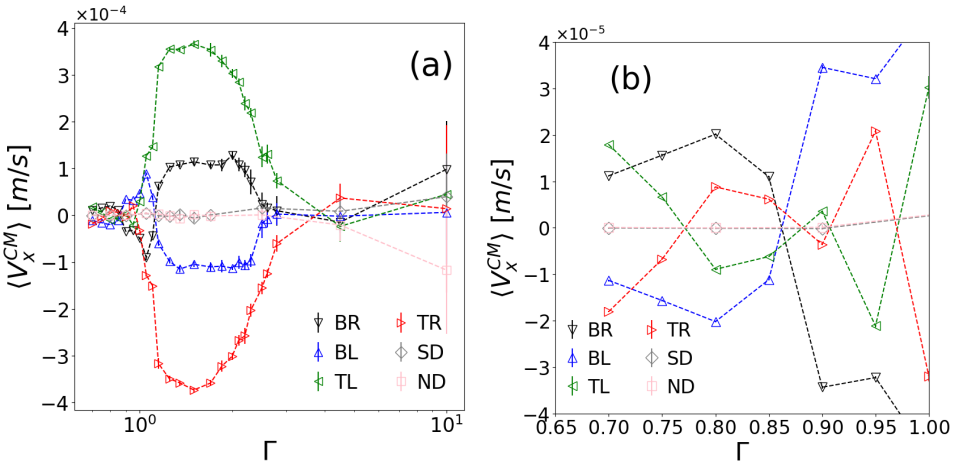

Figure 5.3. a: Time averaged velocity of center of mass as a function of Γ for different monodispersed packings. Each point is mediated over five independent realizations of the dynamics. Here, differently from random packings, $\langle V_x^{CM} \rangle$ vanishes for $\Gamma \simeq 3$ because moderate vibrations destroy the asymmetric configuration of defects. d: zoom on low Γs to highlight the sign changes with fixed structure. In both panels $f = 100$ Hz. Images reprinted from [147].

values for which the system fluidizes (typically $\Gamma > 10$), the CM performs Brownian-like trajectories and $\langle V_x^{CM} \rangle$ vanishes. We recall that a dense vibrofluidized granular system has several timescales, the smallest associated with fast vibrational motion occurring in the grains local cages, the largest associated with slow re-arrangements of the global contact network. What we observe here is a rapid divergence of the largest timescale when Γ is reduced below ~ 10. The value of $\langle V_x^{CM} \rangle$, therefore, does not depend crucially on the trajectory's duration, provided it is longer than the small timescales, e.g. $\ll 10^{-1}$ s. The scenario of Fig. 5.2b is then quite coherent with the other cases of opposite behaviour at different timescales encountered several times in the previous chapters (Par. 2.2.2, 3.1.2, 3.2.5). In Fig. 5.2c, we plot the trajectories in the xy plane of the CM and the single grains in the cubic setup with PBC on both the horizontal directions (i.e. the PC geometry of Fig. 5.1h). Here, the single grains perform the same motion of the CM but with stronger fast vibrations with respect to the quasi-2D case. The dynamics (tracked for one hour) is characterized by long drifts with an almost fixed orientation interrupted by sudden changes of direction. The study of this setup confirms that the formation of collective motion can occurs also with more than one free direction of motion.

From this first analysis on random packings, several questions arise: What makes these packings coherently move? What defines the verse of the drifts? What triggers the abrupt changes in the intermittent drifts?

5.1.3 Ordered packings with defects: the effect of symmetries

The observation that average motion is erased by fast particle re-arrangement (fluidization) is a first hint of its correlation with the system's spatial configuration. For this reason, we study ordered packings with defects where the asymmetry of the

structure is properly designed. In Fig. 5.3a we show $\langle V_x^{CM} \rangle$ for different packings and values of Γ. In the FC and SD cases, for which the symmetry w.r.t. the z-axis is not broken, no net drift is observed. Regarding the packings that break such a symmetry, we have that when the defect configuration is mirrored with respect to the z-axis, e.g. going from BL to BR or from to TR to TL etc., at a given value of Γ, $\langle V_x^{CM} \rangle$ changes its sign remaining with comparable magnitude. Moreover, a reflection of the configuration with respect to x, e.g. going from BL to TL or from to TR to BR etc., always changes the magnitude of the drift but the sign is inverted only for a few values of Γ. Remarkably, also the variation of Γ with keeping the same layout of defects brings to multiple inversions of $\mathrm{sgn}(\langle V_x^{CM} \rangle)$ in the narrow region $0.8 \leq \Gamma \leq 1.05$ zoomed in Fig. 5.3b. We also note that, for ordered packings with defects, the driving condition for which the steady drifts vanish is anticipated to $\Gamma \sim 3$. We verified that, for these values of the shaker acceleration, the configurations of defects in the bulk are not more stable so the system fully crystallizes except for a few partially fluidized upper layers.

To summarize the results of this analysis we have that: i) defect asymmetry w.r.t. z is needed to observe a non-zero mean velocity of the CM, ii) a reflection w.r.t. z inverts the verse of the motion, iii) the asymmetry alone is not enough to define the verse of the motion, the driving determines it too.

5.2 Bulk structure and collective dynamics

5.2.1 Sensitivity to structural deformations

Given the complicated interplay between external parameters and drifts revealed so far, we now focus on changes occurring during a trajectory, when external parameters are fixed. Such changes are more evident and frequent in random packings: there we measure the coordination number of the contact network $Z(t)$ and compare its time evolution with that of the instantaneous $V_x^{CM}(t)$, see Fig. 5.4a-d. We measure the instantaneous coordination number by $Z(t) = N^{-1} \sum_{ij} \Theta(R_i + R_j + \delta - |\boldsymbol{r}_{ij(t)}|)$ where $0 < \delta \ll R_i + R_j$ allows detecting nearest neighbour not strictly in contact due to vibrations. In all these panels abrupt variations in $V_x^{CM}(t)$ occur together with jumps of $Z(t)$. Such jumps do not correspond to a significant re-arrangement of particles (a 0.01% variation of $Z(t)$ can be sufficient, see panel d): this confirms that the collective motion is sensible also to small deformations of the contact network. The same correlation is present also in the 3D setup with PBC on x and y (Fig. 5.4c corresponds to Fig. 5.1h). Here the collective drift is two-dimensional so we plot the modulus and the orientation showing that both of them undergo sharp variations correlated with the ones of $Z(t)$. In Fig. 5.4d, we verified that structural deformations and the collective dynamics are connected also in the realistic cylindrical setup treated in the previous chapters. This simple test strongly suggests that the origin of the long memory effects observed in experiments and simulations of this setup is rooted in the slow exploration of the spatial configuration space. Obviously, the coordination number is not directly related to the packing asymmetry and one can refine the above analysis looking for more appropriate quantities that better correlate with the behaviour of the drift. In general, the characterization of a random network through its topology is a

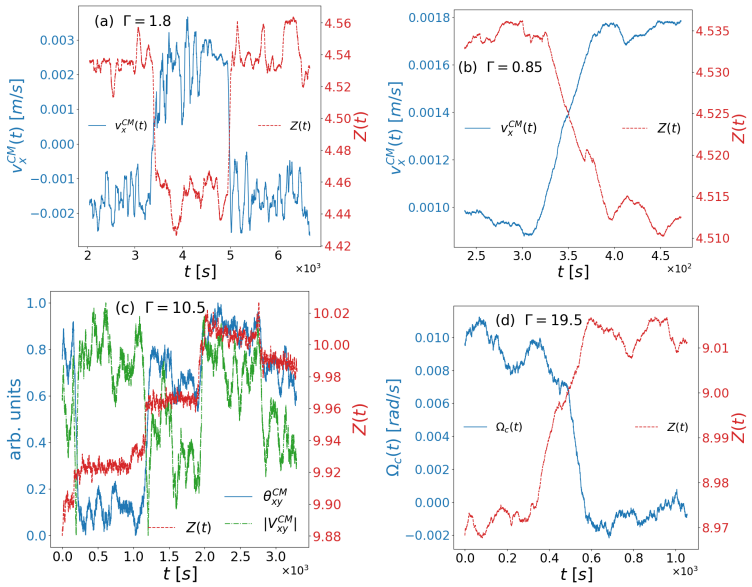

Figure 5.4. Comparison between the time evolution of the CM velocity and the mean coordination number of the contact network $Z(t)$. Trajectories are smoothed with a running average. a,b: Random packings (cases with upside-down triangles and circles in Fig. 5.2a). c: 3D cubic setup, here V_{xy}^{CM} is two-dimensional so we plot both the modulus and the orientation θ_{xy}^{CM}. d: 3D cylindrical geometry where the collective variable is the angular velocity of the rotation around the central axis Ω_c (see Eqs. (3.1) for definition). Images reprinted from [147].

non-trivial task [10, 200]. The fact that, on one hand, at fixed Γ the drift can significantly change for weak deformations of the contact network (as observed for random packings) and, on the other hand, it can change direction by varying the driving parameters with a fixed structure (as occurs in the ordered packings with defects) reveals an intriguing and challenging scenario. Analogous problems about the relation between structure and dynamics have been discussed recently for glassy systems [64, 52, 191, 54, 92, 179]. In our study, the athermal nature of the system (that needs mechanical driving to reach a stationary state) is a peculiar feature that has no counterpart in thermal glasses [86].

5.2.2 Asymmetric interaction with the external source of energy

The observations so far suggest looking for some observables that mediate between bulk structure and dynamics. In the 2D system, the tangential interaction between the vertical walls and the grains is switched off by proper tuning of the parameters in the HM model (see appendix A). Thus, the CM dynamics on the x direction is entirely ruled by the following equation:

$$\dot{V}_x^{\mathrm{CM}} = M_{\mathrm{tot}}^{-1} F_x^T(r_{xj}, r_{zj}, v_{xj}, \omega_{yj}) \tag{5.1}$$

where F_x^T is the total x-component of the external tangential force exerted by the plate and the index j refers to the bottom particles, the only ones on which F_x^T acts directly (for ordered packings $j \in [1, 9]$). The above equation, together with the

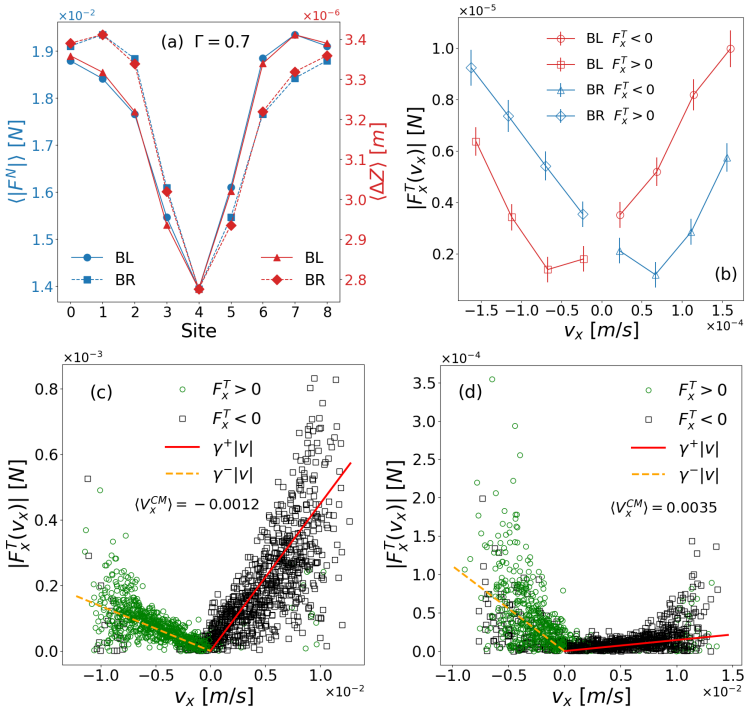

Figure 5.5. a: Time averaged modulus of the normal force and compenetration between the plate and the bottom particles for BR and BL configurations. Site 4 is under the double defect (see Fig 5.1b-c). b,c,d: Scatter plots with bins of the total x-tangential force modulus exerted by the plate VS the total velocity of the bottom particles for ordered packings with defects (b) and random packings (c,d) shaken at $\Gamma = 0.7$. In the latter, $\gamma^{\pm} = |\langle F_x^T | v_x \gtrless 0\rangle| / \langle v_x | v_x \gtrless 0\rangle$ linearly interpolate the data clouds. Images reprinted from [147].

explicit form of the HM model, suggests looking at the profiles along x of the mean normal pressure and the mean compenetration between the plate and the bottom particles. Indeed, the tangential force is proportional to the normal overlap below the Coulomb threshold and the normal force modulus above it (see Eqs. (2.4)). These obsevables are shown in Fig. 5.5a, for the BR and BL configurations: each profile is asymmetric and properly inverted under an z-reflection. This tells us that defects in the bulk actually influence how the boundaries interact with the external source of energy. The fact that the distribution of stress at the bottom is affected by the contact network is clearly something that we expect, what is remarkable in our opinion is its global dynamical consequence. In order to better understand the connection between bulk asymmetry and drifts, we characterise the dependence of F_x^T upon $v_x = \sum_j v_{xj}$ for two z-reflected ordered configurations with defects by the scatter plot shown in Fig. 5.5b (a discussion on the role of the ω_{yj}s is provided in appendix E.2). As we expect from the numerical model (Eqs. (2.4)) such dependence is typical of a frictional force but, quite surprisingly, its intensity depends on the sign of the velocity. Moreover, also this frictional asymmetry is inverted under a z-reflection. A quick comparison with Fig. 5.2b makes clear that the drift occurs in the verse that feels lower friction. We also show, in panels c and d, scatter plots for two random packings where this bias is even more pronounced and indeed $\langle V_x^{CM} \rangle$ is far larger. All this makes clear that structural disorder and defects introduce an asymmetric interaction with the external source of energy.

5.3 The stick-slip ratchet model

Putting together the different analyses done up to now, we find it reasonable to interpret our results in the framework of Brownian ratchets [89, 161]. The ingredients needed for a ratchet effect are two symmetry breakings, one in space and one in time, and when one of the two is removed the effect disappears. For example in granular and active matter, these conditions can be realized by inserting an asymmetric object in an out of equilibrium bath [51, 81, 61] (see also Par. 1.4.3). In the case under study, the time symmetry breaking is induced by energy dissipation (in friction), while space symmetry breaking is more ambiguous for two reasons: i) it is elusive in the random packings; ii) in the ordered packings with defects is more clear but it is strictly related to the dissipative dynamics at low vibration amplitude, in fact, it is washed out when the amplitude increases. The ratchet effect appearing here, therefore, is of a novel type where there is not a distinction between an object and the surrounding bath: it is the bath itself that, for certain driving conditions, remains stuck in a slowly varying spatial configuration that allows the formation of a steady current. In other words, the spatial symmetry breaking is fundamentally transient, but it can be amplified and/or stabilised by dynamical effects.

5.3.1 Model definition: From periodic to slipping potential

Following the interpretation of the phenomenon under study as a ratchet effect, we want now to provide a minimal model able to capture the essential features of our numerical analysis, at least in the regime where the re-arrangement time is infinite. Our model is a variation of the well known periodically rocked ratchet in

an asymmetric periodic potential [23] that consists of an overdamped particle with the following equation of motion:

$$\dot{x} = -\partial_x \left[V(x) + xA\sin(2\pi f t)\right] + \xi(t) \tag{5.2}$$

where $V(x) \propto \left[\sin(\tilde{k}x) + 1/4\sin(2\tilde{k}x)\right]$ has the shape of a periodic sawtooth with smoothed edges and an intrawell characteristic frequency tuned by $\tilde{k}$. $\xi(t)$ is a Gaussian white noise for which $\langle\xi(t)\xi(t')\rangle = 2D\delta(t-t')$. In this model, the interplay between the sinusoidal/random forcing and the periodic asymmetric potential gives raise to a steady current for x. Current sign changes can be observed varying A at fixed D and vice-versa provided that they are both different form zero.

In our system, we can't assume the CM of the packing as moving in a periodic potential (see analogous cases in [196, 110]) because the interaction between the bottom plate and the granular packing does not depend on the mean horizontal position of the latter. Nevertheless, it is reasonable to think that it can be trapped for small displacements because of local deformations of the grains in contact with the lower wall. We have then replaced the periodic potential with a confining but slipping one. This choice is further motivated by the numerical evidence of a stick-slip behaviour in the difference of the mean x-coordinates of two adjacent horizontal layers (see Fig. 5.6a). Our model describes the horizontal dynamics of the granular medium by reducing it to two coarse-grained variables x and x_0, identifying the average position of the upper (more mobile) and the lower (more trapped) region respectively. The lower region transmits the external forcing to the upper one by vertical vibrations while its horizontal motion is hindered by the mutual compenetration between the particles and the bottom wall. Beyond a given tangential stress threshold, however, the lower layers undergo a sudden change of mobility from zero to a finite value so that they slip and reach in a very short time the mobile ones. All this is described by the following overdamped dynamics:

$$\dot{x} = -\frac{\mathcal{K}(\Delta x)}{\gamma}\Delta x + A\cos(2\pi f t) + \sqrt{2D}\eta(t) \tag{5.3a}$$

$$\dot{x}_0 = s\frac{\mathcal{K}(\Delta x)}{\gamma_0}\Delta x \tag{5.3b}$$

$$\mathcal{K}(\Delta x) = \left[1 + \mathrm{sign}(\Delta x)\epsilon\right]k \tag{5.3c}$$

where $\Delta x = x - x_0$ and $\eta(t)$ is a Gaussian white noise with zero mean and unitary variance: $\langle\eta(t)\eta(t')\rangle = \delta(t-t')$, γ^{-1} is the mobility of the upper region, $\gamma_0^{-1} \gg \gamma^{-1}$ is the slipping mobility of the lower one, and $s = 0, 1$ denotes the state of the system (stick $s = 0$, slip $s = 1$). Regarding $\mathcal{K}(\Delta x)$, it represents a non-isotropic stiffness whose degree of asymmetry is tuned by the dimensionless parameter $-1 < \epsilon < 1$. In order to implement the stick-slip dynamics we have defined a high-strain region (HS) to be $\Delta x > \frac{\gamma F^*}{k(1+\epsilon)} \cup \Delta x < \frac{-\gamma F^*}{k(1-\epsilon)}$ and a low-strain (LS) one to be $|\Delta x| < \frac{\gamma F^*}{Mk}$ with $M > \max(1+\epsilon, 1-\epsilon)$. The rest of possible values of Δx belong to the medium-strain region (MS). The state variable s goes into $s = 1$ when Δx enters into HS, while it goes into $s = 0$ when Δx come back to LS. In MS, s does not change, it depends upon its last update (all simulations start in MS with $s = 0$). The equations of motion (5.3) have been numerically integrated [208] and the stick-slip

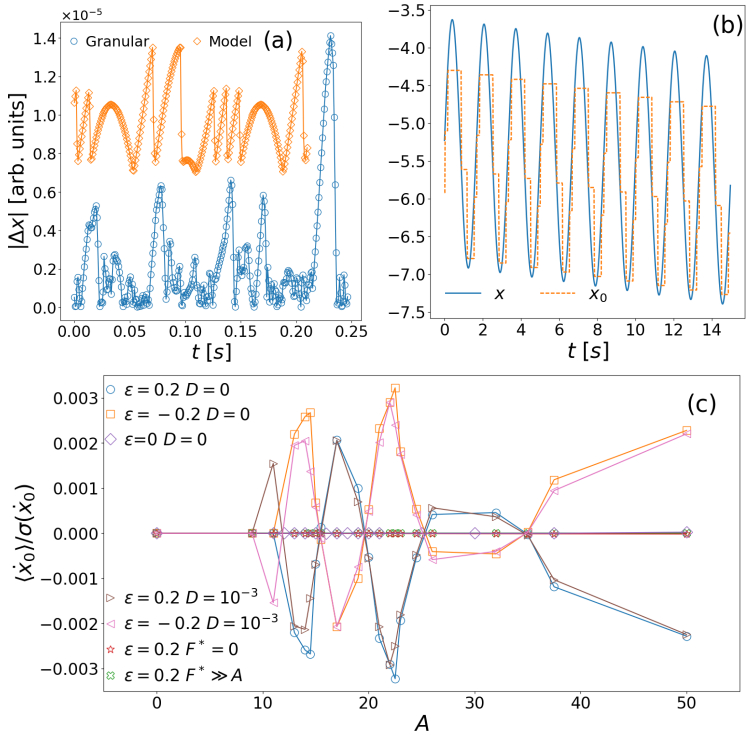

Figure 5.6. a: Stick-slip in the difference of the mean x-coordinates of two adjacent horizontal layers in a granular simulation and in the relative motion Δx of the model. b: Typical trajectories of the model with drift and oscillations. Note that x and x_0 follow the same average motion. c: Signal to noise ratio of $\dot{x}_0$ as a function of A. For $D = 10^{-3}$, the typical shape of the curve is close to the deterministic case. Eqs. (5.3) has been numerically integrated with $k = 1$ s^{-2}, $\gamma = 1$ s^{-1}, $f = 2$ s^{-1}, $\gamma_{\text{slip}}^{-1} = 500$ s, $M = 10$, $F^* = 1$. Images reprinted from [147].

behaviour of $|\Delta x|$ is shown in Fig. 5.6a, while Fig. 5.6b shows a trajectory of x, x_0 in the deterministic case ($D = 0$), where it is more evident the drift+oscillation dynamics of both variables that follow the same average motion.

5.3.2 Model phenomenology

In Fig. 5.6c we show the signal to noise ratio of $\dot{x}_0$ as a function of A for different values of D and ϵ obtained by numerical integration of Eqs. (5.3). We note that after an amplitude threshold, the system exhibits a net motion. The amplitude threshold is related to the minimal forcing necessary to overcome F^*. We also verified that by setting $F^* \gg A$ the system is always trapped and no net motion can be observed. Also the opposite limit $F^* = 0$, where the potential well is never stuck, does not show any drift. The behaviour of $\dot{x}_0$ as a function of A reveals a rich phenomenology that fairly resembles the one observed in the granular simulation (do a comparison with Fig. 5.2b). We have many sign changes that occur with the same ϵ and a symmetric reflection of the curves as $\epsilon \to -\epsilon$. Moreover, for $\epsilon = 0$ we have no mean drift for all the amplitudes as it happens for symmetric packings. We also note that the essential phenomenology of the model in this particular regime where $\gamma^{-1} \ll \gamma_0^{-1}$, $f \ll \gamma_0^{-1}$ and $A/f \gg \sqrt{D/f}$ is fully contained in the deterministic dynamics. This represents a quite surprising fact with respect to the results of the ancestor model [23] where the sign changes as a function of A are observed only in presence of both periodic and random forcing. We can understand this by thinking that the stick-slip dynamics introduces a kind of effective randomness in the model. We point out that the phenomenology of the model when the noise becomes comparable or dominant with respect to the periodic forcing could be really different but a detailed study of that goes beyond the scope of this thesis. The important point for our analysis is that the features needed to recover the behaviour of the granular packings are not affected by the presence of a small noise (see triangles in Fig. 5.6c). The signal-to-noise ratio of $\dot{x}_0$ as a function of A in presence of a small noise is very similar to the deterministic case except for the low-A region where we can see that the presence of the random force anticipates the threshold for the drift appearance. This particular regime would be of particular interest for a future study of the model.

5.4 Collective dynamics from the ratchet perspective

In this chapter, using DEM numerical simulations, we proposed a series of ideal experiments with appropriate geometries and granular packing realizations to put in evidence the existence of a random-to-direct motion energy conversion based upon the concurrent time and space symmetry breaking. As in many ratchet-like phenomena, the same geometry can lead to opposite drifts, depending on the parameters of the energy injection (here the vibration maximum acceleration), however when vibration is fixed a specular reflection of the geometry induces an inversion of the drift. We reproduced these behaviours through a simple model of a vibrated particle in an asymmetric potential with friction, where the potential minimum can slip toward the particle. Many pieces of evidence, as the common sensibility to deformations in the bulk structure, strongly suggests that the collective motion reported

and explained here is the translational counterpart of the rotational drifts discussed in Chap. 3.

5.4.1 A different interpretation of the predictions from the granular lattice model

As anticipated in 4.3.1 the results of this chapter make clear that the long-range correlations and slow timescales predicted by the lattice model (Cap. 4) does not directly explain the collective dynamics of the real systems. The analysis of Par. 5.1.2 highlights that a necessary condition for the drifts occurrence is the presence of spatial asymmetries in the configuration of the granular packings, an ingredient not considered in the modelization of the 1D granular lattice. Here we want to propose some future numerical analysis to test the connection between the predictions of the NHHP in the granular lattice model and the numerical evidences of this chapter despite the aforementioned crucial difference. The first point is the following: Fig. 5.5a shows that the asymmetric configurations of defects in the bulk imply asymmetric pressure and compenetration profiles at the bottom boundary of the system. This occurs in simulation where only the bottom particles feels an external force on the x-direction (Par. 5.2.2) i.e. the same condition realized in the NHHP with $\gamma_a, T_a = 0$. Will this long-range influence of the internal structure on the boundaries persists also with external (random and/or deterministic) forces acting on the bulk particles? Simulations of the 2D setup with a Langevin bath coupled with all the grains or just with tangential interacting vertical walls will answer this question determining whether the emergence of asymmetric boundary profiles as an effect of asymmetries in the bulk is a NHHP-like property or not. The second point starts by realizing that the 2D system ideally mapped in the 1D granular lattice shown in Fig. 4.2 is essentially the same as the ordered packing with no defect (ND) of Fig. 5.1g. Trusting the 2D $\rightarrow$ 1D mapping, one would expect the presence of long-range correlations and slow timescales for vibrated ND packings too. Nevertheless, this does not happen, at least in the form of slow collective translational drifts in the x-direction. For example, a refined analysis of the dynamical structure factor of the system could lead to the evidence of collective vibrational modes, but here the idea is different. We consider that the NHHP "predicts" for the ND packing a sort of critical regime without a typical correlation length other than the system size (i.e. a scale-free regime). Considering the symmetry of this packing as an unperturbed condition and properly parametrizing the perturbation of such a state as ϵ, and the response to it as P, a signature of a scale-free behaviour would be having $\lim_{\epsilon\to 0} P(\epsilon) \neq P(0) = 0$ i.e. a singular limit with a finite response in the limit of zero perturbation. A numerical strategy to do that is the following: we construct the bulk asymmetric defects by replacing the missing grains in the BR configuration (or any other non-symmetric one) with grains of mass $m_d \neq m$ (larger or smaller is the same) and then we define $\epsilon = |m_d - m|$ and $P = \langle V_x^{CM} \rangle$. Then, through different simulations with a fixed Γ and m_d approaching to m we can study the limit $\lim_{\epsilon\to 0}\langle V_x^{CM}\rangle(\epsilon)$. After that, with the same motivation given for the first point, this analysis could be done also in presence of external forces acting on the bulk particles. To summarize, the correct outcome of the numerical tests proposed here to determine the connection between the ratchet scenario and the granular lat-

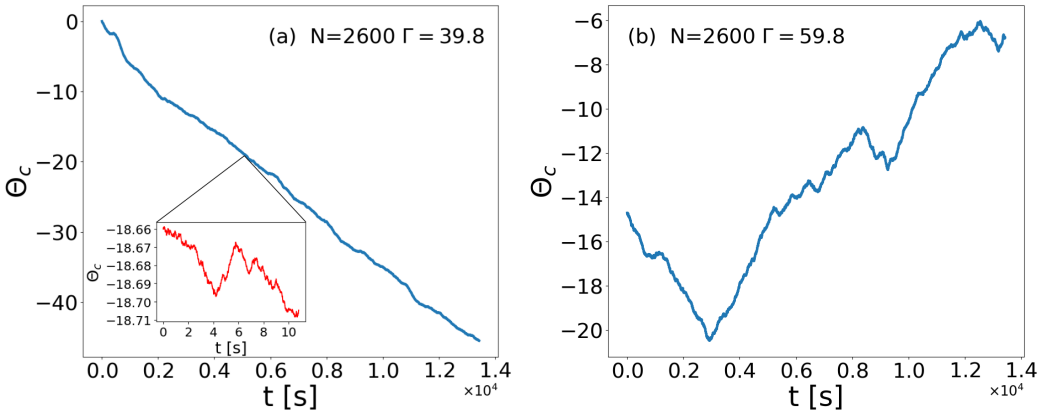

Figure 5.7. a: Angular trajectories of the collective variable Θ_c in the cylindrical setup (see Eqs. (3.2) and 3.1) with $N = 2600$ for $\Gamma = 39.8$ (a) and $\Gamma = 59.8$ (b). In the left panel, we have an overall motion described by a negative persistent drift. Nevertheless, zooming the trajectory reveals that subsets of the trajectory can travel in the positive verse for short time (inset). In the right panel, we observe many subsequent drifts with different amplitudes and durations directly in the overall motion.

tice model would change the interpretation of the NHHP from the prediction of the slow collective drifts to the prediction of the critical regime that, as a response to an (even infinitesimal) spatial symmetry breaking, exhibits spontaneous slow collective drifts.

5.4.2 The slowness that keeps you going

The interpretation of this phenomenon as a ratchet effect in which the spatial symmetry breaking is stabilized thanks to the low driving condition, allows drawing some (non-exhaustive) conclusions about the occurrence of slow timescales in dense vibrofluidized granular systems. When studying phenomena with two or more well-separated characteristic timescales a natural question that arises is: Where is the memory stored? There must be something in the system that remains correlated during and after the relaxation of the faster variables. As an example, in Fig. 5.7a we plot the trajectories of the collective travelled angle Θ_c in the cylindrical setup coming from the simulations discussed in Sec. 3.1. Here we can clearly see that it is performing a constant negative rotational drift. Nevertheless, by zooming a small region of time ($\sim$ 10 s) we can see that there are subsets of the trajectory in which Θ_c travels in the positive verse for 1 - 2 seconds. A very naive way to describe these short counter-drifts is thinking that the collective variable assumes a positive angular velocity for a while but still "remembers" that it has to go in the positive verse. The anthropic version of such behaviour manifests when, on the way to the office, we come back home on the fly to take the wallet we forgot on the table. The correlation between structure and collective dynamics investigated in this chapter sheds light on these memory effects: the slow dynamics is ruled by the particular spatial configuration in which the granular system is found during the motion. Re-arrangements of such a structure, induced by instabilities in the bulk or by the less caged particles at the boundaries (Par. 3.1.3), can occur. These

can be transient/reversible giving raise to very short counter-drifts as in Fig. 5.7a, or persistent/irreversible inducing a substantial change in the drift verse and/or magnitude as in Fig. 5.4. From this point of view, it seems reasonable to say that the memory of the system is stored in the spatial structure of the packings. All this makes sense because here the notions of persistence and slowness are relevant for the typical observation times of the phenomenon. What we call persistent or slow is indeed transient and fast with respect to the time that the systems would need to explore a consistent number of different spatial configurations. To be a little more formal, we define three timescales: τ_f related to the fast vibrational dynamics of the grains in their cage, τ_o referred to the observation timescales of the phenomenon and τ_r that is the relaxation time of the structural re-arrangements. In this thesis, for low driving, we are always in the regime where $\tau_f \ll \tau_o \ll \tau_r$ where we observe zero or few drift changes depending on the stability of the particular packing realization with which the dynamics starts. Enlarging the observation time and raising Γ (but not enough to have a full fluidization of the system) we can have $\tau_f \ll \tau_o \sim \tau_r$. The trajectory of the collective angle travelled in the cylindrical setup shown in Fig. 5.7b realizes this condition: we have many subsequent drifts with different amplitudes and durations. From this perspective we can refine the explanation of the different behaviours at different scales found in the MSD of the tracer (Par. 2.2.2) and the collective dynamics (Par. 3.1.2): the effect of lowering Γ is, on one hand, to supply less energy to the system (lower amplitude of the fast fluctuations) but, on the other hand, it makes τ_r larger allowing more steady drifts that increase the displacement of the collective variables with respect to a reference starting point. In this sense, the slowness of the re-arrangements makes the collective dynamics more persistent and in turn more efficient.

Chapter 6

Energy transfer to a dense granular system

In Par. 1.2.2 of chapter 1, we introduced the non-trivial relation between the properties of a NESS reached by a vibrated granular system and the parameters that characterize the external driving mechanism. In this thesis, we have been mainly interested in those properties that emerge over slow timescales as the superdiffusion and the slow drifts discussed in the previous chapters. Nevertheless, we want to dedicate this last chapter to fast variables showing that also in this realm one can find interesting non-equilibrium properties. An additional motivation for this study is that in all the setups considered in this thesis, the energy transfer to the system always occurs at the typical timescales of the external vibrations which are much faster than the ones of the collective motion. Contrary to the study of granular phases reported in Par. 1.2.3, that require the characterization of the density and the velocity fields, we concentrate on a very simple observable i.e. the total kinetic energy K of a dense vibrofluidized granular system. We will report the experimental and numerical results contained in [145].

6.1 Energy acquired VS energy injected

A fundamental open question in driven granular systems is how the dissipation mechanisms relevant for different dynamical behaviours are related to the external energy injection. These mechanisms involve several scales, from particle-particle collisions to the interaction with boundaries. From this perspective, the study of the relation between the system kinetic energy K and the external energy supplied to it represents a good framework to address this problem. Such a relationship involves the non-equilibrium response beyond the linear regime and affects fluidization properties of the granular medium, with important consequences in industrial applications [53], where usually energy is fed via mechanical vibrations with frequency f and amplitude A. As anticipated in Par. 1.2.3, if the driving signal is sinusoidal, a good adimensional parameter accounting for the input energy is the shaker strength $S = (2\pi f)^2 A^2/(gd)$. In some cases, a relation $K \sim S^\alpha$, with $S \sim (Af)^2$, has been derived [120, 111, 127, 214, 42]. Experimental studies focused on the specific role of the forcing mechanisms, such as vibration amplitude,

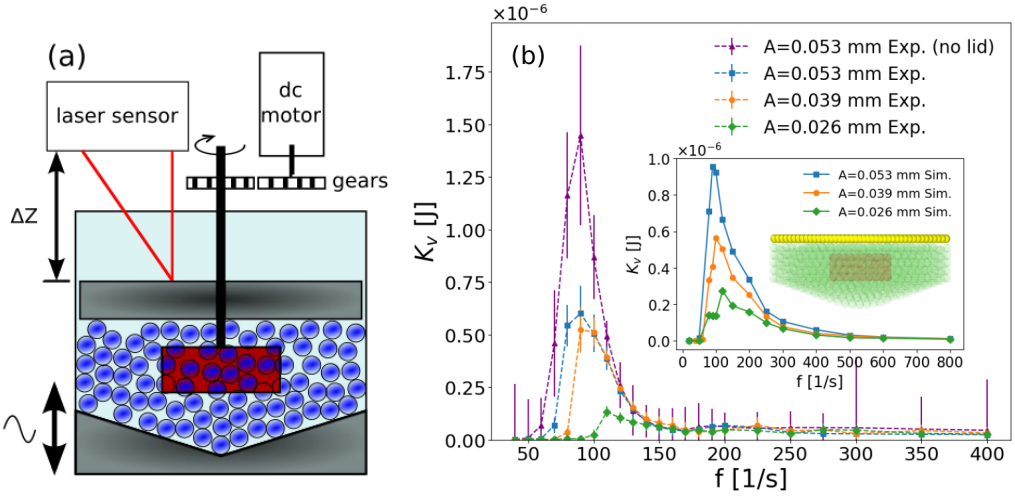

Figure 6.1. a: Experimental setup. A vane (red rectangle) is coupled to a dc motor and is suspended in the dense granular system of spherical particles. The container is vertically vibrated with sinusoidal oscillations of frequency f and amplitude A. On the top of the granular medium, there is a plate, whose vertical displacement ΔZ is measured with a laser sensor. b: Vane kinetic energy K_v in experiments as a function of f, for different values of A. Error bars are ± 1 standard deviation. The inset reports K_v measured in numerical simulations and a snapshot of the setup reproduced in silico. Numerical parameters $k_n = 12 \times 10^7$ Pa and $\gamma_n = 2.9 \times 10^7$ $(\mathrm{ms})^{-1}$. Rendering of the simulations realized with OVITO [188]. Images reprinted from [79, 145].

frequency or velocity [210, 211, 201, 79, 78, 115, 7, 80, 56]. In particular, an optimal frequency for energy transfer is found when the system is in a bouncing-bed state and A and f are varied keeping S fixed [210, 211]. In this state the granular medium detaches from the driving plate and a resonant behaviour is achieved via a synchronization between plate vibration and bed bouncing.

Here we consider a condition where the input energy S fed into the system is increased by increasing f (keeping A fixed). Our main result is a nonmonotonic behaviour of $K(S)$ observed in both the kinetic energy of a driven vane immersed in the medium and in the kinetic energy of the granular medium itself. We show that there is an optimal frequency where the system reaches maximum kinetic energy. Differently from previous results [210, 211], our system is not in a bouncing-bed or resonant state, and the granular internal energy is nonmonotonic with f, even if the energy input always increases. Our results can be interpreted as an example of negative specific heat, shedding light on the findings reported in [38]: Here, we investigate the complementary process, where the granular temperature decreases when the input energy increases.

6.2 Non-monotonic energy transfer and role of dissipation

Our results are obtained through an experimental/numerical setup (Fig. 6.1a) that is almost identical to the one described in Par. 2.1.1. There are two main dif-

ferences: (i) A rigid lid ($M_{\text{lid}} = 218$ g) covers the system to confine particles and to allow for a spectral analysis of the system oscillations in the experiments, (ii) The vane is subjected to a constant torque $\mathcal{T} = 6 \times 10^{-3}$ N m. Regarding the simulations, we follow the same protocol as the previous sections. We rebuild the experimental apparatus in silico through LAMMPS (see Fig. 6.1), then we validate our simulations by comparing the results for the tracer and finally we perform simulations without the tracer to focus on the granular medium properties. In this case, both in experiments and simulations the system is vertically shaken with a sinusoidal signal:

$$z_p(t) = A \sin(2\pi f t). \tag{6.1}$$

The numerical model used for the simulations is also here the Hertz-Mindlin one (Sec. 2.2.1). The values of the parameters used in the simulations are reported in appendix A; we point out that, for the purposes of this study, the relevant coefficients of the model are the stiffness of the non-linear contact k_n and the viscous damping coefficient γ_n.

Once turned on the shaker, the system reaches a steady state where the dc motor imposes to the vane an angular velocity $\Omega(t)$ that fluctuates around a non-zero value $\langle\Omega\rangle$. The behaviour of this last observable is related to the rheological response of the medium and is discussed in [79, 145]. Since we are mainly interested in the study of the total granular kinetic energy, we focus on the vane velocity fluctuations around the average: $K_v = I[\langle\Omega^2\rangle - \langle\Omega\rangle^2]/2$, where $I = 353$ g mm^2 is the momentum of inertia. Being interested in these fast timescales, we perform numerical simulations of ~ 60 s i.e. far shorter than in previous chapters. As shown in the rest of the chapter, K_v is a good proxy for the global granular energy.

In the right panel of Fig. 6.1 we report K_v measured in experiments as a function of f for different values of A. We also show a case with no lid to demonstrate the robustness of the observed behaviour. In the inset, we report results of numerical simulations showing that the model well reproduces the behaviour of the real system. The numerics allow us to investigate a wider range of vibration frequencies, $f \in (0, 1000]$ Hz, with respect to the experiments.

As shown in Fig. 6.1b, the vane kinetic energy is a nonmonotonic function of f (at fixed A): K_v grows abruptly from zero to a finite value at a frequency threshold f_1, related to the detachment condition [42], $2\pi f_1 = \sqrt{g/A}$. Then, after a maximum, K_v starts to decrease, signalling that the granular medium leaves the state of maximal fluidization, hindering the motion of the vane by an increased effective viscosity. One can define a so-called friction recovery frequency, $f_2 > f_1$, at which the system kinetic energy decays to about $1/2$ of its maximum value. This behaviour is related to dissipation mechanisms of the granular medium that depend on the viscoelastic properties of the material.

To better characterize the intrinsic behaviour of the granular medium and its response to the external vibrations, we exploit numerical simulations (without the suspended vane) focusing on the total translational kinetic energy (the rotational kinetic energy being negligible, see Fig. 6.3a) $K = \sum_{i=1}^{N} m\langle \boldsymbol{v}_i^2\rangle/2$, where $\boldsymbol{v}_i$ is the grain velocity.

In Fig. 6.2a we report $K(S)$, varying f at fixed A, for several values of γ_n. The nonmonotonic behaviour shows that the granular system reaches the maximal ki-

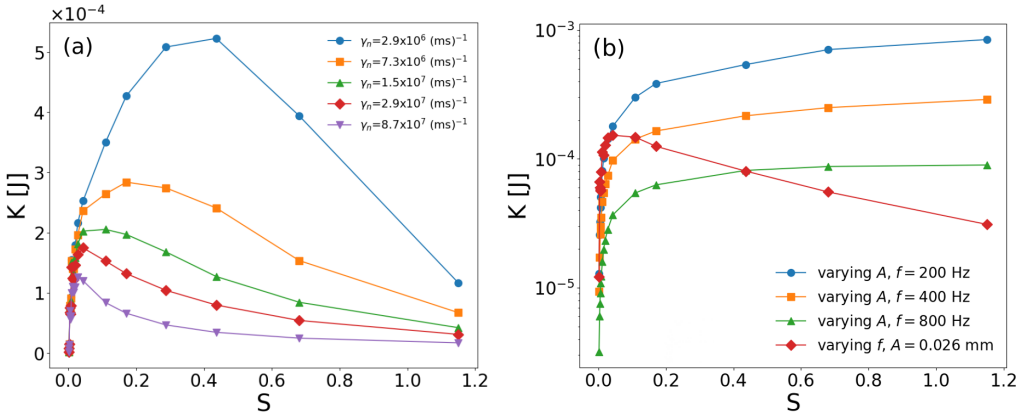

Figure 6.2. a: Total kinetic energy K of the granular medium versus S, varying f at fixed $A = 0.026mm$, for several values of γ_n, with $k_n = 6.1 \times 10^7$ Pa. b: The same quantity versus S, varying A for three fixed frequencies (200 Hz, 400 Hz and 800 Hz), and varying f for one fixed amplitude (A=0.026 mm). Parameters are $k_n = 6.1 \times 10^7$ Pa and $\gamma_n = 2.9 \times 10^7$ (ms)$^{-1}$. Images reprinted from [145].

netic temperature at an optimal value of the input energy. When the input energy exceeds a certain threshold, related to f_2, the system cools down because the dissipation effects increase. A key result is represented by the maximum position of the kinetic energy for different values of viscous damping coefficient γ_n. We find that the peak shifts to the left when the dissipation in the system is increased. It is interesting to note that this shift doesn't occur if we vary k_n signalling that the friction-recovery mechanism is not governed by the elastic contribution of the interaction (see Fig. 6.3b). Therefore the system can transfer more energy to the grain motion when it is vibrated at an optimal frequency. If the frequency increases, the overall external energy injected is larger but the dissipation mechanisms become dominant and the granular kinetic temperature decreases. This behaviour can be interpreted as an instance of negative specific heat [213, 38], occurring due to the subtle interplay between forcing and dissipation. Conversely, if we increase S by increasing A at fixed f, we find a monotonic behaviour. Namely, dissipative mechanisms are not activated and the kinetic energy keeps growing with the input energy as shown in Fig. 6.2b. These features are a consequence of the permanent contact with the driving plate, which makes dissipation dominate at high frequencies. This is a novel phenomenon different from the resonant behaviour in the bouncing-bed state clearly described in Ref. [210, 211], where the optimal frequency is an increasing function of dissipation. Striking differences are also provided by the spectral analysis of the top plate oscillations which indicates that, in our system, the energy transfer is not maximized in the most coherent states (see Par. 6.5.1).

6.3 Single-particle dynamics

The macroscopic features above described can be related to microscopic properties by investigating the single-grain dynamics. As already discussed in Par. 3.1.3, in dense systems, the diffusive motion of a single particle is hindered by the presence

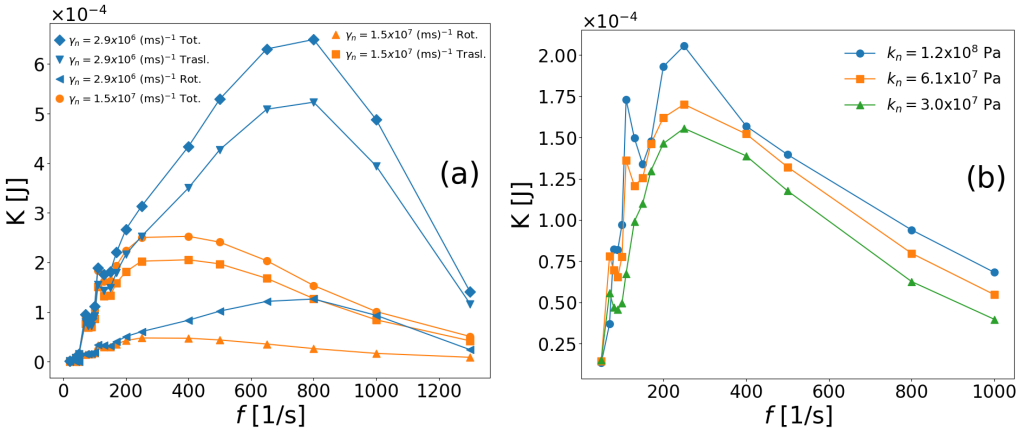

Figure 6.3. Mean translational kinetic energy of the whole system K versus the driving frequency f at fixed $A = 0.026$ mm. a: Comparison between the translational kinetic energy, the rotational one and the total (translational plus rotational). We show two curves reported in Fig. 6.2a as a function of f, instead of S. The rotational degrees of freedom follow the same non-monotonic behaviour but with smaller absolute values so that their contribution does not affect the qualitative behaviour of the total kinetic energy. b: Study of the mean kinetic energy for different values of non-linear stiffness: k_n is varied at fixed $\gamma_n = 2.9 \times 10^7$ $(\mathrm{ms})^{-1}$. The three curves have the same shape (the peak position doesn't change) but are vertically ordered by k_n. This implies larger kinetic energy and therefore less dissipation in the system with higher stiffness. Images reprinted from [145].

of many surrounding particles, inducing a cage effect [175, 144, 77]. Focusing on the MSD of a particle, one observes that, after a ballistic motion at short times, a plateau develops, signalling that the particle is trapped inside a cage. Then, at longer times, the particle manages to explore a larger region of the system and its MSD grows linearly in time. The relevant quantities are the cage size S_c and the trapping time inside a cage τ_c, both estimated from the first point of the MSD after the ballistic regime.

This picture is fully supported by Fig. 6.4a, where we show the MSD (averaged over about 20 particles randomly chosen in the system) in the horizontal XY plane, the plane relevant for the vane's motion. Rescaling time by the trapping time τ_c and the MSD by the squared cage size, we find that curves collapse.

The nonmonotonic behaviours described above for K_v and K can be rationalized by the study of S_c and τ_c, as reported in the insets of Fig. 6.4b. We find that τ_c is a decreasing function of the frequency, $\tau_c \sim f^{-0.67}$, whereas S_c is a nonmonotonic function of S, varying f at fixed A, with a maximum at $S \simeq 10^{-2}$. At low frequencies, the cage size tends to be very small but the particles need a long time to be trapped. Conversely, at high frequencies, cages are still small but the particles are trapped in a short time. Moreover at low frequencies, since the system is weakly perturbed by the input energy, a particle can explore larger regions for increasing S. However, for larger S (increased through f), collisions become more frequent and the explored cage region decreases accordingly. If we estimate the average particle speed v_{XY} on the XY plane as $v_{\mathrm{XY}} \sim S_c/\tau_c$, we find a nonmonotonic behaviour, in agreement with the behaviour of K (Fig. 6.4b). This analysis shows that the single-

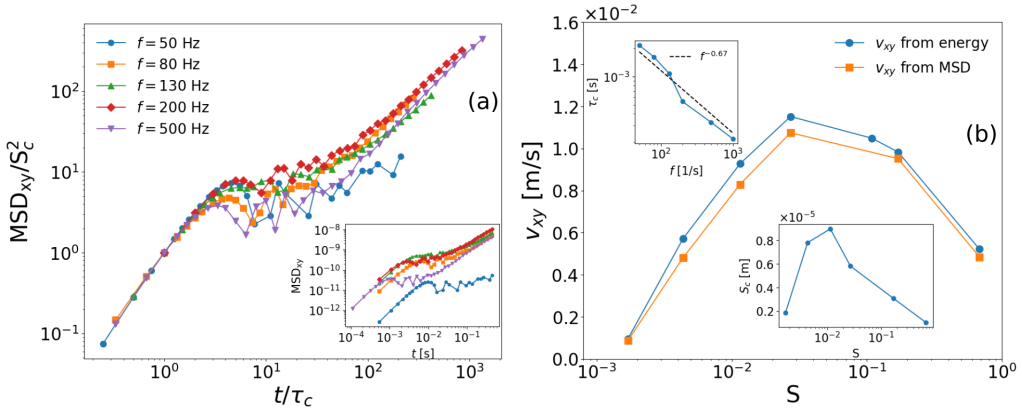

Figure 6.4. a: Single-particle MSD in the XY plane rescaled by the square of the cage size versus the time in units of τ_c, for different values of the driving frequency. Inset: single-particle MSD in the XY plane versus time. b: Comparison between the average particle speed in the XY plane obtained from the mean kinetic energy of the whole system (circles) and from the ratio between the cage size S_c and the trapping time τ_c (squares). Bottom inset: S_c as a function of the input energy S, varying f at fixed A. Top Inset: τ_c as a function of f. Simulation parameters for both panels are $A = 0.026$ mm, $k_n = 6.1 \times 10^7$ Pa and $\gamma_n = 2.9 \times 10^7$ $(\text{ms})^{-1}$. Images reprinted from [145].

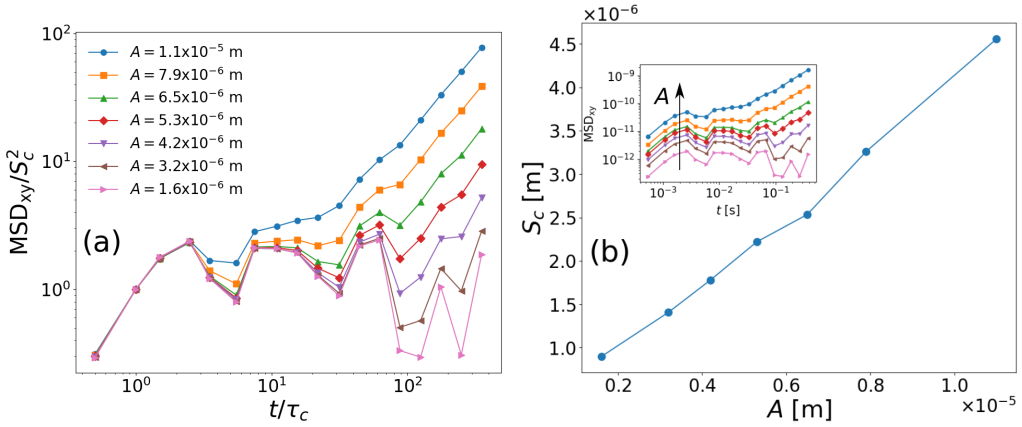

Figure 6.5. a: Single-particle MSD in the XY plane rescaled by S_c^2 as a function of the rescaled time t/τ_c. Different curves correspond to different driving amplitudes while the frequency is fixed at $f = 200$ Hz. b: Size of the cage S_c versus the driving amplitude A. The inset shows the MSD not rescaled. Simulations with $k_n = 6.1 \times 10^7$ Pa and $\gamma_n = 2.9 \times 10^7 (\text{ms})^{-1}$. Images reprinted from [145].

particle dynamics reflects the same phenomenology occurring at the macroscopic scale. Moreover, the nonmonotonic behaviour of S_c could be related to a change in the effective number of degrees of freedom in the system as the input energy is varied, in agreement with the explanation of negative specific heat suggested in Ref. [38] for cooling granular gases of aggregating particles (see Par. 6.5.2).

We show in Fig. 6.5 the rescaled MSD on the xy-plane averaged over 20 particles and the relative cage size S_c for different values of A. Here we see that the collapse is very good up to time $t/\tau_c \sim 1$ (so the trapping time τ_c does not vary with A) while

S_c (and consequently the speed $v_{xy} = S_c/\tau_c$) grows monotonically with the driving amplitude. These last results show that the same phenomenology as a function of A at fixed frequency is present both at the macroscopic scale (K) and at the single-particle one (v_{xy}).

As a remark, we note that in the MSDs of Fig. 6.5 and 6.4 there is not evidence of the long memory effect due to the slow collective drift (Sec. 3.1.3). We verified that, with the top lid and for the typical driving parameters used for this study ($f \in [20, 1300]$ Hz, $A \in [0.014, 0.026]$ mm), the collective motion is still present but far weaker so it is not visible on observation times of ~ 60 seconds. We believe that this is due to the very small driving amplitudes (i.e. one order of magnitude lower than the one used in Chap. 2 and 3). Although in the previous chapters we had shown many times that the drift is strengthened for low drivings, it cannot be true in the limit $\Gamma \to 0$ limit. We expect that below a given Γ, reducing the amplitude implies a reduction of the drift magnitude as suggested by the study of ordered packing with defects in Fig. 5.3a.

6.4 The generalized driven-damped oscillator

Here we present a generalized model of a driven-damped oscillator that reproduces qualitatively the phenomenology of K studied in the simulations. In particular, our model shows i) a nonmonotonic behaviour of the energy as a function of the driving frequency f with a maximum in f^*; ii) an increasing behaviour of the energy as a function of the driving amplitude A; iii) the shift to the left of the frequency f^* when the dissipation in the system is increased.

The model is obtained starting from an equation of motion for a generic particle in the system and then assuming that the energy of the whole system follows the same behaviour of that of the single particle. This assumption is consistent with the previous analysis that shows a common phenomenology of single-particle quantities and macroscopic ones. In addition, the same assumption is done in experiments of positron emission particle tracking (PEPT) where the time-averaged behaviour of a single tracked particle is considered representative of that of the global system. This technique is the one used in [210, 211].

6.4.1 Newton equation for a caged particle

The granular system is very dense in all regimes of shaking, so the short-time dynamics of the grains is expected to take place inside their cages formed by the surrounding particles. This short-time dynamics presents multiple relevant timescales such as the one represented by the integration time dt ($\tau_1 \sim 10^{-5}$ s), that is a fraction of the duration of a single collision, and the one fixed by the inverse of the driving frequency $\tau_d = 1/f \sim 10^{-3} - 10^{-1}$ s. A third one is represented by the average time between two collisions, reported in Fig. 6.4b (but also observed for the XYZ diffusion), which spans values in the range $\tau_c \sim 10^{-4} - 10^{-3}$ s. These timescales are thus ordered as follows: $\tau_1 < \tau_c < \tau_d$ for all the cases presented in our study. To estimate the mean kinetic energy over many collisions, we are interested in a time coarse-graining on a scale larger than τ_c. At the same time, we want to write a differential equation for the coordinates of a particle in which the

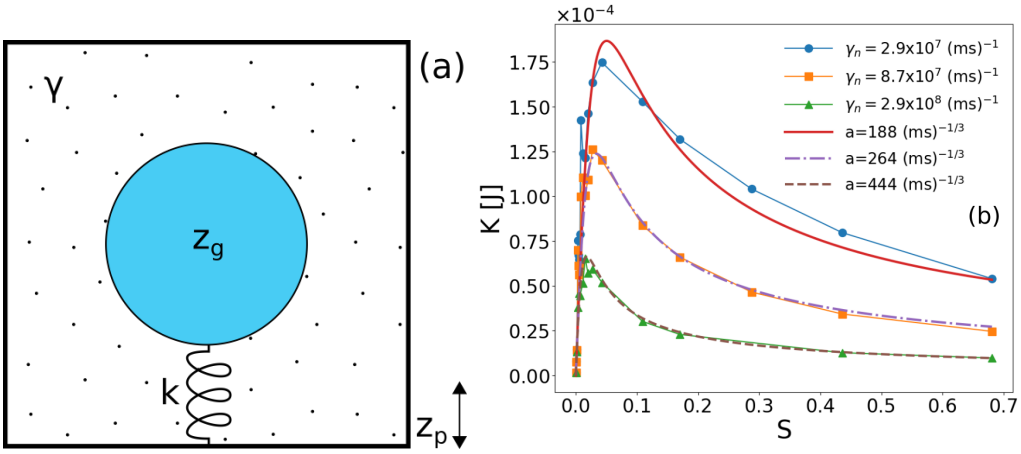

Figure 6.6. a: Coarse-grained description of the single-particle dynamics. The springs k and the viscosity γ represent the cage that mediates the vibration of the shaker. b: Mean kinetic energy from Eq. (6.5) for different values of a, with $2\pi f_k = 11905$ s^{-1}, $A = 0.026$ mm and $m_{\text{eff}} = 912.6$ g, compared with K measured in numerical simulations with $A = 0.026$ mm and $k_n = 6.1 \times 10^7$ Pa. Images reprinted from [145].

shaker dynamics appears as an external driving. In view of these arguments, we concentrate on timescales larger than τ_c but smaller than τ_d. To make our model as simple as possible we only consider the motion in the z direction. Therefore we consider a single particle of mass m confined in a one-dimensional cage that consists of one spring of stiffness k with a resting length l_0 connected with the bottom of a vibrating box. The latter really represents the experimental/numerical container that oscillates following $z_p(t) = A\cos(2\pi ft)$. The fact that the cage is made of fast vibrating particles also induces an effective viscosity with coefficient γ.

Our simplified coarse-grained description is sketched in Fig. 6.6a where we refer to the coordinate of the grain as z_g. We remind here that the coefficients of the HM model used in the simulation (k_n and γ_n) depend on the material properties and act on the fast timescale τ_1. How they are connected with the effective viscosity γ and stiffness k is not trivial. A reasonable value for k can be estimated considering that the modelled spring is actually made by a column of grains. Every grain with radius r and Young modulus Y can be thought of as a microscopic vertical spring with an elastic constant $\tilde{k}$ given by $\tilde{k} = \pi Yr/2$ (for simplicity we are considering the grains as cylinders instead of spheres). Now the effective stiffness of the column results from the parallel of a mean number $\bar{n}$ of such microscopic springs: $k = \tilde{k}/\bar{n}$. For the parameters of our simulations and fixing $\bar{n} = 4.5$ we find that $k \sim \mathcal{O}(10^5)$ N/m. Regarding the effective viscosity, we will do an ansatz in the following. Looking at Fig. 6.6a, it is straightforward to write for z_g:

$$\ddot{z_g}(t) + 4\pi f_s \dot{z_g}(t) + (2\pi f_k)^2 \xi(t) = 0, \tag{6.2}$$

where $\xi(t) = z_g - z_p - l_0$, $2\pi f_s = \gamma/(2m)$ and $2\pi f_k = \sqrt{k/m} \sim \mathcal{O}(10^4)$ s^{-1}. Now we come to the crucial hypothesis of our approach, i.e. the ansatz on f_s. Some previous studies [79, 210] suggest that the dissipation of energy due to interparticle collisions increases significantly when the driving frequency f grows. This is also visible in our data from Fig. 6.4b, where we see that τ_c becomes smaller for increasing f.

Indeed, a reduction of the time between collisions means a growth of the number of dissipative events in the system (i.e. the collisions themselves). The simplest way to insert this dependence of the internal dissipation on the external driving is to take f_s as an increasing function of f: $f_s = af^\alpha$ with $a, \alpha > 0$. Bringing the variable $z_p(t)$ contained in $\xi(t)$ to the right-hand side of Eq. (6.2) and adding gravity, we obtain the following equation:

$$\begin{aligned} & \ddot{z_g}(t) + 4\pi a f^\alpha \dot{z_g}(t) + (2\pi f_k)^2 z_g(t) \\ = \; & (2\pi f_k)^2 A\cos(2\pi f t) + (2\pi f_k)^2 l_0 - g. \end{aligned} \tag{6.3}$$

This is the equation for a driven-damped harmonic oscillator with characteristic frequency f_k, viscous constant $4\pi a f^\alpha$ and external driving $(2\pi f_k)^2 A\cos(2\pi f t)$ that oscillates around the equilibrium position $z_g^{eq} = l_0 - g/(2\pi f_k)^2$. The stationary solution of Eq. (6.3) is:

$$\begin{aligned} z_g(t) &= \frac{f_k^2 A}{\sqrt{(f_k^2 - f^2)^2 + 4a^2 f^{2(\alpha+1)}}} \cos(2\pi f t - \phi) + z_g^{eq}, \\ \phi &= \arctan\left(\frac{2a f^{\alpha+1}}{f_k^2 - f^2}\right). \end{aligned} \tag{6.4}$$

Deriving $z_g(t)$, taking the square and then integrating over a period $1/f$ we can find the mean quadratic velocity of the particle:

$$\langle \dot{z_g}^2 \rangle = \frac{\frac{1}{2} A^2 f_k^4 (2\pi f)^2}{4a^2 f^{2(\alpha+1)} + \left(f_k^2 - f^2\right)^2}. \tag{6.5}$$

As showed in Fig. 6.6b for the specific value $\alpha = 2/3 \sim 0.67$ taken from the behaviour of τ_c (but it holds in general for $\alpha > 0$), $\langle \dot{z_g}^2 \rangle$ has a nonmonotonic behaviour for $f < f_k$ and its maximum value shifts to the left as a is increased. In Fig. 6.6b we show the behaviour of the mean total kinetic energy $K = m_{\text{eff}} \langle \dot{z_g}^2 \rangle / 2$ as a function of S, for several values of a. From a fitting procedure, we found $2\pi f_k = 11905\ s^{-1}$, which is of the order $\sqrt{k/m}$ if the effective stiffness k is estimated by considering series-parallel microscopic elastic constants relative to the grain material, as above illustrated. The prefactor m_{eff} represents an effective mass and we find an optimal agreement with data for $m_{\text{eff}} = 912.6$ g, which is of the order of the total mass of the system. Therefore, the driven damped oscillator model with a frequency-dependent viscosity predicts the general phenomenology of the 3D granular system, with a good quantitative agreement for high values of γ_n.

6.5 Physical interpretation of the phenomenon

Once reported the experimental/numerical analysis of the observed non-monotonic energy transfer together with the good agreement between data and predictions of the generalized driven damped oscillator, here we discuss some relevant aspects of its physical interpretation. We first explain why this phenomenon cannot be interpreted as a simple resonance and how it deviates from apparently similar results of some previous studies. Then, we provide some arguments that suggest the interpretation

of the decreasing trend for $f > f^*$ as an instance of negative specific heat. Finally, we discuss the connection between the fast variables considered in this chapter and the long memory effects discussed in the previous ones.

6.5.1 Beyond a simple resonance

What we have shown in the previous sections can remind the phenomenology of a broad vibrational resonance. Nevertheless, many arguments coming from both the analytical model and the experimental data suggests a quite different interpretation.

Eq. (6.5) has a very simple form and its nonmonotonic behaviour can be explained in terms of competitive mechanisms. From Eq. (6.5) we see that the mean quadratic velocity of the particle is proportional to the input energy of the shaker divided by an adimensional factor: $\langle \dot{z_g}^2 \rangle = V(f)/U(f,\alpha)$ where $V(f) = \frac{1}{2}A^2(2\pi f)^2$ is proportional to the strength of the shaker $S = (2\pi f)^2 A^2/(gd)$ while $U(f,\alpha) = u_1 + u_2$. Here $u_1(f,\alpha) = 4a^2 f_k^{-4} f^{2(\alpha+1)}$ and $u_2(f) = (1 - f^2/f_k^2)^2$ can be considered the two competitive terms if $f < f_k$. In this regime, u_2 is a decreasing function of f and enhances energy transfer, while u_1 (that contains the dissipation) increases with f and therefore has an opposite effect. In order to better understand the underlying mechanisms, we remind that for an ordinary driven-damped oscillator (namely with a viscous coefficient that does not depend on f) the mean quadratic velocity is the same as Eq. (6.5), with the only difference that the dissipative term is proportional to the square of the rescaled driving frequency: $u_1 = u_1(f,0)$. From this point of view, $1/u_2$ can be interpreted as an energy gain factor: It grows before the resonant frequency ($f = f_k$) and then decreases. In the case of the ordinary damped oscillator, therefore, the nonmonotonic behaviour is entirely explained by the nonmonotonic behaviour of u_2 alone, indeed dissipation does not change the peak position but only smoothes it. On the contrary, when $\alpha > 0$ the nonmonotonic behaviour has a different origin, coming from the competition between dissipation (u_1) and gain (u_2). This can be rigorously checked, deriving Eq. (6.5) to find the condition for the maximum:

$$f_k^4 - f^4 - 4\alpha a^2 f^{2(\alpha+1)} = 0, \tag{6.6}$$

that turns out to be satisfied by $f = f_k$ only for $\alpha = 0$. The competition is apparently present also in the ordinary driven-damped oscillator but in that case it is balanced by the $(2\pi f)^2$ contained in $V(f)$ at the numerator in such a way that the nonmonotonic behaviour of the energy can be explained only by the resonance. We finally note that another way to see competitive terms in Eq. (6.5) is to rewrite it as $\langle \dot{z_g}^2 \rangle = (u_1/V + u_2/V)^{-1}$. In this form we have the inverse of a sum of two terms that, for $f < f_k$, depend in the opposite way and with different powers on f. This clearly gives rise to an extremal point also in the limit $f \ll f_k$, that is consistent with the values of the fitted parameters.

We stress that these mechanisms substantially differ from the standard resonance phenomenon, due to the presence of the damping term $f_s \sim a f^\alpha$. Indeed, an increase of f induces the grains to absorb the injected energy in a faster-vibrating motion, experiencing a larger number of collisions (dissipative events) per unit of time. This means that at higher f, both the energy input and the energy output increase. The two phenomena compete and, because of their different functional

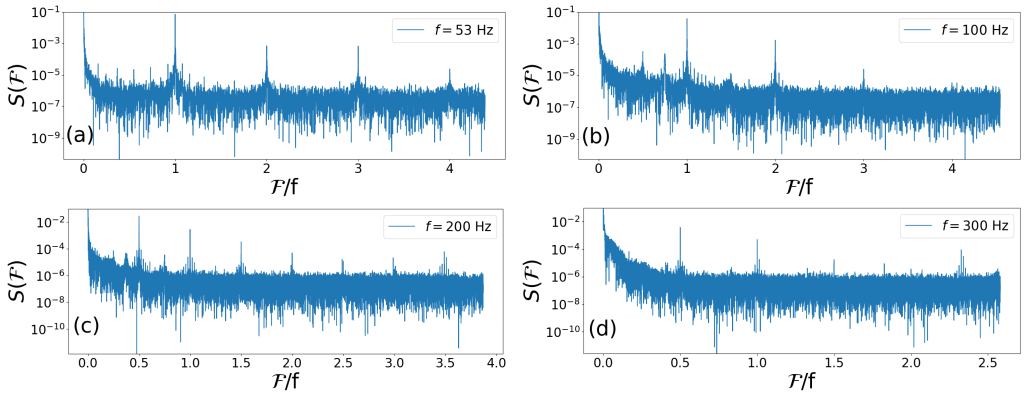

Figure 6.7. Experimental data for the spectra of the vertical z-coordinate of the top plate for different shaking frequencies f and $A = 0.053$ mm. Images reprinted from [145].

dependencies upon f, an extremal point appears. We note that the maxima in the curves of Fig. 6.2 and 6.6 occur at frequencies much smaller than the fitted f_k. Conversely, the ordinary resonance always occurs at the fixed characteristic frequency f_k, independently of the viscous coefficient. For $\alpha > 0$, the dissipation controls the position of the peak, reproducing the key feature of molecular dynamic simulations. Evidence about the difference between the phenomenon reported here and a resonance comes also from experimental data. In Fig. 6.7, we show the spectra of the z-coordinate (measured with a laser sensor, see [79] for details) of the top plate for different values of the driving frequency f and $A = 0.053$ mm. This figure sheds light on the relationship between chaotic motion and energy transfer in our system. We see that the most coherent motion (pronounced peaks on the driving frequency and its harmonics) is obtained for $f = 53$ Hz (panel a), before the energy maximum. Around the driving frequency where our maximum in the energy occurs (panel b, $f = 100$ Hz), we see that the peaks on the harmonics are less pronounced and more broadband. For increasing driving f (decreasing transferred energies), we see a more and more chaotic spectrum with the appearance of distinct peaks at non-integer multiple of f (panel c) and the disappearance of the peaks in the harmonics (panel d). Our scenario, therefore, is that of an increasing chaoticity - with f - of the granular dynamics, irrespective of the energy transfer, i.e. both before and after the energy maximum. This is quite different from the one observed in [210, 211] where the energy transfer to the system is optimized at the frequency such that the granular system is more regular and shows the most defined peaks in its spectrum. A more detailed discussion about the deviations of our results and the one of [210, 211] is reported in [145].

6.5.2 An instance of negative specific heat

Once provided arguments about the non-resonant origin of the phenomenon under study, we want to highlight its relation with other counter-intuitive phenomena, forbidden by standard thermodynamic arguments, that can occur in non-equilibrium systems. Negative differential mobility and negative specific heat are typical examples [26, 171, 213, 38]. This kind of nonmonotonic behaviour in the current-force

relation is due to the combination of competing mechanisms. It is worth mentioning two relevant previous studies where negative specific heat has been claimed. The first one [213] regards a minimal model with three non-degenerate energy levels $0 \leq \epsilon_0 < \epsilon_1 < \epsilon_2$ where the transitions are defined following the Metropolis rates: $R_{ij} = \min[1, e^{(\epsilon_i - \epsilon_j)/k_b T_{ij}}]$ with different temperatures T_{ij}. By forbidding the $0 \leftrightarrow 1$ transition and taking T_{02} fixed to a sufficiently small value, the system is driven into a steady-state where the total energy decreases by increasing T_{12}. The trick here is that the population growth of the high-energy state ϵ_2 obtained raising T_{12} brings to an effective growth of ϵ_0 because the $2 \to 0$ transition is weakly counterbalanced by the very cold bath. The second relevant study regards a free granular gas of aggregating particles [38]. A combined approach of numerical simulation and kinetic theory showed that despite the gas being in a cooling state where total energy $E(t)$ decreases in time, the energy per particle $E(t)/N(t)$ (i.e. the kinetic temperature) increases. This is possible because the aggregating dynamics can reduce the total number of particle clusters $N(t)$ faster than the energy loss rate.

We point out that our study unveiled a similar case of competing effects in a dense many-body system with dissipative interactions: The interplay between external forcing and internal dissipation in granular media can result in a nonmonotonic behaviour of the system kinetic energy as a function of the input energy, representing an instance of negative specific heat. This arises at different scales, from rheological behaviour (tracers dynamics) to single-particle motion. Moreover, our analysis explains the important role played by the vibration frequency, triggering specific dissipation mechanisms. In a nutshell, what is happening at high frequencies is that the system has a greater amount of available energy but is forced to adsorb it less efficiently. This is also confirmed by the model we propose: by simply modifying a driven-damped oscillator with a frequency-dependent viscous parameter, we recover the behaviour observed in experiments and simulations. We finally remark that the occurrence of negative specific heat in this system may have a deep impact on applications in several fields related to granular matter physics.

6.5.3 Fast timescales and collective motion

The behaviour of the granular system under study on fast timescales is not the main focus of the thesis, nevertheless, we mentioned it many times. Indeed, in presence of the collective motion, the grains overall dynamics can be described as a superposition of fast vibrations around an almost fixed position with respect to the neighbours and the slow drift coherently shared by the whole system. Although the model for the collective variable proposed in Par. 3.2.3 consists of two independent stochastic processes each with its thermostat, we are aware of the fact that the real energy injection occurs on fast timescales (i.e. the characteristic time of the driving mechanism $\sim 10^{-2}$ s). If the transferred energy is too high, the system fluidizes losing the property of having a slow rearranging structure that allows the formation of slow drifts. From this point of view, the energy adsorption on fast timescales results to be strictly related to the possibility for the system to exhibit the slow collective motion. These last remarks together with the analysis reported in the previous sections suggest that the driving frequency f can have an intriguing role also for the dynamics of slow timescales (we recall that in the other chapters

we always vary Γ through A). The behaviour of S_c in Fig. 6.4b showed that, after a certain threshold, raising f helps the compaction of the system. We then expect for this control parameter an opposite effect with respect to A for what concerns memory effects. A systematic study of that is still lacking but represents an immediate perspective.

Conclusions and perspectives

Writing conclusions is often weird: It makes you think about what you thought in the past. That can cause a scientific identity crisis. At the end of his book, *"Of Flies, Mice, and Men"* [96], the Nobel prize for medicine Francois Jacob (1920-2013) tells about "day science" and "night science". The first expression refers to the scientific process as it is told in retrospect: *"[...] a well-ordered series of ideas and experiments linked in strict logical sequence."* The "night science", instead, includes all the dead ends and the uncertainties one inevitably runs into when doing research. Calculations started with wrong assumptions, numerical artefacts mistaken for good results, misinterpretation of experimental data are just some examples of that. Despite the frustration that these wrong turns imply, it is not straightforward for me to simply judge them as useless. Still having doubts about this, I just want to mention that behind this thesis there is a lot of "night science".

However, since this is a PhD thesis and not an early 20th-century European novel, we will conclude with the "day science" approach.

Summary of the results

We investigated the emergence of slow timescales in dense vibrofluidized granular materials by means of numerical simulations and theoretical models. The application of the discrete element method (DEM) allowed us to reproduce in silico a 3D experimental setup used to study the rotational diffusion of a tracer suspended in a vertically vibrated cylindrical container filled with a dense granular fluid. The most relevant experimental result namely the occurrence of long memory effects for sufficiently low drivings has been observed with good agreement also in the numerics. These effects manifest in the tracer dynamics as a low-frequency decay in the velocity power spectral density (VPSD) and superdiffusion at late times in the mean squared displacement (MSD). The study of the grains trajectories made possible by simulations led to the discovery of collective behaviour of the granular medium that is the origin of the anomalous diffusion of the intruder. It consists of a global slow rotation of the whole granular system that can persist over extremely long timescales i.e. about four orders of magnitude larger than the collision time. We identified the average angular velocity of the grains as the representing collective variable and we characterized it as the sum of two independent Ornstein-Uhlenbeck processes with two well-separated characteristic times. This has been the starting point to develop a phenomenological model made of three linearly coupled stochastic differential equations that correctly reproduces the numerical/experimental VPSD and

MSD of the tracer. A parallel modelling approach was proposed in order to explain the emergence of slow timescales without introducing them empirically. We considered a 1D lattice with a velocity field undergoing viscous interactions defined on it. By coupling this lattice with Brownian baths only at the boundary sites we incorporated in a multivariate Ornstein-Uhlenbeck process three main characteristics of dense vibrofluidized granular materials: i) frictional interaction, ii) permanent contacts, iii) non-homogeneous energy injection. At the cost of this greater abstraction in the description of the system, we obtained analytical predictions of power-law decaying correlation functions and timescales diverging with the system size. We have shown that these properties are not hindered by localization phenomena induced by random couplings.

All the aforementioned results share a missing ingredient i.e. they do not consider the role of the spatial configurations in which the granular system remains stuck when vibrated at low drivings. We addressed this problem by DEM simulations of a simplified 2D setup that reduces the emergence of the collective motion to its essential ingredients. We showed that a steady drift is generated in correspondence to a persistent spatial symmetry breaking induced by disorder or asymmetric defects in the bulk structure. The extremely slow exploration of the configurational space through rare re-arrangements during the dynamics makes these drifts very long. The observed interplay between friction and structural asymmetries in addition to the complex behaviour of the drifts velocity as a function of the external driving suggest the interpretation of this phenomenon as a ratchet effect. A minimal model of a ratchet in a stick-slip moving potential corroborates this intuition. We also provided strong evidence that this mechanism underlies also the collective rotations observed in the realistic 3D system.

We also considered that, in all the analysed setups, the energy stored in the collective mode is always supplied to the system on much faster timescales (i.e. the typical ones of the external driving). Because of this, a study on the energy transfer to a dense vibrated granular packing has been provided at the end of the thesis. There we report the numerical evidence of a shaking regime where the internal kinetic energy of the system is a decreasing function of the injected one if the last is raised by varying the driving frequency. A modified driven damped oscillator model with a frequency-dependent viscous constant reproduces the observed phenomenology.

Open questions and future outlooks

During the thesis, we stressed many times the presence of open questions and possible future perspectives stimulated by our research. Here we collect them together and propose some additional ones.

Conserved momentum

The numerical study of the cylindrical setup with conserved momentum still presents many unresolved issues (Par. 3.1.4). First of all, the presence of a marked backscattering peak in the VPSD of the collective variable. An intriguing perspective is that such a broad resonance could be related to the conversion mechanisms between

translational and rotational momentum. A more systematic analysis is needed to explore this scenario. The presence of an unexpected slow component in the averaged motion of the diffusing grains has to be further investigated too. Moreover, without tangential interaction with the walls, the presence of long memory effects in the rotational degrees of freedom is even more important for the drift formation because of the constraint of conservation. This, together with the analysis of single-particle rotations (appendix E), makes clear that the relationship between individual and collective memory deserves further study.

Estimate of a granular correlation length

The phenomenological models proposed in Sec. 3.2 could be used to estimate a correlation length of the granular system from numerical data. We propose the following procedure. One can independently fit the parameter $\tau_i(l)$, $q_i(l)$ of the local velocity field calculated over regions of different sizes l in a blade free simulation. A useful definition could be for example $\Omega_c(l) = \mathcal{N}_l^{-1} \sum_i \dot{\theta}(t, \mathbf{r}^i_{xy}) \Theta(l - |\mathbf{r}^i_{xy}|)$ where $\mathcal{N}_l = \sum_i \Theta(l - |\mathbf{r}^i_{xy}|)$. Then, for each l, a fit of the vane VPSD with a reduced number of free parameters (i.e. three instead of seven) can be performed. Finally, one has to verify for which value of l the best fit occurs. An alternative method would be the data-driven approach of [21] using numerical data of both the collective variable and the vane.

Relation between fast and slow timescales

The mechanism of external energy supply treated in Chap. 6 has to be extended in a wider region of the (A, f) plane. Moreover, we want to test the possibility to ease the formation of global rotations through the high-frequency compaction of the system. In general, the transfer of energy from the fast timescales of the driving to the slow ones of the drifts has still to be understood and characterized.

Extension and conceptual relevance of the lattice model

An important extension of the granular lattice model (Chap. 4) is the reintroduction of the positional dynamics. As explained in appendix C.5, the corresponding mathematical structure is relevant also for active systems. Another point to be clarified is whether the slow collective dynamics predicted by the lattice model is related to the one observed in the realistic setups. As discussed in Par. 4.3.1 and 5.4.1, the real system and the idealized one share many essential ingredients except for a very important one i.e. the spatial symmetry breaking which is not included in the model. Nevertheless, the realistic drift could be also interpreted as a singular response of the granular packing being in an NHHP-like critical point. A numerical experiment for the future to verify this scenario has been outlined in Par. 5.4.1.

The role of system size and disorder

The numerical study of the 2D setup (Chap. 5) made clear the role of spatial configurations for the formation of slow collective drifts opening up a number of interesting questions. For example, the effects of the system size on the magnitude

of the drift is a non-trivial problem since the origin of the collective motion and the resistance against it both can depend upon bulk volume (through the concentration of defects) and upon external surfaces (through friction). Another important issue concerns the role and the characterization of disorder. Which are the right observable of the force and contact networks to look at in order to better predict the magnitude and the verse of the drift at a given Γ? Is the structure alone sufficient to do such a prediction? We argue that these problems can be an interesting testing ground for the application of machine learning techniques.

Appendices

Appendix A

Tables of parameters for numerical simulations

In this appendix, we report tables with the numerical values of the parameters used for the DEM simulations discussed in the different chapters of this thesis. Basically, the majority of them are the same in all cases but depending on the particular purpose of the numerical analysis some has been varied. The superscript $s(p)$ refers to parameters that mimic the properties of steel(plexiglass). We recall here that the Young modulus of steel and plexiglass has been reduced of 3 and 2 orders of magnitude respectively (see Par. 2.2.1).

Simulations for chapters 2 and 3

Y^s	210 Mpa	ν^p	0.37
ν^s	0.293	μ^{sp}	0.5
μ^{ss}	0.5	k_n^{sp}	617×10^5 Pa
k_n^{ss}	153×10^6 Pa	k_t^{sp}	$[73 - 132]\times10^6$ Pa
k_t^{ss}	$[190 - 355]\times10^6$ Pa	γ_n^{sp}	$[3.1 - 12]\times10^6$ $(\mathrm{sm})^{-1}$
γ_n^{ss}	3.1×10^4 $(\mathrm{sm})^{-1}$	γ_t^{sp}	$[1.0 - 1.6]\times10^5$ $(\mathrm{sm})^{-1}$
γ_t^{ss}	$9.3\times[10^1 - 10^3]$ $(\mathrm{sm})^{-1}$	t_{ray}	6.75×10^{-5} s
Y^p	[33 - 50] Mpa	dt	1.35×10^{-5} s

Table A.1. Numerical values of the parameters used in the simulations discussed in Chap. 2 and Chap. 3: conical-shaped based cylindrical setup with and without the free vane. Simulations of the conical-shaped based cylindrical setup with and without the free vane. Intervals in square brackets refer to parameters that have been varied (up to also unphysical values) to test the robustness of superdiffusion and collective dynamics with respect to a change of the model details (not reported in this thesis). Despite the real vane is made of plexiglass, it interacts with the grains with the steel-steel interaction parameters due to a limitation of a previous version of the LAMMPS granular package. Probably, some quantitative disagreement between experiments and simulations for the intruder dynamics may be ascribed to this artefact. The *sp* parameters refer to the grain-boundaries interactions.

Simulations for chapters 5

Y^s	210 Mpa	ν^p	0.37
ν^s	0.293	μ^{sp}	0.5
μ^{ss}	0.5	k_n^{sp}	617×10^5 Pa
k_n^{ss}	153×10^6 Pa	k_t^{sp}	725×10^5 Pa
k_t^{ss}	190×10^6 Pa	γ_n^{sp}	1.2×10^7 $(\mathrm{sm})^{-1}$
γ_n^{ss}	3.1×10^4 $(\mathrm{sm})^{-1}$	γ_t^{sp}	1.0×10^5 $(\mathrm{sm})^{-1}$
γ_t^{ss}	9.3×10^3 $(\mathrm{sm})^{-1}$	t_{ray}	6.75×10^{-5} s
Y^p	50 Mpa	dt	1.35×10^{-5} s

Table A.2. Numerical values of the parameters used in the simulations discussed in Chap. 5: quasi-2D setup (with and without PBC) and 3D cubic setup with PBC on x and y directions. The vertical walls of the 2D setup have $k_t^{sp}, \gamma_t^{sp}, \mu^{sp} = 0$. For the results related to the cylindrical system we refer to Tab. A.1.

Simulations for chapters 6

Y^s	210 Mpa	$\gamma_n^{ss} = \gamma_t^{sp}$	$2.3\times[10^3 - 10^6]$ $(\mathrm{sm})^{-1}$
ν^s	0.293	ν^p	0.37
$\mu^{ss} = \mu^{sp}$	0.5	Y^p	50 Mpa
k_n^{ss}	$[30 - 120]\times10^6$ Pa	k_n^{sp}	617×10^5 Pa
$k_t^{ss} = k_t^{sp}$	190×10^6 Pa	t_{ray}	6.75×10^{-5} s
$\gamma_n^{ss} = \gamma_n^{sp}$	$2.9\times[10^5 - 10^8]$ $(\mathrm{sm})^{-1}$	dt	1.35×10^{-5} s

Table A.3. Numerical values of the parameters used in the simulations discussed in Chap. 6: conical-shaped based cylindrical setup with and without the forced vane. Intervals in square brackets refer to the values used to vary the elastic and dissipative properties of the grains in the numerical analysis of the energy transfer. Also here we have the same constraint on the grain-vane interaction discussed in Tab. A.1.

Appendix B

The multivariate Ornsten-Uhlenbeck process

In this appendix, we briefly review the solution of the multivariate Ornstein-Uhlenbeck process giving particular attention to the quantities on which this thesis is mainly focused on. We basically follow [76].

The process is defined as:

$$d\boldsymbol{X}(t) = -\hat{A}\boldsymbol{X}(t) + \hat{B}d\boldsymbol{W}(t) \tag{B.1}$$

where $\hat{A}$ and $\hat{B}$ are constant matrices and $d\boldsymbol{W}(t)$ is the increment of the multidimensional wiener process. It is related to the Gaussian white noise $\boldsymbol{\eta}(t)$ used many times in this thesis by $d\boldsymbol{W}(t) = \boldsymbol{\eta}(t)dt$. Its general solution is:

$$\boldsymbol{X}(t) = \exp(-\hat{A}t)\boldsymbol{X}(t) + \int_0^t \exp\left[-\hat{A}(t-t')d\boldsymbol{W}(t')\right] \tag{B.2}$$

from which we can calculate:

$$\begin{aligned}
&\hat{\sigma}(t,s) \equiv \langle [\boldsymbol{X}(t) - \langle \boldsymbol{X}(t)\rangle]\,[\boldsymbol{X}(s) - \langle \boldsymbol{X}(s)\rangle]^T\rangle \\
&= \exp(-\hat{A}t)\langle \boldsymbol{X}(0)\boldsymbol{X}^T(0)\rangle \exp(-\hat{A}s) \\
&+ \textstyle\int_0^{\min(t,s)} \exp\left[-\hat{A}(t-t')\right]\hat{B}\hat{B}^T \exp\left[-\hat{A}^T(s-t')\right]dt'
\end{aligned} \tag{B.3}$$

If $\hat{A}$ is symmetric and $\hat{B}$ is diagonal, the above equation reduce to Eq. (4.6) of the main text. From now on we assume $\hat{A}$ semi positive definite which implies stationarity.

B.1 Correlation matrix and spectrum in the stationary state

The stationary correlation matrix is obtained by Eq. (B.3) by neglecting the transient:

$$\hat{G}_s(t-s) = \begin{cases} \exp\left[-\hat{A}(t-s)\right]\sigma & t > s \\ \sigma \exp\left[-\hat{A}^T(s-t)\right] & t < s \end{cases} \tag{B.4}$$

where $\hat{\sigma} = \lim_{t\to\infty} \hat{\sigma}(t,t)$ is the stationary covariance matrix defined in Cap. 4. From the above equation it is clear that: $\hat{G}_s(t-s) = [\hat{G}_s(s-t)]^T$. We recall here the property:

$$\hat{A}\hat{\sigma} + \hat{\sigma}\hat{A}^T = \hat{B}\hat{B}^T \tag{B.5}$$

that follows from Eq. (B.3) in the stationary state.

The spectrum matrix is defined as the Fourier transform of the correlation matrix:

$$\begin{aligned} \hat{S}(\omega) &= \tfrac{1}{2\pi}\textstyle\int_{-\infty}^{\infty} \exp(-i\omega\tau)\hat{G}_s(\tau)d\tau \\ &= \tfrac{1}{2\pi}\textstyle\int_0^{\infty}\left[(-i\omega+\hat{A})\tau\right]\sigma d\tau + \int_{-\infty}^{0}\sigma\exp\left[(-i\omega+\hat{A}^T)\tau\right]d\tau \\ &= \tfrac{1}{2\pi}\left[(\hat{A}+i\omega)^{-1}\sigma + \sigma(\hat{A}^T - i\omega)^{-1}\right]. \end{aligned} \tag{B.6}$$

From the last equality we have: $(\hat{A}+i\omega)\hat{S}(\omega)(\hat{A}^T - i\omega)$. That with Eq. (B.5) gives Eq. (3.9)

$$\hat{S}(f) = \frac{1}{2\pi}(\hat{A}+i\omega)^{-1}\hat{B}\hat{B}^T(\hat{A}^T - i\omega)^{-1}$$

B.2 Spectrum of the three variable model (Sec. 3.2)

From Eqs. (3.15), defining the following vector of variables $\boldsymbol{X}(t) = \{\omega(t), \Omega_1(t), \Omega_2(t)\}$ and noises $\boldsymbol{\eta}(t) = \{\eta(t), \eta_1(t), \eta_2(t)\}$, using Eq. (3.9), with:

$$\hat{A} = \begin{pmatrix} \mu & -\mu & -\mu \\ \alpha\mu_1 & \mu_1 & 0 \\ 0 & 0 & \mu_2 \end{pmatrix}, \quad \hat{B} = \begin{pmatrix} \sqrt{2\mu q} & 0 & 0 \\ 0 & \sqrt{2\mu_1 q_1} & 0 \\ 0 & 0 & \sqrt{2\mu_2 q_2} \end{pmatrix}. \tag{B.7}$$

we can compute the VPSD of the tracer obtaining:

$$S_{00}(\tilde{f}) = \frac{\mu/\pi\left[\tilde{f}^4 q + \tilde{f}^2\left(\mu_1^2 q + \mu_1\mu q_1 + \mu_2^2 q + \mu_2\mu q_2\right) + \mu_1^2\mu_2^2 q + \mu_1^2\mu_2\mu q_2 + \mu_1\mu_2^2\mu q_1\right]}{\tilde{f}^6 + \tilde{f}^4\left(\mu_1^2+\mu_2^2+\mu^2-2\mu\mu_\alpha\right) + \tilde{f}^2\left(\mu_1^2\mu_2^2 + \mu_1^2\mu^2 + 2\mu_1\mu^2\mu_\alpha + \mu_2^2\mu^2 - 2\mu_2^2\mu\mu_\alpha + \mu^2\mu_\alpha^2\right) + \mu_2^2\mu^2(\mu_\alpha+\mu_1)^2} \tag{B.8}$$

where $\tilde{f} = 2\pi f$ and $\mu_\alpha = \mu_1\alpha$.

Appendix C

Supplemental materials for the granular lattice model (Cap. 4)

C.1 Subleading terms in the large system limit

Here we show how performing the large system limit ($L \gg 1$) subleading terms $\sim 1/L$ occur. Starting from Eq. (4.10) of the main text we consider the contribution proportional to b_L^2:

$$b_L^2 \Pi^2 \sum_{lk} \frac{\sin(jl\Pi)\sin(mk\Pi)\sin(lL\Pi)\sin(kL\Pi)}{\Delta(\alpha) - \cos(k\Pi) - \cos(l\Pi)} \tag{C.1}$$

where $\Pi = \pi/(L+1)$ and we note that: $\sin(lL\Pi)\sin(kL\Pi) = (-1)^{k+l+2}\sin(l\Pi)\sin(k\Pi)$. Considering a generic function f we can write

$$\begin{aligned}\Pi^2 \sum_{lk} (-1)^{k+l+2} f(jl\Pi, mk\Pi) = \Pi^2 \sum_{nh} \big[& f(2jn\Pi, 2mh\Pi) - f(2jn\Pi + j\Pi, 2mh\Pi) \\ & + f(2jn\Pi + j\Pi, 2mh\Pi + m\Pi) - f(2jn\Pi, 2mh\Pi + m\Pi)\big]\end{aligned} \tag{C.2}$$

that taking the large system limit $L \gg 1$ and replacing sums with integrals as $\Pi \sum_{m=0}^{m=L/2} f(2m\Pi) \to \frac{1}{4}\int_0^\pi dx f(x)$ becomes:

$$\begin{aligned}\frac{1}{4}\int_0^\pi dz ds \big[& f(jz, ms) - f(jz + j\Pi, ms) + f(jz + j\Pi, ms + m\Pi) \\ & - f(jz, ms + m\Pi)\big] \sim \mathcal{O}(1/L), \quad L \gg 1, \quad m \vee j \ll L\end{aligned} \tag{C.3}$$

because all the terms at the zeroth-order vanish in the integrand. This explains why it is possible to neglect the term proportional to b_L^2 in Eq. (4.10) of the main text once the large system limit is taken and for $j \vee m$ small enough. This is consistent with the idea that the effect of the bath acting on the Lth site can be neglected only if σ_{jm} is calculated for sites that are far away from L.

C.2 Covariance matrix in the NHHP

Here we give some details about the calculations necessary to derive the asymptotic predictions of Eqs. (4.14) from Eq. (4.13) of the main text. To do so we start from the latter equation in a form more suitable for next calculations:

$$\sigma_{jm}^{\mathrm{NHHP}} = \lim_{L\to\infty} \frac{4T_1}{\pi^2} \int_{\frac{\pi}{L+1}}^{\frac{\pi L}{L+1}} dz \int_{\frac{\pi}{L+1}}^{\frac{\pi L}{L+1}} ds \sin(jz)\sin(ms) g(z,s). \tag{C.4}$$

where

$$g(z,s) = \frac{\sin(z)\sin(s)}{2-\cos(z)-\cos(s)}. \tag{C.5}$$

In this expression we have shown the explicit form of the large L limit because the integrand of the function g is a function of both z and s that is singular in the point $(0,0)$. Indeed, its right value in the origin comes from the limit for large L of the integration domain $[\frac{\pi}{L+1}, \frac{\pi L}{L+1}] \times [\frac{\pi}{L+1}, \frac{\pi L}{L+1}]$ in the zs plane. More specifically we have that $0 \leq g(z,s) \leq 1 \ \forall z,s \in [0,\pi]$ and that $\lim_{z\to 0} g(z^a, z^b) \sim z^{a-b}$ if $a \geq b$. In the remainder, we consider the integration intervals as $[\frac{\pi}{L+1}, \pi]$ because the singularity is just in the origin. Integrating two times by parts and noting that $g(\pi, s) = g(z, \pi) = 0 \ \forall \ z, s$ we have:

$$\begin{aligned}\sigma_{jm}^{\mathrm{NHHP}} = \lim_{L\to\infty} \frac{4T_1}{\pi^2 jm} \Bigg[& \cos\left(\frac{j\pi}{L+1}\right)\cos\left(\frac{m\pi}{L+1}\right) g\left(\frac{\pi}{L+1}, \frac{\pi}{L+1}\right) \\ & + \cos\left(\frac{m\pi}{L+1}\right) \int_{\frac{\pi}{L+1}}^{\pi} dz \cos(jz)\, \partial_z g\left(z, \frac{\pi}{L+1}\right) \\ & + \cos\left(\frac{j\pi}{L+1}\right) \int_{\frac{\pi}{L+1}}^{\pi} ds \cos(ms)\, \partial_s g\left(\frac{\pi}{L+1}, s\right) \\ & + \int_{\frac{\pi}{L+1}}^{\pi} ds dz \cos(jz)\cos(ms)\, \partial_{zs} g(z,s) \Bigg]. \end{aligned} \tag{C.6}$$

We want to show that $\sigma_{jm}^{\mathrm{NHHP}} \sim (jm)^{-1}$ so we have to demonstrate that the sum of the terms in the square brackets is $\mathcal{O}(1)$ for $m, j \gg 1$ in the large L limit. The first term clearly tends to 1 when $L \to \infty$ regardless the value of j and m (remember that $j, m \ll L$). Reintroducing $\Pi = \pi/(L+1)$ we can express Eq. (C.6) as:

$$\sigma_{jm}^{\mathrm{NHHP}} \sim \frac{4T_1}{\pi^2 jm}\left[1 + C_{jm}\right] \quad \text{where} \quad C_{jm} = \lim_{L\to\infty} \left[\cos(m\Pi) I_j + \cos(j\Pi) I_m + I_{jm}\right] \tag{C.7}$$

and where I_j, I_m and I_{jm} are respectively the integrals of the second, third and fourth term in the square brackets of Eq. (C.6). The estimate of the asymptotic behaviour of such integrals is not trivial because of the presence of the derivatives of $g(z,s)$ that diverge in the origin. We then proceed by estimating upper bounds. It is important to note that, in order to demonstrate $\sigma_{jm}^{\mathrm{NHHP}} \sim (jm)^{-1}$, requiring $C_{jm} \sim \mathcal{O}(1)$ or $|C_{jm}| \leq 1$ is not enough because it would bring contributions as $-1 \pm o(1/j)$ that imply the emergence of a faster decay. The right thing to do is instead to show that $|C_{jm}| \leq c$ with $c < 1$. In this way, we could be sure that C_{jm} cannot cancel 1 in Eq. (C.7). Starting by I_j, we define $u(z) = \partial_z g(z, \frac{\pi}{L+1})$ and rewrite it as:

$$I_j = \int_{\frac{\pi}{L+1}}^{\pi + \frac{\pi}{L+1}} dz \cos(jz)\, u(z) + \mathcal{O}(1/L) \tag{C.8}$$

Now we note that the interval of integration is much larger than the period $T_j = \frac{2\pi}{j}$ of the cosine so we can split it in a sum of contributions over consecutive periods.

Without loss of generality we can assume j even and exploit the periodicity of the cosine obtaining:

$$I_j = \sum_{k=1}^{k=j/2} \int_{(k-1)T_j+\Pi}^{kT_j+\Pi} dz \cos(jz) u(z) = \frac{1}{j} \int_{\Pi}^{2\pi+\Pi} dx \cos(x) \sum_{k=1}^{k=j/2} u\left(\frac{x}{j} + (k-1)T_j\right) \tag{C.9}$$

where we have have changed variable as $x = jz + 2\pi(k-1)$ and reintroduced the symbol $\Pi = \frac{\pi}{L+1}$. Now we use the fact that $T_j \ll 1$ to exchange the sum over k with an integral as $\sum_k f\left((k-1)T_j\right) \to T_j^{-1} \int d\phi_j f(\phi_j)$ and return to an expression with g:

$$\begin{aligned} I_j &= \frac{1}{2\pi} \int_{\Pi}^{2\pi+\Pi} dx \cos(x) \int_0^{\pi-\frac{2\pi}{j}} d\phi_j u\left(\frac{x}{j} + \phi_j\right) \\ &= \frac{1}{2\pi} \int_{\Pi}^{2\pi+\Pi} dx \cos(x) \left[g\left(\frac{x}{j} + \pi - \frac{2\pi}{j}, \Pi\right) - g\left(\frac{x}{j}, \Pi\right)\right]. \end{aligned} \tag{C.10}$$

The function g can be regularly expanded in series around the point $(\pi, 0)$. Doing this, it's easy to verify that the integral of the first term in the brackets gives $\mathcal{O}(1/j)$ contributions. We can't perform such an estimate for $g(x/j, \Pi)$ because the derivatives near the origin are not well-defined. Nevertheless, we know that $g(x/j, \Pi) \in [0, 1] \ \forall \ x \in [\Pi, 2\pi/ + \Pi]$ if j is sufficiently large so we can estimate an upper bound for I_j (and I_m) as: $\lim_{L\to\infty} |I_{j(m)}| \leq 1/\pi$ for $j \gg 1$. This happens because, given T a 2π-large interval with $T_{+(-)}$ the sub-interval where the cosine is positive(negative) and $g(x) \in [0, 1]$ if $x \in T$, we can write:

$$\left| \int_T \cos(x) g(x) \right| = \left| \left| \int_{T_+} \cos(x) g(x) \right| - \left| \int_{T_-} \cos(x) g(x) \right| \right| \leq \frac{1}{2} \int_T |\cos(x)| = 2 \tag{C.11}$$

With the same kind of calculations leading to Eq. (C.10) we obtain:

$$I_{jm} = \frac{1}{4\pi^2} \int_{\Pi}^{2\pi+\Pi} dx dy \cos(x) \cos(y) g\left(\frac{x}{j}, \frac{y}{m}\right) + \mathcal{O}((mj)^{-1}). \tag{C.12}$$

Using inequalities similar to the ones of Eq. (C.11) but for 2D integrals we estimate the upper bound of Eq. (C.12) as $\lim_{L\to\infty} |I_{jm}| \leq 2/\pi^2$ for $j, m \gg 1$. Putting together these results in the definition of C_{jm} of Eq. (C.7) we are sure that in the large L limit:

$$|C_{jm}| \leq \lim_{L\to\infty} \left[|I_j| + |I_m| + |I_{jm}|\right] = \frac{2}{\pi}\left(1 + \frac{1}{\pi}\right) \simeq 0.83926 < 1 \quad \text{for} \quad j, m \gg 1 \tag{C.13}$$

We conclude that $\sigma_{jm}^{\text{NHHP}} \sim (jm)^{-1}$ from which Eq. (4.14a) of the main text is straightforward.

It is important to note that, in order to obtain Eqs. (C.9) and (C.10), we need both j and $m \gg 1$. So we have to use another way to estimate the asymptotic behaviour of $\sigma_{1m}^{\text{NHHP}}$. It can be rewritten as

$$\sigma_{1m}^{\text{NHHP}} = \frac{4T_1}{\pi^2} \int_0^{\pi} dz ds \sin(ms) g_1(s, z) \quad \text{where} \quad g_1(s, z) = \frac{\sin^2(z)\sin(s)}{2 - \cos(z) - \cos(s)} \tag{C.14}$$

and g_1 is regular in the origin because $\lim_{z\to 0} g_1(z^a, z^b) = 0 \ \forall \ a, b > 0$. We can perform the integral over z obtaining

$$\int_0^\pi dz g_1(z,s) = \pi\left[-2+\cos(s)+\sqrt{6-2\cos(s)}\sin(s/2)\right]\sin(s) \tag{C.15}$$

where the first two terms in the brackets vanish when also the integral over s is performed (m is an integer). We have now that $\sigma_{1m}^{\mathrm{NHHP}} = \frac{4T_1}{\pi^2}\int_0^\pi ds \sin(ms) f(s)$ where $f(s) = \sin(s)\left[\sqrt{6-2\cos(s)}\sin(s/2)\right]$. Integrating four times by parts and noting that $f(0) = f(\pi) = f''(\pi) = 0$ while $f''(0) = 2$ we obtain:

$$\sigma_{1m}^{\mathrm{NHHP}} = \frac{8T_1}{\pi m^3} + R_m \sim \frac{8T_1}{\pi m^3} + \mathcal{O}(m^{-5}), \quad m \gg 1 \tag{C.16}$$

where $R_m = (m)^{-4}(\pi)^{-1}\int_0^\pi ds \sin(ms) f^{(4)}(s)$ and:

$$|R_m| \leq m^{-4}\pi^{-1}|\max(f^{(4)}(s))|\int_0^\pi ds|\sin(ms)| = 2m^{-5}\pi^{-1}|\max(f^{(4)}(s))|. \tag{C.17}$$

The last quantity needed for the Eqs. (4.13) of the main text is
$\sigma_{11}^{\mathrm{NHHP}} = \int_0^\pi dz ds \sin(z)\sin(s) g(z,s) = \pi^2 - 8\pi/3$ that is finite and does not depend on m so the asymptotic behaviour for ζ_{1m} directly follows from the ones derived for Eqs. (4.14a) and (4.14b) of the main text.

C.3 Covariance matrix in the HHP

In order to derive Eq. (4.16) from Eq. (4.10) of the main text we have to discuss the contributions coming from the sum $\sum_n b_n^2 \sin(ln\Pi)\sin(kn\Pi)$ that compares in the latter. As explained in the first appendix, the term proportional to b_L^2 gives a subleading term $\mathcal{O}(1/L)$ in the large system limit while the one proportional to b_1^2 gives $4T_1(1+\alpha)(\pi)^{-2}\Sigma_{jm}(\alpha)$. Regarding the other contributions, we exploit orthogonality to express the remaining sum as:

$$\sum_{n=2}^{n=L-1}\sin(ln\Pi)\sin(kn\Pi) = \frac{L+1}{2}\delta_{kl} - \sin(l\Pi)\sin(k\Pi) - \sin(lL\Pi)\sin(kL\Pi) \tag{C.18}$$

where again the last term gives $\mathcal{O}(1/L)$ for $L \gg 1$. Thus, using this equation and neglecting subleading terms, Eq. (4.10) of the main manuscript becomes:

$$\sigma_{jm}(\alpha) = \Pi^2 \sum_{lk} \frac{\sin(jl\Pi)\sin(mk\Pi)}{\Delta(\alpha) - \cos(k\Pi) - \cos(l\Pi)}\left[\frac{2\alpha T_a(L+1)}{\pi^2}\delta_{kl} + \frac{4T_1}{\pi^2}\left(1+\alpha\left(1-\frac{T_a}{T_1}\right)\right)\sin(l\Pi)\sin(k\Pi)\right] \tag{C.19}$$

that in the large system limit gives Eq. (4.16) of the main manuscritp.

In the main text we proceed from Eq. (4.16) by considering constant amplitude of noises i.e. $T_1 = T_a\gamma_a/(\gamma+\gamma_a)$. In this way the term proportional to $\Sigma(\alpha)$ vanishes and one can shorten calculations concentrating just on the integral over

z. To verify that the asymptotic behaviour of Eq. (4.19) of the main text holds also without constant amplitude of noises we have to show that $\Sigma_{jm}(\alpha)$ does not decay slower than $\exp(-\sqrt{\alpha}m)$. We then consider the fourier transform $\tilde{\Sigma}_{j\omega}(\alpha) = \int dm \exp(i\omega m)\Sigma_{jm}(\alpha)$ for small ω:

$$\begin{aligned} &\tilde{\Sigma}_{j\omega} \sim \int_0^\pi dz \frac{\sin(jz)\sin(z)\omega}{1+\alpha-\cos(z)+\frac{\omega^2}{2}} \quad \text{so} \\ &\Sigma_{jm} \sim \int_0^\pi dz \frac{\sin(jz)\sin(z)}{1+\alpha-\cos(z)} \exp\left[-m\sqrt{2(1+\alpha-\cos(z))}\right] \end{aligned} \tag{C.20}$$

and for this last expression is simple to show that $|\Sigma_{jm}| \leq \frac{\pi}{\alpha}\exp(-\sqrt{2\alpha}m)$. Then we are sure that its behaviour for large m will be subleading with respect to $\exp(-\sqrt{\alpha}m)$.

To complete the discussion about the exponential decay in the HHP we need to evaluate the result of Eq. (4.18) of the main manuscript. We then write such integral after one integration by parts obtaining:

$$\begin{aligned} &\frac{2\alpha T_a}{\pi}\int_0^\pi dz \frac{\sin^2(mz)}{\Delta(\alpha)-2\cos(z)} \\ &= \frac{2\alpha T_a}{\pi}\left[\frac{\pi}{2(4+\alpha)} - \int_0^\pi dz \frac{z\sin(z)}{(\Delta(\alpha)-2\cos(z))^2} - \int_0^\pi dz \frac{\sin(mz)\sin(z)}{2m(\Delta(\alpha)-2\cos(z))^2}\right] \end{aligned} \tag{C.21}$$

from which we have that $\sigma^{\mathrm{HHP}}_{mm}(\alpha) = T_a\sqrt{\frac{\alpha}{4+\alpha}} + o(m^{-1})$.

C.4 Spatial correlation in the cooling state

An important question that often arises in granular systems regards the relation between the properties of the cooling dynamics and the one of the NESS obtained with the injection of energy. In our case, we obtain the cooling state by switching off all the temperatures in the lattice (matrix $\hat{B}$ with all zero entries). In this situation, the covariance matrix is simply given by Eq. (4.7a) of the main text. Where the brackets $\langle\rangle$ refer to a mean on the initial conditions. Exploiting the symmetry of $\hat{A}$ we can rewrite it as:

$$\sigma_{jm}(t,s) = \sum_{nhkl} S_{hn}e^{-\lambda_n t}S^+_{nk}\langle v_k(0)v_l(0)\rangle S_{lh}e^{-\lambda_h s}S^+_{hj} \tag{C.22}$$

Keeping initial conditions identically and independently distributed around 0 with the variance 1 so that $\langle v_k(0)v_l(0)\rangle = \delta_{kl}$ and exploiting orthogonality of the eigenvectors we have:

$$\sigma_{jm}(t,s) = \sum_n S_{jn}e^{-\lambda_n(t+s)}S^+_{nm} \tag{C.23}$$

That in the Toeplitz case for $t = s$ becomes:

$$\sigma_{jm}(t) = \frac{\exp(-2(2\gamma+\gamma_a)t)\Pi}{\pi}\sum_n \sin(jn\Pi)\sin(nm\Pi)\exp(4\gamma t\cos(n\Pi)). \tag{C.24}$$

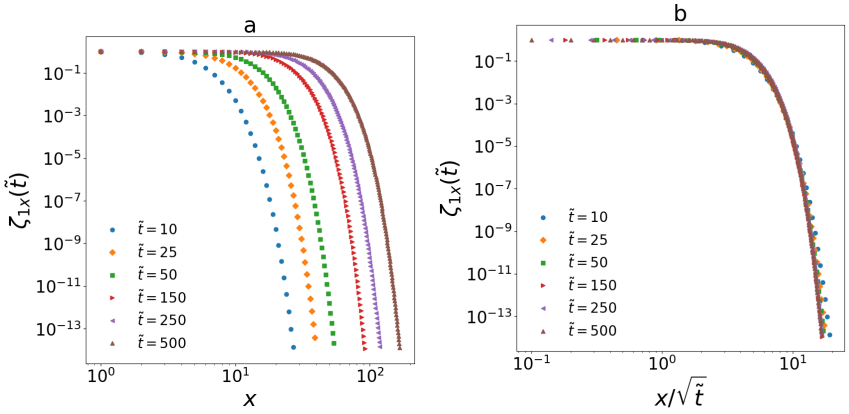

Figure C.1. Spatial correlation function in the cooling state after different times $\tilde{t}$ (a). We observe a collapse by rescaling the horizontal axis by $\sqrt{\tilde{t}}$ (b). Here we have considered $L = 200$. Images reprinted from the supplementary information of [148].

where we note that for $t = 0$ $\sigma_{jm}(0) = \delta_{jm}$ as imposed by the initial state. The same uncorrelated condition, expected for non-interacting systems, is also obtained with $\gamma = 0$. Another important properties of the $\sigma_{ij}(t)$ is that the dependence on γ_a is factored out from the sum so, when calculating $\zeta_{jm} = \sigma_{jm}/\sqrt{\sigma_{jj}\sigma_{mm}}$, it simplifies. Moreover, also the dependence from γ can be removed just by using the adimensional time $\tilde{t} = \gamma t$. To conclude, during the cooling the behaviour of spatial correlations is crucially different from the one observed in the two heated phases studied in the main text. In particular, the parameter α does not play a crucial role as in the NESS. This is an intriguing result because we found that an external source of energy makes something more than just keeping alive the dynamics that characterizes the system when it cools down.

In Fig. C.1 we show $\zeta_{1x}(\tilde{t})$ for different times $\tilde{t}$ and we clearly observe that it presents a finite cutoff that grows with the delay time $\tilde{t}$. We can understand it by thinking that the information is propagating through the system in time. In Fig. C.1b we show how rescaling the space with $\sqrt{\tilde{t}}$ all the curves collapse. So the information propagates as $\xi(t) \propto \sqrt{\gamma t}$. This result is fully consistent with diffusion-like coarsening dynamics of vortices, found in other models for granular velocity fields [199, 16, 18]. In those models however the cooling state is closer to "dilute" situations where interactions are sequences of separate binary collisions.

C.5 Reintroduction of space and connection with active matter

Although it is reasonably justified from empirical observations, neglecting the positional dynamics remains the main approximation of our model. A way to reintroduce it in our description is to consider a harmonic potential between nearest neighbors in the lattice. The equation of motion for each particle would then be of this form

$$\dot{x}_i = v_i \tag{C.25a}$$

$$\dot{v}_i = -(\gamma_{a(b)} + 2\gamma)v_i - 2kx_i + k(x_{i+1} + x_{i-1}) + \gamma(v_{i+1} + v_{i-1}) + \sqrt{2T_{a(i)}\gamma_{a(b)}}\xi_i(t) \tag{C.25b}$$

where we consider again a bath on the boundaries characterized by (γ_b, $T_{1(L)}$) and a bath on the bulk (γ_a, T_a).

It is interesting to note that we can obtain equations of the same form when considering a 1D chain of (overdamped) active particles with harmonic interactions, where self-propulsion is modelled using a colored noise η (Active Ornstein-Uhlenbeck Particles AOUP):

$$\dot{x}_i = -k(x_i - x_{i+1}) - k(x_i - x_{i-1}) + \eta_i(t) \tag{C.26a}$$

$$\dot{\eta}_i = -\gamma_a\eta_i + \sqrt{2T_a\gamma_a}\xi_i(t) \tag{C.26b}$$

where ξ_i are Gaussian white noises with unitary variance. Time-deriving the first of these equations and following standard manipulations, we get [122]:

$$\dot{x}_i = v_i \tag{C.27a}$$

$$\dot{v}_i = -(\gamma_a + 2k)v_i - 2k\gamma_a x_i + k\gamma_a(x_{i+1} + x_{i-1}) + k(v_{i+1} + v_{i-1}) + \sqrt{2T_a\gamma_a}\xi_i(t) \tag{C.27b}$$

which are formally equivalent to Eqs. (C.25). If we consider the particles fixed on the lattice and neglect the positional dynamics we find the analogous of the granular case studied in the main with a transition in $\gamma_a = 0$. While in the granular chain removing the bath on the bulk has a specific and realistic physical condition (granular materials are often driven only through boundaries) in the active case it seems meaningless. A self-propelled harmonic chain modelled by Eqs. (C.27) has been studied taking account the positional dynamics and assuming spatially homogeneous self-propulsion [43]. The authors perform calculations based on translational invariance (they solve the system in the Bravais reciprocal lattice). This assumption is crucial and it is also the main difference with our approach in which we are interested in the effect of non-homogeneous heating. The interesting connection with our investigation is that they found a correlation length that scales as $\xi \sim \sqrt{1/\gamma_a}$ as in our case [43].

The study of correlations in this kind of 1D system with both positional dynamics and non-homogeneous heating is, up to our knowledge, still lacking. We are currently working in this direction.

C.6 Correlations in the bulk and finite size effects

In the main text, we focused on the correlation function with respect to the first site ζ_{1m} in the limit $L \gg m \gg 1$. These conditions, particularly in the NHHP,

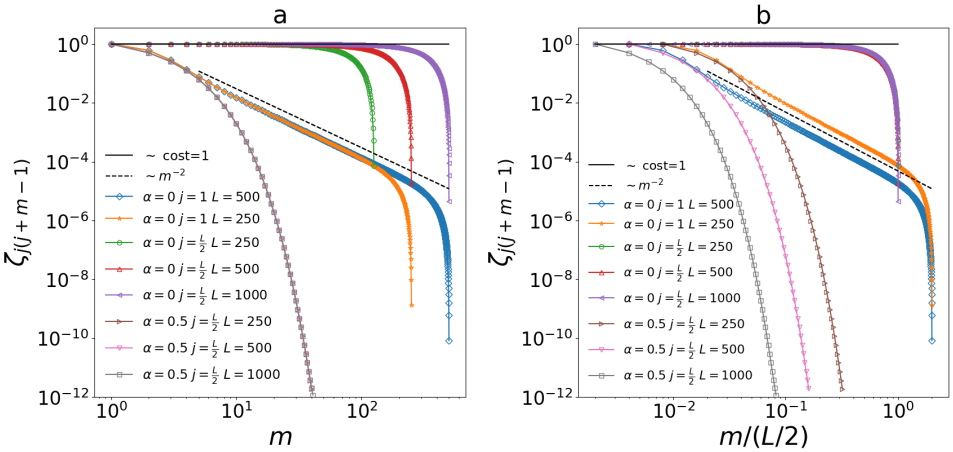

Figure C.2. a: Spatial correlation function with respect to the site $j = 1, \frac{L}{2}$ for $\beta = 2$, $T_1 = T_a = T_L = 0.001$ and different values of α and L. The entries of $\hat{\sigma}$ are obtained from from Eq. (4.6) for $t = s \gg 1$ and diagonalising $\hat{A}$. b) Same curves shown in the left panel but as a function of the rescaled distance $m/(L/2)$. The collapse of the cutoff in the NHHP is a signature of scale-free correlations [45]. Images reprinted from [148].

were crucial ingredients for calculations. Moreover, in Fig. 4.3a and Fig. 4.4a we have always shown the correlation function in the case of $T_L = 0$ in order to treat cases more compatible with our calculations where the terms proportional to $T_L \sim \mathcal{O}(1/L)$ are neglected. In this condition, the only source of stochasticity is the bath on the first site so the finite-size effects do not substantially affect the shape of ζ_{1m}. Thus, the power-law regime in the NHHP spans almost all the system size.

Here we want to discuss the behaviour of spatial correlations between particles in the bulk (i.e. ζ_{jm} with $1 \ll j, m \ll L$) and the finite size effects for $T_L \neq 0$. In Fig. C.2a we show $\zeta_{j(j+m-1)}$ with $j = 1, L/2$ for different values of L and α. In all the cases we have $T_1 = T_a = T_L \neq 0$. The correlation function with respect $L/2$ is representative for the bulk and we can see from Fig. C.2a that in the HHP it presents an exponential decay with a correlation length independent from L while in the NHHP it decays slower than a power-law: $\zeta^{\text{NHHP}}_{L/2(L/2+m-1)}$ remains essentially constant up to a sharp cutoff that increases by raising L. Regarding ζ^{NHHP}_{1m} for $T_L \neq 0$, we can still observe the power-law decay $\sim m^{-2}$ predicted in the previous paragraphs but with a sharp cutoff that occurs when m is large enough and depending on L. In Fig. C.2b we show the same curves as a function of $m/(L/2)$ and we note that the cutoffs of the correlation functions in the NHHP collapse signalling that their size scales linearly with L. In other words, this confirms that also when the boundary effects affect the shape of ζ_{jm}, the NHHP presents scale-free correlations. Indeed the only typical correlation length that one can define grows with system size. As we expect, the correlation functions in the HHP separate when plotted as a function of $m/(L/2)$ because their decay is strictly defined by α regardless of L.

Appendix D

The Inverse Participation Ratio

Here we introduce the inverse participation ratio (IPR) and we show how to use his scaling with the system size to distinguish localized and delocalized states.

Lets define the state α as $\boldsymbol{\psi}^{(\alpha)}$ that, when localized around a site i_0 with a localization length $l > 0$, takes the form $\psi_i^{(\alpha)} = A \exp(-|i - i_0|/l)$ where A is a normalization factor. By exploiting the fact that:

$$\sum_{i=0}^{L} \left(\psi_i^{(\alpha)}\right)^2 = A^2 \left[\sum_{i \leq i_0} \left(e^{-a}\right)^i + \sum_{i \geq i_0} \left(e^{-a}\right)^i - 1\right] \quad \text{and} \quad \sum_{i=0}^{L} \left(e^{-a}\right)^i = \frac{1 - e^{-aL}}{1 - e^{-a}},$$

it is easy to show that, for large L, normalization implies $A = \sqrt{(1 - e^{-a})/(1 + e^{-a})}$ where $a = 2/l$. Now let's define the IPR as:

$$\mathcal{I}^{(\alpha)} = \frac{1}{\sum_i \left(\psi_i^{(\alpha)}\right)^4}. \tag{D.1}$$

By substituting in the above equation the expression for a localized state we obtain:

$$\left(\mathcal{I}^{(\alpha)}\right)^{-1} = \left[\frac{1 - e^{-a}}{1 + e^{-a}}\right]^2 \frac{1 + e^{-2a}}{1 - e^{-2a}} \sim \frac{1}{2l}.$$

Being in the large L limit we can always choose $2 \ll l \ll L$ so we expanded the above expression for $2/l = a \ll 1$ at the first order. We then have $\mathcal{I}^{(\alpha)} \sim 2l$ from which is clear that a scaling of the IPR with the system size can arise just from a scaling of $l(L)$ itself.

By considering delocalize states things change. Let's take as an example the fundamental state for a linear chain with PCB $\psi_i^{(0)} = \frac{1}{\sqrt{L}}$. It is easy to see that IPR scales linearly with the system size:

$$\mathcal{I}^{(0)} = \frac{1}{\sum_i L^{-2}} = L. \tag{D.2}$$

By taking the fundamental state with fixed boundary conditions (i.e. the sine) such scaling is the same. To summarize, we have seen that the scaling of the IPR is qualitatively different if one considers localized or delocalized states: in the first case

it scales linearly with the localization length, in the second one it is proportional to the system size.

The quantity shown in Fig. 4.6b is the density of the IPR and it is defined as:

$$D_{\mathcal{I}}(\lambda) = \frac{\sum_\alpha \mathcal{I}^{(\alpha)} \delta(\lambda - \lambda_\alpha)}{\sum_\alpha \delta(\lambda - \lambda_\alpha)}. \tag{D.3}$$

It accounts for the IPR in the infinitesimal interval $[\lambda - \epsilon, \lambda + \epsilon]$, the density of states $\rho(\lambda) = \sum_\alpha \delta(\lambda - \lambda_\alpha)$ at the denomintator is such that:

$$\int_{\lambda_\alpha - \epsilon}^{\lambda_\alpha + \epsilon} d\lambda \rho(\lambda) D_{\mathcal{I}}(\lambda) = \mathcal{I}^{(\alpha)}.$$

Appendix E

Persistent dynamics of single-particle angular velocity

In this appendix, we show that the phenomenon discovered in [130] (i.e. persistent rotation of vertically shaken disks around their own axis) is observed also in all the setups considered in our study. We also discuss some intriguing connections between this local memory effect and the collective one on which this thesis is focused on. The notation used below is introduced in Chap 5.

E.1 Persisent grain rotations in different conditions

We concentrate just on the main observable related to this behaviour namely the trajectories of the absolute angle $\theta_{\alpha i}(t) = \int_0^t \omega_{\alpha i}(t')dt'$ (Fig. E.1). Unlike disks, spherical grains can rotate around the three axis $\alpha = \{x, y, z\}$. For a direct comparison between the single-particle dynamics and the collective one, we suggest comparing Fig. E.1 with Fig. 5.3 of the main text. We start by the most similar condition with respect to [130] considering a 2D polydispersed vertical layer confined with hard walls both in the x and the y direction. In Fig. E.1a, we plot $\theta_{yi}(t)$ for all the 60 grains in the system. We can see that the single-particle rotation around the y axis (i.e. the equivalent that we would have had with disks) shows a persistent motion for almost all the grains in the system. Here, the presence of hard walls in the x direction prevents the occurrence of the collective drift. Nevertheless, in Fig. E.1b, we report the same analysis performed in the equivalent setup with PBC on x that allow the formation of the global translation: here is clear that the single-particle persistent motion and the collective one can be observed at the same time. Panel c of the same figure shows the results obtained for the ordered monodispersed system with no defects. We see that there is not any evident long memory effect in the single-particle rotational dynamics consistently with the lack of a collective translational drift. Figs. E.1d-e refers to two ordered packings with specular defects and panel f to the system with a configuration of defects symmetric w.r.t. z. Also in all these cases the persistent motion of the grain rotation is observed but we note two additional remarkable facts: i) the distribution of the trajectory verses for TR and TL is approximately specular ii) the SD case shows long memory effects just in the single-particle dynamics (we recall that no net collective drift is observed for

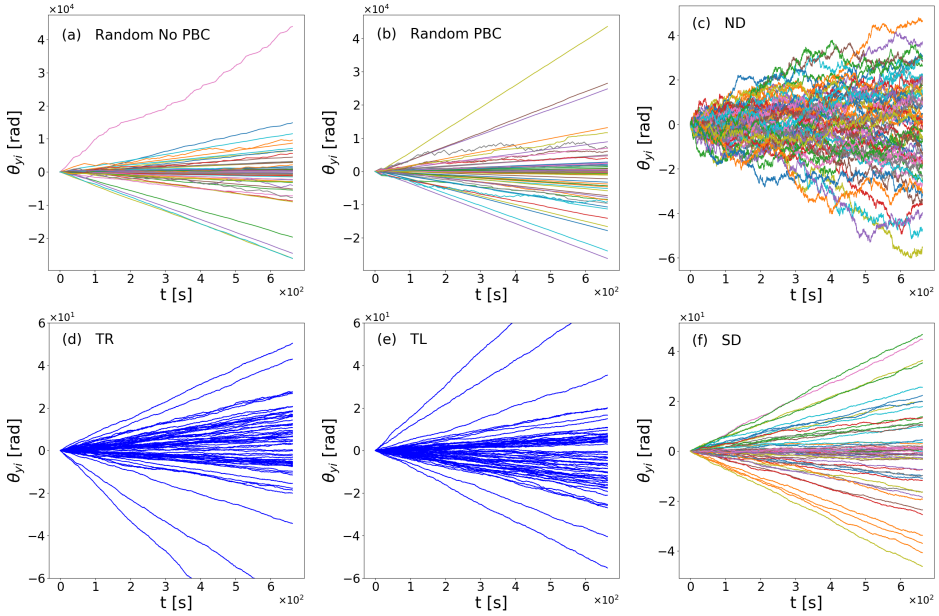

Figure E.1. Trajectories of the single-grain absolute angles around the y-axis for the following cases: polydispersed packing with hard (a) and periodic (b) boundary conditions on x, monodispersed ordered packing with no defects (c), ordered packings with the TR (d) and TL (e) specular configurations of defects, ordered packing with the symmetric SD configuration of defects (f). All the data refer to simulations with $f = 100$ and $\Gamma = 0.7$ except the first panel with $\Gamma = 0.85$. To see the correspondent behaviour of the collective motion see Fig. 5.3 of the main text. Images reprinted from supplemental materials of [147].

SD). This last behaviour is consistent with the claim of [130] that the rotational transport is triggered by local symmetry breakings of the granular packing. The SD configuration is indeed globally symmetric but creates an asymmetric cage of nearest neighbours for many bulk particles. Regarding the mirroring of the trajectories going from TR $\rightarrow$ TL, it suggests an intriguing relation between the distribution of the ω_{yi}s, the global asymmetry of the packing and consequently the persistent translational motion. In the section below we sketch some ideas on that.

The trajectories of $\theta_{\alpha i}(t)$ for a subset of grains in the 3D setups are reported in Fig. E.2. We note that persistent single-grain rotations are present in all the cases shown. In the cylindrical setup (panel a) we concentrate on $\theta_{zi}(t)$ instead of $\theta_{yi}(t)$ because, in this geometry, despite the vertical vibrations, the equivalent hard wall that is parallel to the free direction is the lateral one. Here we show a case at lower Γ with respect to the one shown in Fig. 3.9 and indeed we observe steadier rotations. Regarding the 3D cubic setup where both the x and the y directions are free, we observe persistent dynamics for both $\theta_{yi}(t)$ and $\theta_{xi}(t)$.

E.2 Connection with global translation

The mirroring of the ω_{yi} distribution going from TR to TL hinted by Fig. E.1d-e suggests studying the single-particle angular velocity of the bottom grains. Indeed,

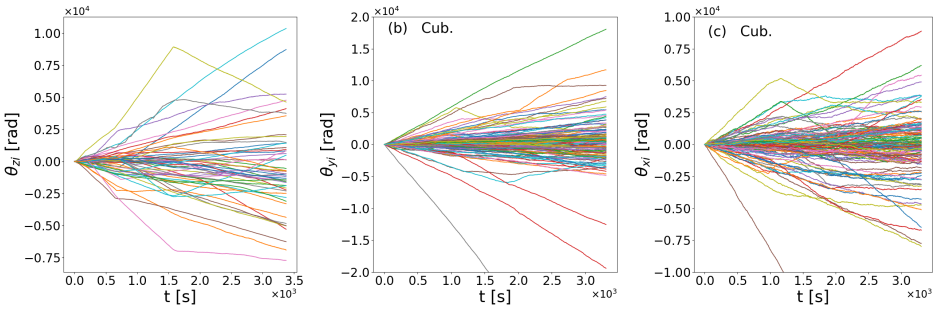

Figure E.2. Trajectories of the single-grain absolute angles for the cylindrical setup with $\Gamma = 19.5$ (a) and the cubic one with $\Gamma = 10.5$ (b,c). In both cases $f = 200$ and $N = 2600$. Images reprinted from supplemental materials of [147].

the total tangential force exerted by the bottom plate to the system depends on these degrees of freedom too; so they can be very important in order to understand the origin of the global dynamical asymmetry discussed in Chap. 5 (see Fig. 5.5). In Fig. E.3a, we show the θ_{yi}s of the bottom particles at $\Gamma = 0.7$ for the two mirrored configurations. We see that referring to the orientation of the y-axis of Fig. 5.1, all the bottom particles of TR and TL rotate respectively in the negative (anti-clockwise) and positive (clockwise) verse. Remarkably, these verses correspond to the ones that, in case of pure rolling, would involve a translation with the same sign of the collective motion observed for the two configurations (i.e. negative for TR and positive for TL). From this analysis, one could be tempted to conclude that the collective translation is simply the consequence of the coordinated rolling of the bottom particles acting as the "wheels" of the packing. Nevertheless, the real situation is quite more complex. First of all, we can see from Fig. E.3b, where the ratio between $R\omega_{yi}$ and v_{xi} of the bottom particles is reported, that the condition of pure rolling ($\langle R\omega_{yi}\rangle/\langle v_{xi}\rangle \simeq 1$) is only partially satisfied signalling that also sliding is occurring. Moreover, going toward higher Γ we don't observe anymore such a correspondence between the rolling of the bottom particles and the collective translation. Indeed, in Fig. E.3c, we can see that the bottom θ_{yi} for $\Gamma = 1.25$ rotates in both the verses within the same configuration. We verified that in this case the ratio $\langle R\omega_{yi}\rangle/\langle v_{xi}\rangle$ is even more different from the unity (not shown). It is worth noting that also in [130] two different regimes of rotations at low and high Γ were found. As a final analysis, we verified that, in simulations of TR and TL *without* periodic boundary conditions along the x-axis, the coordinated rolling of the bottom particles disappears and their motion is not persistent (Fig. E.3d). However, the long memory effect of the rotations is very strong on the upper layers (see the inset).

After all these remarks, we can say that the slow collective translations and the persistent single-particle rotations influence each other. But neither of these phenomena can be explained as the simple consequence of the other. In all the cases in which the collective motion is observed (i.e. when a free direction of motion is present) the persistent rotations are observed too. When the global translation is hindered by hard boundaries we still have steady rotations but with different properties with respect to the ones observed in presence of PBC. As an example,

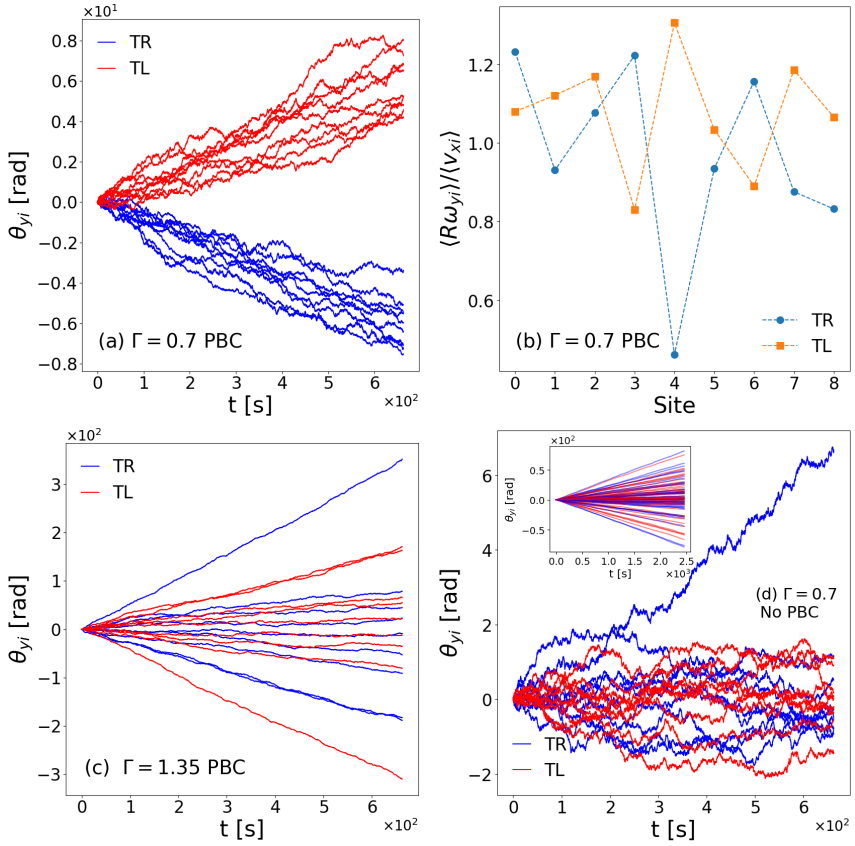

Figure E.3. Trajectories of the single-grain absolute angle in the bottom layer for TR/TL configuration with PBC at $\Gamma = 0.7$ (a), $\Gamma = 1.25$ (c) and $\Gamma = 0.7$ without PBC (d). In this last panel, the inset contains all the trajectories to show that the absence of persistent rotations regards mainly the bottom layer. b: In order to check the pure rolling condition, we show the ratio of the averaged velocity at the contact point and the averaged translational one of the grain centers for both TL and TR. All the data refers to simulations with $f = 100$.

we have seen that the rotational dynamics of the bottom particles for TR and TL qualitatively changes according to the presence or absence of PBC (compare panel a and d of Fig. E.3).

To conclude, we point out that our numerical study of long memory effects in the single-particle rotational degrees of freedom for spherical grains in both 2D and 3D geometries represents a considerable extension of the experimental work reported in [130]. We have provided much evidence about the robustness of this phenomenon and suggested some interesting connections with the collective motion on which the thesis is focused on. A further study of the mechanisms underlying this interplay of memory effects, its origin rooted in the structure and the resulting asymmetric interaction with the bottom plate represents a promising perspective that we reserve for the future.

Bibliography

[1] http://lammps.sandia.gov/.

[2] Sand: photo by Drew McNaughton | Unsplash. Coal: photo by Klim Musalimov | Unsplash. Cereals: photo by Pierre Bamin | Unsplash. Salt: photo by Universal Eye | Unsplash. Satrun rings: photo by Sergei Tokmakov | Pixabay.

[3] https://www.youtube.com/watch?v=aHrdY4BC71k&t=1s.

[4] https://docs.lammps.org/pair_granular.html.

[5] https://sourceforge.net/p/lammps/mailman/message/36606495/.

[6] https://github.com/lammps/lammps/releases/tag/stable_5Jun2019.

[7] J. A. Åström, H. J. Herrmann, and J. Timonen. Granular packings and fault zones. *Phys. Rev. Lett.*, 84:638–641, Jan 2000.

[8] V. Achilleos, G. Theocharis, and C. Skokos. Chaos and Anderson-like localization in polydisperse granular chains. *Phys. Rev. E*, 97:042220, Apr 2018.

[9] M. Adachi, P. Yu, and M. Sperl. Magnetic excitation of a granular gas as a bulk thermostat. *npj Microgravity*, 5(1):19, Aug 2019.

[10] R. Albert and A.-L. Barabási. Statistical mechanics of complex networks. *Rev. Mod. Phys.*, 74:47–97, Jan 2002.

[11] P. W. Anderson. Absence of diffusion in certain random lattices. *Phys. Rev.*, 109:1492–1505, Mar 1958.

[12] V. I. Arnold. *Mathematical Methods of Classical Mechanics*. Springer-Verlag, New York, 1989.

[13] E. Azanza, F. Chevoir, and P. Moucheront. Experimental study of collisional granular flows down an inclined plane. *J. Fluid Mech.*, 400:199–227, 1999.

[14] E. R. Bagnold. *Physics of Blown Sand and Sand Dunes*. Chapman and Hall, London, 1941.

[15] A. Baldassarri, F. Dalton, A. Petri, S. Zapperi, G. Pontuale, and L. Pietronero. Brownian forces in sheared granular matter. *Phys. Rev. Lett.*, 96:118002, Mar 2006.

[16] A. Baldassarri, U. Marini Bettolo Marconi, and A. Puglisi. Cooling of a lattice granular fluid as an ordering process. *Phys. Rev. E*, 65:051301, May 2002.

[17] A. Baldassarri, A. Puglisi, and A. Prados. Hydrodynamics of granular particles on a line. *Phys. Rev. E*, 97:062905, Jun 2018.

[18] A. Baldassarri, A. Puglisi, and A. Sarracino. Coarsening in granular systems. *C. R. Physique*, 16:291–302, 2015.

[19] M. Baldovin, F. Cecconi, M. Cencini, A. Puglisi, and A. Vulpiani. The role of data in model building and prediction: A survey through examples. *Entropy*, 20:807, 2018.

[20] M. Baldovin, A. Puglisi, and A. Vulpiani. Langevin equation in systems with also negative temperatures. *J. Stat. Mech.*, 2018(4):043207, apr 2018.

[21] M. Baldovin, A. Puglisi, and A. Vulpiani. Langevin equations from experimental data: The case of rotational diffusion in granular media. *PLoS ONE*, 14:e0212135, 2019.

[22] L. Banchi and R. Vaia. Spectral problem for quasi-uniform nearest-neighbor chains. *Journal of Mathematical Physics*, 54(4):043501, 2013.

[23] R. Bartussek, P. Hänggi, and J. G. Kissner. Periodically rocked thermal ratchets. *EPL (Europhysics Letters)*, 28(7):459–464, dec 1994.

[24] C. Battle, C. P. Broedersz, N. Fakhri, V. F. Geyer, J. Howard, C. F. Schmidt, and F. C. MacKintosh. Broken detailed balance at mesoscopic scales in active biological systems. *Science*, 352(6285):604–607, 2016.

[25] R. P. Behringer and B. Chakraborty. The physics of jamming for granular materials: a review. *Reports on Progress in Physics*, 82(1):012601, nov 2018.

[26] O. Bénichou, P. Illien, G. Oshanin, A. Sarracino, and R. Voituriez. Microscopic theory for negative differential mobility in crowded environments. *Phys. Rev. Lett.*, 113:268002, Dec 2014.

[27] D. Bi, S. Henkes, K. E. Daniels, and B. Chakraborty. The statistical physics of athermal materials. *Annual Review of Condensed Matter Physics*, 6(1):63–83, 2015.

[28] D. Bi, J. Zhang, R. P. Behringer, and B. Chakraborty. Fluctuations in shear-jammed states: A statistical ensemble approach. *EPL (Europhysics Letters)*, 102(3):34002, may 2013.

[29] G. Bird. *Molecular Gas Dynamics*. Clarendon Press, Oxford, 1976.

[30] G. Bird. *Molecular Gas Dynamics and the Direct Simulation of Gas Flows*. Clarendon Press, Oxford, 1994.

[31] C. Bizon, M. D. Shattuck, J. B. Swift, W. D. McCormick, and H. L. Swinney. Patterns in 3d vertically oscillated granular layers: Simulation and experiment. *Phys. Rev. Lett.*, 80(1):57–60, 1998.

[32] M. E. Blake. *Ancient Roman Construction in Italy From the Prehistoric Period to Augustus*. Carnegie Institution of Washington, Washington D. C., 1947.

[33] J.-P. Bouchaud. The subtle nature of financial random walks. *Chaos: An Interdisciplinary Journal of Nonlinear Science*, 15(2):026104, 2005.

[34] A. P. J. Breu, H.-M. Ensner, C. A. Kruelle, and I. Rehberg. Reversing the brazil-nut effect: Competition between percolation and condensation. *Phys. Rev. Lett.*, 90:014302, Jan 2003.

[35] J. Brey, A. Prados, and B. Sanchez-Rey. Thermodynamic description in a simple model for granular compaction. *Physica A: Statistical Mechanics and its Applications*, 275(3):310–324, 2000.

[36] J. J. Brey, J. W. Dufty, C. S. Kim, and A. Santos. Hydrodynamics for granular flow at low density. *Phys. Rev. E*, 58:4638–4653, 1998.

[37] N. Brilliantov and T. Pöschel. *Kinetic Theory of Granular Gases*. Oxford University Press, London, 2010.

[38] N. V. Brilliantov, A. Formella, and T. Pöschel. Increasing temperature of cooling granular gases. *Nature Communications*, 9(1):797, Feb 2018.

[39] N. V. Brilliantov, F. Spahn, J.-M. Hertzsch, and T. Pöschel. Model for collisions in granular gases. *Phys. Rev. E*, 53:5382–5392, May 1996.

[40] R. Brown. Xxvii. a brief account of microscopical observations made in the months of june, july and august 1827, on the particles contained in the pollen of plants; and on the general existence of active molecules in organic and inorganic bodies. *The Philosophical Magazine*, 4(21):161–173, 1828.

[41] E. Caglioti, V. Loreto, H. J. Herrmann, and M. Nicodemi. A "tetris-like" model for the compaction of dry granular media. *Phys. Rev. Lett.*, 79:1575–1578, Aug 1997.

[42] R. Capozza, A. Vanossi, A. Vezzani, and S. Zapperi. Suppression of friction by mechanical vibrations. *Phys. Rev. Lett.*, 103:085502, Aug 2009.

[43] L. Caprini and U. M. B. Marconi. Time-dependent properties of interacting active matter: Dynamical behavior of one-dimensional systems of self-propelled particles. *Phys. Rev. Research*, 2:033518, Sep 2020.

[44] L. Caprini, U. Marini Bettolo Marconi, and A. Puglisi. Spontaneous velocity alignment in motility-induced phase separation. *Phys. Rev. Lett.*, 124:078001, Feb 2020.

[45] A. Cavagna, A. Cimarelli, I. Giardina, G. Parisi, R. Santagati, F. Stefanini, and M. Viale. Scale-free correlations in starling flocks. *Proceedings of the National Academy of Sciences*, 107(26):11865–11870, 2010.

[46] F. Cecconi, M. Cencini, and A. Vulpiani. Transport properties of chaotic and non-chaotic many particle systems. *J. Stat. Mech.*, 2007(12):P12001, 2007.

[47] C. Cercignani. *Theory and application of the Boltzmann equation.* Elsevier, New York, 1975.

[48] J. P. D. Clewett, K. Roeller, R. M. Bowley, S. Herminghaus, and M. R. Swift. Emergent surface tension in vibrated, noncohesive granular media. *Phys. Rev. Lett.*, 109:228002, Nov 2012.

[49] L. A. Cobus, S. E. Skipetrov, A. Aubry, B. A. van Tiggelen, A. Derode, and J. H. Page. Anderson mobility gap probed by dynamic coherent backscattering. *Phys. Rev. Lett.*, 116:193901, May 2016.

[50] A. Coniglio, H. J. Herrmann, and M. Nicodemi. *Unifying Concepts in Granular Media and Glasses.* Elsevier, Amsterdam, 2004.

[51] G. Costantini, U. Marini Bettolo Marconi, and A. Puglisi. Granular Brownian ratchet model. *Phys. Rev. E*, 75:061124, Jun 2007.

[52] C. Coulais, R. P. Behringer, and O. Dauchot. How the ideal jamming point illuminates the world of granular media. *Soft Matter*, 10:1519–1536, 2014.

[53] P. Coussot. *Rheometry of Pastes, Suspensions, and GranularMaterials: Applications in Industry and Environment.* John Wiley & Sons, New York, 2005.

[54] E. D. Cubuk, S. S. Schoenholz, J. M. Rieser, B. D. Malone, J. Rottler, D. J. Durian, E. Kaxiras, and A. J. Liu. Identifying structural flow defects in disordered solids using machine-learning methods. *Phys. Rev. Lett.*, 114:108001, Mar 2015.

[55] P. A. Cundall and O. D. L. Strack. A discrete numerical model for granular assemblies. *Géotechnique*, 29(1):47–65, 1979.

[56] K. E. Daniels and R. P. Behringer. Hysteresis and competition between disorder and crystallization in sheared and vibrated granular flow. *Phys. Rev. Lett.*, 94:168001, Apr 2005.

[57] O. Dauchot, G. Marty, and G. Biroli. Dynamical heterogeneity close to the jamming transition in a sheared granular material. *Phys. Rev. Lett.*, 95:265701, Dec 2005.

[58] L. de Arcangelis, E. Lippiello, M. Pica Ciamarra, and A. Sarracino. Induced and endogenous acoustic oscillations in granular faults. *Philosophical Transactions of the Royal Society A: Mathematical, Physical and Engineering Sciences*, 377(2136):20170389, 2019.

[59] P. G. de Gennes. Granular matter: a tentative view. *Rev. Mod. Phys.*, 71:S374–S382, Mar 1999.

[60] J. Deseigne, O. Dauchot, and H. Chaté. Collective motion of vibrated polar disks. *Phys. Rev. Lett.*, 105:098001, Aug 2010.

[61] R. Di Leonardo, L. Angelani, D. Dell'Arciprete, G. Ruocco, V. Iebba, S. Schippa, M. P. Conte, F. Mecarini, F. De Angelis, and E. Di Fabrizio. Bacterial ratchet motors. *Proceedings of the National Academy of Sciences*, 107(21):9541–9545, 2010.

[62] A. Di Renzo and F. P. Di Maio. Comparison of contact-force models for the simulation of collisions in DEM-based granular flow codes. *Chemical Engineering Science*, 59(3):525–541, 2004.

[63] T. J. Doerries, S. A. M. Loos, and S. H. L. Klapp. Correlation functions of non-Markovian systems out of equilibrium: analytical expressions beyond single-exponential memory. *J. Stat. Mech.*, 2021(3):033202, mar 2021.

[64] R. Díaz Hernández Rojas, G. Parisi, and F. Ricci-Tersenghi. Inferring the particle-wise dynamics of amorphous solids from the local structure at the jamming point. *Soft Matter*, 17:1056–1083, 2021.

[65] S. Edwards. *Granular Matter: An Interdisciplinary Approach*. Springer- Verlag, New York, 1994.

[66] S. Edwards and R. Oakeshott. Theory of powders. *Physica A: Statistical Mechanics and its Applications*, 157(3):1080–1090, 1989.

[67] A. Einstein. *Investigations on the Theory of the Brownian Movement*. Dover, New York, 1956.

[68] P. Eshuis, K. van der Weele, D. Lohse, and D. van der Meer. Experimental realization of a rotational ratchet in a granular gas. *Phys. Rev. Lett.*, 104:248001, Jun 2010.

[69] P. Eshuis, K. van der Weele, D. van der Meer, R. Bos, and D. Lohse. Phase diagram of vertically shaken granular matter. *Physics of Fluids*, 19(12):123301, 2007.

[70] F. Evers and A. D. Mirlin. Anderson transitions. *Rev. Mod. Phys.*, 80:1355–1417, Oct 2008.

[71] G. Falasco, M. Baiesi, L. Molinaro, L. Conti, and F. Baldovin. Energy repartition for a harmonic chain with local reservoirs. *Phys. Rev. E*, 92:022129, Aug 2015.

[72] M. Falcioni and A. Vulpiani. *Meccanica Statistica Elementare*. Springer-Verlag, Mailand, 2015.

[73] K. Feitosa and N. Menon. Fluidized granular medium as an instance of the fluctuation theorem. *Phys. Rev. Lett.*, 92:164301, Apr 2004.

[74] R. P. Feynman, R. B. Leighton, and M. Sands. *The Feynman Lectures on Physics*, volume 1. Reading, MA: Addison-Wesley, 1963.

[75] R. Friedrich, J. Peinke, and C. Renner. How to quantify deterministic and random influences on the statistics of the foreign exchange market. *Phys. Rev. Lett.*, 84:5224–5227, May 2000.

[76] C. Gardiner. *Stochastic Methods*. Springer-Verlag, Berlin, 2009.

[77] F. Giacco, L. de Arcangelis, M. Pica Ciamarra, and E. Lippiello. Rattler-induced aging dynamics in jammed granular systems. *Soft Matter*, 13:9132–9137, 2017.

[78] F. Giacco, L. Saggese, L. de Arcangelis, E. Lippiello, and M. Pica Ciamarra. Dynamic weakening by acoustic fluidization during stick-slip motion. *Phys. Rev. Lett.*, 115:128001, Sep 2015.

[79] A. Gnoli, L. de Arcangelis, F. Giacco, E. Lippiello, M. P. Ciamarra, A. Puglisi, and A. Sarracino. Controlled viscosity in dense granular materials. *Phys. Rev. Lett.*, 120:138001, Mar 2018.

[80] A. Gnoli, A. Lasanta, A. Sarracino, and A. Puglisi. Unified rheology of vibro-fluidized dry granular media: From slow dense flows to fast gas-like regimes. *Scientific Reports*, 6(1):38604, Dec 2016.

[81] A. Gnoli, A. Petri, F. Dalton, G. Pontuale, G. Gradenigo, A. Sarracino, and A. Puglisi. Brownian ratchet in a thermal bath driven by Coulomb friction. *Phys. Rev. Lett.*, 110:120601, Mar 2013.

[82] A. Gnoli, A. Puglisi, A. Sarracino, and A. Vulpiani. Nonequilibrium Brownian motion beyond the effective temperature. *PLoS ONE*, 9(4):5–9, 2014.

[83] A. Gnoli, A. Sarracino, A. Puglisi, and A. Petri. Nonequilibrium fluctuations in a frictional granular motor: Experiments and kinetic theory. *Phys. Rev. E*, 87:052209, May 2013.

[84] G. Gradenigo and E. Bertin. Generalized Edwards thermodynamics and marginal stability in a driven system with dry and viscous friction. *Phys. Rev. E*, 95:030106, Mar 2017.

[85] G. Gradenigo, E. E. Ferrero, E. Bertin, and J.-L. Barrat. Edwards thermodynamics for a driven athermal system with dry friction. *Phys. Rev. Lett.*, 115:140601, Sep 2015.

[86] G. Gradenigo, A. Sarracino, D. Villamaina, T. S. Grigera, and A. Puglisi. The ratchet effect in an ageing glass. *J. Stat. Mech.*, 2010:L12002, 2010.

[87] G. Gradenigo, A. Sarracino, D. Villamaina, and A. Puglisi. Fluctuating hydrodynamics and correlation lengths in a driven granular fluid. *J. Stat. Mech.*, 2011(8), 2011.

[88] L. Hagen. Über den Druck und die Bewegung des trockenen Sandes. *Monatsberichte der königlich, preußischen Akademie der Wissenschaften zu Berlin*, page 35, 19. Jan. 1852.

[89] P. Hänggi and F. Marchesoni. Artificial brownian Motors: Controlling transport on the nanoscale. *Rev. Mod. Phys.*, 81:387–442, Mar 2009.

[90] S. Havlin, J. E. Kiefer, and G. H. Weiss. Anomalous diffusion on a random comblike structure. *Phys. Rev. A*, 36:1403–1408, Aug 1987.

[91] M. Heckel, A. Sack, J. Kollmer, and T. Pöschel. Granular dampers for the reduction of vibrations of an oscillatory saw. *Physica A: Statistical Mechanics and its Applications*, 391:4442–4447, 10 2012.

[92] H. G. E. Hentschel, I. Procaccia, and S. Roy. Diffusion in agitated frictional granular matter near the jamming transition. *Phys. Rev. E*, 100:042902, Oct 2019.

[93] H. Hu, A. Strybulevych, J. H. Page, S. E. Skipetrov, and B. A. van Tiggelen. Localization of ultrasound in a three-dimensional elastic network. *Nature Physics*, 4(12):945–948, Dec 2008.

[94] T. Hughes. *The Finite Element Method: Linear Static and Dynamic Finite Element Analysis*, volume 78. Dover Publications, INC., Mineola, New York, 01 2000.

[95] R. Ishiwata, R. Yaguchi, and Y. Sugiyama. Correlations and responses for a system of n coupled linear oscillators with asymmetric interactions. *Phys. Rev. E*, 102:012150, Jul 2020.

[96] F. Jacob. *Of Flies, Mice, and Men.* Harvard University Press, Cambridge, Massachusetts and London, England, 1998 (translated from french by G. Weiss).

[97] H. M. Jaeger, S. R. Nagel, and R. P. Behringer. Granular solids, liquids, and gases. *Rev. Mod. Phys.*, 68:1259–1273, Oct 1996.

[98] H. Janssen. *Z. Ver. Dt. Ing.*, 39:1045, 1895.

[99] P. Jop, Y. Forterre, and O. Pouliquen. A constitutive law for dense granular flows. *Nature*, 441(7094):727–730, Jun 2006.

[100] L. P. Kadanoff. Built upon sand: Theoretical ideas inspired by granular flows. *Rev. Mod. Phys.*, 71:435–444, Jan 1999.

[101] A. S. Keys, A. R. Abate, S. C. Glotzer, and D. J. Durian. Measurement of growing dynamical length scales and prediction of the jamming transition in a granular material. *Nature Physics*, 3(4):260–264, 2007.

[102] R. Khosropour, J. Zirinsky, H. K. Pak, and R. P. Behringer. Convection and size segregation in a couette flow of granular material. *Phys. Rev. E*, 56(4):4467–4473, 1997.

[103] R. Klages, G. Radons, and I. M. Sokolov. *Anomalous Transport.* Wiley-VCH, 2008.

[104] T. M. Knowlton, G. E. Klinzing, W. C. Yang, and J. W. Carson. The importance of storage, transfer, and collection. *Chemical Engineering Progress; (United States)*, 90:4, 4 1994.

[105] B. Kou, Y. Cao, J. Li, C. Xia, Z. Li, H. Dong, A. Zhang, J. Zhang, W. Kob, and Y. Wang. Granular materials flow like complex fluids. *Nature*, 551(7680):360–363, Nov 2017.

[106] W. T. Kranz, F. Frahsa, A. Zippelius, M. Fuchs, and M. Sperl. Integration through transients for inelastic hard sphere fluids. *Phys. Rev. Fluids*, 5:024305, Feb 2020.

[107] W. T. Kranz, M. Sperl, and A. Zippelius. Glass transition for driven granular fluids. *Phys. Rev. Lett.*, 104:225701, Jun 2010.

[108] A. Kudrolli and J. Henry. Non-Gaussian velocity distributions in excited granular matter in the absence of clustering. *Phys. Rev. E*, 62(2):R1489–92, 2000.

[109] A. Kudrolli, M. Wolpert, and J. P. Gollub. Cluster formation due to collisions in granular material. *Phys. Rev. Lett.*, 78(7):1383–1386, 1997.

[110] K. V. Kumar, S. Ramaswamy, and M. Rao. Active elastic dimers: Self-propulsion and current reversal on a featureless track. *Phys. Rev. E*, 77:020102(R), Feb 2008.

[111] V. Kumaran. Temperature of a granular material "fluidized" by external vibrations. *Phys. Rev. E*, 57:5660–5664, May 1998.

[112] A. Lasanta, A. Manacorda, A. Prados, and A. Puglisi. Fluctuating hydrodynamics and mesoscopic effects of spatial correlations in dissipative systems with conserved momentum. *New J. Phys.*, 17(8):083039, 2015.

[113] A. Lasanta and A. Puglisi. An itinerant oscillator model with cage inertia for mesorheological granular experiments. *Journal of Chemical Physics*, 143(6), 2015.

[114] J. Laskar, F. Joutel, and F. Boudin. Orbital, precessional, and insolation quantities for the earth from -20 myr to +10 myr. *Astronomy and Astrophysics*, 270:522–533, 1993.

[115] H. Lastakowski, J.-C. Géminard, and V. Vidal. Granular friction: Triggering large events with small vibrations. *Scientific Reports*, 5(1):13455, Sep 2015.

[116] P. A. Lee and T. V. Ramakrishnan. Disordered electronic systems. *Rev. Mod. Phys.*, 57:287–337, Apr 1985.

[117] D. S. Lemons and A. Gythiel. Paul Langevin's 1908 paper "On the Theory of Brownian Motion" ["Sur la théorie du mouvement brownien," C. R. Acad. Sci. (Paris), 530–533 (1908)]. *American Journal of Physics*, 65(11):1079–1081, 1997.

[118] B. D. Lubachevsky. How to simulate billiards and similar systems. *Journal of Computational Physics*, 94(2):255–283, 1991.

[119] S. Luding. From microscopic simulations to macroscopic material behavior. *Computer Physics Communications*, 147(1):134–140, 2002. Proceedings of the Europhysics Conference on Computational Physics Computational Modeling and Simulation of Complex Systems.

[120] S. Luding, E. Clément, A. Blumen, J. Rajchenbach, and J. Duran. Anomalous energy dissipation in molecular-dynamics simulations of grains: The "detachment" effect. *Phys. Rev. E*, 50:4113–4122, Nov 1994.

[121] C. Lutz, M. Kollmann, and C. Bechinger. Single-file diffusion of colloids in one-dimensional channels. *Phys. Rev. Lett.*, 93:026001, Jul 2004.

[122] C. Maggi, U. M. B. Marconi, N. Gnan, and R. Di Leonardo. Multidimensional stationary probability distribution for interacting active particles. *Scientific reports*, 5:10742, 2015.

[123] A. Manacorda, C. A. Plata, A. Lasanta, A. Puglisi, and A. Prados. Lattice models for granular-like velocity fields: hydrodynamic description. *J. Stat. Phys.*, 164(4):810–841, 2016.

[124] U. M. B. Marconi, A. Puglisi, L. Rondoni, and A. Vulpiani. Fluctuation–dissipation: Response theory in statistical physics. *Physics Reports*, 461(4):111 – 195, 2008.

[125] G. Marty and O. Dauchot. Subdiffusion and cage effect in a sheared granular material. *Phys. Rev. Lett.*, 94:015701, Jan 2005.

[126] J. D. Maynard. Acoustical analogs of condensed-matter problems. *Rev. Mod. Phys.*, 73:401–417, May 2001.

[127] S. McNamara and S. Luding. Energy flows in vibrated granular media. *Phys. Rev. E*, 58:813–822, Jul 1998.

[128] S. Miller and S. Luding. Event-driven molecular dynamics in parallel. *Journal of Computational Physics*, 193(1):306–316, 2004.

[129] J. M. Montanero and A. Santos. Monte carlo simulation method for the Enskog equation. *Phys. Rev. E*, 54:438–444, Jul 1996.

[130] C. F. Moukarzel, G. Peraza-Mues, and O. Carvente. Rotational transport via spontaneous symmetry breaking in vibrated disk packings. *Phys. Rev. Lett.*, 125:028001, Jul 2020.

[131] M.Tuckerman. *Statistical Mechanics: Theory and Molecular Simulation*. Oxford University Press, Oxford, 2008.

[132] R. Munroe. What makes sand soft? *The New York Times*, Nov. 10 2020.

[133] F. Mura, G. Gradziuk, and C. P. Broedersz. Nonequilibrium scaling behavior in driven soft biological assemblies. *Phys. Rev. Lett.*, 121:038002, Jul 2018.

[134] R. Méndez-Sánchez, L. Gutiérrez, A. Morales, J. Flores, A. Díaz-de Anda, and G. Monsivais. Anderson localization phenomenon in one-dimensional elastic systems. *Acta Physica Polonica A*, 124:1063, Dec 2013.

[135] S. R. Nagel. Experimental soft-matter science. *Rev. Mod. Phys.*, 89:025002, Apr 2017.

[136] M. Nakagawa, S. A. Altobelli, A. Caprihan, E. Fukushima, and E.-K. Jeong. Non-invasive measurements of granular flows by magnetic resonance imaging. *Experiments in Fluids*, 16(1):54–60, Nov 1993.

[137] J. P. Oleson, C. Brandon, S. M. Cramer, R. Cucitore, E. Gotti, and R. L. Hohlfelder. The romacons project: a contribution to the historical and engineering analysis of hydraulic concrete in roman maritime structures. *International Journal of Nautical Archaeology*, 33(2):199–229, 2004.

[138] L. Onsager and S. Machlup. Fluctuations and irreversible processes. *Phys. Rev.*, 91:1505–1512, Sep 1953.

[139] R. Pagnani, U. M. Bettolo Marconi, and A. Puglisi. Driven low density granular mixtures. *Phys. Rev. E*, 66:051304, Nov 2002.

[140] D. J. Parker. Positron emission particle tracking and its application to granular media. *Review of Scientific Instruments*, 88(5):051803, 2017.

[141] J. Perrin. *Gli Atomi*. Editori Riuniti, Roma, 1981.

[142] P. Philippe and D. Bideau. Compaction dynamics of a granular medium under vertical tapping. *EPL (Europhysics Letters)*, 60(5):677–683, dec 2002.

[143] C. Plata, A. Manacorda, A. Lasanta, A. Puglisi, and A. Prados. Lattice models for granular-like velocity fields: finite-size effects. *J. Stat. Mech.*, 2016(9):093203, 2016.

[144] A. Plati, A. Baldassarri, A. Gnoli, G. Gradenigo, and A. Puglisi. Dynamical collective memory in fluidized granular materials. *Phys. Rev. Lett.*, 123:038002, Jul 2019.

[145] A. Plati, L. de Arcangelis, A. Gnoli, E. Lippiello, A. Puglisi, and A. Sarracino. Getting hotter by heating less: How driven granular materials dissipate energy in excess. *Phys. Rev. Research*, 3:013011, Jan 2021.

[146] A. Plati and A. Puglisi. Slow time scales in a dense vibrofluidized granular material. *Phys. Rev. E*, 102:012908, Jul 2020.

[147] A. Plati and A. Puglisi. Collective drifts in vibrated granular packings: the interplay of friction and structure. *Preprint arXiv:2110.07931*, 2021.

[148] A. Plati and A. Puglisi. Long range correlations and slow time scales in a boundary driven granular model. *Scientific Reports*, 11(1):14206, Jul 2021.

[149] S. Plimpton. Fast parallel algorithms for short-range molecular dynamics. *Journal of Computational Physics*, 117(1):1–19, 1995.

[150] G. Pontuale, A. Gnoli, F. V. Reyes, and A. Puglisi. Thermal convection in granular gases with dissipative lateral walls. *Phys. Rev. Lett.*, 117:098006, Aug 2016.

[151] V. L. Popov. *Contact Mechanics and Friction*. Springer-Verlag, Berlin, 2010.

[152] T. Pöschel and T. Schwager. *Computational Granular Dynamics*. Springer, Berlin, 2005.

[153] A. Puglisi, A. Gnoli, G. Gradenigo, A. Sarracino, and D. Villamaina. Structure factors in granular experiments with homogeneous fluidization. *The Journal of Chemical Physics*, 136(1):014704, 2012.

[154] A. Puglisi, V. Loreto, U. M. B. Marconi, A. Petri, and A. Vulpiani. Clustering and non-Gaussian behavior in granular matter. *Phys. Rev. Lett.*, 81:3848–3851, 1998.

[155] A. Puglisi, V. Loreto, U. Marini Bettolo Marconi, and A. Vulpiani. Kinetic approach to granular gases. *Phys. Rev. E*, 59:5582–5595, May 1999.

[156] A. Puglisi, A. Sarracino, G. Gradenigo, and D. Villamaina. Dynamics of a massive intruder in a homogeneously driven granular fluid. *Granular Matter*, 14(2):235–238, Apr 2012.

[157] A. Puglisi, A. Sarracino, and A. Vulpiani. Temperature in and out of equilibrium: A review of concepts, tools and attempts. *Physics Reports*, 709-710:1–60, 2017.

[158] A. Puglisi and D. Villamaina. Irreversible effects of memory. *EPL (Europhysics Letters)*, 88(3):30004, nov 2009.

[159] A. Puglisi, P. Visco, A. Barrat, E. Trizac, and F. van Wijland. Fluctuations of internal energy flow in a vibrated granular gas. *Phys. Rev. Lett.*, 95:110202, Sep 2005.

[160] M. Rackl and K. J. Hanley. A methodical calibration procedure for discrete element models. *Powder Technology*, 307:73–83, 2017.

[161] A. Rahman. Correlations in the motion of atoms in liquid argon. *Phys. Rev.*, 136:A405–A411, Oct 1964.

[162] P. Reimann. Brownian Motors: noisy transport far from equilibrium. *Physics Reports*, 361(2):57–265, 2002.

[163] G. Reydellet, F. Rioual, and E. Clément. Granular hydrodynamics and density wave regimes in a vertical chute experiment. *EPL (Europhysics Letters)*, 51(1):27–33, jul 2000.

[164] P. Richard, M. Nicodemi, R. Delannay, P. Ribière, and D. Bideau. Slow relaxation and compaction of granular systems. *Nature Materials*, 4(2):121–128, Feb 2005.

[165] K. Ridgway and R. Rupp. Flow of granular material down chutes. *Chem. Proc. Eng.*, 51:82, 1970.

[166] Z. Rieder, J. L. Lebowitz, and E. Lieb. Properties of a harmonic crystal in a stationary nonequilibrium state. *Journal of Mathematical Physics*, 8(5):1073–1078, 1967.

[167] H. Risken. *The Fokker–Planck equation: Methods of Solution and Applications.* Springer, Berlin, 1989.

[168] N. Rivas, S. Luding, and A. R. Thornton. Low-frequency oscillations in narrow vibrated granular systems. *New Journal of Physics*, 15(11):113043, nov 2013.

[169] M. Rodhes. *Principles of powder technology.* John Wiley and Sons, 1997.

[170] R. J. Rubin. Statistical dynamics of simple cubic lattices. model for the study of Brownian motion. *Journal of Mathematical Physics*, 1(4):309–318, 1960.

[171] M. Saeki. Impact damping with granular materials in a horizontally vibrating system. *Journal of Sound and Vibration*, 251(1):153–161, 2002.

[172] A. Sarracino, F. Cecconi, A. Puglisi, and A. Vulpiani. Nonlinear response of inertial tracers in steady laminar flows: Differential and absolute negative mobility. *Phys. Rev. Lett.*, 117:174501, Oct 2016.

[173] A. Sarracino, D. Villamaina, G. Costantini, and A. Puglisi. Granular Brownian motion. *J. Stat. Mech.*, 04013:P04013–P04030, 2010.

[174] A. Sarracino, D. Villamaina, G. Gradenigo, and A. Puglisi. Irreversible dynamics of a massive intruder in dense granular fluids. *EPL (Europhysics Letters)*, 92(3):34001, 2010.

[175] S. B. Savage and M. Sayed. Stresses developed by dry cohesionless granular materials sheared in an annular shear cell. *J. Fluid Mech.*, 142:391–430, 1984.

[176] C. Scalliet, A. Gnoli, A. Puglisi, and A. Vulpiani. Cages and anomalous diffusion in vibrated dense granular media. *Phys. Rev. Lett.*, 114:198001, May 2015.

[177] M. Schienbein and H. Gruler. Langevin equation, fokker-planck equation and cell migration. *Bulletin of Mathematical Biology*, 55(3):585–608, May 1993.

[178] M. Schröter, D. I. Goldman, and H. L. Swinney. Stationary state volume fluctuations in a granular medium. *Phys. Rev. E*, 71:030301, Mar 2005.

[179] M. Schröter, S. Ulrich, J. Kreft, J. B. Swift, and H. L. Swinney. Mechanisms in the size segregation of a binary granular mixture. *Phys. Rev. E*, 74:011307, Jul 2006.

[180] Z. Schwartzman-Nowik, E. Lerner, and E. Bouchbinder. Anisotropic structural predictor in glassy materials. *Phys. Rev. E*, 99:060601(R), Jun 2019.

[181] V. F. Sears. The itinerant oscillator model of liquids. *Proceedings of the Physical Society*, 86(5):953–964, nov 1965.

[182] J.-E. Shea and I. Oppenheim. Fokker-Planck equation and Langevin equation for one Brownian particle in a nonequilibrium bath. *The Journal of Physical Chemistry*, 100(49):19035–19042, 1996.

[183] M. F. Shlesinger, B. J. West, and J. Klafter. Lévy dynamics of enhanced diffusion: Application to turbulence. *Phys. Rev. Lett.*, 58:1100–1103, Mar 1987.

[184] L. E. Silbert, D. Ertaş, G. S. Grest, T. C. Halsey, D. Levine, and S. J. Plimpton. Granular flow down an inclined plane: Bagnold scaling and rheology. *Phys. Rev. E*, 64:051302, Oct 2001.

[185] M. Smoluchowski. Zur kinetischen theorie der brownschen molekularbewegung und der suspensionen. *Ann. Phys., NY*, 21:756, 1906.

[186] M. Smoluchowski. Experimentell nachweisbare, der üblichen thermodynamik widersprechende molekularphänomene. *Physik. Zeitschr.*, 13:1069, 1912.

[187] I. M. Sokolov. Models of anomalous diffusion in crowded environments. *Soft Matter*, 8:9043–9052, 2012.

[188] M. Sperl, W. T. Kranz, and A. Zippelius. Single-particle dynamics in dense granular fluids under driving. *EPL (Europhysics Letters)*, 98(2):28001, apr 2012.

[189] A. Stukowski. Visualization and analysis of atomistic simulation data with ovito-the open visualization tool. *Modeling and Simulation in Materials Science and Engineering*, 18(1), Jan 2010.

[190] J. Tang and R. P. Behringer. How granular materials jam in a hopper. *Chaos: An Interdisciplinary Journal of Nonlinear Science*, 21(4):041107, 2011.

[191] H. Tong and H. Tanaka. Revealing hidden structural order controlling both fast and slow glassy dynamics in supercooled liquids. *Phys. Rev. X*, 8:011041, Mar 2018.

[192] L. Trujillo, M. Alam, and H. J. Herrmann. Segregation in a fluidized binary granular mixture: Competition between buoyancy and geometric forces. *EPL (Europhysics Letters)*, 64(2):190–196, oct 2003.

[193] R. Turner. Motion of a heavy particle in a one dimensional chain. *Physica*, 26(4):269–273, 1960.

[194] P. B. Umbanhowar, F. Melo, and H. L. Swinney. Localized excitations in a vertically vibrated granular layer. *Nature*, 382:793–796, 1996.

[195] C. Van den Broeck, R. Kawai, and P. Meurs. Microscopic analysis of a thermal Brownian Motor. *Phys. Rev. Lett.*, 93:090601, Aug 2004.

[196] M. van den Broek, R. Eichhorn, and C. V. den Broeck. Intrinsic ratchets. *EPL (Europhysics Letters)*, 86(3):30002, may 2009.

[197] D. van der Meer, P. Reimann, K. van der Weele, and D. Lohse. Spontaneous ratchet effect in a granular gas. *Phys. Rev. Lett.*, 92:184301, May 2004.

[198] N. G. van Kampen. A power series expansion of the master equation. *Canadian Journal of Physics*, 39:551, 1961.

[199] T. Van Noije, M. Ernst, R. Brito, and J. Orza. Mesoscopic theory of granular fluids. *Phys. Rev. Lett.*, 79:411, 1997.

[200] A. Vespignani and G. Caldarelli. *Large Scale Structure and Dynamics of Complex Networks: From information technology to finance and natural science.* World Scientific Publishing Co. Pte. Ltd., 5 Toh Tuck Link, Singapore 596224, 2007.

[201] V. Vidal, C. Oliver, H. Lastakowski, G. Varas, and J.-C. Géminard. Friction weakening by mechanical vibrations: A velocity-controlled process. *The European Physical Journal E*, 42(7):91, Jul 2019.

[202] D. Villamaina, A. Baldassarri, A. Puglisi, and A. Vulpiani. The fluctuation-dissipation relation: how does one compare correlation functions and responses? *J. Stat. Mech.*, 2009(07):P07024, 2009.

[203] P. Visco. Work fluctuations for a Brownian particle between two thermostats. *J. Stat. Mech.*, 2006:06006, 2006.

[204] H. D. Vollmer. Two particle model for the diffusion of interacting particles in periodic potentials. *Zeitschrift für Physik B Condensed Matter*, 33(1):103–109, Mar 1979.

[205] S. Warr, J. M. Huntley, and G. T. H. Jacques. Fluidization of a two-dimensional granular system: Experimental study and scaling behavior. *Phys. Rev. E*, 52:5583–5595, Nov 1995.

[206] C. A. Weber, T. Hanke, J. Deseigne, S. Léonard, O. Dauchot, E. Frey, and H. Chaté. Long-range ordering of vibrated polar disks. *Phys. Rev. Lett.*, 110:208001, May 2013.

[207] M. B. Weissman. $\frac{1}{f}$ noise and other slow, nonexponential kinetics in condensed matter. *Rev. Mod. Phys.*, 60:537–571, Apr 1988.

[208] J. Wilkie. Numerical methods for stochastic differential equations. *Phys. Rev. E*, 70:017701, Jul 2004.

[209] C. R. K. Windows-Yule, N. Rivas, D. J. Parker, and A. R. Thornton. Low-frequency oscillations and convective phenomena in a density-inverted vibrofluidized granular system. *Phys. Rev. E*, 90:062205, Dec 2014.

[210] C. R. K. Windows-Yule, A. D. Rosato, D. J. Parker, and A. R. Thornton. Maximizing energy transfer in vibrofluidized granular systems. *Phys. Rev. E*, 91:052203, May 2015.

[211] C. R. K. Windows-Yule, A. D. Rosato, A. R. Thornton, and D. J. Parker. Resonance effects on the dynamics of dense granular beds: achieving optimal energy transfer in vibrated granular systems. *New Journal of Physics*, 17(2):023015, feb 2015.

[212] H. P. Zhang and H. A. Makse. Jamming transition in emulsions and granular materials. *Phys. Rev. E*, 72:011301, Jul 2005.

[213] R. K. P. Zia, E. L. Praestgaard, and O. G. Mouritsen. Getting more from pushing less: Negative specific heat and conductivity in nonequilibrium steady states. *American Journal of Physics*, 70(4):384–392, 2002.

[214] V. Zivkovic, M. J. Biggs, and D. H. Glass. Scaling of granular temperature in a vibrated granular bed. *Phys. Rev. E*, 83:031308, Mar 2011.

[215] R. Zwanzig. Nonlinear generalized langevin equations. *J. Stat. Phys.*, 9(3):215–220, Nov 1973.

[216] R. Zwanzig. *Nonequilibrium Statistical Mechanics*. Ofxord University Press, Oxford, 2001.